CONTENTS

FOREWORD

This book is based on my doctoral thesis "Dark Matter in Early-Type Galaxies With X-Ray Haloes. A Spectroscopic Study of Dynamics and Abundance Indices" defended in April 2004 at the Department of Physics, University of Trieste, Italy. Many parts of the text and many figures were updated to include the latest results in the rapidly developing field of research of elliptical galaxies. Also, some completely new portions of the text have been written: the Jeans analysis of a number of ellipticals in Chapters 2 and 3 is added and a section dedicated to globular clusters and planetary nebulae as tracers of the mass in ellipticals at larger distances from the center is included.

The book is organized as follows. In Introduction I give the basic features of elliptical galaxies and present a detailed review of the dark matter research in these galaxies. Particular attention is given to the research of the integrated stellar spectra. In Chapter 1 I present theoretical concepts related to the stellar kinematics in elliptical galaxies; I also describe the reduction procedures which I apply. In this Chapter all observational results regarding galactic kinematics of the galaxies from my samples are given. Dynamical modelling of these galaxies is given in Chapter 2: after introducing basic theoretical concepts I present the modelling results for two- and three-integral modelling procedures. Chapter 3 is dedicated to the galaxies with X-ray haloes: basic formulas related to the hot gas in the X-ray haloes are given and applied to the galaxies from my samples which possess X-ray haloes. A comparison is made between the results for the mass-to-light ratio obtained using this approach and the results obtained using stellar dynamics. In Chapter 4 I study abundance indices for some galaxies from my samples and make comparison with the results from chemodynamical modelling. In Chapter 5 I present the results of the total mass (and the total mass-to-light ratios) of elliptical galaxies based on globular clusters and planetary nebulae; wherever it was possible the comparison with other techniques was done. Finally, in Chapter 6 I draw the conclusions. Some additional information related to mathematical (ill-posed problems and regularization; non-negative least-squares; self-organizing maps), dynamical (orbits in different potentials) and observational (total flux as function of radius) aspects is given in the Appendices; I also present the stellar kinematics and abundance indices in the table form.

I would like to thank my thesis advisors John Danziger and Francesca Matteucci for their help, encouragement and support. They provided guidance and posed interesting and important problems yet allowing me a large amount of freedom in solving them.

I would like to thank the following colleagues from the Trieste Observatory and the Department of Astronomy of the University of Trieste where the biggest part of the work on this book was done for numerous discussions and advice: Simone Zaggia for the help in obtaining spectra of galaxies from the Fornax sample and the help in the data reduction, Antonio Pipino for calculation of different photo-chemical evolution models, Francesco Calura for stimulating discussions about different aspects of elliptical galaxies, Piercarlo Bonifacio for the help with the data reduction. While I was at the Trieste Observatory I had the pleasure to have discussions with the members of the staff of the Observatory/Dept. of Astronomy: Andrea Biviano, Stefano Borgani, Marisa Girardi, Christian Marinoni, Marino Mezzetti, Pierluigi Monaco,

Massimo Persic, Simone Recchi and Paolo Tozzi. I also acknowledge useful discussions that I had during my stay in Trieste with: Paolo Salucci, Giuseppe Bertin, Luca Ciotti, Eduardo Simonneau, Gary Mamon and the late Dennis Sciama. I thank Fabio Mardirossian and Stefano Cristiani for their continual help in their role of the Director of the Trieste Observatory. I express my gratitude to the late Giuliano Giuricin who helped me in the initial phases of this work.

I am grateful to Giuseppe Furlan, the head of the ICTP TRIL (Training and Research in Italian Laboratories) program and Elena Dose, the secretary of the ICTP TRIL program for their continual help during my work on the thesis.

I am grateful to Francesco Bertola for his willingness to referee my thesis and his report. I would like to thank Salvatore Serio, president of the SAIt (Società Astronomica Italiana), for his encouragement.

I would like to express my deepest thanks to my colleague and friend Milan M. Ćirković who initiated and supported the publishing of this book. He carefully read the manuscript and gave me a lot of useful scientific and technical advices which certainly improved the quality of this book.

I would especially like to thank the colleague Slobodan Ninković from the Belgrade Astronomical Observatory for numerous interesting discussions. Big thanks goes to Milan S. Dimitrijević and Zoran Knežević in their role as Director of the Belgrade Astronomical Observatory for their understanding and help. I thank Zoran Knežević for his very useful comments on the manuscript and his help in obtaining financial support for printing of this book. I also thank Luka Č. Popović for his help. I thank my colleague Tatjana Milovanov for a careful typesetting of the manuscript of the book.

I acknowledge the help and interesting discussions with Jelena Milogradov-Turin and Trajko Angelov from the Department of Astronomy of the University of Belgrade.

The spectra of several galaxies were obtained courtesy of Marcella Carollo and Kenneth C. Freeman. Olivier Hainout kindly provided photometry data for IC3370. Nicola Caon kindly provided Fornax galaxies photometry data in machine readable form. I acknowledge the use of the Gauss-Hermite Fourier Fitting Software developed by R.P. van der Marel and M. Franx and the use of the Two-integral Jeans Modelling Software developed by R.P. van der Marel and J.J. Binney. This research has made use of the NASA/IPAC Extragalactic Database (NED) which is operated by the Jet Propulsion Laboratory, California Institute of Technology, under contract with the National Aeronautics and Space Administration.

I would like to thank my late parents, Svetozar (1928-2001) and Ljiljana (1935-2006), and brother, Rastko, for their help, support and encouragement.

I thank my wife, Hana Ovesni, for her love, patience, understanding and a great interest for my work. I am grateful to Kristinka Ovesni, Darinka Ovesni and Goran Miličić for their encouragement and help.

In closing of this brief Foreword, it remains only to thank Ministry of Science and Environmental Protection of the Republic of Serbia for a grant towards printing expenses.

Belgrade,
winter solstice 2006

INTRODUCTION

Galaxies are large systems that contain stars, gas, dust, planets and, most probably, dark matter. A large galaxy can contain $10^{11} - 10^{12}$ stars. The amount of gas and dust can vary from a few percent of the total stellar mass (as in lenticular galaxies) to about ten percent for the most gas-rich objects (spiral galaxies). As noted by Binney and Tremaine (1987), in reply to the statement of Sandage made in 1961 that "galaxies are to astronomy what atoms are to physics", some analogy between galaxies and atoms indeed exists: galaxies are relatively isolated systems and they maintain their identity throughout their lives, except for occasional collisions and mergers with other galaxies and, perhaps, weak interaction with the tenuous intergalactic medium. Also, a galaxy is a dynamical and chemical unit. However, there are some differences: for galaxies the laws from the world of atoms do not hold: a huge number of processes in some galaxy may, but not necessarily, be present in some other galaxy. That is why Binney and Tremaine suggested a more appropriate analogy: the relationship between galaxies and astronomy should be regarded as the relationship between ecosystems and biology — this analogy takes into account their complexity, their relative isolation and their ongoing evolution.

I.1. CLASSIFICATION OF GALAXIES

Galaxies can be classified according to the Hubble's classification system (see Figure 1) into four main types: ellipticals, lenticulars, spirals and irregulars. Early-type (elliptical and lenticular) galaxies belong to the left-hand end of the Hubble's tuning-fork diagram. The original suggestion of E. Hubble was that galaxies evolve from the left-hand end to the right. This suggestion has now been abandoned.

Elliptical galaxies have the surface brightness that falls off smoothly with radius, and in most cases can be fitted by $R^{1/4}$ or de Vaucouleurs law (see e.g. Binney and Merrifield 1998):

$$I(R) = I_e \exp\{-7.67[(R/R_e)^{0.25} - 1]\}, \tag{I.1}$$

where R_e is the effective radius, that is the radius of the isophote containing half of the total luminosity and I_e is the surface brightness at R_e. Thus, the following equation holds:

$$2\int_0^{R_e} \mathrm{d}R\, I(R) 2\pi R = \int_0^{\infty} \mathrm{d}R\, I(R) 2\pi R = 7.22\pi R_e^2 I_e. \tag{I.2}$$

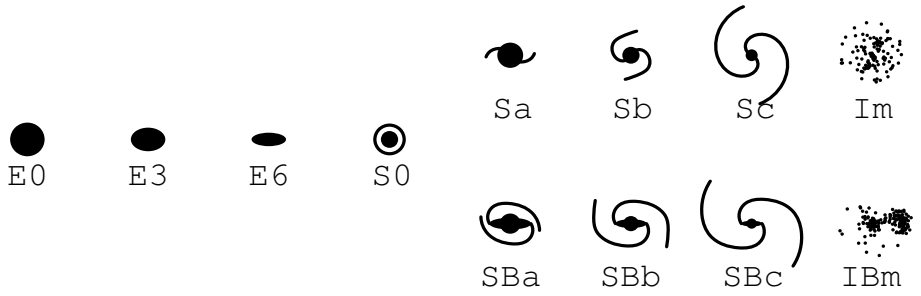

Figure I.1: The Hubble tuning-fork diagram. On the left-hand end there are elliptical galaxies, in the middle there are lenticulars (S0) and on the right-hand end there spirals (Sa⟶Sc) and irregulars. Lower part of the right-hand end is occupied by galaxies with bars (letter "B").

In TABLE (A5-1) in Appendix 5 we give the fraction of the total flux at the given radius; for example, 96 per cent of the total flux of a given galaxy is contained within $10R_e$.

It is however important to note that for some galaxies the brightness profiles show significant departures from the best-fitting $R^{1/4}$ profile. In such cases it is useful to fit the brightness profile by the generalized de Vaucouleurs law (also called the Sersic profile) (see Box 4.1 in Binney and Merrifield 1998):

$$I(R) = I_e \mathrm{e}^{\{-b_n[(R/R_e)^{1/n}-1]\}}, \tag{I.3}$$

where n is a positive real number and b_n is a dimensionless parameter whose value is determined by the definition of effective radius R_e, and is chosen such that half the total luminosity predicted by this law comes from $R < R_e$; for example for $n = 4$ (the case of the Vaucouleurs law), $b_4 = 7.66924944$ (see Ciotti 1991 for details). When Eq. (I.3) is used with $n < 4$ the predicted brightness profile as a function of radius given as $R^{1/4}$ will be placed downwards (the case of low-luminosity elliptical galaxies). If, however, one uses $n > 4$ the model profile curves will be placed upwards in the $R^{1/4}$ plots (this is the case of the very luminous elliptical galaxies, particularly cD galaxies).

The shape of elliptical galaxies varies in form from round to elongated. One can use the simple formula $n = 10[1 - (b/a)]$, where (b/a) denotes the apparent axial ratio, to write the type of these galaxies: En. Therefore, E0 are round galaxies, and E6 are highly elongated systems as seen projected on the sky. In Fig. I.2 (left) it is shown a round galaxy NGC 3379 (type E0, sometimes also classified as E1; see the photometry of this galaxy in Chapter 1) and in the same Figure (right) we show a moderately flattened (E3) galaxy IC 1459; both of these galaxies will be studied in Chapters that follow.

Here it should be noted that in general the line of sight to a given galaxy will be inclined at an angle to a galaxy's equatorial plane. One therefore defines the galaxy's inclination, i as the angle between the normal to the equatorial plane and the line of sight (see Fig. I.3). When $i = 0^\circ$ we speak of the face-on case and when $i = 90^\circ$

we speak of the edge-on case. Majority of galaxies are somewhere in between: i.e. $0 < i < 90°$. With a we denote the major *observed* axis and with b we denote the minor *observed* axis. It can be shown (see for example Binney and Merrifield 1998) that whenever $i < 90°$ it is in principle not possible to determine a galaxy's true shape from observed photometry alone.

Figure I.2: *Left:* Round (E0) galaxy NGC 3379. The image size is 7×7 arcmin. *Right:* Flattened (E3) galaxy IC 1459. The image size is 6.8×6.8 arcmin. Both images were taken by the 2MASS (Two Micron All Sky Survey) project with a 1.3m telescope.

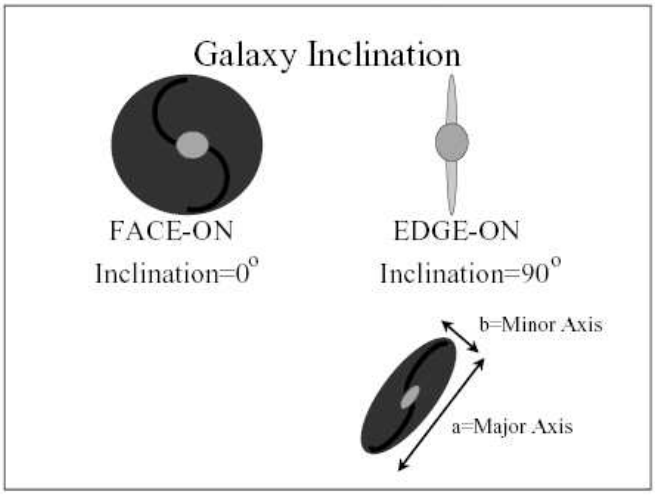

Figure I.3: Inclination of an observed galaxy: two extreme cases ($i = 0°$ is the face-on case and $i = 90°$ is the edge-on case). Majority of galaxies are somewhere in between: $0 < i < 90°$.

Research over the last 20 years has brought new knowledge about ellipticals and we now know that these galaxies are much more complex systems than they were hitherto assumed. The elliptical galaxies contain little or no gas or dust. The old stars that are prevalent are cool, evolved, and therefore of late spectral types. In the middle of the Hubble's diagram there is a class of galaxies designated as type S0, known as lenticular galaxies. They have a smooth central brightness condensation similar to an elliptical galaxy that is surrounded by a large region of less steeply declining brightness. They have disks that do not show any conspicuous structure. Because of their appearance, and also because of their stellar content (e.g., spectral type), they look more like ellipticals rather than spiral galaxies. The problems may arise in the classification of S0 galaxies. For example, for a close well-studied galaxy NGC 3379 it is not certain whether it is a bona fide normal elliptical or a face-on lenticular galaxy. The example of IC 3370 also presented in this book provides another case of a problematic classification (its distance is ~ 42 Mpc, for the Hubble constant $h_0 \sim 0.7$; this value of the Hubble constant will be used throughout this book). The remark of Gregg et al. (2004) therefore seems appropriate: "If after such detailed investigations, we are unable to discern the morphological type of NGC 3379, at a distance of only 10 Mpc, then it is practically impossible to establish the true morphology of other early type galaxies at greater distances in clusters such as Coma, let alone at high redshift".

Spiral galaxies (including our own, Milky Way) consist of three main parts: spheroid, thin disk and dark halo. Spirals contain a prominent disk that is composed of Population I stars, gas, and dust. The disk also contains spiral arms, in which are embedded bright O and B stars, gas, and dust – this is a place in which the stars are currently forming. Hubble divided spirals into a sequence of four classes (types), called Sa, Sb, Sc, and Sd. Along this sequence (Sa$\longrightarrow$ Sd) the relative luminosity of the spheroid (that contains older Population II stars) decreases, the relative mass of the gas increases, and the spiral arms become more loosely wound. The Milky Way is sometimes classified as Sbc, expressing the fact that its Hubble type is between Sb and Sc. Rotation curves of spirals are typically flat, a fact of considerable importance for the dark matter studies (see below).

Irregular galaxies are galaxies where one cannot easily distinguish a particular pattern. The majority of irregulars are low-luminosity gas-rich system such as the Magellanic Clouds (see Fig. I.1 – the letters "I" and "m" refer to irregulars of the type similar to that of the Magellanic Clouds).

I.2. THE DARK MATTER PROBLEM IN EARLY-TYPE GALAXIES

The problem of the dark matter in galaxies remains perhaps the most important astrophysical problem in contemporary cosmology and extragalactic astronomy. Although its nature is still unknown, general opinion is that it exists and that it is a necessary ingredient of every viable cosmological model (see recent overview of the dark matter problem in galaxies in Binney (2003): in that paper the problems of the cold dark

matter (CDM) and Modified Newtonian Dynamics (MOND) theory are presented).[1] In the summer of 2006 the news based on the recent work by D. Clowe and collaborators (Clowe et al. 2006) was highly publicised and drew attention not only in the field of researchers working on the dark matter problem. From their observations of a cluster merger 1E0657-558 (at redshift $z = 0.296$) using gravitational lensing maps they came to the conclusion that the majority of the matter in the system is unseen (dark). Work by Clowe et al. shows that the total mass of the system "cannot be explained with an alternation of the gravitational force law". We need to stress here that this discovery is related to clusters of galaxies, whereas in this book we deal with individual (field) galaxies, galaxies is groups and galaxies in a particular Fornax cluster of galaxies.

The existence of the dark matter in spiral galaxies (late-type galaxies), like our own, Milky Way is rather clear mainly because of existence of cool gas which provides a powerful tool for obtaining rotation curves (that provide dependence of circular speed on radius from the center of the galaxy), that are, for most spirals, nearly flat thus indicating presence of dark mass in their outer parts – dark haloes (see, e.g., Binney and Tremaine 1987, Persic, Salucci and Stel 1996, Sofue and Rubin 2001, Bahcall et al. 2004). There are problems in the determination of its shape, but observations tend to conclude that the dark halo is flattened (see, e.g., Samurović, Ćirković and Milošević-Zdjelar 1999).

However, the problem of dark matter in elliptical (early-type) galaxies is more complicated – it is more difficult to confirm the presence of dark haloes around ellipticals. Since elliptical galaxies contain little or no cool gas usually one cannot use 21-cm observations to trace kinematics of neutral hydrogen out to large radii, as is possible in the case of spirals. The support against gravitational collapse in ellipticals comes from essentially random motions rather than ordered rotation. In an attempt to check whether ellipticals have dark haloes one can use stellar kinematics, but since their outer parts are very faint, it is usually difficult to obtain spectra to constrain kinematics at large radii. An additional problem is related to the fact that one does not *a priori* know anything about the orbits of stars in ellipticals. Current investigations lead to the conclusion that there is less unambiguous evidence for the dark matter in ellipticals than in the case of spirals. Moreover, there are hints that in ellipticals the dark matter is not needed at all or, more precisely, not needed in some early-type galaxies, out to a given observed distance from the galactic center.

Recent reviews on the dark matter problem in elliptical galaxies can be found for example in Danziger (1997), Binney and Merrifield (1998) and Bertin (2000). We here briefly present different approaches that can be used in order to determine the presence of the dark haloes around early-type galaxies. As in Danziger (1997) we split the different methodological approaches in three large groups that are then subdivided: gas, test particles and lensing methods.

[1] In this book all the calculations were done in the framework of the classical Newtonian dynamics – no attempts were made to perform calculations within alternative theories (e.g. MOND theory of Milgrom 1983).

(a) GAS The gas in the early type-galaxies can be found in the X-ray haloes, this is a *hot gas* with temperature $T \sim 10^7$ K. Studies of X-ray haloes strongly suggest the existence of dark matter out to large distances from the center (review in Mathews and Brighenti 2003a). We refer the reader to Chapter 3 where we present relevant calculations and apply them to the galaxies from our samples that possess X-ray haloes. Here we note that the present observational situation is interesting: for example, Sivakoff et al. (2004) used the X-ray observations by CHANDRA and assuming hydrostatic equilibrium found that for the X-ray bright galaxy NGC 1600 within $\sim 4R_e$ dark matter does not dominate. But two very recent studies based on the CHANDRA data by Humphrey et al. (2006) and Fukazawa et al. (2006) used the same methodology (on different samples) on X-ray data to demonstrate the existence of dark matter beyond $\sim 1R_e$. The gas can also be *warm*, with $T \sim 10^4$ K. This is ionized hydrogen that includes emission line gas and Hα + [NII] regions (e.g. Buson et al. 1993, Zeilinger et al. 1996). Pizzella et al. (1997) analyzed the velocity fields of ionized gas disks in four ellipticals and derived mass-to-light ratios as a function of radial distance. Using triaxial mass distribution they found that M/L ratio changes within individual galaxies, although there is no systematic increase with radius. The mean value for the B–band that was found is $\sim 5M_{\odot}/L_{B\odot}$ out to one effective radius (note that $h_0 = 0.5$ was used in that study). This technique is limited to the inner regions of galaxies. *Cold gas* has been detected in several early-type galaxies out to large distances ($\geq 10R_e$). Bertola et al. (1993) found that variation of mass-to-light ratio in the B–band, $M_{\odot}/L_{B_{\odot}}$ (in this book abbreviated to M/L_B), in ellipticals is similar to that of spiral galaxies. They showed that in spirals and ellipticals there exists a radius where the density of the dark matter is equal to that of the visible matter. Expressed in units of effective radius, R_e, this distance is at 1.2 R_e. Morganti et al. (1995) studied the example of elliptical galaxy NGC 5266 and found that a disk of neutral hydrogen extends out to 10 R_e. They discovered that there was an increase of mass-to-light ratio in the B–band from a value of $M/L_B \sim 2-3$ in the inner region to $M/L_B \sim 12$ at the most distant measured point at ~ 9 R_e. Thus they concluded that there is a hint of a dark matter halo. Oosterloo et al. (2002) studied five dust lane elliptical galaxies and found that in the case of NGC 3108 the regular distribution and kinematics of the HI allowed them to derive the mass-to-light ratio: they calculated the value of $M/L_B \sim 18$ at 6 R_e. The recent result of radio and optical observations of the same galaxy of Jozsa, Oosterloo and Morganti (2003) suggests that the mass-to-light ratio out to $6R_e$ is ~ 15 $M_{\odot}/L_{V\odot}$ (in the V–band, corresponds to $M/L_B \sim 22$ in the B–band). They reached the conclusion that this galaxy possesses a dark halo similar to that observed in spirals.

(b) TEST PARTICLES *Planetary nebulae (PNe)* are a very promising tool for dark matter research because they are detectable even in moderately distant galaxies through their strong emission lines. Hui, Freeman and Dopita (1995) found that the mass-to-light ratio in the central region of a giant elliptical galaxy NGC 5128 is ~ 3.9 and that out to ~ 5 R_e it increases to ~ 10 (in the B–band), thus indicating the existence of the dark halo. In an extension of this work, very recently, Peng, Ford and Freeman (2003) presented their results of an imaging and spectroscopic

survey for PNe in NGC 5128. They detected 1141 PNe, out of which they confirmed 780. They found that PNe exist at distances out to 80 kpc ($\sim 15R_e$) making this study the largest kinematic study of an elliptic galaxy to date, both in the number of velocity tracers and in radial extent.[2] They found that the dark matter is necessary to explain the observed stellar kinematics, but their value of M/L_B is *much* lower than that expected from determinations that use X-ray haloes: within 80 kpc they found the total dynamical mass $\sim 5 \times 10^{11} M_\odot$ with $M/L_B \sim 13$. According to the paper of Bahcall, Lubin and Dorman (1995), which is based on the compilation of the mass-to-light ratios from the literature, at 80 kpc one should expect $M/L_B \sim 112 \pm 28$. It was already found by Hui et al. (1995) that the dynamical mass that they measured within 25 kpc was systematically lower than that measured by Forman, Jones and Tucker (1985) from ROSAT data who calculated a total mass of $1.2 \times 10^{12} M_\odot$ within 20 kpc. Also, van Gorkom et al. (1990) estimated the dynamical mass of NGC 5128 using HI synthesis observations and found that it is much lower than that obtained using X-ray halo: they found that the total mass is $2.5 \times 10^{11} M_\odot$, and the mass within $1.2R_e$ is $1.2 \times 10^{11} M_\odot$. Thus, they found that there exists a constant mass-to-light ratio (that is equal to 3.1) out to at least 8.7 kpc. An interesting example of usage of PNe methodology in dark matter research is that of galaxy NGC 3379. Ciardullo, Jacoby and Dejonghe (1993) used 29 PNe (out to 3.8 R_e) to draw the conclusion that the mass-to-light ratio $M/L_B \sim 7$ and that there is no need for the dark matter. Recently, Romanowsky et al. (2003) observed PNe in three galaxies (NGC 821, NGC 3379 and NGC 4494) and confirmed this conclusion for NGC 3379 using much larger sample of 109 PNe (out to ~ 3.5 R_e (if one takes into account a correct value of the effective radius for NGC 3379 see Chapter 1 for details.) We analyzed this galaxy in some detail using different available data (photometry, long-slit spectra, X-ray data) in Chapters 1 and 2 and we reached the same conclusions, although we stress that some doubts still remain. Very recently, Sluis and Williams (2006) used the Rutgers Fabry–Pérot in order to search for planetary nebulae in NGC 3379 and three other galaxies in order to use the PNe as kinematic tracers of the galaxy potential. They detected 54 PNe in NGC 3379 and found that within $\sim 3R_e$ the total mass-to-light ratio of this galaxy in the B–band is ~ 5, implying very low amount of dark matter in the given region (~ 130 arcsec).

Globular clusters (GCs) can also be used as tracers of dark matter in the early-type galaxies: Mould et al. (1990) obtained optical multislit spectra of two giant elliptical galaxies M49 and M87 from the Virgo cluster. They found that the velocity dispersion profiles of the cluster systems were flat, thus suggesting the existence of an isothermal halo of dark matter in these elliptical galaxies. Grillmair et al. (1994) studied the radial velocities of 47 globular clusters in NGC 1399 in the Fornax cluster. Under the assumption that the clusters were on purely circular orbits, they gave a lower limit on a globally constant mass-to-light (M/L) ratio of 79 ± 20 in the B–band. Their result suggesting that M/L is several times larger than values of mass-to-light ratio determined from the stellar component closer to the core implies that M/L must increase substantially with radius. This galaxy has been analyzed in Chapters 2

[2]This galaxy will be the subject of Chapter 5 and some results based on both planetary nebulae and globular clusters and X-rays for NGC 5128 are given in Samurović (2006).

(using long-slit spectra) and Chapter 6 (using GCs) of this book. Briefly, in Samurović and Danziger (2006) it is shown that — in spite of the observations that show that the velocity dispersion decreases between 4 and 10 R_e — there is evidence that dark matter exists beyond $\sim 3R_e$ (but does not dominate interior to this distance). Another example is that of M49 (= NGC4472) studied by Côté et al. (2003) who showed that the globular clusters radial velocities and density profiles provide "unmistakable evidence" for a massive dark halo. Very recently, Pierce et al. (2006) have obtained Gemini/GMOS spectra for 22 GCs associated with NGC 3379 and found that, in contrast to the results of Romanowsky et al. (2003), their results suggest a constant value of the velocity dispersion (out to ~ 200 arcsec) which imply a normal-sized dark matter halo. They do note, however, that due to possible anisotropies (see below) they could not rigorously determine the dark halo mass. Another very recent example of an early-type galaxy which was studied using GCs is that of NGC 4649 (M60): Bridges et al. (2006) used Gemini/GMOS to obtain spectra of 38 confirmed GCs there. They found that between ~ 100 arcsec ($\sim 1.5R_e$) and 260 arcsec ($\sim 3.5R_e$) the velocity dispersion remains constant indicating the existence of dark matter. They applied different spherical, isotropic and axisymmetric, orbit-based dynamical models; the value of the total mass-to-light ratio that they infer in the outer regions shows an increase of factor of two with respect to the central one.

A large set of dark matter investigations in early-type galaxies is made of studies of *integrated stellar light*. Since this is one of the main subjects of this book in subsequent Chapters we will provide more details later. Here we present briefly the history of observations and modelling procedures. Binney, Davies and Illingworth (1990) in their seminal paper established a two-integral axisymmetric modelling based on the photometric observations. They analyzed galaxies NGC 720, NGC 1052, and NGC 4697 and modelled velocities and velocity dispersions out to ~ 1 R_e. van der Marel et al. (1990) applied this approach to NGC 3379 (out to ~ 1 R_e), NGC 4261 (out to ~ 1 R_e), NGC 4278 (out to ~ 1 R_e) and NGC 4472 (out to 0.5 R_e). Cinzano and van der Marel (1994) modelled the galaxy NGC 2974 out to 0.5 R_e introducing a new method – modelling of the Gauss-Hermite moments (for definitions see Chapter 1) defined previously in van der Marel and Franx (1993). All these modelling procedures did not take into account dark matter, because they dealt with the regions in which dark matter was not expected to make a significant contribution. In this case they showed that this method can provide a hint on the embedded stellar disk. Bertin, Saglia and Stiavelli (1992) and Saglia, Bertin and Stiavelli (1992) developed self-consistent two-component models of ellipticals. They fitted the models to observed photometric and kinematic profiles of individual galaxies and found that the amount of dark matter within one effective radius is not too large (it is of similar order to the luminous mass). In the case of NGC 4472 (under their physical assumptions) it was found that dark matter must be present.

Saglia et al. (1993) presented a kinematical and line strength profiles of NGC 4472, IC 4296 and NGC 7144 and from their dynamical modelling (quadratic programming) concluded that there is a strong evidence for dark matter in these galaxies. Carollo et al. (1995) observed and modelled a set of elliptical galaxies (NGC 2434, NGC 2663, NGC 3706 and NGC 5018). They used two-integral modelling procedure to model

the stellar line-of-sight velocity distribution (using velocity dispersion and Gauss-Hermite h_4 parameter) out to two effective radii. They concluded that the massive dark matter haloes must be present in three of the four galaxies (they were analyzed in this book using a three-integral modelling procedure), and in case of NGC 2663 there was no evidence of the dark matter. In 1997 Rix et al. used the Schwarzschild (1979) method for construction of axisymmetric and triaxial models of galaxies in equilibrium without explicit knowledge of the integrals of motion. They introduced into the analysis velocity, velocity dispersion and Gauss-Hermite parameters h_3 and h_4. They used the galaxy NGC 2434 (from Carollo et al. 1995) to perform a detailed dynamical modelling in order to conclude that this galaxy contains a lot of dark matter: they found that about half of the mass within one effective radius is dark.

Statler et al. (1996) studied stellar kinematical fields of the post-merger elliptical galaxy NGC 1700 out to four effective radii. In a subsequent paper Statler et al. (1999) found, using two-integral axisymmetric models as well as three-integral quadratic programming models that NGC 1700 must have a radially increasing mass-to-light ratio, and that NGC 1700 "appears to represent the strongest stellar dynamical evidence to date for dark halos in elliptical galaxies". Statler and McNamara (2002) observed this galaxy in the X-ray domain, and using gas modelling estimated the gas temperature to be ~ 0.5 keV. Note, however, that these authors found that probably the hypothesis of hydrostatic equilibrium is not applicable in this case, which would therefore make the comparison between mass profiles based on the X-ray data and stellar dynamics difficult. Saglia et al. (2000) modelled the galaxy NGC 1399 using two-integral models (major photometric axis only) out to $\sim 2.5\ R_e$. They marginally detected the influence of the dark component that starts from $1.5\ R_e$.

Kronawitter et al. (2000) modelled a large sample of 21 elliptical galaxies out to 1-2 R_e: for three of them (NGC 2434, NGC 7507, NGC 7626) they found that models based on luminous matter should be ruled out. De Bruyne et al. (2001) modelled NGC 4649 and NGC 7097 using a three-integral quadratic programming method and found that in the case of NGC 4649 a constant mass-to-light ratio ($M/L_V = 9.5$) fit can provide good agreement with the data and that a marginally better fit can be obtained including 10% of dark matter at $1.2\ R_e$. In the case of NGC 7097 both kinematic and photometric data can be fitted out to $1.6\ R_e$ using a constant mass-to-light ratio ~ 7.2. Cretton et al. (2000) modelled the giant elliptical galaxy NGC 2320 using the Schwarzschild orbit superposition method and found that the models with radially constant mass-to-light ratio and logarithmic models with dark matter provide comparably good fits to the data and have similar dynamical structure (but note that the mass-to-light in the V–band is rather large: ~ 15 for the mass-follows-light models and ~ 17 for the logarithmic models).

The Schwarzschild method can be applied in modelling of the central parts of the early-type galaxies; see for example, the paper by van der Marel et al. (1998) in which M32 was analyzed, the Cretton and van der Bosch (1999) paper in which axisymmetric models of NGC 4342 were presented, the Gebhardt et al. (2000) paper in which a black hole in the center of NGC 3379 was modelled, the Gebhardt et al. (2003) paper with the sample of 12 ellipticals that were analyzed using axisymmetric approach. Finally, we mention the paper of Cappellari et al. (2002) that modelled in detail, using the

Schwarzschild formalism, internal parts of one early-type galaxy that is also a subject of this book, IC 1459.

A new promising avenue in studies of integrated light from the early-type galaxies is usage of new integral field spectrographs (like SAURON, cf. Bacon et al. 2001, de Zeeuw et al. 2002) that should provide information on line-of-sight velocity distribution and spectral indices in two dimensions improving the limitations of long-slit spectroscopy that is limited by time to few position angles. Unfortunately, this technique is at the moment limited to the interior parts of the galaxies (out to $\sim 1\ R_e$, Emsellem, 2002, priv. communication). Therefore, long-slit spectroscopy with its long exposures still remains a necessary tool in dark matter studies. Recently, on the theoretical grounds, Mamon and Łokas (2005) found that the stellar component should dominate the dark matter component out to at least $1\ R_e$.

There are numerous studies of early-type dwarf galaxies in the Local Group that investigate the *internal dynamics* of dwarf ellipsoidal galaxies. A successful fit to the data is obtained when one assumes that they are embedded in a dark halo with mass of $\sim 10^7\ M_\odot$, and a luminous mass component with a mass-to-light ratio in V–band $M/L_V = 2.5$ (see, e.g. Mateo 1998).

A serious problem with the determination of the mass in the early–type galaxies is related to the fact that one does not *a priori* know anything about the orbits of stars in ellipticals which leads to a well known mass–anisotropy degeneracy (see Tonry 1983, see also Binney and Merrifield 1998, Chap 11.2).

(c) LENSING METHODS In this group of methods, we include weak gravitational lensing that enables determination of the dependence of the velocity dispersion on the luminosity of the lensing galaxies and is suitable for studies of the dark matter in outer part of galaxies. It was found that a Navarro-Frenk-White (NFW) profile provides a good fit to the data (Kleinheinrich et al. 2003). Strong gravitational lenses can also be used for probing of the galaxy haloes, but only in the inner regions of galaxies (few tens of kiloparsecs) (see, for example, Prada et al. 2003). we also mention the Lenses Structure and Dynamics (LSD) Survey that gathers kinematic data for distant (up to $z \sim 1$) early-type galaxies that are gravitational lenses (review in Treu et al. 2004). The results of this survey suggest that extended dark matter haloes are detected in the early-type galaxies and that the dark matter contributes 50-75% to the total mass within the Einstein radius (cases of the lens galaxies MG2016+112 in Treu and Koopmans (2002) and 0047-281 in Koopmans and Treu 2003).

I.3. THE AIM OF THIS BOOK

This book is dedicated to the detailed study of the kinematics of the early-type galaxies that is extracted from the integrated spectra of their stars and from the observations of different mass tracers (such as PNe and GCs). Since the existence of dark matter in the early-type galaxies can be established only in a study that takes into account all available observational data, the observational data that we had were then used in combination with the photometry data and the X-ray data in cases where galaxies possess X-ray haloes. A substantial part of the book is devoted to

the construction of realistic dynamical models of the early-type galaxies: a publicly available code for two-integral modelling (van der Marel 2006) was used and we built our own package for three-integral dynamical modelling (based on the Schwarzschild (1979) method and Rix et al. (1997) paper) that we describe in detail. A reduction of long-slit spectra of all of the galaxies that we had at our disposal (except for three galaxies from Carollo et al. (1995) sample for which we took the data from the literature) was made. Some photometric data from the literature was also used. Comparison of our results with the results of other aforementioned techniques in cases where such data existed revealed both agreement and discrepancies. Finally, in an attempt at making a link between the dynamics and chemical evolution we calculated abundance indices and compared them with the up-to-date chemical evolution models (Matteucci 2001, Pipino and Matteucci 2003).

Chapter 1
THEORETICAL CONCEPTS, OBSERVATIONS AND REDUCTION

1.1. STELLAR KINEMATICS: THEORETICAL APPROACH

Stars are moving in a given galaxy under the influence of a gravitational potential $\Phi(\mathbf{x}, t)$. If one wants to give a full description of the state of a collisionless system such as galaxy at any time t, one can use the number of stars $f(\mathbf{x}, \mathbf{v}, t)\ d^3\mathbf{x}\ d^3\mathbf{v}$ that have positions in the small volume $d^3\mathbf{x}$ that is centered on $\mathbf{x}$ and have velocities in the small range $d^3\mathbf{v}$ that is centered on $\mathbf{v}$. The function $f(\mathbf{x}, \mathbf{v}, t)$ is called the distribution function (or phase-space density) of the system. This is obviously a non-negative function: $f \geq 0$.

In the case of all external galaxies, one cannot obtain data necessary for the reconstruction of the distribution function directly: one can observe line-of-sight velocities and angular coordinates. Since individual stars cannot be resolved, one has to deal with integrated stellar light that represents the average of the stellar properties of numerous unresolved stars that lie along each line of sight (LOS). Each star will have a slightly different LOS velocity, and therefore its spectral features will be shifted by a different amount: $\Delta u = c\Delta\lambda/\lambda = v_{\rm LOS}$. The final galaxy spectrum will be shifted and broadened, as shown in Fig. (1.1), for the galaxy IC 3370.

The first step in the analysis of the shifts and broadenings is to define the line of sight velocity distribution (LOSVD, also called velocity profile, VP): this is a function $F(v_{\rm LOS})$ that defines the fraction of the stars that contribute to the spectrum that have LOS velocities between $v_{\rm LOS}$ and $v_{\rm LOS} + dv_{\rm LOS}$ and is given as $F(v_{\rm LOS})dv_{\rm LOS}$. Now, if one assumes that all stars have identical spectra $S(u)$ (where u is the spectral velocity in the galaxy's spectrum), then the intensity that is received from a star with LOS velocity $v_{\rm LOS}$ is $S(u - v_{\rm LOS})$. When one sums over all stars one gets:

$$G(u) \propto \int dv_{\rm LOS} F(v_{\rm LOS}) S(u - v_{\rm LOS}). \tag{1.1}$$

This relation represents the starting point for a study of stellar kinematics in external galaxies (cf. Binney and Merrifield 1998, hereafter BM98). The observer gets $G(u)$ for a LOS through a galaxy by obtaining its spectrum. If the galaxy is made of

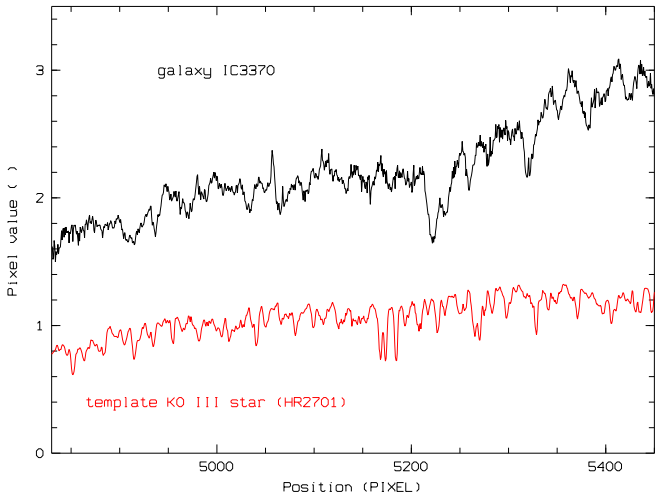

Figure 1.1: Reduced central spectrum of the galaxy IC 3370 (above) and template star (below). Spectra have been wavelength calibrated: x axis is in Angstroems. Note the effects of velocity dispersion and redshift in the case of the galaxy; y axis is in arbitrary units.

certain type of stars, one can estimate $S(u)$ using a spectrum of a star from the Milky Way galaxy (see Fig. (1.1), lower part).

The solution of Eq. (1.1) seems rather simple. It would be enough to take its Fourier transform:

$$\tilde{F}(k) \propto \frac{\tilde{G}(k)}{\tilde{S}(k)} \tag{1.2}$$

where quantities with tilde sign are the Fourier transforms of the original functions. This is however a very difficult task, since $\frac{\tilde{G}(k)}{\tilde{S}(k)}$ will be plagued by large errors that vary from point to point and the simple derivation of $F(v_{\rm LOS})$ will not be easy (for details, see BM98). Therefore, less direct methods have been invented to solve this problem.

First we can define the simplest properties of a LOSVD. Its mean value is given as:

$$\bar{v}_{\rm LOS} = \int dv_{\rm LOS} v_{\rm LOS} F(v_{\rm LOS}). \tag{1.3}$$

Its dispersion is given as:

$$\sigma^2_{\rm LOS} = \int dv_{\rm LOS} (v_{\rm LOS} - \bar{v}_{\rm LOS})^2 F(v_{\rm LOS}). \tag{1.4}$$

One possible solution is to assume that the LOSVD has the Gaussian form. Sargent et al. (1977) invented the method known as Fourier Quotient Method, that has a problem of large errors for the ratio $\frac{\tilde{G}(k)}{\tilde{S}(k)}$ that vary from point to point. The cross-correlation method based on the calculation of the cross-correlation function between

the galaxy and the stellar spectra was pioneered by Simkin (1974) and developed further by Tonry and Davis (1979) and Statler (1995).

The LOSVD can be modelled as truncated Gauss-Hermite ($F_{\rm TGH}$) series that consists of a Gaussian that is multiplied by a polynomial (van der Marel and Franx 1993, also Gerhard 1993):

$$F_{\rm TGH}(v_{\rm LOS}) = \Gamma\frac{\alpha(w)}{\sigma}\exp(-\frac{1}{2}w^2)\left[1+\sum_{k=3}^{n}h_kH_k(w)\right] \tag{1.5}$$

here Γ represents the line strength, $w \equiv (v_{\rm LOS}-\bar{v})/\sigma$, $\alpha \equiv \frac{1}{\sqrt{2\pi}}\exp(-w^2/2)$, where $\bar{v}$ and σ are free parameters. h_k are constant coefficients and $H_k(w)$ is a Gauss-Hermite function, that is a polynomial of order k. We will truncate the series at $k=4$ (although higher values are also possible), for which the polynomials are:

$$\begin{aligned} H_0(w) &= 1, \\ H_1(w) &= \sqrt{w}, \\ H_2(w) &= \frac{1}{\sqrt{2}}(2w^2-1), \\ H_3(w) &= \frac{1}{\sqrt{6}}(2\sqrt{2}w^3-3\sqrt{2}w), \end{aligned} \tag{1.6}$$

and

$$H_4(w) = \frac{1}{\sqrt{24}}(4w^4-12w^2+3).$$

It can be shown (van der Marel and Franx 1993) that $H_l(w)$ (in this case, $l=0,\ldots,4$) are orthogonal with respect to the weight function $\alpha^2(w)$.

Now the LOSVD can be calculated by varying the values of $\bar{v}$, σ, h_3 and h_4 until the convolution of the function $F_{TGH}(v_{\rm LOS})$ with a template star spectrum best reproduces the observed galaxy spectrum. The optimal fit is then reached using a non-linear least-squares fitting algorithm. If the form of the LOSVD is close to the Gaussian form, then $\bar{v}$ and σ will be approximately equal to $\bar{v}_{\rm LOS}$ and $\sigma_{\rm LOS}$. Parameters h_3 and h_4 are important because they measure asymmetric and symmetric departures from the Gaussian respectively. If one detects a positive (negative) value of the h_3 parameter that would mean that the distribution is skewed towards higher (lower) velocities with respect to the systemic velocity. On the other hand, if one detects $h_4>0$ this means that the distribution is more peaked than the Gaussian at small velocities with more extended high-velocity tails; for $h_4<0$ the distribution is more flat-topped than the Gaussian. In the study of the dark matter in the early type galaxies the value of the h_4 parameter plays a crucial role because it is constraining the level of tangential anisotropy which is extremely important since it is well known that the excess of tangential motions can mimic the existence of the dark matter haloes in these galaxies (Gerhard 1993, Danziger 1997). The influence of changes in their values on the form of the LOSVD is given in Fig. (1.2).

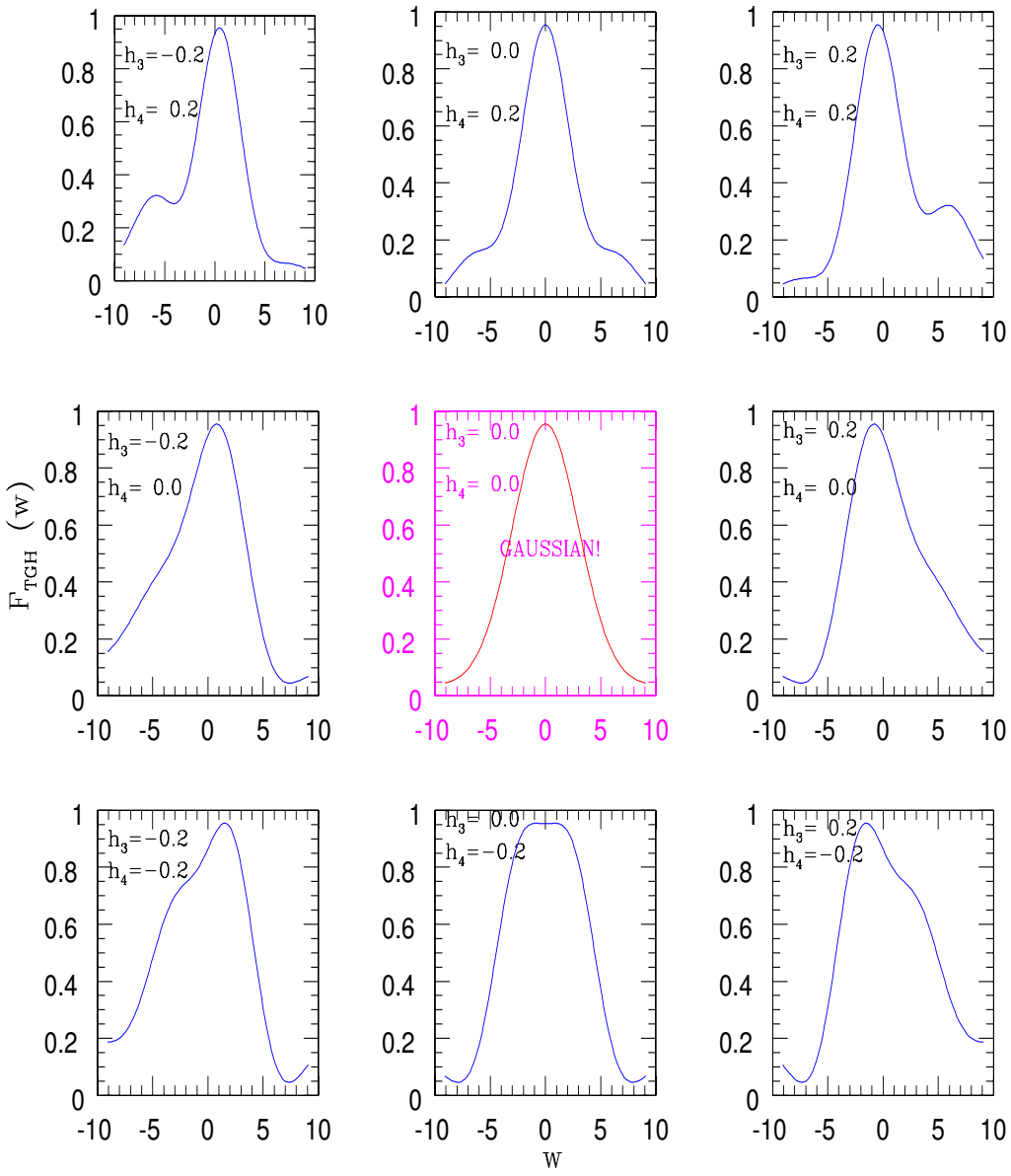

Figure 1.2: Plots demonstrating various combinations of h_3 and h_4 on the shape of the function $F_{\mathrm{TGH}}(w)$. Pure Gaussian is in the center (both h_3 and h_4 are equal to zero). h_3 parametrizes the skewness of the line profile, while h_4 measures whether the profile is more or less peaked than a Gaussian. Units of the variable w are arbitrary.

For the extraction of the stellar kinematics we used van der Marel's freely available "Gauss-Hermite Fourier Fitting Software". Since this package was written for the Sun FORTRAN compiler for the Sun UNIX platform, initial testing was done using Sun Sparc (Sun-Blade-100) platform. Later, it was modified and ported to the x86 GNU/Linux PC platform that uses a GNU FORTRAN compiler. Detailed tests were done, and it was found that the results obtained in two different environments were in the excellent agreement. All the results presented in this book were obtained in the GNU/Linux environment. The results from this Chapter regarding galaxies IC 1459, IC 3370, NGC 3379 and NGC 4105 are presented in the paper by Samurović and Danziger (2005).

1.2. OBSERVATIONS

1.2.1. GENERAL REMARKS

We have used different long-slit data obtained from different sources that will be called *Samples* hereafter. They are:

Sample 1. Observations obtained courtesy of J. Danziger (ESO NTT was used) which include spectra of IC 1459 and IC 3370.

Sample 2. Observations obtained courtesy of A. Graham and S. Zaggia (Double Beam Spectrograph attached to the Australian National University 2.3 m telescope at Siding Springs Observatory was used) which include the spectra of the following galaxies: NGC 1336, NGC 1339, NGC 1373, NGC 1374, NGC 1379, NGC 1399, NGC 1404 and NGC 1419 (from Fornax cluster – see Graham et al. (1998)).

Sample 3. Observations obtained courtesy of M. Carollo and K. Freeman (again Double Beam Spectrograph attached to the Australian National University 2.3 m telescope at Siding Springs Observatory was used) which include the galaxy NGC 3379. Galaxy NGC 4105 was observed using ESO 2.2 m telescope with EFOSC.

Details of the instrumental setup will be given in detail when each sample will be analyzed. Here we present the details of the reduction procedures that are common for all the observations. Note that in this book we will also deal with *Sample 4* which includes three galaxies taken from the literature: NGC 2434, NGC 3706 and NGC 5018 (Carollo et al. 1995). For all galaxies for which we had the observational data we extracted stellar kinematic parameters (velocity, velocity dispersion, h_3 and h_4 parameters) and spectral indices.

All the reduction procedures of the long-slit spectra were done using the ESO `MIDAS` package[3]. All the standard `MIDAS` commands and the commands from the context `long` were used, and where necessary small routines were written using `MIDAS` command language, `MCL`. First, we combined the spectra taken under the same conditions

[3] `MIDAS` is developed and maintained by the European Southern Observatory (`http://www.eso.org/esomidas/`).

using `COMBINE/LONG` command. This was a very efficient way to remove the cosmic particle hits from the raw data. The bias, that is composed of a DC offset that is noiseless, and a noise component generated by the process of CCD readout, was subtracted: we have made a combined bias frame out of all available bias frames. A correction for the dark current was not made. For flat-fielding which performs the corrections for variations in pixel sensitivity across the CCD array, we combined available flat-field frames into a single flat-field frame which was normalized to unity. Frames of interest (galaxy's and stellar) were then divided by this single frame. For the purpose of the wavelength calibration we used spectra of different lamps (for example Helium-Argon) which were available for each observation. Interactive identification of lines was done using `MIDAS` commands that were embedded in a small `MCL` script: typical RMS uncertainty was ~ 0.03 Å. Sky subtraction was of a crucial importance because the outer parts of the galaxies are very faint, and sky removal had to be done very carefully. The command `SKYFIT/LONG` was used taking an average of ~ 30 rows near the edges of the exposure frames. For the extraction of the kinematical parameters of the galaxies rebinning into a logarithmic scale was done using simple `MIDAS` commands. Finally, the frames were trimmed by removing the rows and columns near the edges of the frames. In some cases we will present comparisons of our extracted kinematical parameters with those taken from literature (see below). The agreement is typically very good.

We used `IRAF`[4] for extraction of photometric profiles and for conversion of the `MIDAS` format into the `IRAF` format required by the Fourier Fitting package.

1.2.2. SAMPLE 1

IC 3370

GENERAL INFORMATION

IC 3370 is a bright galaxy, classified as E2-E3 (elliptical) galaxy, absolute blue magnitude -21.4, heliocentric radial velocity 2930 ± 24 km s^{-1} (taken from the LEDA database). It covers 2.9×2.3 arcmin on the sky (RC3). However, it is a rather unusual elliptical galaxy and according to Jarvis (1987, hereafter referred to as J87) it should be classified as S0pec (see below). One arcsec in the galaxy corresponds to ~ 203.02 pc. The effective radius is $35''$ (=7.10 kpc).

PHOTOMETRIC OBSERVATIONS

We used frames kindly provided by O. Hainaut using ESO NTT and EMMI in the RILD mode on July 3-4, 2002 in the B-band. The photometry of IC 3370 is very interesting and it is given in detail in J87. We present here some additional elements that are complementary to that study and are of importance for the analysis that we are undertaking.

[4] `IRAF` is distributed by NOAO, which is operated by AURA Inc., under contract with the National Science Foundation (`http://iraf.noao.edu`).

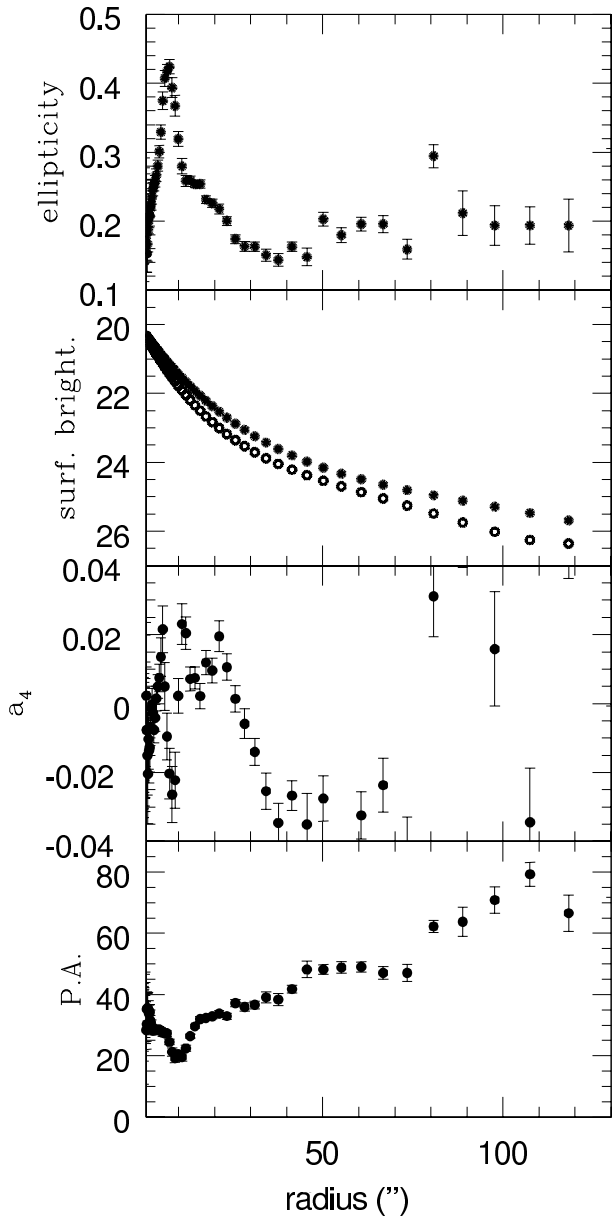

Figure 1.3: Photometric profiles for IC 3370 (in the B-band). From top to bottom: ellipticity, surface brightness for the B filter in mag arcsec^{-2} (for major axis: full circles; for minor axis: open circles), a_4 parameter and position angle.

LONG-SLIT SPECTRA

One should note that J87 took for the major axis the position angle (PA) of 40°, Carollo, Danziger and Buson (1993) took for the same axis P.A. of 51°, while the spectra in this study were taken using P.A. = 60°. The reason for these differences lies in a very particular photometry of this galaxy that has strong isophotal twisting as shown in J87 and in Fig. (1.3) (see position angle (P.A.) plot). This may be evidence for the fact that this galaxy is triaxial, because the isophotes of an axisymmetric system must always be aligned with one another (see, for example, BM98). Fasano and Bonoli (1989) using a sample of 43 isolated ellipticals found that the twisting observed in these galaxies is intrinsic (triaxiality). Jarvis has taken the mean position angle of isophotes to be equal to $40 \pm 2°$ which is true for the data up to $80''$. However, at larger radii the PA tends to increase, so the usage of larger value of 60° (and 150° for the minor axis) is justified (see Fig. (1.3)).

In Fig. (1.3) we present relevant photometric data obtained using `IRAF` task `ellipse`: ellipticity, magnitude in the B-band for major axis (filled circles) and minor axis (open circles), a_4 parameter (fourth harmonic deviations from ellipse) and the position angles, as a function of distance. The value of a_4 is positive up to one effective radius (for almost all values of radius), thus indicating that the isophotes are disky, while beyond one effective radius, the isophotes become boxy since a_4 is negative. Since a_4 increases rapidly up to $\sim 5''$ this can lead to the conclusion of the embedded disk. The existence of the stellar disk was shown in J87. The photometric data in the case of IC 3370, as well as in case of other galaxies that we present here, will be necessary for the dynamical modelling presented in the next Chapter. Long-slit spectra observations provided by J. Danziger were taken during 1998 March 1-3, using ESO NTT and EMMI in the Red Medium Spectroscopy mode. The central wavelength was chosen to be near the Mg_2 feature: $\sim$ 5150 Å with a range of $\sim$ 700 Å. Several exposures were taken for three different position angles: for the galactic major axis (P.A. = 60°) total exposure of 21,600 s, for the minor axis (P.A. = 150°) total exposure of 7,200 s. Also, the spectra of the intermediate axis were taken (P.A.=20°), and the total exposure time was 14,400 s. The spectra were rebinned at the telescope over 2 pixels giving a scale of 0.56 arcsec pixel^{-1}. We did the standard data reduction procedures in ESO `MIDAS`, as described previously. Wavelength calibration was done using the Helium-Argon comparison lamp spectra. Sky subtraction was done by taking an average of 30 rows near the edges of the exposure frames. Finally the spectra were rebinned on a logarithmic scale. Also, spectra of several template stars were reduced as described above, continuum divided, and averaged over several rows in order to obtain one stellar template spectrum of high signal-to-noise ratio (S/N). In Fig. (1.1) we showed a central galactic spectrum and a template star spectrum (K0 III star HR2701). The instrumental dispersion was $\sim$ 3.5 Å ($\sim$ 190 km s^{-1}) and was determined using a Helium-Argon spectrum in a region $\sim$ 5000 Å. This is important for the conversion of the abundance indices to the Lick system discussed in Chapter 4.

In Fig. (1.4) we show the major axis kinematic parameters. This galaxy indeed shows behaviour that is characteristic for an S0 galaxy: for example, its major axis kinematics can be compared to that of NGC 1461, lenticular galaxy from the Fisher (1997) sample. Note the usual behaviour of h_3 parameter: when the velocity rises,

h_3 decreases, and vice versa. In Fig. (1.5) we present intermediate and minor axis kinematic profiles: IC 3370 has minor axis rotation that provides an additional hint (apart from the isophotal twist) of the triaxiality. Note the small values (consistent with zero) of h_3 and h_4 at the large distances from the center for the major axis and their generally small values in the two other cases – they provide evidence of the lack of excessive tangential motions, that may mimic the dark matter in the outer parts of the galaxy.

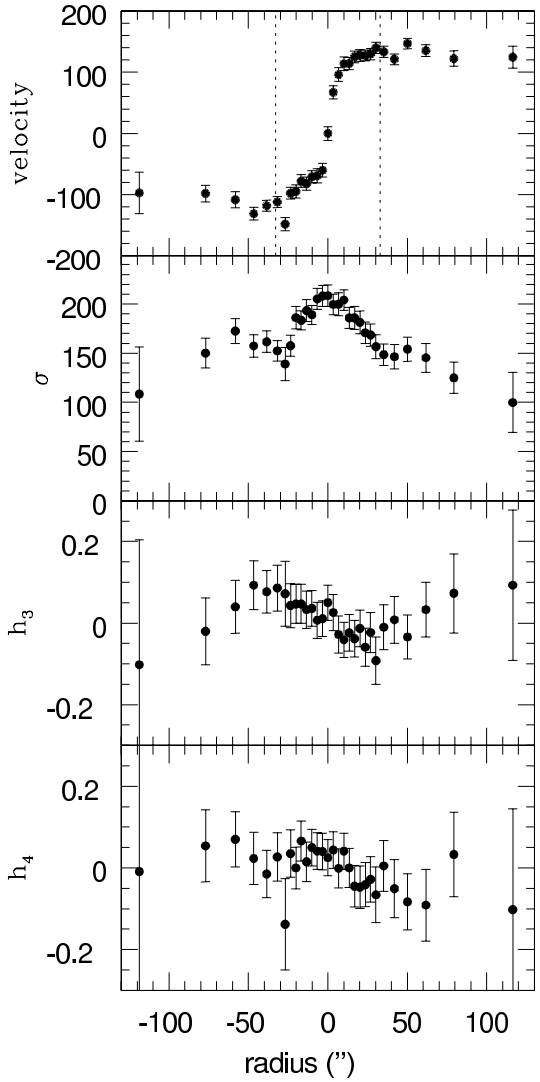

Figure 1.4: Kinematic profiles for the major axis of IC 3370 (P.A.= 60°). From top to bottom: velocity, velocity dispersion, h_3 and h_4 parameters. One effective radius is plotted using dashed lines.

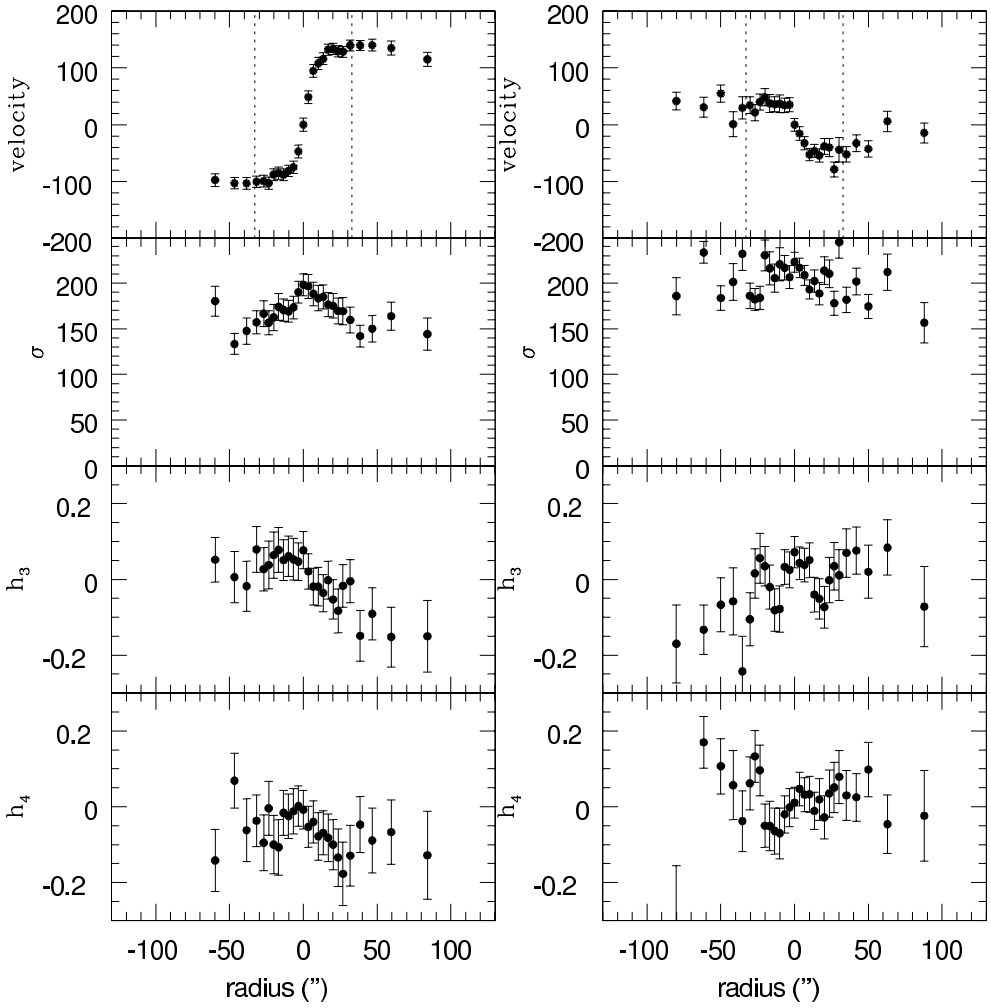

Figure 1.5: Kinematic profiles for the intermediate (P.A.= 150°, left) and minor (P.A.= 20°, right) axes of IC 3370. From top to bottom: velocity, velocity dispersion, h_3 and h_4 parameters. One effective radius is plotted using dashed lines.

IC 1459

GENERAL INFORMATION

IC 1459 is a giant E3 elliptical galaxy. Its absolute blue magnitude is -20.52, heliocentric radial velocity 1663 ± 74 km s^{-1} (taken from the LEDA database). It covers 5.2×3.8 arcmin on the sky (RC3). One arcsec in the galaxy corresponds to ~ 117.16 pc. The effective radius is $33''$ (=3.87 kpc). One of its most characteristic features is a fast counterrotating stellar core (Franx and Illingworth 1988). It has other peculiarities: twisted isophotes (Williams and Schwarzschild 1988), a dust lane and patches near the nucleus (Sparks et al. 1986) and an ionized gaseous disk at the core that ro-

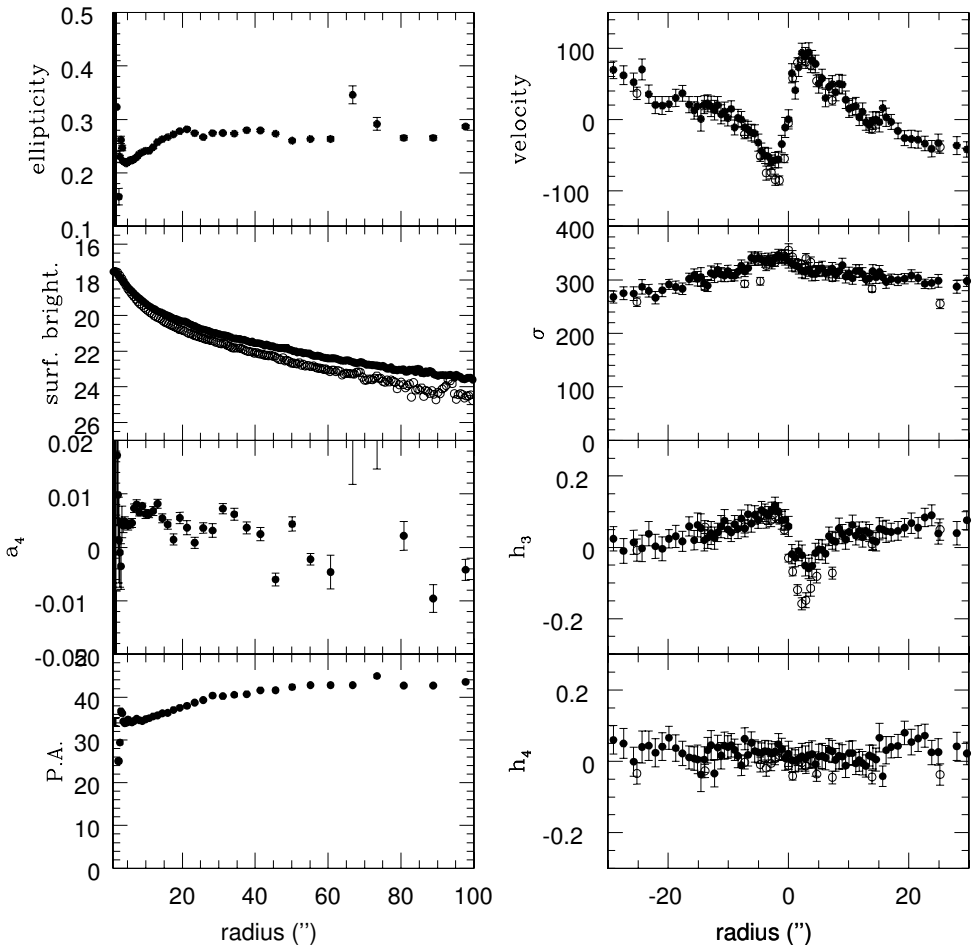

Figure 1.6: *Left*: Photometric profiles for IC 1459 (in the V-band). From top to bottom: ellipticity, surface brightness for the B filter (see text) in mag arcsec^{-2} (for major axis: full circles; for minor axis: open circles), a_4 parameter and position angle. *Right*: Comparison of the kinematic profiles for the major axis of IC 1459 (P.A.= 40°, black circles) and the data taken from Cappellari et al. (2002) (P.A.= 39°, open circles). From top to bottom: velocity, velocity dispersion, h_3 and h_4 parameters.

tates along the major axis in the same direction as the majority of stars in the galaxy – this is the opposite direction to that of the stellar core (Forbes et al. 1995). The nucleus of IC 1459 has a strong (1Jy) compact radio source (Slee et al 1994). Recently, Fabbiano et al. (2003) observed this galaxy with Chandra ACIS-S.

Verdoes Kleijn et al. (2000) analyzed kinematical observations of the nuclear gas disk, and found a central black hole of mass $M_{\rm BH} = (2-6) \times 10^8 M_\odot$. Cappel-

lari et al. (2002) observed IC 1459 using several slit positions and constructed axisymmetric three-integral models of this galaxy using the Schwarzschild orbit superposition method. They found, using stellar and gas kinematics, that $M_{\rm BH} = (1.1 \pm 0.3) \times 10^9 M_\odot$.

PHOTOMETRIC OBSERVATIONS

Photometric observations made by J. Danziger during 1997 August 28-30 using the ESO NTT and EMMI in the Red Medium Spectroscopy mode in the V-band were used. We present the results obtained using the aforementioned `IRAF` routine in Fig. (1.6) where surface brightness was transformed to the B-band using relation $B-V = 0.99$ taken from the LEDA database. The photometric profile was compared with that of Franx and Illingworth (1988) and it was found that they were in good agreement.

LONG-SLIT SPECTRA

Long-slit spectra observations provided by J. Danziger were done during the same nights using the same telescope and setup as in the case of IC 3370. The central wavelength was chosen to be near the Mg_2 feature: $\sim$ 5150 Å. The range that was covered was $\sim$ 700 Å. Several exposures were taken for two different position angles: for the galactic major axis (P.A. = 40°) total exposure of 35,100 s, and for the minor axis (P.A. = 130°) total exposure of 3,600 s. Because of the fact that only one exposure was available for the minor axis, the removal of the cosmic ray hits was not successful and we have taken the minor axis stellar kinematics from Cappellari et al. (2002). We compared the results for the major axis and plot the comparison in Fig. (1.6). Cappellari et al. (2002) used the Cerro Tololo Inter-American Observatory (CTIO). The agreement is good, except for the velocity and h_3 parameter near the galactic center where some discrepancy exists. Note, however, that Cappellari et al. (2002) used P.A.=39° and observations that we had were made at P.A.=40°. In the outer parts agreement is excellent for the whole velocity profile. The spectra were rebinned at the telescope over 2 pixels giving a scale of 0.56 arcsec pixel $^{-1}$. We made standard reduction procedures in ESO `MIDAS`, as described previously. Wavelength calibration was done using a Helium-Argon comparison lamp spectra. Finally the spectra were rebinned on the logarithmic scale. Again, spectra of several template stars were reduced as described above, continuum divided, and averaged over several rows in order to obtain one stellar template spectrum of high signal-to-noise ratio (S/N). This time the template star HR5852 was used. The instrumental dispersion was $\sim$ 3.5 Å ($\sim$ 190 km s^{-1}) and was determined using Helium-Argon spectrum in a region $\sim$ 5000 Å.

In Fig. (1.7) we show the major and minor axis kinematic parameters. Major axis data show the rapid increase of velocity in the inner $\sim 3''$: velocity rises to $\sim$ 100 km s^{-1}(note however a small asymmetry in our determination of velocity). Velocity dispersion is large at the centre: $\sim$ 350 km s^{-1}, and decreases rapidly to $\sim$ 240 km s^{-1} (at $\sim$ 40 $''$). There is a plateau in velocity dispersion between $\sim 20''$ and $30''$ after which velocity dispersion decreases. The h_3 parameter shows a typical behaviour,

i.e. it rises (falls) when velocity rapidly increases (decreases). In the outer parts it shows small departures from zero. The h_4 parameter shows very small departures from zero in the inner parts, and in the outer parts there is an increase of its value, suggesting existence of the radial anisotropy. Minor axis data provide evidence of small velocities, and larger central velocity dispersion (~ 380 km s^{-1}). Both h_3 and h_4 parameters show very small departures from zero throughout the observed parts of the galaxy.

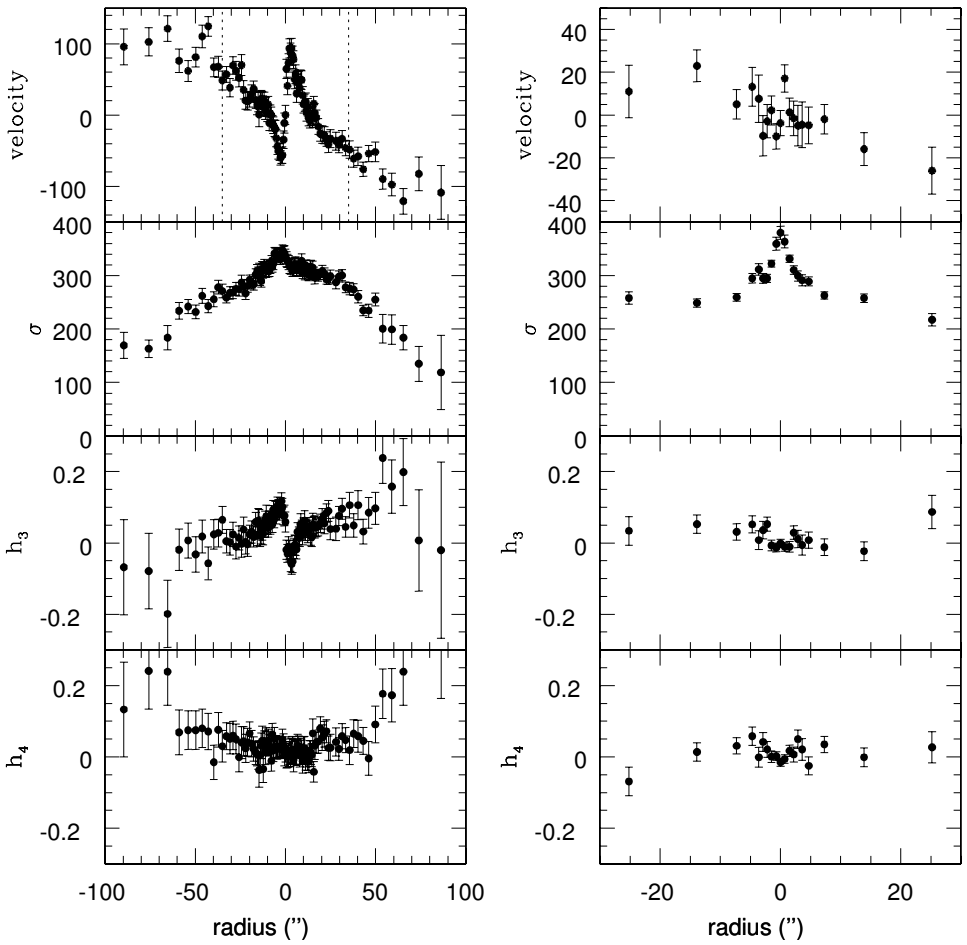

Figure 1.7: Stellar kinematics of IC 1459. *Left*: major axis data. *Right*: minor axis data (taken from Cappellari et al. 2002). From top to bottom: velocity, velocity dispersion, h_3 and h_4 parameters. One effective radius in case of the major axis is plotted using dashed line. Note that in case of the minor axis it is out of scale.

1.2.3. SAMPLE 2

In this subsection we will describe the sample and present the stellar kinematic results for the early-type galaxies in the Fornax cluster obtained courtesy from A. Graham and S. Zaggia. These observations include 13 galaxies (major axes data) and represent a sample of 86% of Fornax galaxies brighter that $B_T = 15$ mag. From the observed galaxies we chose 8 galaxies for which we could extract the full velocity profiles and whose spectra extend to the distances larger than one effective radius (except for NGC 1336, see below). A detailed description of the observations is given in Graham et al. (1998) (hereafter G98) and here we provide only some details that will be of importance for the modelling procedures. In TABLE 1-1 we give the basic observational data of Sample 2.

TABLE 1-1

GRAHAM ET AL. (1998) SAMPLE

Name	α_{1950} (h m s)	δ_{1950} ($\circ$ $\prime$ $\prime\prime$)	Type	$v_{\rm hel}$ km s^{-1}	B_T (mag)	r_e ($\prime\prime$)	$\frac{r_{\rm obs}}{r_e}$	μ_e	P.A. $\circ$	Exp. (hr)
(1)	(2)	(3)	(4)	(5)	(6)	(7)	(8)	(9)	(10)	(11)
NGC 1336	3 24 35.9	-35 53 10	E4	1444±66	13.3	30	0.8	23.6	20	1
NGC 1339	3 26 06.1	-32 27 26	E4	1356±48	12.7	15	2.0	21.5	175	2
NGC 1373	3 33 03.3	-35 20 06	E3	1373±34	14.2	11	2.0	22.4	140	3.5
NGC 1374	3 33 21.1	-35 23 29	E0	1331±36	11.9	26	1.5	22.3	120	1
NGC 1379	3 34 08.7	-35 36 22	E0	1365±46	12.0	24	2.0	22.0	7	0.75
NGC 1399	3 36 34.2	-35 36 46	E0	1446±36	10.0	42	2.0	24.2	112	3
NGC 1404	3 36 57.3	-35 45 17	E2	1942±44	10.9	26	3.0	21.2	160	2.5
NGC 1419	3 38 50.3	-37 40 09	E0	1649±220	13.6	9	2.0	21.7	50	1

NOTE: Column (1): name; (2) and (3): coordinates (R.A. and Dec.); (4): morphological type (according to Ferguson (1989)); (5): heliocentric radial velocity (from the LEDA database); (6): total apparent blue magnitude; (7): effective radius in arcsecs; (8): approximate radial radial range of the kinematical data (in units of effective radius); (9): blue surface brightness at 1 effective radius given in (mag/sq.arcsec.); (10): major axis position angle; (11): total exposure time (in hours).

The spectra were obtained during two runs in November and December 1996. The blue arm of the Double Beam Spectrograph was attached to the Australian National University's 2.3 m telescope at Siding Spring Observatory. The spatial scale on the chip was 0.91 arcsec pixel^{-1}. A spectrograph slit width of 2 arcsec on the sky with a length greater than the spatial extent of the CCD was used. FWHM for the arc lines of was found to be equal to 2.7 pixels or 1.50Å, giving a resolution of 86 km s^{-1} at 5200 Å. We did the whole reduction procedure (explained in section 1.2.3 of this Chapter). The Neon-Argon lamp frames were used for the wavelength calibration. The spectra of several template stars were reduced and used for the extraction of the full velocity profiles. The template star HD4128 was used in extracting the stellar kinematics of

the following galaxies: NGC 1336, NGC 1379, NGC 1374, NGC 1399 and NGC 1419. The template star HD4188 was used in case of these galaxies: NGC 1339, NGC 1373 and NGC 1404. Note that in the presentation of the photometric data we used Caon et al. (1994) data that give the cos4 parameter that represents the amplitude of the residual cos4 coefficient (multiplied by 100) of the isophotal deviation from the best fitting ellipse. In all the plots of this *Sample*, East (E) side is given with the positive values of the radius (right hand side), and the west side (W) is given with the negative values of the radius (left hand side).

NGC 1336 (Fig. (1.8))

One arcsec in this galaxy corresponds to ~ 100 pc. The effective radius is $30''$ (=3.00 kpc). The velocity has a slow increase and does not reach large values (maximum of 50 $\mathrm{km\,s^{-1}}$, with large error bars). Velocity dispersion profiles show a lack of symmetry and have a decreasing trend (error bars are large, so this should be taken with caution). G98 suggested the existence of a bar – note the large cos4 parameter in the photometetric profile inside $10''$, and also the small positive values of h_4 in this region.

NGC 1339 (Fig. (1.9))

One arcsec in the galaxy corresponds to ~ 93.95 pc and the effective radius is $15''$ (=1.41 kpc). The data for the rotation curve extend to $\sim 2R_e$ and the velocity remains constant. The velocity dispersion falls from the central value of ~ 170 $\mathrm{km\,s^{-1}}$ to ~ 100 $\mathrm{km\,s^{-1}}$ (at $\sim 1R_e$) and then begins to rise: at the last measured point $\sigma \approx 125$ $\mathrm{km\,s^{-1}}$. The parameter h_3 behaves as usual when the galaxy has such a rotation curve: it rises when velocity rises, and declines when velocity declines. h_4 shows signs of an increase: only in the very internal part its value is consistent with zero.

NGC 1373 (Fig. (1.10))

One arcsec in the galaxy corresponds to ~ 95.13 pc. The effective radius is $11''$ (=1.05 kpc). The rotation curve is rather symmetric and with a small degree of rotation. On the contrary, the velocity dispersion shows clear signs of asymmetry. Also, there is a trend of rising velocity dispersion values in the outer parts. From h_3 and h_4 it is difficult to draw conclusions. There is a hint that h_4 has small positive values throughout the observed regions of the galaxy.

NGC 1374 (Fig. (1.11))

One arcsec in the galaxy corresponds to ~ 92.22 pc. The effective radius is $26''$ (=2.40 kpc). The rotation curve is another example of the steep increase of the velocity in the inner parts ($\sim 5''$). As noted by G98, although the overall velocity profile is symmetric there are important departures from symmetry, which are also visible in the velocity dispersion profiles: when the plateau of $\sigma \sim 150$ $\mathrm{km\,s^{-1}}$ is reached at $\sim 10''$ the velocity dispersion changes behavior beyond one effective radius. h_3 and h_4 profiles also show a lack of symmetry.

NGC 1379 (Fig. (1.12))

One arcsec in the galaxy corresponds to $\sim$ 94.58 pc. The effective radius is 24″ (=2.27 kpc). This galaxy has a slow rotation (the value of the maximum velocity: ~ 40 km s^{-1}). Velocity profiles show a lack of symmetry twice: first, near the central region and, second, in the outer regions – on the E side velocity approaches zero, and on the W side it tends to be constant $\sim 30-40$ km s^{-1}. The velocity dispersion does not show a tendency to decline beyond one effective radius.

NGC 1399 (Fig. (1.13))

One arcsec in the galaxy corresponds to $\sim$ 100.19 pc. The effective radius is 42″ (=4.21 kpc); note, however, that this value might be problematic: Caon et al. (1994) calculated a value of 127″(=12.72 kpc) by fitting their extended photometry. We calculated the effective radius of 42 arcsec using the curve of growth. This is the largest galaxy in the Fornax cluster and is positioned in the center of the cluster. The rotation curve shows evidence for a kinematically distinct inner component. The velocity reaches (at W side) at $\sim$ 20″ a value of ~ 30 km s^{-1} which then steadily falls to zero (at $\sim$ 50″). At the E side the velocity remains constant at ~ 30 km s^{-1} (starting from 10″). The velocity dispersion is very high at the center ~ 320 km s^{-1} and quickly declines to ~ 250 km s^{-1} (at 10″) and then remains approximately flat. The h_3 parameter remains slightly positive throughout the whole observed galaxy. The h_4 parameter shows small departures from zero but which can be considered to be consistent with zero throughout the whole observed galaxy.

NGC 1404 (Fig. (1.14))

One arcsec in the galaxy corresponds to $\sim$ 134.55 pc. The effective radius is 26″ (=3.50 kpc). This galaxy shows a steep gradient of velocity: it rises to ~ 100 km s^{-1} within 10″. Note, however, that there is a flattening at the inner $\sim$ 2″ (note the different binning used in extracting stellar kinematics for this galaxy with respect to the other galaxies in the Fornax cluster). The velocity remains constant beyond one effective radius, $v \sim 80$ km s^{-1} and the profile looks symmetric with respect to the center. The velocity dispersion profiles are in general symmetric, too. There are two local maxima at $\pm$2″ from the center. Beyond these two points the velocity dispersion decreases at a nearly constant rate until it reaches a plateau at $\sim$ 12″. Departures from symmetry can be seen in the outer parts of the galaxy ($\sim 3R_e$). In these outer regions the velocity dispersion again becomes $\sigma \sim 200$ km s^{-1}. The h_3 parameter shows the usual behaviour for the case of the galaxy with rapidly increasing velocity (see the note for NGC 1339) and is consistent with zero at large distances from the center ($\sim 3R_e$). h_4 is slightly negative, but within the error bars it is consistent with zero throughout the whole observed galaxy.

NGC 1419 (Fig. (1.15))

One arcsec in the galaxy corresponds to $\sim$ 114.25 pc, and the effective radius is $9''$ (=1.03 kpc). As noted by G98 the velocity and dispersion profiles of this galaxy are very similar to those of NGC 1336. The velocity is small and is almost consistent with zero in the inner parts. The velocity dispersion is approximately constant ($\sigma \sim 100$ km s^{-1}) within the observed parts of this galaxy. Not much can be said about h_3 and h_4: in the outer regions they appear to be consistent with zero.

1.2.4. SAMPLE 3

These are observations of early-type galaxies obtained courtesy of M. Carollo and K. Freeman. The galaxy NGC 3379 was observed using the Double Beam Spectrograph attached to the Australian National's University 2.3 m telescope at Siding Springs Observatory. The galaxy NGC 4105 was observed using ESO 2.2 m telescope with EFOSC.

For NGC 3379 the long slit spectra of the major axis (P.A.=70°) were taken on March 13-14, 1997 and the total exposure time was 6,000 s. In both cases: (i) the scale was 0.59 arcsec pixel $^{-1}$, (ii) wavelength calibration was done using Neon-Argon lamp, and (iii) the template star was cpd-43. The instrumental dispersion was $\sim$ 2 Å($\sim$ 100 km s^{-1}) and was determined using a Neon-Argon spectrum in a region $\sim$ 5000 Å. For NGC 3379 the surface brightness was taken from the paper of Capaccioli et al. (1990), whereas ellipticity, a_4 parameter and position angle as function of radius using images from the ESO archive (I-band) were extracted using standard `IRAF` commands (see Fig. (1.16)).

NGC 3379 (Fig. (1.16), Fig. (1.17))

NGC 3379 is a bright E0 galaxy (note however the ellipticity $\epsilon \approx 0.15$ in Fig. (1.16); there are still some doubts whether this is a bona fide normal elliptical or a face-on lenticular galaxy, cf. Gregg et al. 2004), with heliocentric radial velocity of 911 km s^{-1}, and absolute B–magnitude -20.57. One arcsec in the galaxy corresponds to $\sim$ 63.12 pc. The effective radius is $55''$ (=3.46 kpc) (see Capaccioli et al. 1990). We verified this value using the curve of growth.

Since we had only major axis (P.A.=70°) data, we have taken data from Statler and Smecker-Hane (1999) for the major and the minor axis (P.A.=340°). We compared the results for the inner region which we have in common for the major axis and found that they are in an excellent agreement (see Fig. (1.16) (right)). The data that we had extend out to ≈ 30 $''$, so in the modelling procedures (see next Chapter) we will use Statler and Smecker-Hane (1999) measurements because their data extend to a larger radius ($80''$ that is ≈ 1.5 R$_e$) and are also available for the minor axis.

This galaxy shows steep increase of velocity: it rises to $\sim$ 60 km s^{-1} in the inner $20''$. After a plateau between $\sim 20''$ and $\sim 60''$ the velocity shows a tendency to decrease. The velocity dispersion peaks at $\sim$ 230 km s^{-1} and then decreases rapidly. There is a plateau between $\sim 20''$ and $\sim 50''$. One can see that there is an obvious asymmetry at $\sim 80''$. However, other observations show that there is a decreasing

trend out to 6 R_e (see next Chapter). The h_3 parameter is small out to $\sim$ 50 $''$, but shows departures from zero at $\sim 70''$. h_4 remains small throughout the whole observed galaxy, except in the outer parts for which there is a hint of departures from zero, but since error bars are large, it is difficult to draw firm conclusions. Minor axis data suggest that NGC 3379 does not show significant rotation on the minor axis. The velocity dispersion profile is similar to that of the minor axis. The h_3 and h_4 parameters are small throughout the whole observed galaxy on the minor axis (see Fig. (1.17)).

NGC 4105 (Fig. (1.18), Fig. (1.19))

GENERAL INFORMATION

NGC 4105 is an E galaxy, with heliocentric radial velocity of 1918 $\mathrm{km\,s^{-1}}$, and absolute B–magnitude -20.72. One arcsec in the galaxy corresponds to $\sim$ 134.14 pc. The effective radius is $35''$ (=4.69 kpc).

PHOTOMETRIC OBSERVATIONS

Photometric data were extracted from frames obtained courtesy of M. Carollo and K. Freeman using standard `IRAF` routines (Fig. (1.18)). Note that the surface brightness is given in the R-band .

LONG-SLIT SPECTRA

Long slit spectra were obtained on March 9-13, 1994 using ESO 2.2 m telescope with EFOSC. The total exposure time for the major axis (P.A.=150°) was 27,900 s. The total exposure time for the minor axis (P.A.=60°) was 14,400 s. The scale was 0.336 arcsec pixel $^{-1}$. The wavelength calibration was done using Helium-Argon lamp. The template star was HR5582. The instrumental dispersion was $\sim$ 4.2 Å($\sim$ 280 $\mathrm{km\,s^{-1}}$) and was determined using Helium-Argon spectrum in a region $\sim$ 5000 Å.

On the major axis this galaxy shows a maximum value of the velocity $\sim$ 60 $\mathrm{km\,s^{-1}}$ (see Fig. (1.19), left). Note that there is a hint of a counterrotating stellar core in the inner $3''$. In general, there is a lack of symmetry about the galaxy center. The central value of the velocity dispersion is large: $\sim$ 320 $\mathrm{km\,s^{-1}}$. It declines in the inner $\sim 5''$ after which there is a tendency that to remain constant (out to $\sim$ 20 arcsec). h_3 also shows a hint of the effects of the counterrotating stellar core in the inner $3''$. At the larger radii the value of h_3 is consistent with zero. The h_4 parameter remains small (slightly negative, but consistent with zero) throughout the whole observed galaxy. On the minor axis NGC 4105 shows rather complex behaviour and again a lack of symmetry is evident (see (Fig. (1.19)). The velocity dispersion decreases from the central value of $\sim$ 320 $\mathrm{km\,s^{-1}}$ to $\sim$ 200 $\mathrm{km\,s^{-1}}$. Not much can be said about h_3 and h_4 parameters, except that they show asymmetries.

1.2.5. SAMPLE 4

In this sample we include three galaxies from Carollo et al. (1995) for which these authors found an indication of existence of a dark halo: NGC 2434 (a galaxy studied in detail also in Rix et al. 1997, see next Chapter), NGC 3706 and NGC 5018. The

details concerning these galaxies are given in the above two papers for each galaxy. Stellar kinematics for all galaxies are given in Carollo et al. (1995). Here, we give only a brief overview and present kinematical data (see related Figures) which we obtained in electronic form courtesy of M. Carollo.

NGC 2434 (Fig. (1.20))

This is E0-1 galaxy, with heliocentric radial velocity $v = 1390 \pm 27$ km s^{-1} (taken from the NED database). Total apparent corrected B–magnitude is 11.29 (taken from the LEDA database). Details on photometry can be found in Carollo and Danziger (1994a). One arcsec in the galaxy corresponds to ~ 96.31 pc. The effective radius is $24''$ (=2.31 kpc). This galaxy possesses a strong isophotal twisting in the inner $\sim 10''$. Isophotes are disky in the inner $\sim 3''$. The velocity does not reach large values: at $\sim 2R_e$ it is ~ 30 km s^{-1}. The velocity dispersion peaks at ~ 260 km s^{-1}, and then declines rapidly. Note that from ~ 15 $''$ outwards it remains constant. h_3 parameters have small values throughout the observed galaxy. Note, however, that the velocity data in combination with the h_3 data may indicate the existence of the counterrotating stellar core (a case similar to that of NGC 4105). Apart from small positive values in the inner region, the h_4 parameter is zero in the outer regions thus providing (in combination with the flat velocity dispersion profile) a strong indication of the existence of the dark halo (but see the modelling in the next Chapter).

NGC 3706 (Fig. (1.21))

This is an E galaxy (according to the LEDA database), with heliocentric radial velocity 3215 ± 150 km s^{-1} (taken from the NED database). The total corrected apparent B–magnitude is 12.32 (taken from the LEDA database). Details on photometry can be found in Carollo and Danziger (1994a). One arcsec in the galaxy corresponds to ~ 222.75 pc. The effective radius is $27''$ (=6.01 kpc). This galaxy does not show strong isophotal twisting: the P.A. decreases slowly from $\sim 80°$ (at $\sim 2''$) to $\sim 70°$(at $\sim 100''$). The rotation curve (and h_3 behaviour) is very similar to that of galaxies NGC 1339 and NGC 1404. The central velocity dispersion is rather high: 340 km s^{-1} and declines rapidly in the inner $\sim 20''$. At $\sim 2R_e$ it does show a plateau (albeit only on one side – data on the opposite side are unfortunately unavailable). The h_4 parameter has small positive values in the inner region and in the outer regions small negative values (that deviate from zero).

NGC 5018 (Fig. (1.22))

This is an E-S0 galaxy (according to the LEDA database), with heliocentric radial velocity 2897 km s^{-1}. The total corrected apparent B–magnitude is 11.7 (all data are from ESO Lauberts and Valentijn catalog, as quoted in Carollo and Danziger (1994b). Details of photometry can be found in Carollo and Danziger (1994b). The effective radius is $22''$ (=4.26 kpc) and one arcsec corresponds to 193.58 pc. The galaxy does not show an isophotal twist. Note the asymmetry in velocity: maximum

on one side $\sim$ 100 $\mathrm{km\,s^{-1}}$, and on the other side maximum $\sim$ 50 $\mathrm{km\,s^{-1}}$. The velocity dispersion has a double peaked maximum values (at $\sim$ 240 $\mathrm{km\,s^{-1}}$). There exists a decreasing trend in the velocity dispersion. The h_3 parameter shows complex variations (especially in the region where the velocity is negative). The h_4 parameter remains positive throughout the whole observed galaxy .

All the galaxies discussed so far will be modelled in the next Chapter.

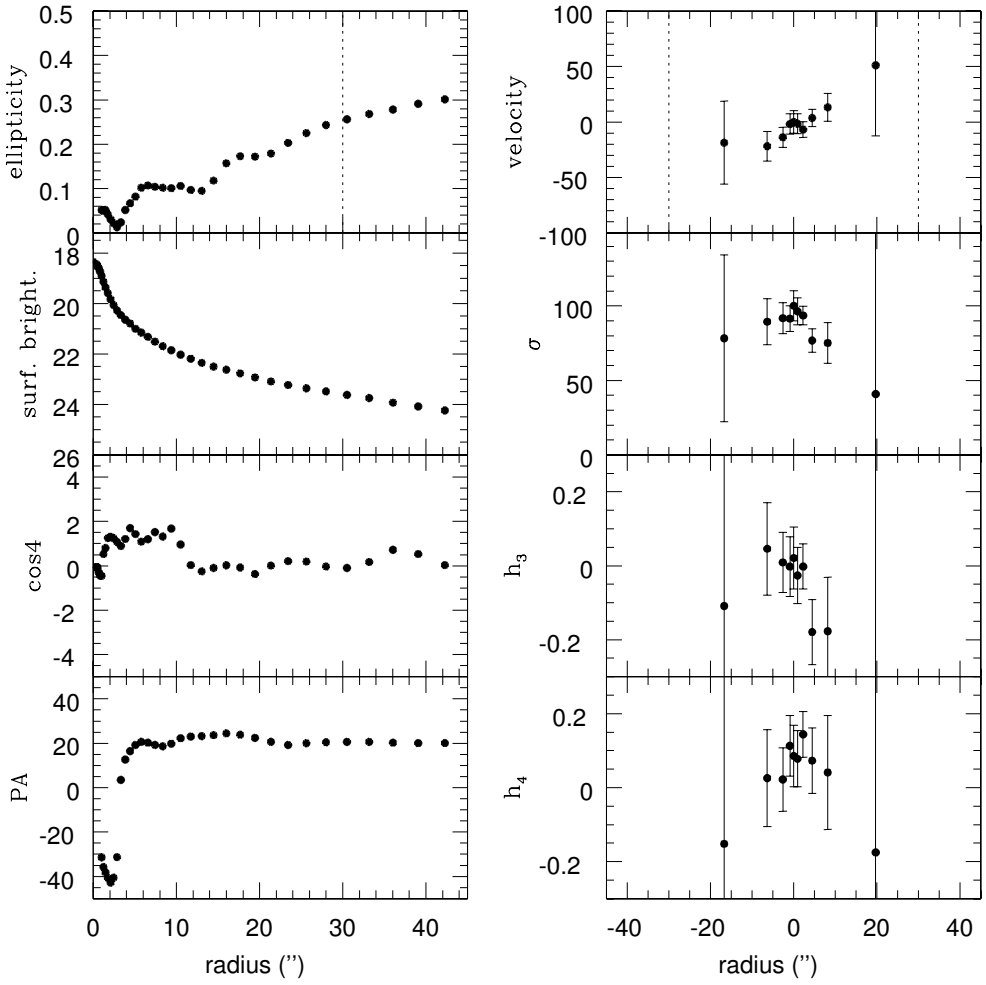

Figure 1.8: *Left*: Photometric profiles of NGC 1336 in the B-band (taken from Caon et al. 1994). From top to bottom: ellipticity, surface brightness (in mag/sq.arcsec.), cos4 parameter, position angle. *Right*: stellar kinematics of NGC 1336. From top to bottom: velocity, velocity dispersion, h_3 and h_4 parameters. Dashed line indicates one effective radius.

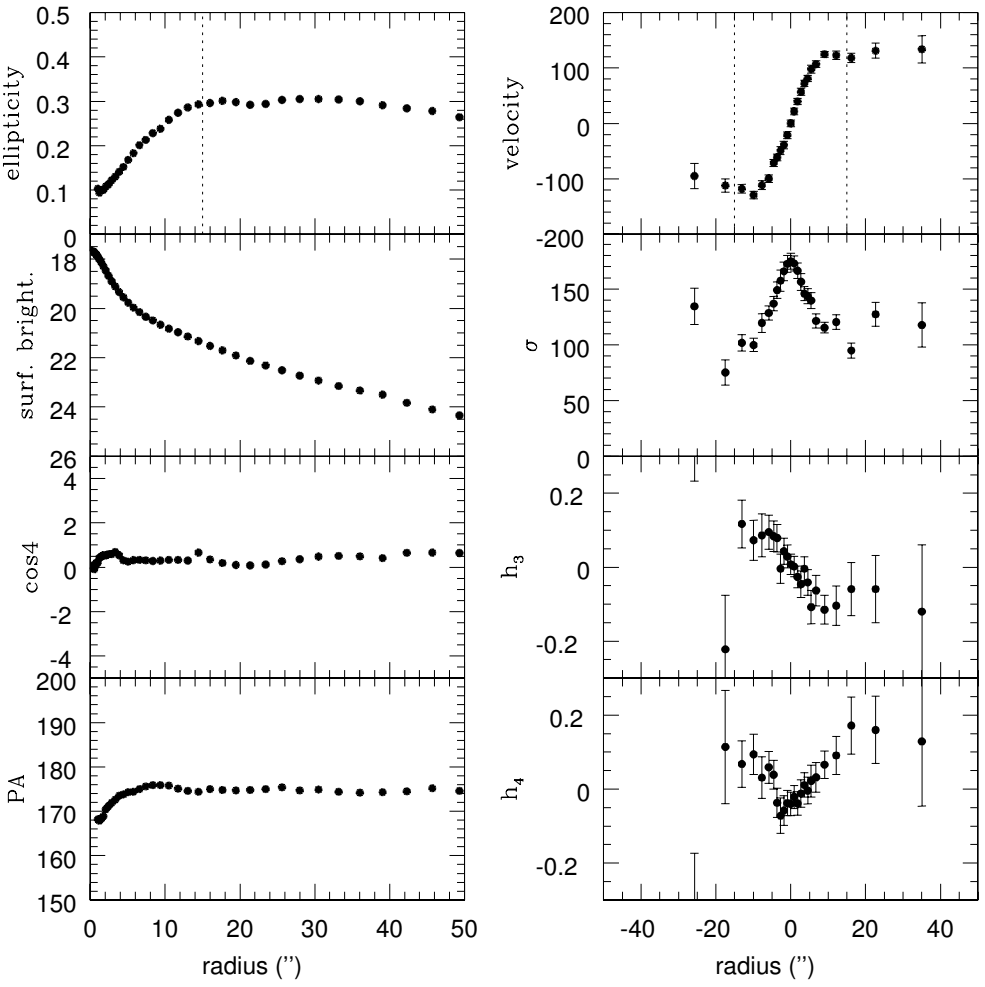

Figure 1.9: *Left*: Photometric profiles of NGC 1339 in the B-band (taken from Caon et al. 1994). From top to bottom: ellipticity, surface brightness (in mag/sq.arcsec.), cos4 parameter, position angle. *Right*: stellar kinematics of NGC 1339. From top to bottom: velocity, velocity dispersion, h_3 and h_4 parameters. Dashed line indicates one effective radius.

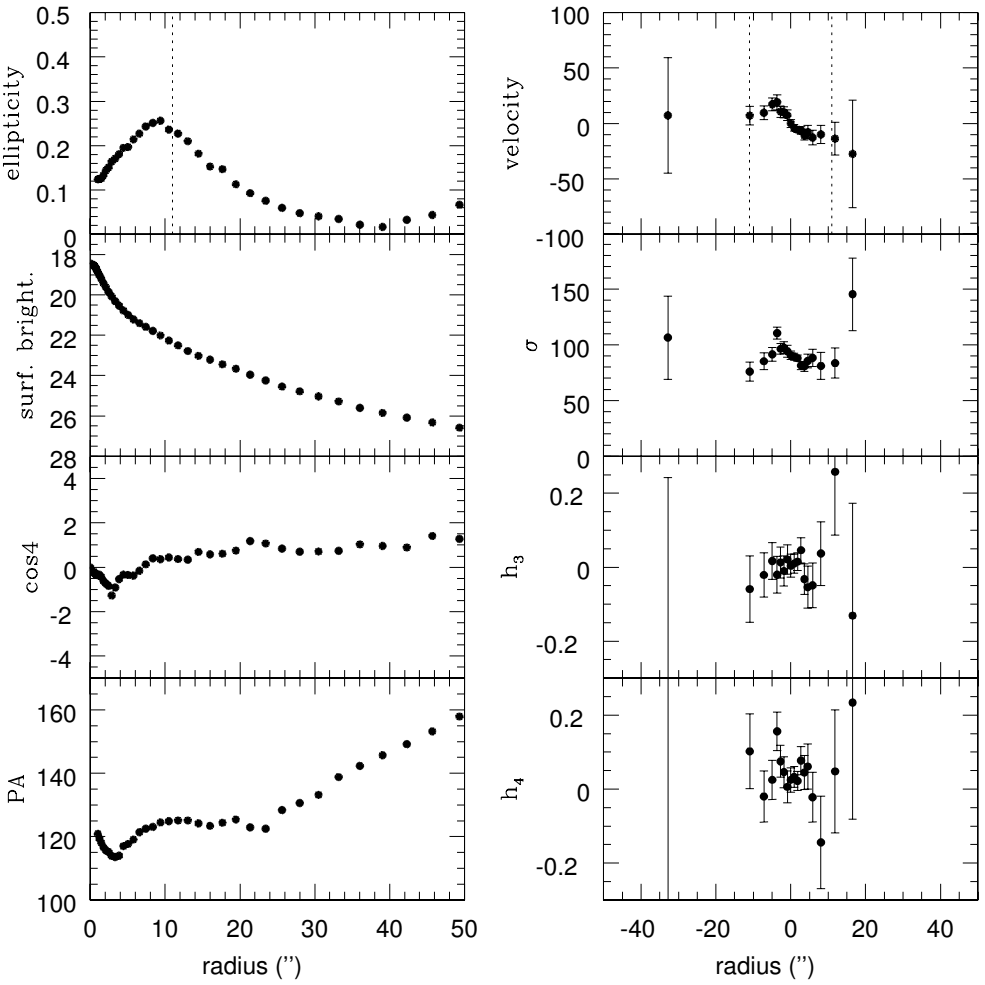

Figure 1.10: *Left*: Photometric profiles of NGC 1373 in the B-band (taken from Caon et al. 1994). From top to bottom: ellipticity, surface brightness (in mag/sq.arcsec.), cos4 parameter, position angle. *Right*: stellar kinematics of NGC 1373. From top to bottom: velocity, velocity dispersion, h_3 and h_4 parameters. Dashed line indicates one effective radius.

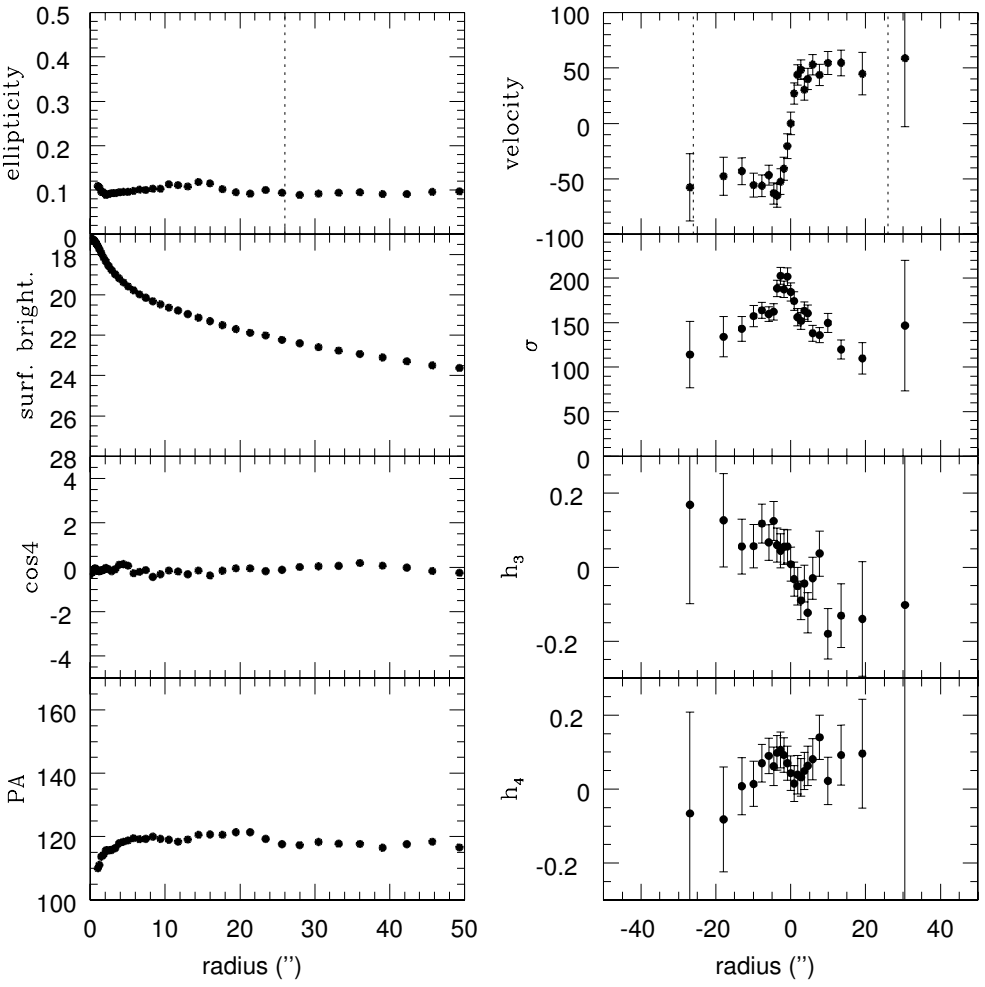

Figure 1.11: *Left*: Photometric profiles of NGC 1374 in the B-band (taken from Caon et al. 1994). From top to bottom: ellipticity, surface brightness (in mag/sq.arcsec.), cos4 parameter, position angle. *Right*: stellar kinematics of NGC 1374. From top to bottom: velocity, velocity dispersion, h_3 and h_4 parameters. Dashed line indicates one effective radius.

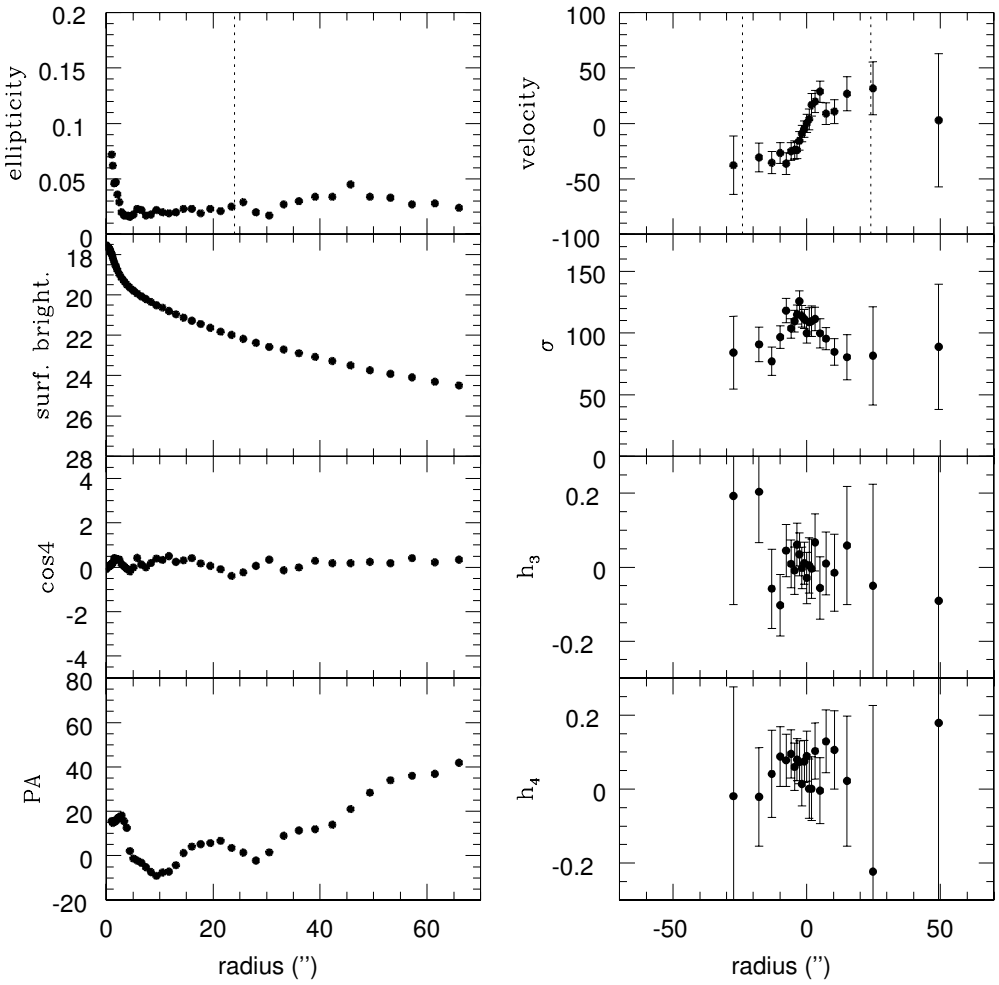

Figure 1.12: *Left*: Photometric profiles of NGC 1379 in the B-band (taken from Caon et al. 1994). From top to bottom: ellipticity, surface brightness (in mag/sq.arcsec.), cos4 parameter, position angle. *Right*: stellar kinematics of NGC 1379. From top to bottom: velocity, velocity dispersion, h_3 and h_4 parameters. Dashed line indicates one effective radius.

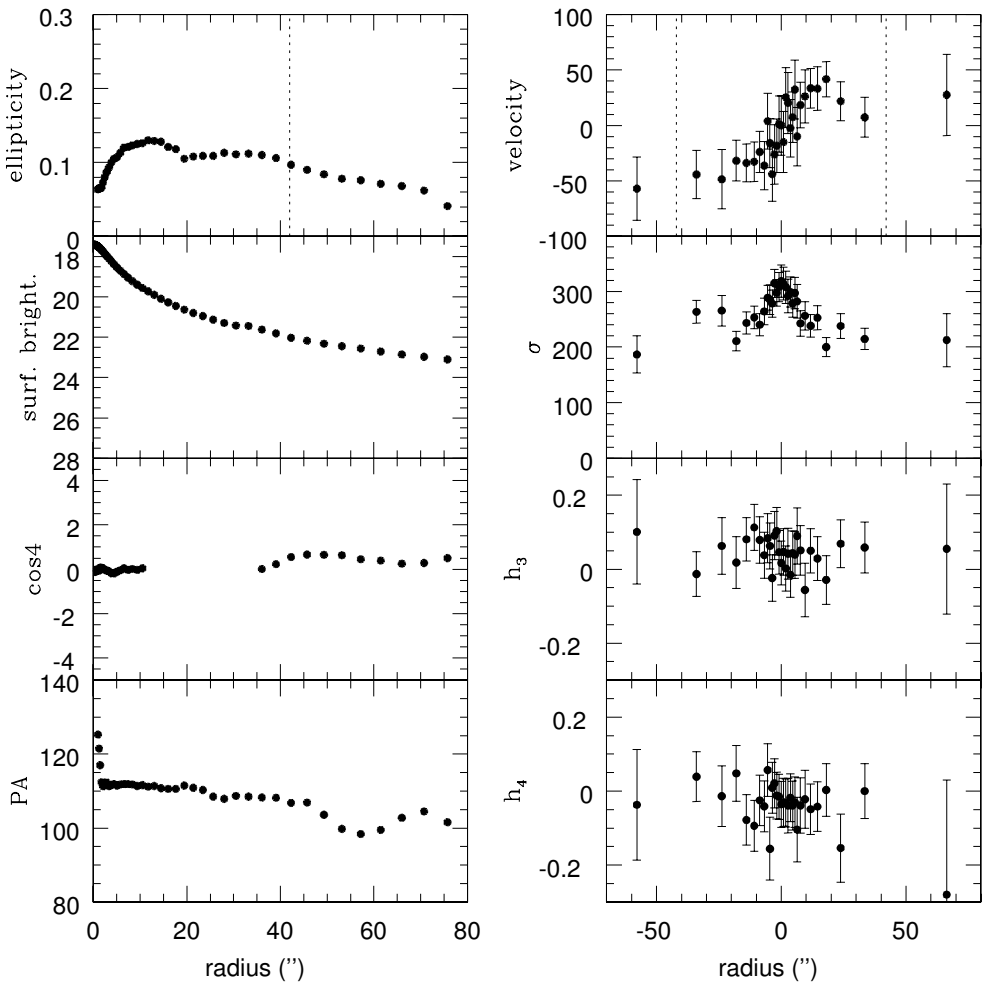

Figure 1.13: *Left*: Photometric profiles of NGC 1399 in the B-band (taken from Caon et al. 1994). From top to bottom: ellipticity, surface brightness (in mag/sq.arcsec.), cos4 parameter (note lack of data between $10''$ and $35''$), position angle. *Right*: stellar kinematics of NGC 1399. From top to bottom: velocity, velocity dispersion, h_3 and h_4 parameters. Dashed line indicates one effective radius.

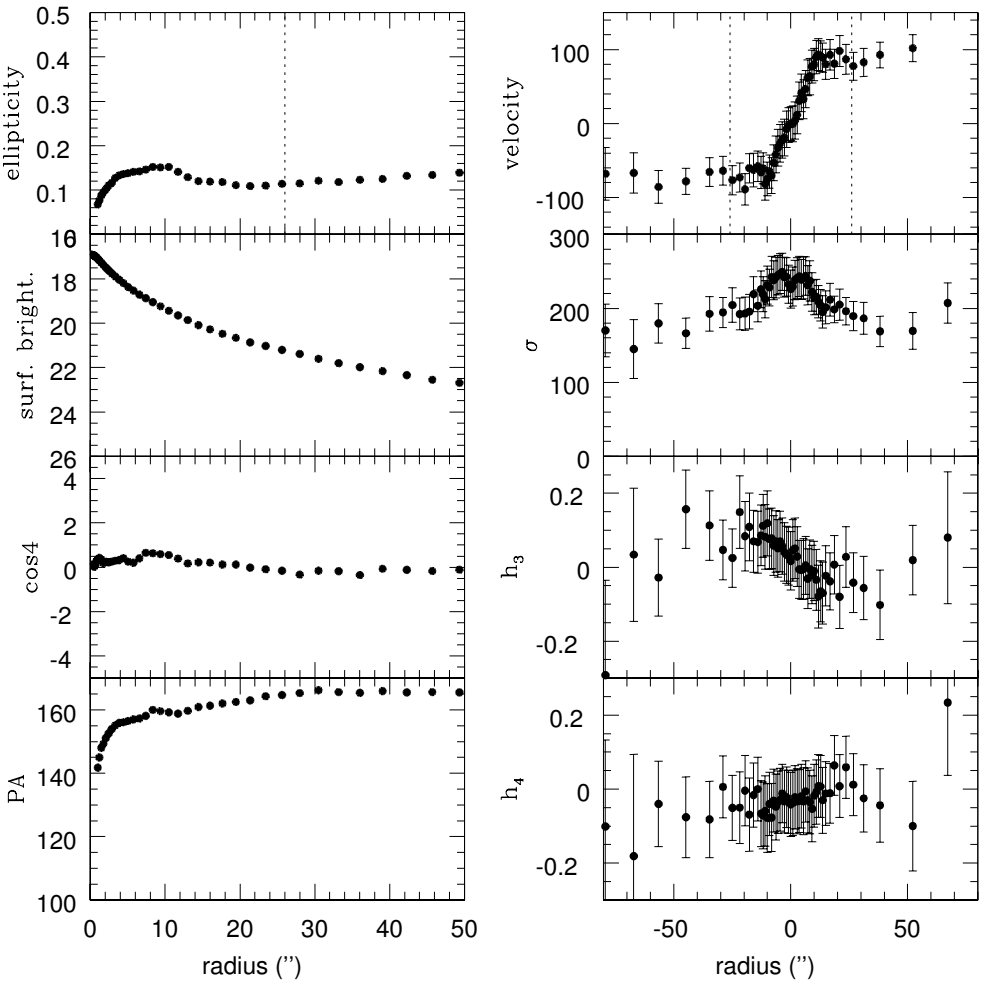

Figure 1.14: *Left*: Photometric profiles of NGC 1404 in the B-band (taken from Caon et al. 1994). From top to bottom: ellipticity, surface brightness (in mag/sq.arcsec.), cos4 parameter, position angle. *Right*: stellar kinematics of NGC 1404. From top to bottom: velocity, velocity dispersion, h_3 and h_4 parameters. Dashed line indicates one effective radius.

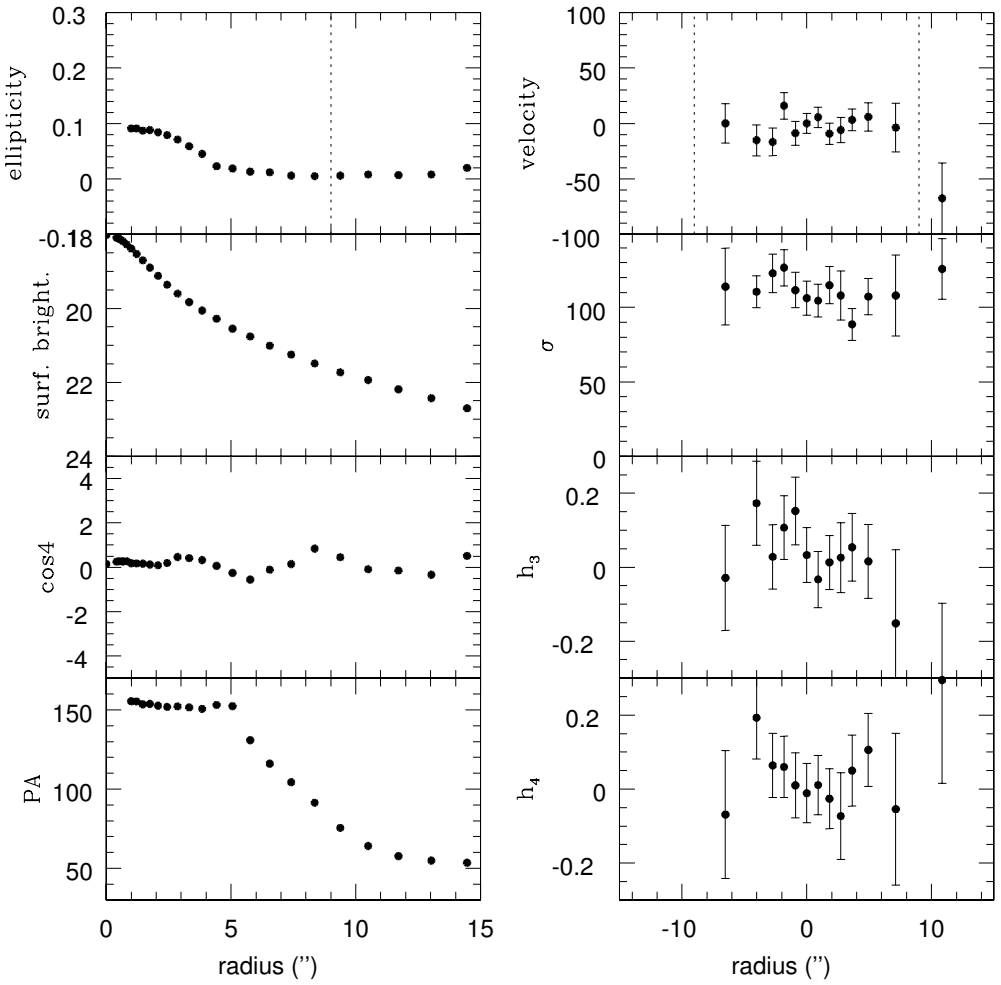

Figure 1.15: *Left*: Photometric profiles of NGC 1419 in the B-band (taken from Caon et al. 1994). From top to bottom: ellipticity, surface brightness (in mag/sq.arcsec.), cos4 parameter, position angle. *Right*: stellar kinematics of NGC 1419. From top to bottom: velocity, velocity dispersion, h_3 and h_4 parameters. Dashed line indicates one effective radius.

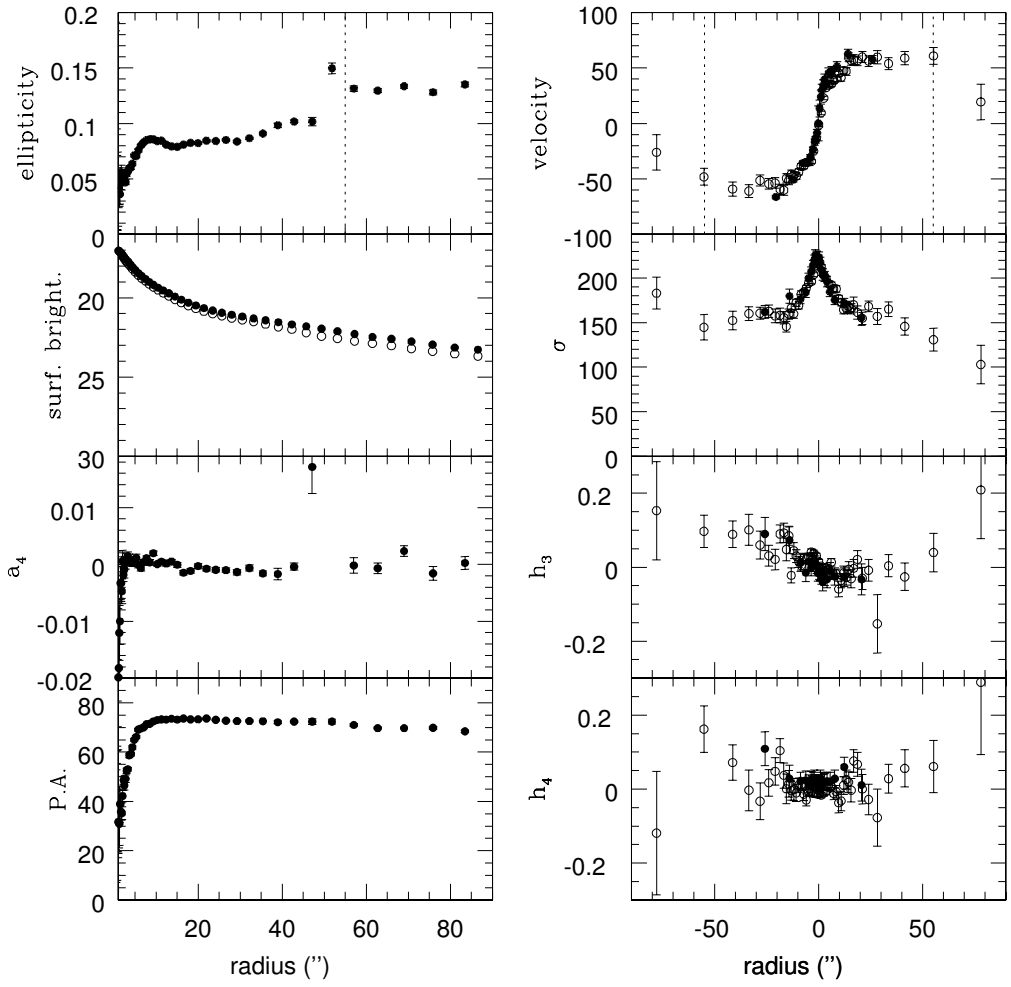

Figure 1.16: *Left*: Photometric profiles of NGC 3379 in the B-band. From top to bottom: ellipticity, surface brightness from Capaccioli et al. (1990) (in mag/sq.arcsec.) for major (black circles) and minor (open circles) axis, cos4 parameter, position angle. *Right*: Comparison of stellar kinematics of our extraction (black circles) and Statler and Smecker-Hane (1999). From top to bottom: velocity, velocity dispersion, h_3 and h_4 parameters. Dashed line indicates one effective radius.

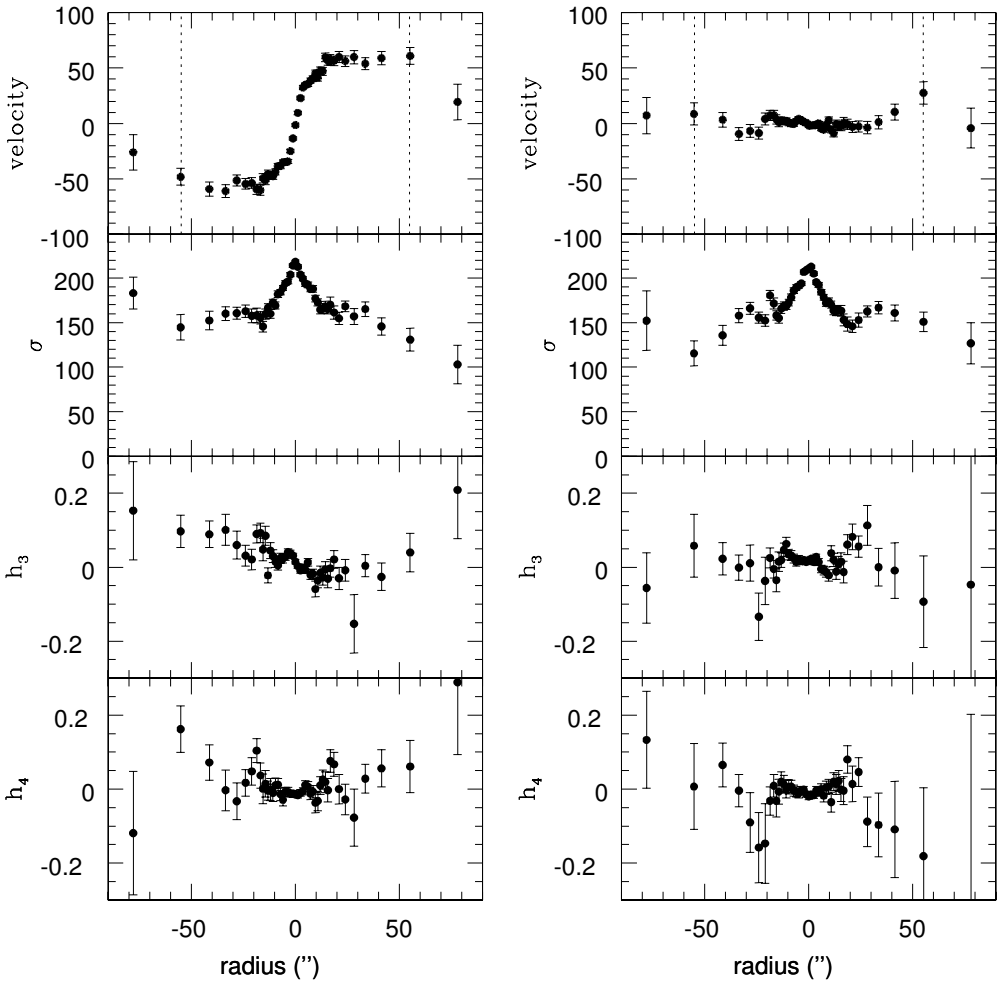

Figure 1.17: Stellar kinematics of NGC 3379 (taken from Statler and Smecker-Hane (1999)) for major (left) and minor (right) axis. From top to bottom: velocity, velocity dispersion, h_3 and h_4 parameters. Dashed line indicates one effective radius.

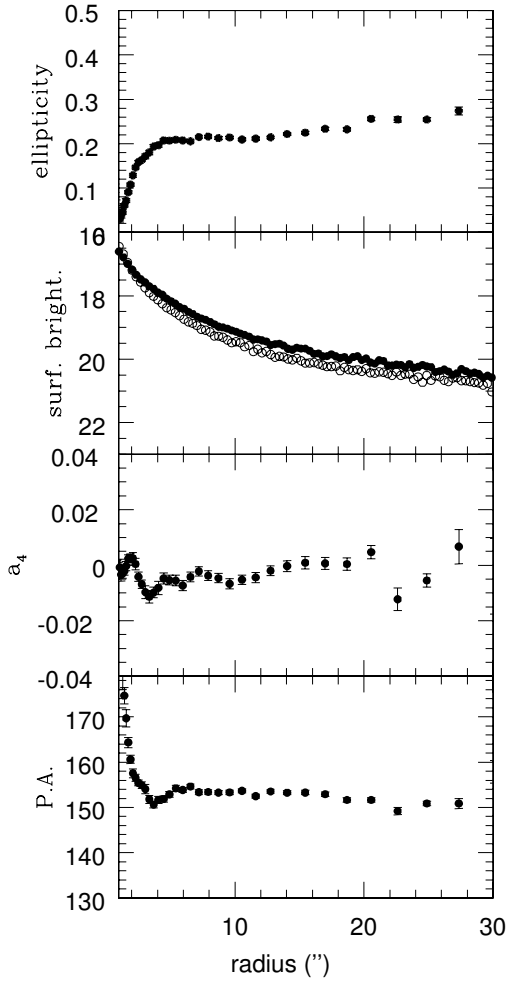

Figure 1.18: Photometric profiles of NGC 4105 in the R-band. From top to bottom: ellipticity, surface brightness (in mag/sq.arcsec.), cos4 parameter, position angle. Note that the effective radius is 35 arcsec and is therefore not shown.

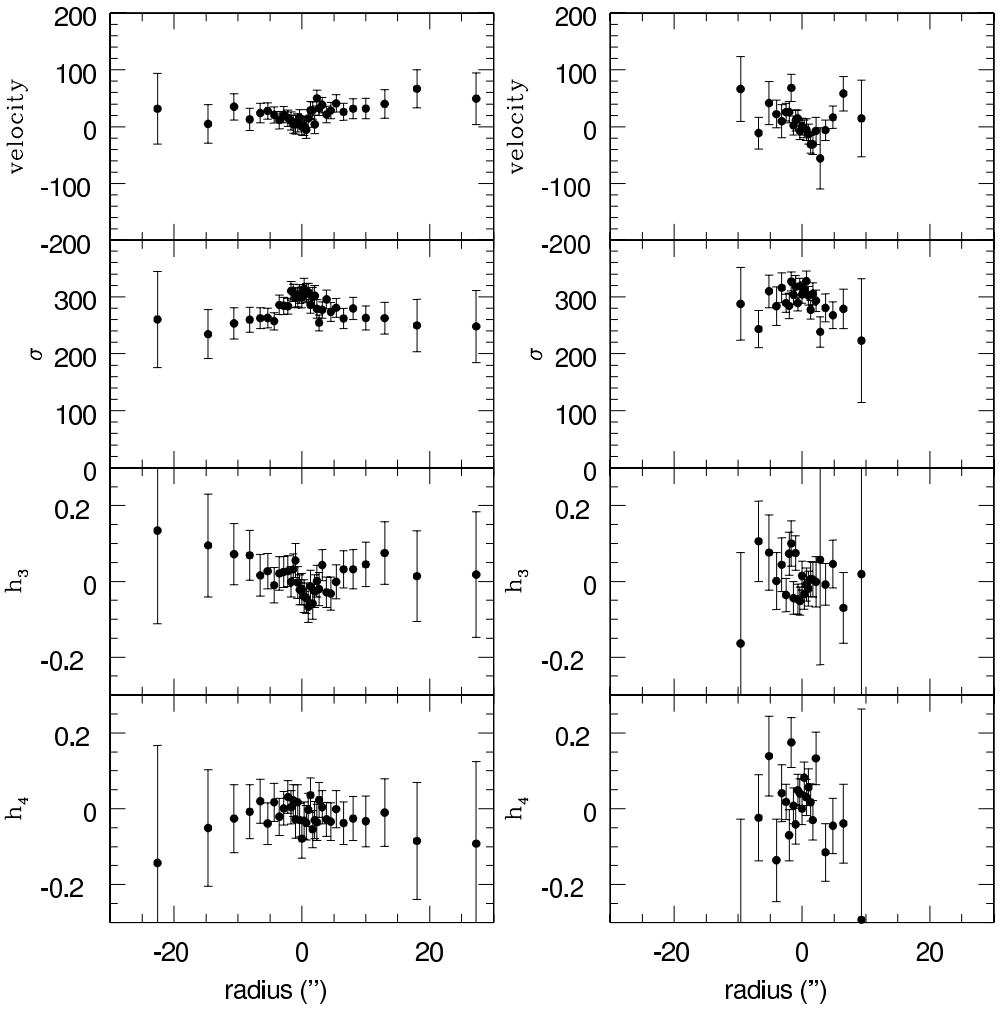

Figure 1.19: Stellar kinematics of NGC 4105 for major (left) and minor (right) axis. From top to bottom: velocity, velocity dispersion, h_3 and h_4 parameters. Note that the effective radius is 35 arcsec and is therefore not shown.

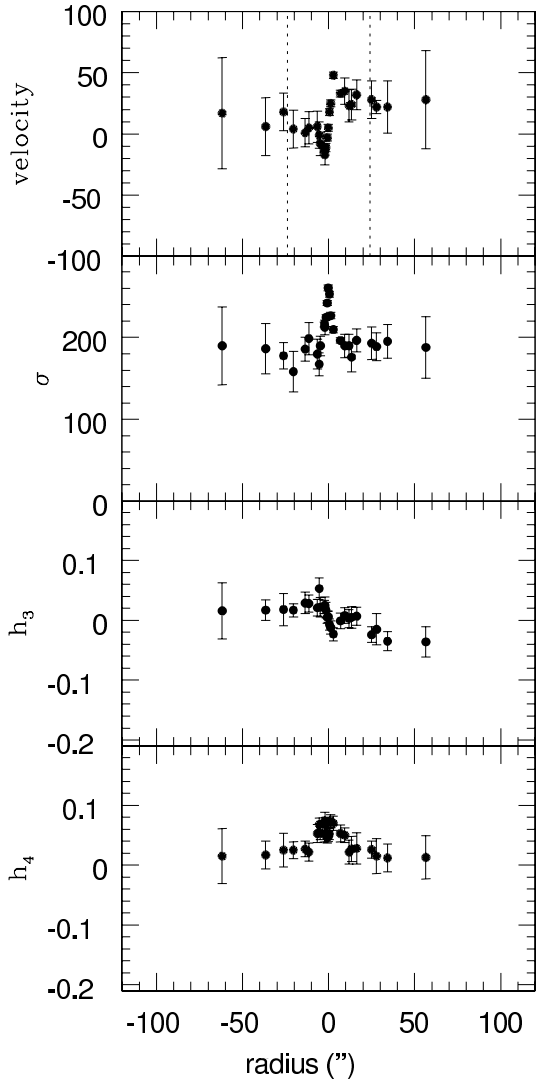

Figure 1.20: Stellar kinematics of NGC 2434 for major axis. From top to bottom: velocity, velocity dispersion, h_3 and h_4 parameters. Dashed line indicates one effective radius. Data taken from Carollo et al. (1995).

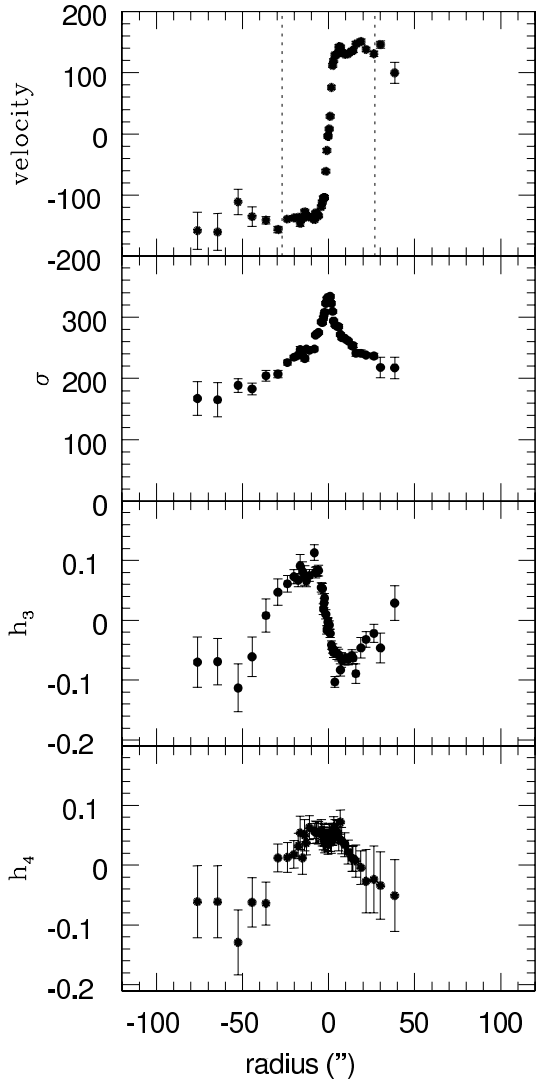

Figure 1.21: Stellar kinematics of NGC 3706 for major axis. From top to bottom: velocity, velocity dispersion, h_3 and h_4 parameters. Dashed line indicates one effective radius. Data taken from Carollo et al. (1995).

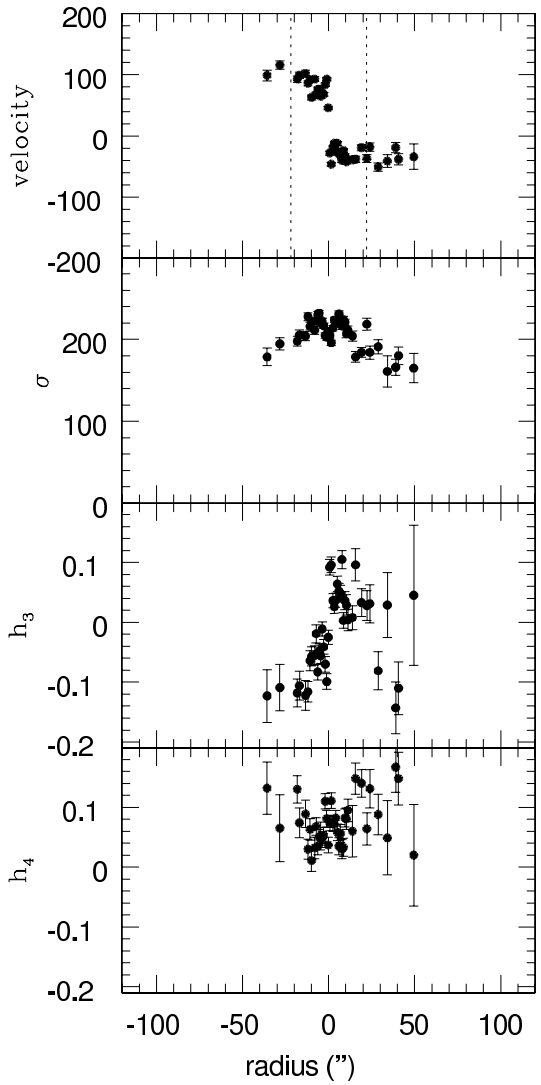

Figure 1.22: Stellar kinematics of NGC 5018 for major axis. From top to bottom: velocity, velocity dispersion, h_3 and h_4 parameters. Dashed line indicates one effective radius. Data taken from Carollo et al. (1995).

Chapter 2
DYNAMICAL MODELLING OF ELLIPTICAL GALAXIES: TWO- AND THREE-INTEGRAL APPROACHES

2.1. TWO-INTEGRAL MODELLING

2.1.1. THEORETICAL INTRODUCTION

DETAILED JEANS MODELLING

In this subsection we present the concept of the Jeans modelling which involves making the predictions of the following kinematic quantities: velocity, velocity dispersion, h_3 and h_4 parameters. This kind of modelling will be applied to the galaxies for which we have at least major and minor axis integrated stellar spectra: IC 3370 and IC 1459 (from Sample 1) and NGC 3379 and NGC 4105 (from Sample 3). All other galaxies for which we have only major data kinematics (Samples 2 and 4) will be modelled using simple Jeans modelling which includes modelling of the velocity dispersion only (but taking account the h_4 parameter). Note that the simple Jeans modelling will also be applied in the case of Sample 3 for the sake of comparison with the detailed Jeans and X-ray modelling (addressed in Chapter 3). Some preliminary results regarding the observations and modelling of elliptical galaxies were given in Samurović (2003, 2005) and some results presented here were published in Samurović and Danziger (2005).

For the two-integral (2I) modelling procedures we used the modelling technique developed by Binney, Davies and Illingworth (1990, hereafter BDI), and subsequently used by van der Marel, Binney and Davies (1990) and Cinzano and van der Marel (1994). Only in Cinzano and van der Marel (1994) does the modelling include h_3 and h_4 parameters. Statler, Dejonghe and Smecker-Hane (1999) used the modified version of this method to analyze mass distribution in NGC 1700. Here we briefly present the assumptions and the modelling steps.

Two-integral modelling is the first step in understanding of the dynamics of the elliptical galaxies, because in cases of small departures from triaxiality (which is far more probable, and true in case of IC 3370 as has been shown previously), comparison

of real systems with the models can provide useful insights. The assumptions of axisymmetry and the fact that the velocity dispersion tensor is everywhere isotropic are the starting points for the procedure that includes the following three steps (cf. BDI): (i) inversion of the luminosity profiles and obtaining three-dimensional luminosity density that provides the mass density (under the assumption of constant mass-to-light ratio); (ii) evaluation of the potential and derivation of the velocity dispersion and azimuthal streaming (under the assumptions that the form of the distribution function is $f(E, L_z)$, where E is the energy and L_z is the angular momentum of the individual star about the symmetry axis of the galaxy and that the velocity dispersion is isotropic) and (iii) comparison of the projected kinematical quantities from the model with the observed kinematic parameters; optionally, a disk, and/or a dark halo can be included in the modelling procedure (see Fig. (2.1)).

The first step in the modelling procedure involves making a least-squares fit for a flattened Jaffe model (Jaffe 1983, Eqs. (2) and (3)) or a flattened modified Hubble model. The brightness distribution in the case of the modified Hubble profile is given as (see Binney and Tremaine 1987, Eq. (2-39)):

$$I(R) = \frac{2j_0 a}{1 + (R/a)^2},$$

(where j_0 is the central luminosity density and a is the core radius), and was used in the 2I modelling procedures of the galaxies for which we have sufficient data: photometry, and major and minor axis long-slit spectra. Because we were mainly interested in the outer parts of galaxies we did not correct for the effects of seeing that are of importance near the centres of galaxies. Six Lucy iterations were used to get a fit of the surface brightness profile to the model. In cases when the disk was taken into account, the surface brightness of the disk was subtracted assuming that the disk is exponential.

For the evaluation of the dynamical quantities one assumes that the spheroid's mass density $\rho(R, z) = \Upsilon_s j(R, z)$ where Υ_s is some constant mass-to-light ratio, and $j(R, z)$ is a luminosity density along the line of sight. Here, it would be appropriate to present an estimate of the typical mass-to-light ratio in elliptical galaxies. van der Marel (1991) found in his sample of 37 bright ellipticals that the average mass-to-light ratio in the B-band is: $M/L_B \equiv \Upsilon_B = (5.95 \pm 0.25)h_{50}$. He also found that the mass-to-light ratio is correlated with the total luminosity: $M/L_B = 3.84 h_{50} (L_B/L_{*,B})^{0.35}$, where $L_{*,B} \equiv 3.3 \times 10^{10} h_{50}^{-2} L_\odot$. Note that in this book $h_0 = 0.70$ was always used, which means that $h_{50} = 0.70/0.50 = 1.4$. For the mass-to-light symbol we will use both M/L_B and Υ_B.

The gravitational potential Φ_s generated by the spheroid is (see BDI):

$$\Phi_s(R, z) = \sum_{l=0}^{5} \tilde{\Phi}_l(R) P_{2l}\left(\frac{z}{\sqrt{R^2 + z^2}}\right), \tag{2.1}$$

where P_k is the Legendre polynomial of order k. Six-point Gaussian evaluation is used to solve the integrals on a logarithmic grid of r values (r, z, θ are the usual cylindrical

coordinates):

$$\tilde{\rho}_l(r) = \int_0^1 \rho(r\sin\theta, r\cos\theta) P_{2l}(\cos\theta) d(\cos\theta) \tag{2.2}$$

and direct evaluation of the integrals for these r values:

$$\tilde{\Phi}_l(r) = -4\pi G \left[\frac{1}{r^{2l+1}} \int_0^r \rho_l(s) s^{2l+2} ds + r^{2l} \int_0^\infty \rho_l(s) \frac{ds}{s^{2l-1}} \right] \tag{2.3}$$

and a linear interpolation of $\tilde{\Phi}_l$ versus $\log r$.

If one includes the disk, it is assumed that its mass-to-light ratio is Υ_d. The disk potential (cf. BDI and references therein) is given as:

$$\Phi_d = -\frac{2\pi G \Upsilon_d I_d(0)}{R_d} \int_0^\infty \frac{J_0(kR) e^{-kz}}{(R_d^{-2} + k^2)^{3/2}} dk, \tag{2.4}$$

where the integral on the right hand side is the Bessel integral. For $z = 0$ this integral can be evaluated analytically. For $z \neq 0$, $R \neq 0$ this integral must be evaluated numerically.

When one has the potential $\Phi = \Phi_s + \Phi_d$ and the luminosity density j, the velocity dispersion σ in the meridional directions, under the assumptions of the distribution function of the form $f(E, L_z)$ is given by Satoh formula:

$$\sigma^2(R,z) = \frac{1}{j(R,z)} \int_z^\infty j d\Phi \tag{2.5}$$

where the integral is along a line of constant R. The mean-square azimuthal speed $\overline{v_\phi^2}$ is given as:

$$\overline{v_\phi^2} = \sigma^2 + R\frac{\partial \Phi}{\partial R} + \frac{R}{j}\frac{\partial (j\sigma^2)}{\partial R}. \tag{2.6}$$

Since we assume, for the moment, in this subsection, that the distribution function is of the form $f(E, L_z)$ the second radial velocity moment, $\overline{v_R^2} \equiv \sigma_R^2$, and the second vertical velocity moment, $\overline{v_z^2} \equiv \sigma_z^2$ are everywhere equal and $\overline{v_R v_z} = 0$. The Jeans equations are:

$$\frac{\partial \rho \overline{v_z^2}}{\partial z} + \rho \frac{\partial \Phi}{\partial z} = 0 \tag{2.7}$$

$$\frac{\partial \rho \overline{v_R^2}}{\partial R} + \rho \frac{\partial \Phi}{\partial R} + \frac{\rho}{R}[\overline{v_R^2} - \overline{v_\phi^2}] = 0. \tag{2.8}$$

We solve them searching for unknowns $\overline{v_\phi^2}$ and $\sigma_R^2 = \sigma_z^2$. Using a free parameter, k, one can, as usual, assign a part of the second azimuthal velocity moment $\overline{v_\phi^2}$ to streaming:

$$\overline{v_\phi} = k\sqrt{\overline{v_\phi^2} - \sigma_R^2}. \tag{2.9}$$

Then we project the dynamical quantities on to the sky to get predictions.

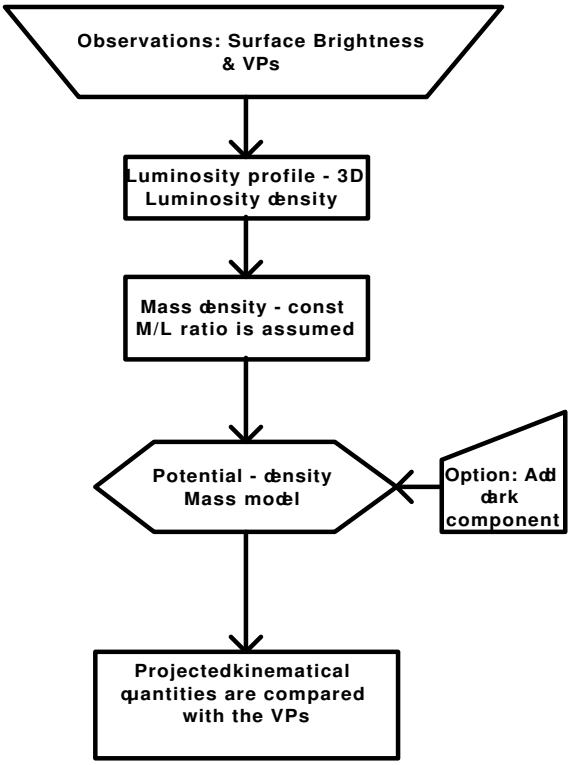

Figure 2.1: Flowchart of the detailed Jeans modelling (two-integral modelling procedure). VP stands for velocity profile.

SIMPLE JEANS MODELLING

In this part we will briefly describe the procedure which we call simple Jeans modelling because it involves modelling of the velocity dispersion only. Some of the details will be repeated in Chapters 3 and 5 when we use the Jeans equations for the modelling based on the X-rays and planetary nebulae and globular clusters, respectively.

We solve the Jeans equation which provides the connection between the velocity dispersion, anisotropy and the dynamical mass distribution (Binney and Tremaine 1987):

$$\frac{1}{\ell_*}\frac{\mathrm{d}(\ell_*\sigma_r^2)}{\mathrm{d}r} + \frac{2\beta_*\sigma_r^2}{r} = -\frac{GM(r)}{r^2} + \frac{v_{\mathrm{rot}}^2}{r} \tag{2.10}$$

where σ_r is the radial stellar velocity dispersion, ℓ_* is the stellar luminosity density which corresponds to the radial (σ_r) and transverse (σ_t) stellar velocity dispersions.

Here, $v_{\rm rot}$ is the rotational speed. A parameter β_* is introduced to describe the nonspherical nature of the stellar velocity dispersion:

$$\beta_* = 1 - \overline{v_\theta^2}/\sigma_r^2, \tag{2.11}$$

where $\overline{v_\theta^2} = \overline{v_\theta}^2 + \sigma_\theta^2$. For $0 < \beta_* < 1$ the orbits are predominantly radial, in this case the line of sight velocity profile is more strongly peaked than a Gaussian profile (positive h_4 parameter), and for $-\infty \leq \beta_* < 0$ the orbits are mostly tangential, so the profile is more flat-topped than a Gaussian (negative h_4 parameter) (Gerhard 1993). In all the cases calculated below we always assumed isotropy, i.e., the value $\beta = 0$ was imposed.

For the stellar luminosity density we adopted the Hernquist (1990) profile:

$$\ell_* = \frac{L}{2\pi}\frac{a}{r}\left(\frac{1}{r+a}\right)^3 \tag{2.12}$$

where $R_e = 1.8153a$. The projected line-of-sight velocity dispersion is calculated as (e.g. Binney and Mamon 1982, Mathews and Brighenti 2003a,b):

$$\sigma^2(R) = \frac{\int_R^{r_t} \sigma_r^2(r)\left[1-(R/r)^2\beta_*\right] \times \ell_*(r)(r^2-R^2)^{-1/2}\, r{\rm d}r}{\int_R^{r_t} \ell_*(r)(r^2-R^2)^{-1/2}\, r{\rm d}r} \tag{2.13}$$

where the truncation radius, r_t, extends to a large distance: for the galaxies analyzed below it was well beyond the last observed point.

To calculate the total mass interior to a given radius r one can use the photometry of a given galaxy and use the simple formula (in this case for the B-band, see Binney and Merrifield 1998) to calculate the *total luminous mass* of the galaxy:

$$\Upsilon_B = 10^{-0.4(M_B - M_{\odot B})}\frac{{\rm M_{tot}}}{{\rm M_\odot}}, \tag{2.14}$$

where M_B is the absolute magnitude of a given galaxy in the B-band and $M_{\odot B}$ is the absolute magnitude of the Sun in the B-band ($M_{\odot B} = +5.48$). The total luminous mass is given with $\rm M_{tot}$, and the mass of the Sun is given with $\rm M_\odot$. The mass $\rm M'_{tot}$ given in TABLE 2-1 below provides the total mass of the given galaxy divided by the given constant mass-to-light ratio: $\rm M'_{tot} = \frac{M_{tot}}{\Upsilon_B}$. For example, for the galaxy NGC 1336 we have $\rm M'_{tot} = 3.2 \times 10^9 M_\odot$ which means that for $\Upsilon_B = 7$ its total mass will be $\rm M_{tot} = 2.24 \times 10^{10} M_\odot$.

Now one can write the cumulative mass of a given galaxy *interior to a given radius* r for the Hernquist (1990) profile:

$$M(r) = {\rm M_{tot}}\frac{(r/R_e)^2}{(r/R_e + k')^2} \tag{2.15}$$

where R_e is effective radius and $k' \simeq 0.5509$ (see for example Napolitano et al. 2005 where this parametrization was used; $k' \simeq 0.5509 \equiv a/R_e = 1/1.8153$). Note that we write k' to avoid confusion between this quantity and the one defined in Eq. (2.9).

This mass, $M(r)$ is then inserted in the Jeans equation Eq. (2.10) and the velocity dispersion is calculated for a given value of the constant mass-to-light ratio.

This kind of modelling will be applied (using the assumptions given above) to the galaxies for which we had only the major axis kinematics data (Samples 2 and 4) and also to Sample 3 for the sake of comparison with the detailed Jeans modelling and X-ray modelling.

2.1.2. MODELLING RESULTS

DETAILED JEANS MODELLING

Using the two-integral axisymmetric modelling procedure we analyzed four galaxies for which we had sufficiently good major and minor axis stellar kinematics and photometry. We assume symmetry about the y-axis and therefore we folded all the observational data taking into account that velocity and h_3 are odd functions of the radius, and that velocity dispersion and h_4 are even functions of the radius. In all the following calculations the Hubble parameter $h = 0.70$ has been assumed. All the inferred mass-to-light ratios are given in the B-band.

Sample 1

Both of the galaxies belonging to Sample 1 will be modelled using detailed Jeans modelling.

IC 3370

As might be expected the axisymmetric modelling of IC 3370 did not give a good fit to the observed data given the strong isophotal twisting present in this galaxy. We used the inclination angle of 50° that gave the best (but far from perfect) results. This inclination angle implies intrinsic axis ratio of ~ 0.7. In Fig. (2.2) and Fig. (2.3) we present our modelling results for major, minor and intermediate axis.

Major axis (Fig. (2.2, panel (a)): for the major axis $k = 0.6$ (dotted lines) gives a good fit in the inner regions (~ 25 arcsec) for the velocity. A good fit is obtained in the outer regions (> 50 arcsec) for the velocity dispersion. On the contrary, $k = 1$ provides a good fit for the velocity in the outer region ($> 1R_e$); the velocity dispersion seems to be fitted well throughout the whole galaxy with $k = 1$. We experimented with the inclusion of the inner embedded disc of 6 arcsec, but this does not change much the results. The decrease of the velocity dispersion follows very closely the constant mass-to-light prediction (out to $\sim 3R_e$). Both h_3 and h_4 are fitted reasonably in all the given cases. The mass-to-light ratio found in all the cases at $\sim 3R_e$ is ~ 5.4. Since in this case, for the major axis, both the h_3 and h_4 parameters are consistent with zero we did not apply the correction of the velocity and velocity dispersion as we did in the case of IC 1459 (see below).

Minor axis (Fig. (2.2, panel (b)): because of the fact that the axisymmetric modelling predicts zero velocity for the minor axis, a successful fit could not be achieved

(the same is true for the h_3 parameter). Modelling of the velocity dispersion therefore provided a possibility for several interesting tests. One can see that $k = 0.6$ (dotted line, $M/L_B = 4.80$, no dark matter, no embedded disc) cannot produce a successful fit for the velocity dispersion. Therefore, in all other tests in the case of the minor axis we used $k = 1$. With the solid line we present the case of $M/L_B = 6.59$ without the embedded disc which provided a better, but still unsatisfactory fit to the data. Again, the inner embedded disc of 6 arcsec was included. Therefore, we increased the mass-to-light ratio to 9.68 (case without the dark matter and with the disc represented with the thick dashed line) to achieve a better agreement. Still better agreement is obtained when one increases further the mass-to-light ratio to 12.65: this is the case without the dark matter and the included disc represented by the thick dot-dashed line. Note, however, the discrepancy in the inner parts of the galaxy.

Intermediate axis (Fig. (2.3, panels (c) and (d)): Several tests were done using lower values of the constant mass-to-light ratio: the modelling of the *uncorrected* values of the observed velocity and velocity dispersion are given in panel (c) and the modelling of the *corrected* points is given in panel (d).

It was argued that the Gauss-Hermite estimates are not the best approximation of the mean line-of-sight velocity and velocity dispersion of the LOSVD (cf. van der Marel and Franx 1993; Statler, Smecker-Hane, and Cecil 1996; De Rijcke et al. 2003), because their real values depend on the h_3 and h_4 parameters. In the case of IC 3370 (intermediate axis) and IC 1459 there are significant departures in the Gauss-Hermite parameters from zero for a major axis so we applied the correction for the velocity and velocity dispersion. Following van der Marel and Franx (1993) we used the following formulas to get the corrected values that are then compared with the modelling results. The corrected values are, for the velocity:

$$v_{\rm corr} = v_{\rm GH} + \sqrt{3}(h_3)_{\rm GH}\sigma_{\rm GH}, \tag{2.16}$$

and for the velocity dispersion:

$$\sigma_{\rm corr} = \sigma_{\rm GH}(1 + \sqrt{6}(h_4)_{\rm GH}), \tag{2.17}$$

where the index "GH" is related to the Gauss-Hermite estimates.

Successful fits for the velocity dispersion are obtained for $k = 1$ (again the $k = 0.6$ case can be ruled out). All the models with $k = 1$ give a good fit for the velocity in the inner parts of the galaxy ($\sim$ 20 arcsec) and they all fail in the outer parts. In a similar manner they all reproduce well the velocity dispersion profile. h_3 and h_4 parameters are fitted reasonably throughout the whole galaxy (modelled h_3 shows departures in the outer region and h_4 shows small departures from the data in the inner part). We note the improvement of the models when the points corrected for non-zero values of h_3 and h_4 are used (see Fig. (2.3), panel d).

Strictly speaking IC 3370 should not be modelled using the axisymmetric modelling technique. However, this technique permits the following conclusion. In IC 3370 up to $\sim 3R_e$ the dark matter halo is not needed for the successful modelling: the mass-to-light ratio varies between ~ 5 (based upon the major axis data) and ~ 13 (based upon the minor axis data). Note however, that $M/L_B \sim 13$ is the upper limit, because it

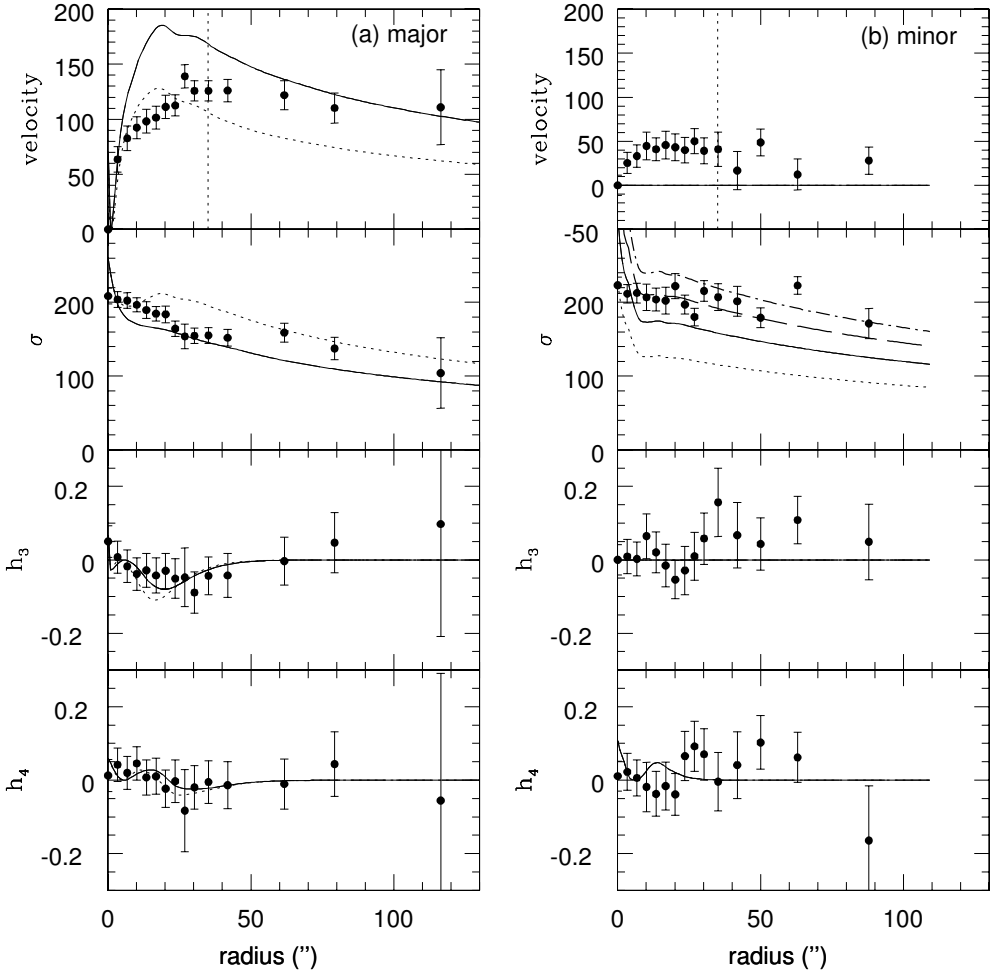

Figure 2.2: Predictions of the two-integral models for IC 3370. *Panel (a)*: major axis predictions. Dotted lines: $k = 0.6$, $M/L_B = 5.42$, no dark matter included, no embedded disc. Solid lines: $k = 1$, $M/L_B = 5.28$, no dark matter included, no embedded disc. *Panel (b)*: minor axis predictions. Dotted line: $k = 0.6$, $M/L_B = 4.80$, no dark matter included, no embedded disc. Solid line: $k = 1$, $M/L_B = 6.59$, no dark matter included, no embedded disc. Thick dashed line: $k = 1$, $M/L_B = 9.68$, no dark matter, embedded disc. Thick dot-dashed line: $k = 1$, $M/L_B = 12.64$, no dark matter, embedded disc. Vertical dotted line indicates one effective radius.

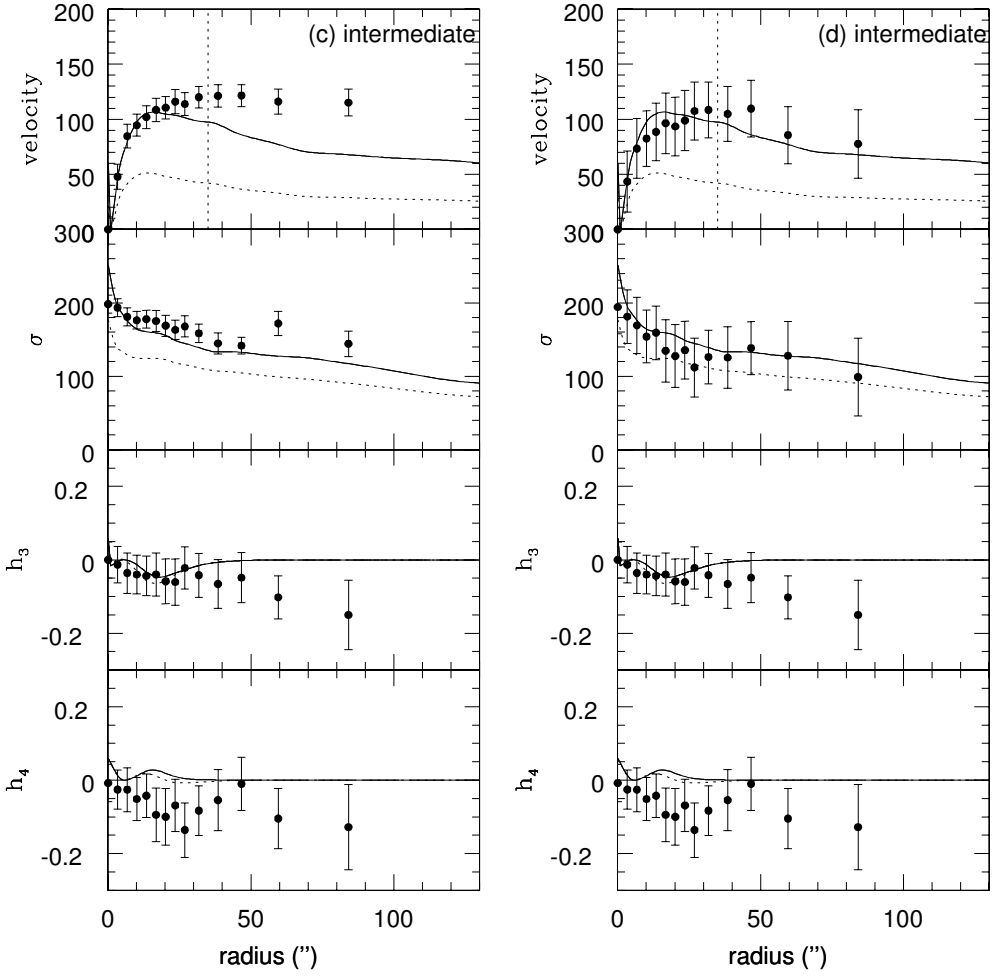

Figure 2.3: Predictions of the two-integral models for IC 3370. Intermediate axis predictions. *Panel (c)*: Intermediate axis predictions for the ***uncorrected*** values of the observed velocity and velocity dispersion. Dotted lines: $k = 0.6$, $M/L_B = 3.64$, no dark matter included, no embedded disc. Solid lines: $k = 1$, $M/L_B = 5.19$, no dark matter included, no embedded disc included. *Panel (d)*: Intermediate axis predictions for the values corrected for non-zero values of h_3 and h_4 of the observed velocity and velocity dispersion. The meaning of the curves is the same as in plot (c). Vertical dotted line indicates one effective radius.

must be stressed that this kind of modelling of the observed minor axis dispersions tends to *overestimate* the mass-to-light ratio (as given in BDI): this modelling, for a given M/L_B underestimates the minor axis dispersions since the model will be flattened by enhanced $\overline{v_\phi^2}$ which does not contribute to the minor axis profile. The real galaxy is flattened by enhanced $\overline{v_r^2}$ which contributes on the minor axis.

IC 1459

This galaxy has a counterrotating core and, therefore, two-integral axisymmetric modelling conceived by BDI based on the photometric profiles will necessarily fail in the inner regions. We tested the inclination angles from 50° to 90° and we decided to use the inclination angle of 65° in all the cases because it provided the best fit to the data (although very far from perfect). This inclination angle implies intrinsic axis ratio of ~ 0.7.

Major axis (Fig. (2.4, (left)): In the case of the major axis we tested $k = 0.6$ value: first, it gave marginally good fit for the velocity in the outer region of the galaxy ($M/L_B = 3.81$), and a marginally good fit in the region slightly beyond $1R_e$ for the velocity dispersion (dashed line), and, second, a case of larger $M/L_B = 6.83$ did not fit the velocity, nor the velocity dispersion (dotted line). In both of these cases no dark matter halo was included, and no embedded disc was assumed. If one takes $k = 1$, there are two cases that we decided to present: first, $M/L_B = 6.83$ (no dark halo, and no embedded disc) (solid lines) the velocity is extremely large (it declines from ~ 350 km s^{-1} at 20 arcsec to ~ 220 km s^{-1} at 100 arcsec); the velocity dispersion can be fitted, very closely, throughout the whole observed galaxy, and second, the case when $M/L_B = 3.81$ (no dark halo, and no embedded disc) (dot-dashed lines) for which the fitted velocity has smaller values (although still much larger than the observed ones): in a region between 20 arcsec and 100 arcsec the velocity decreases from 260 km s^{-1} to 170 km s^{-1}; the velocity dispersion is much lower, and the successful fit is attained only in the outer parts. The h_3 parameter, because of the fact that there is a counterrotating core, cannot be fitted. For the h_4 parameter this modelling did not give a successful fit in the outer parts where there possibly exists a radial anisotropy (judging from the observed non-zero value of the h_4 parameter). Therefore, one can state that only the test with $k = 1$ ($M/L_B = 6.83 \pm 0.13$) can provide a fit to the velocity dispersion. The fact that the predicted velocity is much larger is of a crucial importance and will be addressed below.

The corrections given with Eq. (2.16) and Eq. (2.17) are done only in the case of the major axis, since in the case of minor axis the departures from zero in h_3 and h_4 are minimal. Using the Cinzano and van der Marel modelling technique we did not correct the observed data in the inner regions (interior to ~ 6 arcsec) where the disc may be present and we corrected velocity and velocity dispersion beyond ~ 6 arcsec in order to compare with the models. In this inner region the model LOSVD is a sum of 2 Gaussians, and the modelled velocity dispersion is the physical velocity dispersion which is then compared to the data. We note that the non-zero values of the h_3 and h_4 parameters are not fitted because in the outer regions the models assume Gaussian LOSVDs. After the correction is done one can note the following change

with respect to the uncorrected values (see Fig. (2.5)): the velocity dispersion values in the outer part have increased (h_4 is positive), but the general trend of decline remains. When one now examines the modelling results given in Fig. (2.4) (right panel) one can see that a better fit to the observations is obtained using $k = 0.6$, and the constant mass-to-light ratio $M/L_B = 5.31 \pm 0.10$ that is somewhat lower than the value estimated for the best-fitting in the uncorrected case. This however does not alter the main conclusion: IC 1459 can be successfully fitted without invoking dark matter. Note however, that the error bars for h_4 are rather large in the outer parts. New observations of IC 1459 made (but still unpublished as of September 2006) by Bridges et al. (2003) should hopefully clarify the mass at $\sim 3R_e$.

Minor axis (Fig. (2.4) (right panel)): Three $k = 0.6$ cases are plotted: one for $M/L_B = 3.05$ (dashed line) which does not provide a good fit for the velocity dispersion, and the other one for which $M/L_B = 7.33$ that provides a better agreement (solid line). Finally, a thick short dashed line gives a prediction of the velocity dispersion for $M/L_B = 12.21$ and obviously does not provide a good fit (except marginally at ~ 30 arcsec). A better fit was obtained using $k = 1$: with the dotted lines we present a case with $M/L_B = 8.54$ (no dark matter, no embedded disc). However, a fit with $k = 1$, but with a lower value of mass-to-light ($M/L_B = 3.05$, dot-dashed line) predicts a velocity dispersion that is too low. Finally, if one increases mass-to-light ratio to $M/L_B = 14.23$ (thick long dashed line) one can get a prediction that seems valid at ~ 25 arcsec. Values of both velocity and h_3 parameter are consistent with zero for the minor axis, and h_4 is fitted properly for these cases.

We have shown that in the case of the major axis the best-fitting for the velocity dispersion can be obtained using $k = 1$ and $M/L_B = 6.83 \pm 0.13$ (or 5.31 ± 0.10 obtained using corrected values of v and σ) . However, with these assumptions the velocity is enormously high. This means that one is faced with the same situation that BDI described in the case of NGC 720. Therefore, as in BDI, one can conclude that IC 1459 *cannot have* a distribution function of the form $f(E, L_z)$, and that three-integral modelling is needed.

The results for the minor axis modelling are inconclusive because the observations go out only to $\sim 1R_e$. The slight tendency for the velocity dispersion to flatten in the outer parts of the minor axis could be a result of a predominance of tangential orbits possibly suggested by the trend seen in the h_4 parameter.

Because of the counterrotating core there is a strong hint that IC 1459 is the result of a merger. That is why we compared the results of Bendo and Barnes (2000) who used an N-body code to study the LOSVD of simulated merger remnants with the stellar kinematics that we extracted. A reasonable agreement is seen in Fig. 9 by Bendo and Barnes (2000) (see Fig. (2.6) in this book) which shows the dependence of the Gauss-Hermite parameters as functions of position along the major axis for a typical 3:1 merger (merger between disc galaxies with mass ratios of 3:1). Although in the central parts there is a small discrepancy between the observations and the simulation, in the outer parts there is an obvious trend for an increase in the h_4 parameter. A further detailed comparison is difficult to perform because we do not know how to scale exactly Bendo and Barnes simulation to our observed data because we do not know the effective radius of the simulated merger. In the case of IC 1459

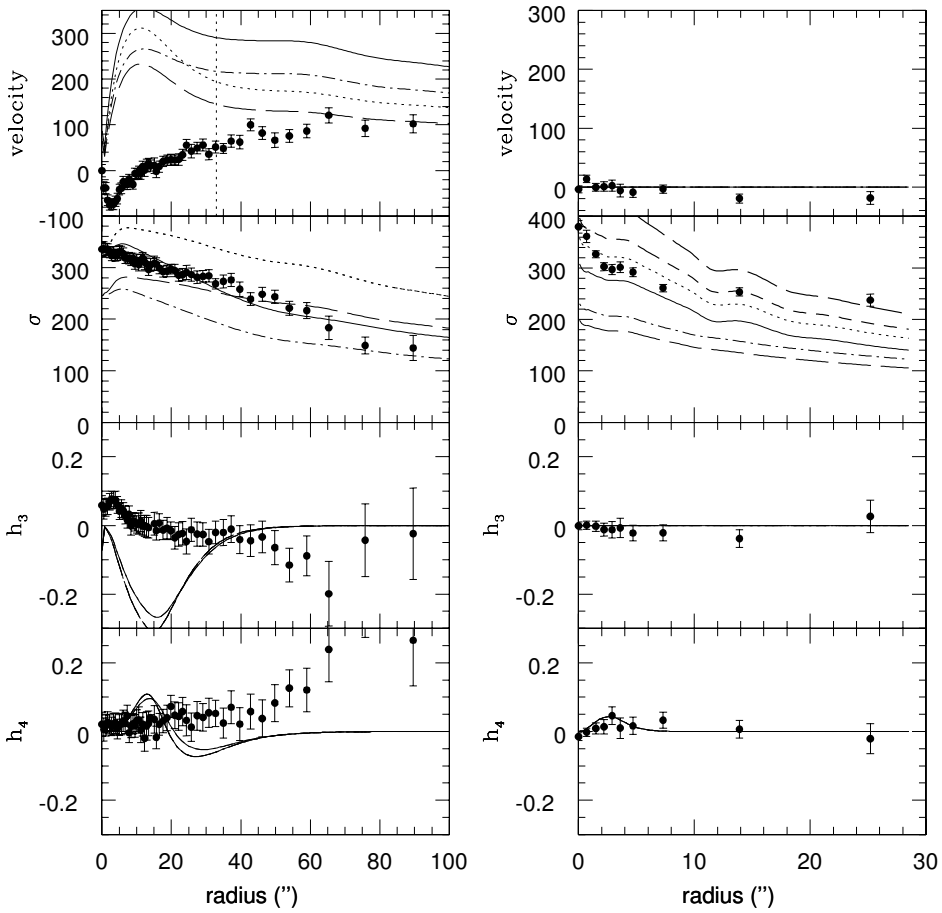

Figure 2.4: Predictions of the two-integral models for IC 1459. Left: major axis predictions. Solid lines: $k = 1$, $M/L_B = 6.83$, no dark matter included, no embedded disc. Dashed lines: $k = 0.6$, $M/L_B = 3.81$, no dark matter included, without embedded disc. Dotted lines: $k = 0.6$, $M/L_B = 6.83$, no dark matter included, without embedded disc. Dot-dashed lines: $k = 1$, $M/L_B = 3.81$, no dark matter included, without embedded disc . Right: minor axis predictions. Dotted line: $k = 1$, $M/L_B = 8.54$, no dark matter included, without embedded disc. Dashed line: $k = 0.6$, $M/L_B = 3.05$, no dark matter included, without embedded disc. Solid line: $k = 0.6$, $M/L_B = 7.33$, no dark matter included, without embedded disc. Dot-dashed line: $k = 1$, $M/L_B = 3.05$, no dark matter included, without embedded disc. Thick long dashed line: $k = 1$, $M/L_B = 14.23$, no dark matter included, without embedded disc. Thick short dashed line: $k = 0.6$, $M/L_B = 12.21$, no dark matter included, without embedded disc. Vertical dotted line indicates one effective radius; in case of the minor axis it is out of scale.

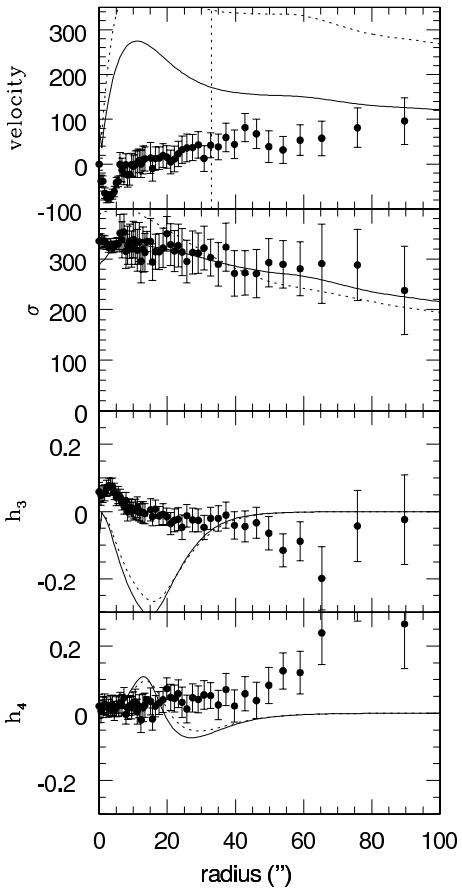

Figure 2.5: Predictions of the two-integral models for the major axis of IC 1459 for *corrected* values of the observed velocity and velocity dispersion (see text for details). Dotted line: $k = 1$, $M/L_B = 9.56$, no dark matter included, no embedded disc. Solid line: $k = 0.6$, $M/L_B = 5.31$, no dark matter included, without embedded disc. Vertical dotted line indicates one effective radius.

we have no way of knowing what the mass ratio of two disc galaxies might have been as well as other parameters involved in the simulation (such as inclination angles of the merging galaxies). For the core region we find $v/\sigma \approx 0.29$. Note, that for a quoted Bendo and Barnes simulation this ratio is about one. This is only a rough comparison but we hope that future studies of the projected kinematics of simulated merger remnants will bring new insights to the problem of the formation of the counterrotating cores and the formation of early-type galaxies in general, as the number of observed kinematical profiles increases.

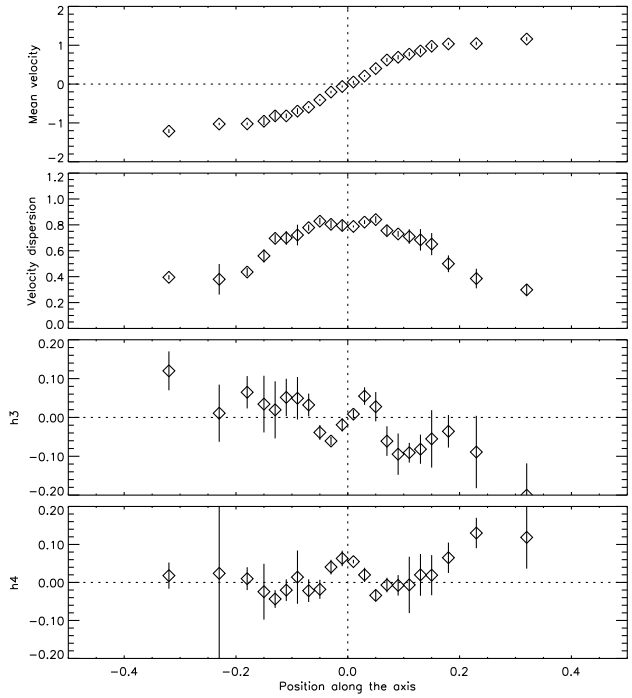

Figure 2.6: Taken from Bendo and Barnes (2000) (their Fig. 9). Parameters of the LOSVD along the major axis for a remnant, a typical 3:1 merger.

Sample 3

NGC 3379

NGC 3379 is a galaxy for which the evidence for dark matter is scarce (Ciardullo et al. 1993, Romanowsky et al. 2003). We present our results for the two-integral axisymmetric modelling for the major and minor axis in Fig. (2.7). The inclination angle that we used in all the cases was 40° because it gave the best fit to the observed data.

Major axis (Fig. (2.7) (left)): When one takes $k = 1$ and does not include either a dark matter halo or an internal embedded disc, using $M/L_B = 5.44$ (dotted lines) one gets an exaggerated value of the velocity but a rather reasonable fit for the velocity dispersion (especially in the inner part). In all other cases for the major axis we will use $k = 0.5$ which provides a better fit to the data in the outer part of NGC 3379. Using a mass-to-light ratio, $M/L_B = 4.75$, without an embedded disc and without a dark halo combination gives a good fit for the velocity dispersion in the outer regions. Also, a case with $M/L_B = 5.44$ (dashed line), without the embedded disc and without a dark halo gives a good fit in the outer part of the galaxy. Both h_3 and h_4 parameters are fitted similarly in all the models and the fit is very close to the observed values. Note that since the outermost points for the velocity dispersion and h_4 parameter

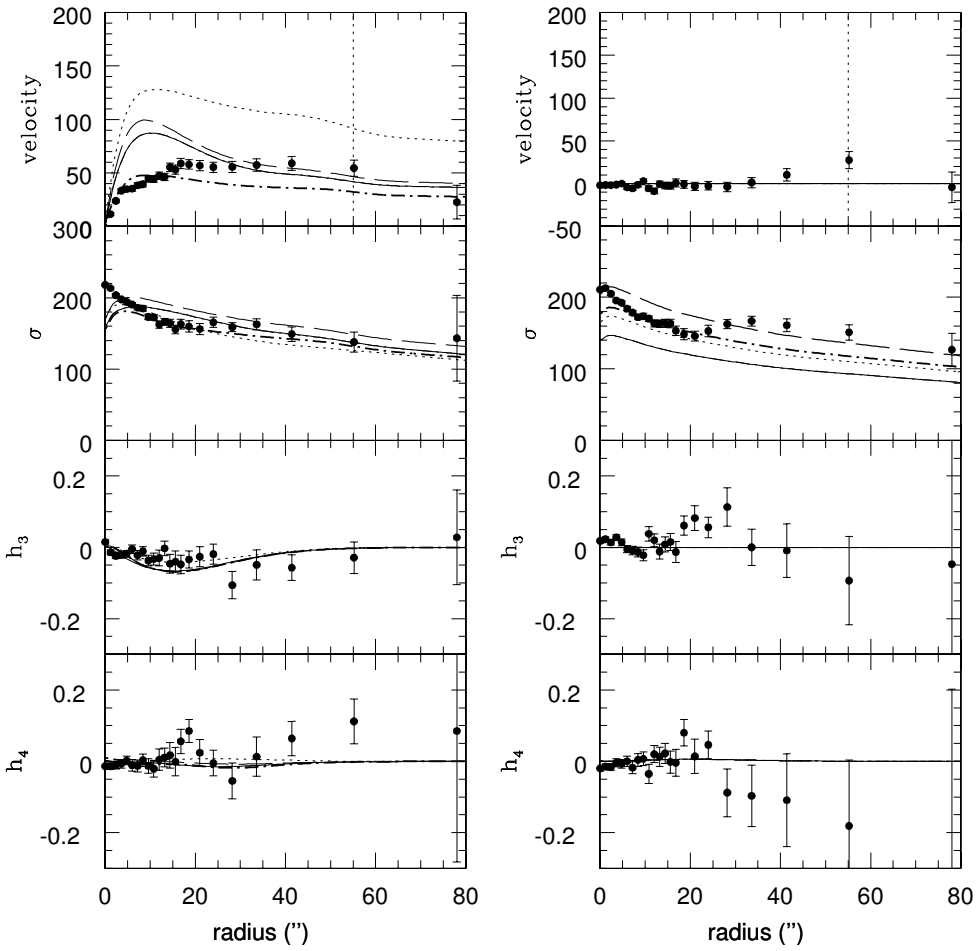

Figure 2.7: Predictions of the two-integral models for NGC 3379 compared to data. Left: major axis predictions. Dotted lines: $k = 1$, $M/L_B = 5.44$, no dark matter included, no embedded disc. Dashed lines: $k = 0.5$, $M/L_B = 5.44$, no dark matter included, without embedded disc. Solid lines: $k = 0.5$, $M/L_B = 4.75$, no dark matter included, embedded disc included. Thick dot-dashed line: $k = 0.4$, $M/L_B = 4.58$ no dark matter included, with embedded disc. Right: minor axis predictions. Dotted line: $k = 1$, $M/L_B = 4.18$, no dark matter included, without embedded disc. Solid line: $k = 0.5$, $M/L_B = 4.18$, no dark matter included, embedded disc included. Thick long dashed line: $k = 0.5$, $M/L_B = 8.91$, no dark matter included, without embedded disc. Thick dot-dashed line: $k = 0.5$, $M/L_B = 6.69$, no dark matter included, with embedded disc. Vertical dotted line indicates one effective radius.

appear to be discordant, we put a greatly increased error bar in order to provide a real uncertainty of these quantities. To get a better fit in the inner regions (interior to ~ 15 arcsec) we performed a test using low $k = 0.4$, inclination angle of 50° and $M/L_B = 4.58$: this is shown in Fig. (2.7) using a thick dot-dashed line.

Minor axis (Fig. (2.7) (right)): Because this galaxy does not show a strong rotation on the minor axis, the velocity was fitted properly in this approach which assumes axisymmetry. In the case of the minor axis we consider various tests related to the velocity dispersion. With a dotted line we present the $k = 1$ case with $M/L_B = 4.18$ without the dark matter, and without a disc: this does not provide a good fit. Neither can the case with $k = 0.5$ without a dark matter halo and a disc, with $M/L_B = 4.18$ which is represented with a dashed line. The thick dot-dashed line represents a case for which $M/L_B = 6.69$ ($k = 0.5$, without dark matter, and with embedded disc) and which provides a good fit in the inner region (out to $\sim 1R_e$), but fails in the outer regions. On the contrary, a test made with $M/L_B = 8.91$ and $k = 0.5$ (thick long dashed line) provides a good fit in the outer regions (beyond $\sim 1R_e$).

Our conclusion based upon the two-integral modelling that we performed is that in NGC 3379 there is no evidence for dark matter out to $\sim 1.46R_e$ and that this galaxy can be fitted with a constant mass-to-light ratio that is between ~ 5 and ~ 9. The minor axis modelling suggests a mass-to-light increasing with radius, while the major axis does not. This discrepancy could be due to the third-integral effects. These results are in agreement with the papers by other authors using entirely different techniques. Ciardullo et al. (1993) found that NGC 3379 does not possess a dark halo, and that mass-to-light ratio is ~ 7 (their observations of PNe extend out to ~ 200 arcsec). Also, they used distance of 10.1 Mpc to NGC 3379; if we apply the value of 13 Mpc used in our calculations the mass-to-light ratio in the B-band will become equal to 5.9 ± 0.9. Romanowsky et al. (2003) obtained the value $M/L_B = 7.1 \pm 0.6$ at ~ 200 arcsec taking the distance of 10.3 Mpc; again if we apply the value of 13 Mpc used in our applications we calculate the mass-to-light ratio in the B-band of 5.8 ± 0.5. Their results are similar to ours at smaller radius and taken together they fail to demonstrate the presence of dark matter over this range of radius. For comparison with some recent observations based on different mass tracers we refer the reader to Chapter 3.

NGC 4105

We present our results for the two-integral axisymmetric modelling for the major and minor axis in Fig. (2.8). The inclination angle that we used in all the cases was 50° because it gave the best fit to the observed data.

Major axis Fig. (2.8) (left)): The case of $k = 0.5$ and $M/L_B = 4.50$ (no dark matter halo, no disc included) provided the best-fitting to the velocity dispersion for the distance > 2 arcsec (dotted line). However, this case (as well as all the others mentioned below) predicts a grossly excessive velocity. The solid lines show the predictions of the case with $k = 1$, $M/L_B = 4.50$ (no dark matter halo, disc included), for which the velocity is again exaggerated, and velocity dispersion is lower than observed (although beyond ~ 2 arcsec within the error bars). We experimented

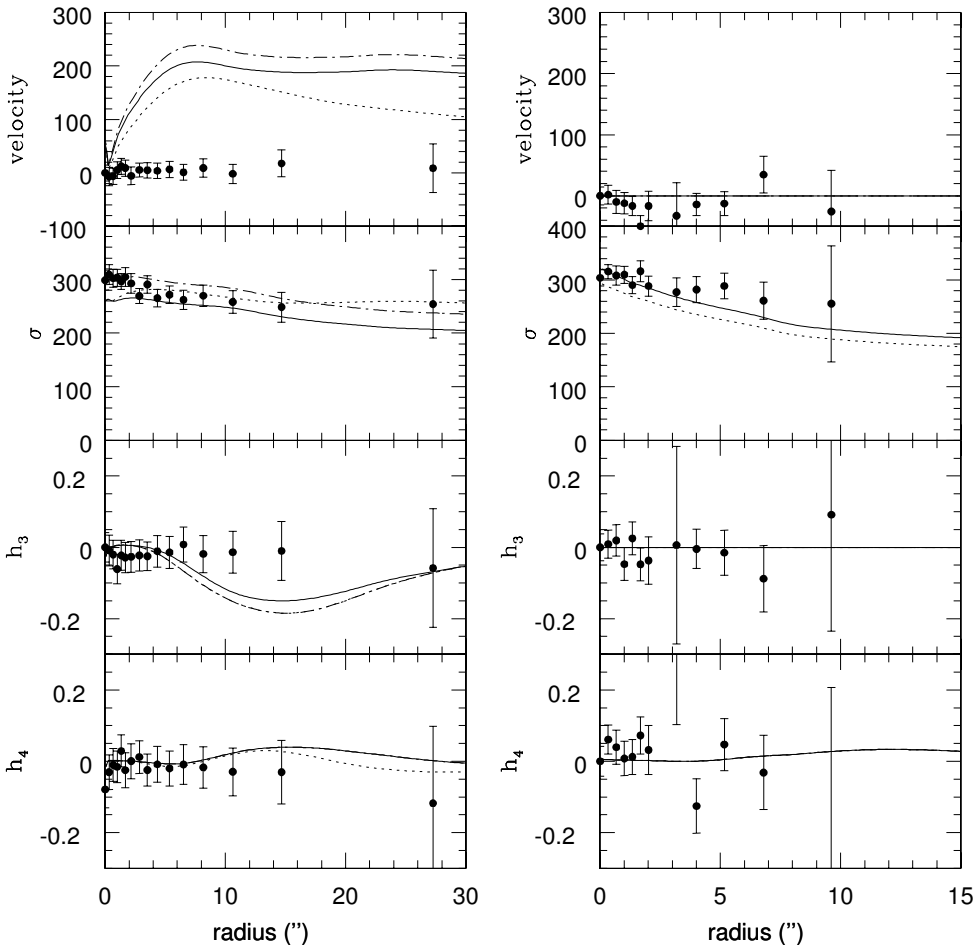

Figure 2.8: Predictions of the two-integral models for NGC 4105 compared to data. Left: major axis predictions. Dotted lines: $k = 0.5$, $M/L_B = 4.50$, no dark matter included, with embedded disc. Solid lines: $k = 1.0$, $M/L_B = 4.50$, no dark matter included, embedded disc included. Dot-dashed lines: $k = 1$, $M/L_B = 5.94$, without dark matter, with embedded disc. Right: minor axis predictions. Dotted line: $k = 0.5$, $M/L_B = 5.86$, no dark matter included, without embedded disc. Dashed line: $k = 1$, $M/L_B = 6.42$, no dark matter included, without embedded disc (overlapped by solid line). Solid line: $k = 1$, $M/L_B = 6.42$, no dark matter included, embedded disc included. Dashed line: $k = 0.5$, $M/L_B = 5.86$, without dark matter, without embedded disc. Note the difference in scales for two different axes.

with the embedded discs of 6 arcsec (radius inside which the P.A. changes): their inclusion did not change much the final results. Finally, with a dot-dashed line we present the case of $k = 1$, $M/L_B = 5.94$ (no dark matter halo, disc included), that predicts an even larger velocity, but a good fit to the velocity dispersion. The h_3 parameter predictions provide a rather good agreement with the observations (apart from the region between 10 and 20 arcsec related to to the large rotational velocity curve which is not seen in the data and is probably related to the problem of the existence of the third integral). The h_4 parameter is fitted properly in all the cases. A good fit for the velocity could not be obtained; various mass distributions could not solve the problem of the fit to this quantity.

Minor axis Fig. (2.8) (right)): The case of $k = 0.5$ and $M/L_B = 5.86$ (no dark matter halo, no disc included) did not provide a successful fit to the velocity dispersion for a radius < 10 arcsec (dotted line). The solid line is for the case of $k = 1$ and $M/L_B = 6.42$ (without dark matter, and without a disc) and this represents the best fit in all cases. Since h_3 and h_4 do not show large departures from zero, they are fitted properly.

Our conclusion for NGC 4105 is that this galaxy should be modelled using a three-integral approach because the rotation and velocity dispersion cannot be fitted simultaneously (the modelling results are very similar to these obtained in the case of IC 1459 above, and NGC 720 from BDI). However, judging by two-integral modelling one can see that the dark matter is not needed (out to $\sim 1\ R_e$) and that a successful fit (only for dispersion, for reasons given above) can be obtained for a constant mass to light ratio $M/L_B \sim 6$.

SIMPLE JEANS MODELLING

In all the modelling procedures performed below for different galaxies we have tested three different possibilities for the constant mass-to-light ratio. The list of the galaxies with the basic data is given in TABLE 2-1. As said in Chap. 2.1.1.1 we modelled only the major axis data: the observed data were folded about the y-axis. Note that the velocity dispersion points were corrected according to Eq. (2.17) given above taking into account the values of the h_4 parameter. With the dotted line we plotted the case for which $\Upsilon_B = 5$, the thin solid line is plotted for $\Upsilon_B = 7$ and with the thick solid line we plotted the case for which $\Upsilon = 10$.

Sample 2

NGC 1336

In Fig. (2.9) we see that all three values of the constant mass-to-light ratio are in agreement with the observed data beyond ~ 6 arcsec. Since the observed data extend to less than one effective radius one can see that interior to this region there is no need for dark matter because $5 \lesssim \Upsilon_B \lesssim 10$.

TABLE 2-1

GALAXIES MODELLED USING SIMPLE JEANS MODELLING

Name	$v_{\rm rot}$ [km/s]	M_B	$M'_{\rm tot}$ $[M_\odot]$	R_e [″]	1″ [pc]
NGC 1336	-	-18.28	3.2×10^9	30	100
NGC 1339	110	-18.63	4.4×10^9	15	94
NGC 1373	-	-17.04	1.0×10^9	11	95
NGC 1374	50	-19.10	6.8×10^9	26	92
NGC 1379	-	-19.21	7.5×10^9	24	95
NGC 1399	-	-20.81	3.3×10^{10}	42	100
NGC 1404	100	-21.08	4.2×10^{10}	26	135
NGC 1419	-	-17.89	2.2×10^9	9	114
NGC 3379	-	-20.60	2.7×10^{10}	55	63
NGC 4105	-	-20.70	3.0×10^{10}	35	134
NGC 2434	-	-19.83	1.3×10^{10}	24	96
NGC 3706	120	-21.12	4.4×10^{10}	27	223
NGC 5018	50	-21.75	7.8×10^{10}	22	194

NOTES - Col. (1): name of the galaxy. Col. (2): rotational speed in $\mathrm{km\,s^{-1}}$ (see text for details). Whenever the rotational velocity is not constant and is low the zero value for $v_{\rm rot}$ was taken in the calculations. Col. (3): absolute magnitude in the B-band taken from the LEDA database. Col. (4): total mass divided by the constant mass-to-light ratio in the B-band (Υ_B) expressed in solar masses (see text for details). Col. (5): effective radius expressed in arcsecs. Col. (6): value of one arcsec of a given galaxy expressed in parsecs.

NGC 1339

Fig. (2.10) shows that in this galaxy there is a hint of the increase of the mass-to-light ratio from $\Upsilon_B = 5$ (beyond ~ 4 arcsec) to $\Upsilon_B = 10$ (beyond ~ 10 arcsec). This may mean that there is dark matter beyond $\sim 1R_e$ due to increase of the velocity dispersion. This galaxy is a good candidate for further investigation of dark matter and therefore the integrated stellar spectra out to a larger distance from the center would be useful. At this point drawing further conclusions is unfortunately not possible.

NGC 1373

In Fig. (2.11) we can see that between ~ 4 and ~ 10 arcsec the mass-to-light ratio, Υ_B varies between 5 and 7 and that beyond one effective radius there is an increase of the velocity dispersion implying the rise of the total mass-to-light ratio to 10. Since the last observed point is at ~ 230 $\mathrm{km\,s^{-1}}$ one may suspect that dark matter starts to provide its contribution beyond $\sim 1R_e$. This is another good candidate for a more detailed study by taking more extended spectra.

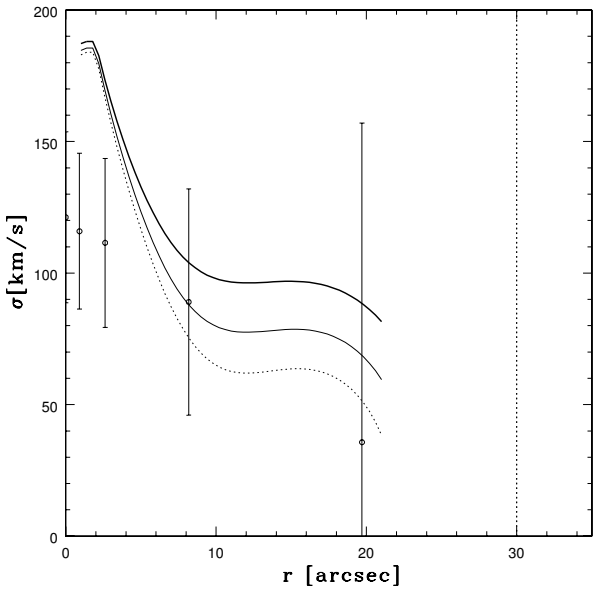

Figure 2.9: Predictions of the simple Jeans modelling for NGC 1336 for the major axis. The dotted line is the case for which Υ_B =5, the thin solid line is the case for which Υ_B =7 and the thick solid line is given for the case for which Υ_B =10. The observed data are corrected using Eq. (2.17). Vertical dotted line indicates one effective radius.

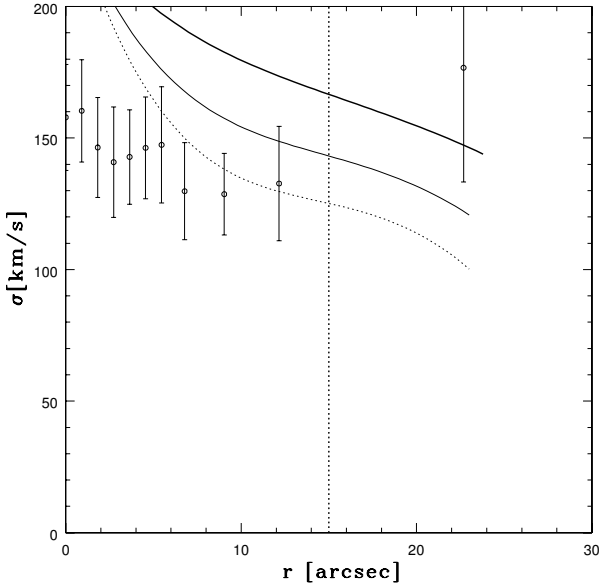

Figure 2.10: Predictions of the simple Jeans modelling for NGC 1339 for the major axis. The meaning of symbols is the same as in Fig. (2.9).

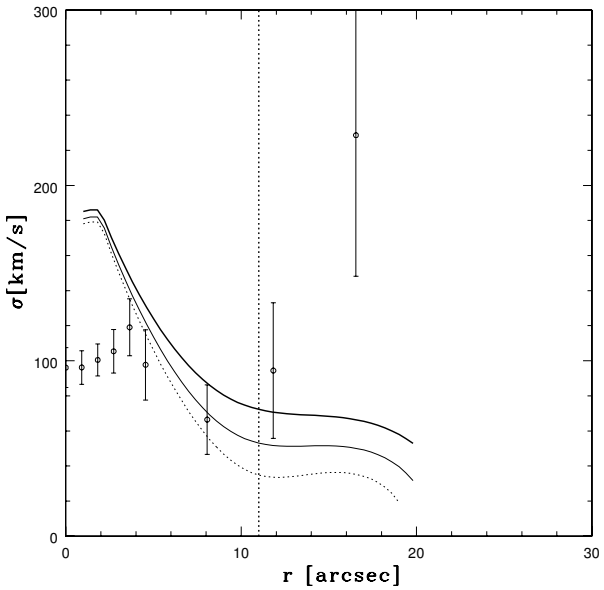

Figure 2.11: Predictions of the simple Jeans modelling for NGC 1373 for the major axis. The meaning of symbols is the same as in Fig. (2.9)

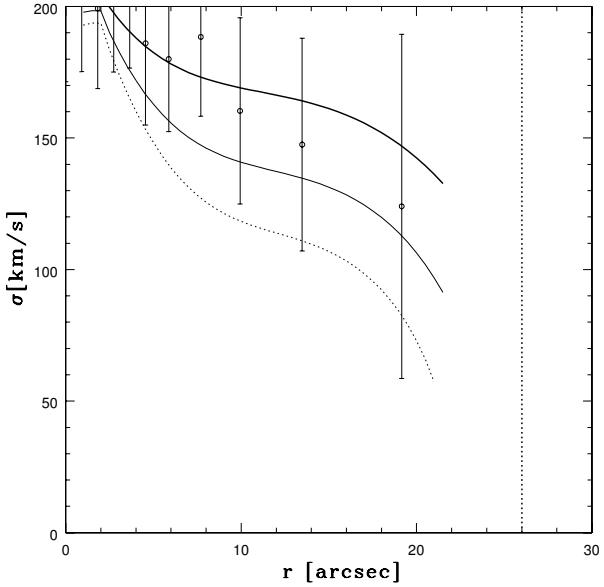

Figure 2.12: Predictions of the simple Jeans modelling for NGC 1374 for the major axis. The meaning of symbols is the same as in Fig. (2.9)

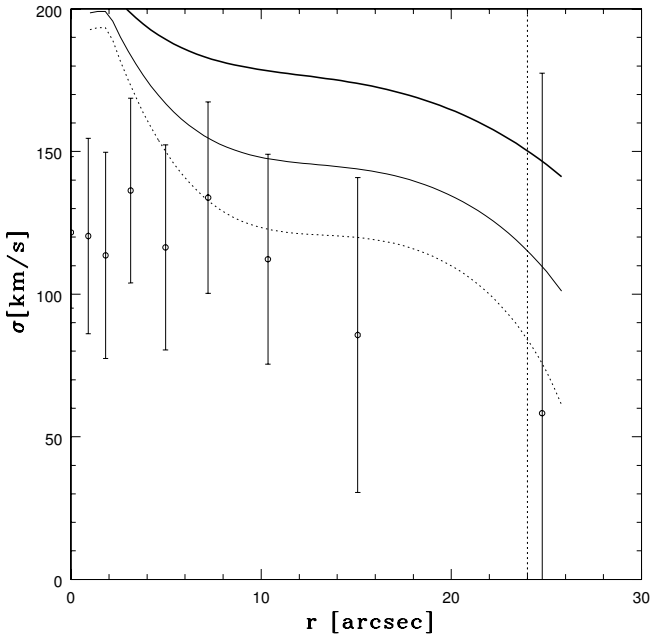

Figure 2.13: Predictions of the simple Jeans modelling for NGC 1379 for the major axis. The meaning of symbols is the same as in Fig. (2.9)

NGC 1374

Fig. (2.12) provides an indication that the mass-to-light ratio in this galaxy interior to $\sim 1R_e$ is between 7 and 10. There is a declining trend of the observed velocity dispersion which indicates small contribution of dark matter in the observed region.

NGC 1379

In Fig. (2.13) we see that the lower value of the constant mass-to-light ratio is present in this galaxy: the value $\Upsilon_B = 5$ provides a good fit to the corrected observed velocity dispersion out to $\sim 1R_e$ beyond ~ 6 arcsec. There is a declining trend in the velocity dispersion which means that dark matter does not provide a significant contribution in the observed region.

NGC 1399

In Fig. (2.14) we see the observed velocity dispersion and the simple Jeans modelling of the central galaxy of the Fornax cluster of galaxies. The observed integrated stellar spectra extend out to $\sim 2R_e$ from the center. This galaxy will be a subject of a more detailed analysis in Chapter 3 when we address its X-ray properties (and what they

can tell us about the total mass of this galaxy) and in Chapter 5 when we study in detail the globular clusters which belong to NGC 1399 and the estimates of its total mass (and the mass-to-light ratio) at much larger distances from the center (out to $\sim 10R_e$). Given the large error bars we can see in Fig. (2.14) that we cannot establish the exact value of the mass-to-light ratio from this kind of modelling. The value $\Upsilon_B = 7$ provides the best fit of the three different values which we tested. It is important to stress that from Fig. (2.14) is also visible that $\Upsilon_B < 10$ in the observed region which means that dark matter does not play an important role within $\sim 2R_e$. This result is in agreement with those obtained in Chapters 3 and 5.

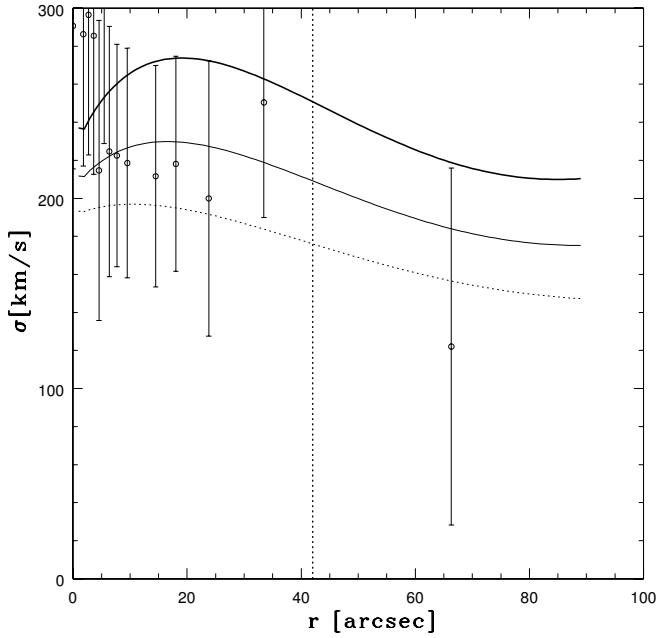

Figure 2.14: Predictions of the simple Jeans modelling for NGC 1399 for the major axis. The meaning of symbols is the same as in Fig. (2.9)

NGC 1404

In Fig. (2.15) we present the results of the simple Jeans modelling for the galaxy NGC 1404 which suggest that this galaxy is best described with the following mass-to-light ratio: $5 < \Upsilon_B < 7$ which means that interior to $\sim 3R_e$ (the last observed point) dark matter does not dominate. This result is in agreement with the result based on the X-rays given in Chapter 3.

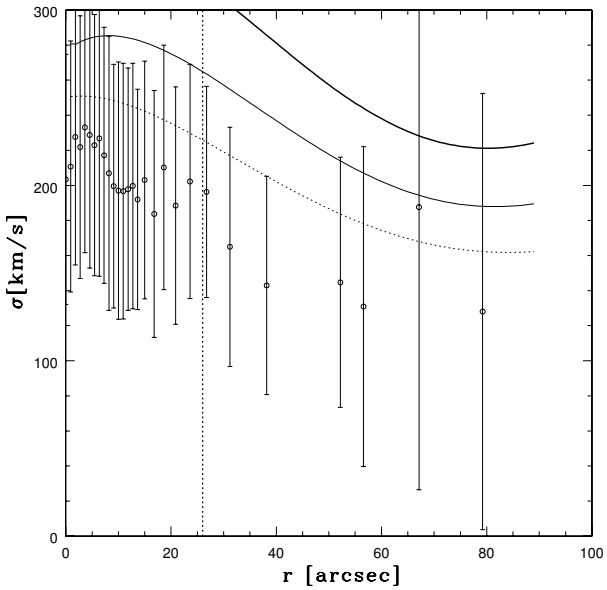

Figure 2.15: Predictions of the simple Jeans modelling for NGC 1404 for the major axis. The meaning of symbols is the same as in Fig. (2.9)

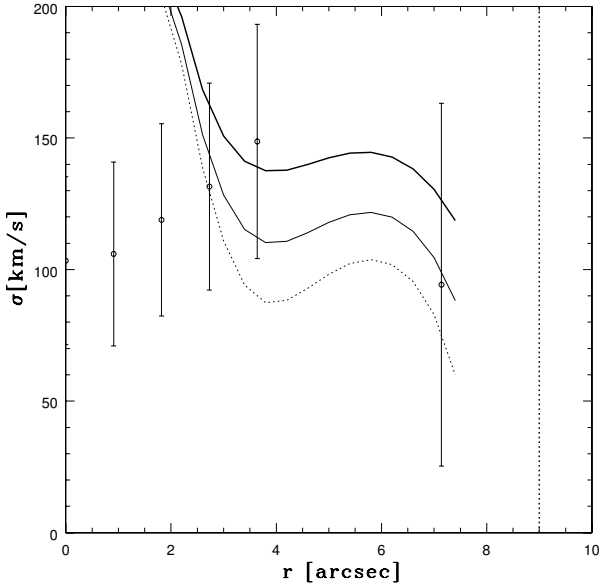

Figure 2.16: Predictions of the simple Jeans modelling for NGC 1419 for the major axis. The meaning of symbols is the same as in Fig. (2.9).

NGC 1419

In Fig. (2.16) we show the observations and simple Jeans modelling for the galaxy NGC 1419 which extend interior to $\sim 1R_e$. It can be seen that: $7 < \Upsilon_B < 10$, which means that dark matter does not provide a significant contribution in the observed region.

Sample 3

Both galaxies from this sample were already a subject of the detailed Jeans modelling earlier in this Chapter. In this Section we present the simple Jeans modelling for the sake of comparison. Note that both of the galaxies belonging to Sample 3 will be addressed in Chapter 3 when we will analyze their X-ray properties.

NGC 3379

In Fig. (2.18) we present the results for the integrated stellar spectra which extend out to $\sim 1.5R_e$ for the galaxy NGC 3379. It can be seen that low mass-to-light ratio, $\Upsilon = 5$ provides the best fit to the observed data. This is a well known result in agreement with all the results from the literature and the results found in this book (Fig. (2.7) in this Chapter and also from the X-ray modelling performed in Chapter 3).

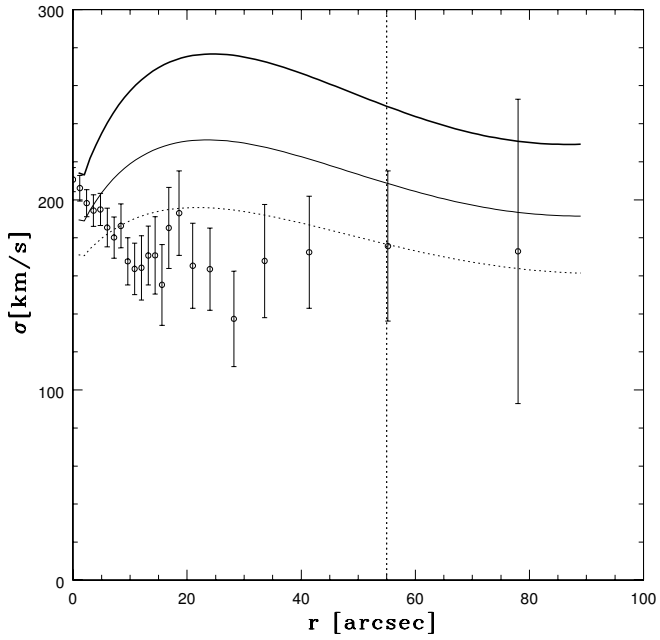

Figure 2.17: Predictions of the simple Jeans modelling for NGC 3379 for the major axis. The meaning of symbols is the same as in Fig. (2.9).

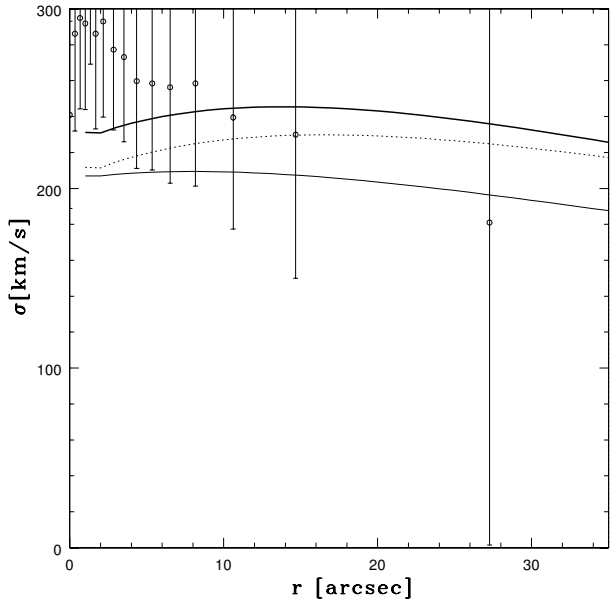

Figure 2.18: Predictions of the simple Jeans modelling for NGC 4105 for the major axis. The meaning of symbols is the same as in Fig. (2.9).

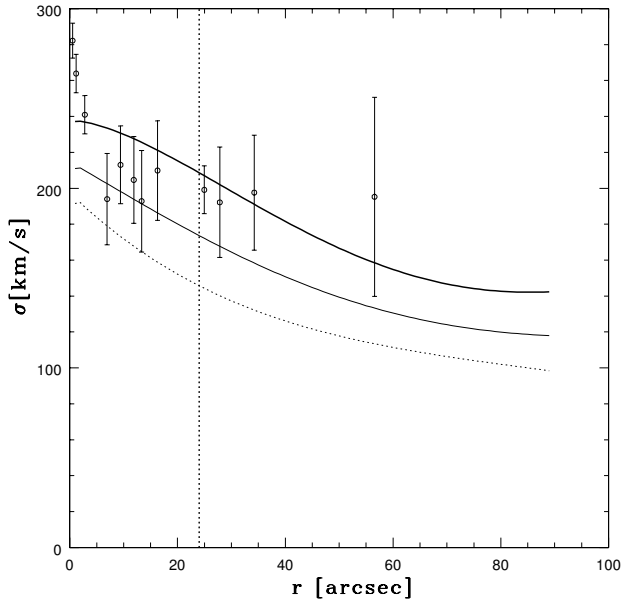

Figure 2.19: Predictions of the simple Jeans modelling for NGC 2434 for the major axis. The meaning of symbols is the same as in Fig. (2.9).

NGC 4105

In Fig. (2.19) we present the results of the simple Jeans modelling of the galaxy NGC 4105 which imply that interior to $\sim 1R_e$ the mass-to-light ratio is between 5 and 10. Therefore, one can conclude that dark matter does not appear to contribute significantly in the observed region. This result is in agreement with the results obtained earlier in this Chapter (see Fig. (2.8)). This galaxy will also be the subject of the X-ray modelling in Chapter 3.

Sample 4

The and kinematic data for three galaxies, NGC 2434, NGC 3706 and NGC 5018, were taken from the literature (Carollo et al. 1995) and the absolute magnitudes are taken from the LEDA database.

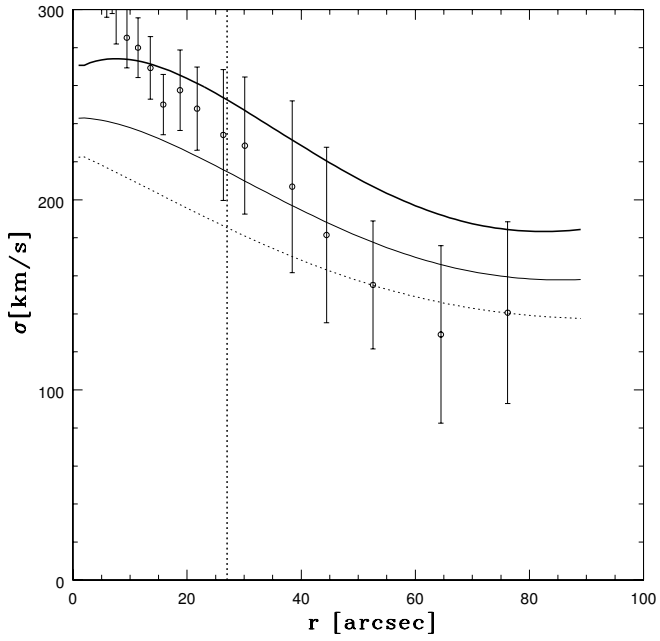

Figure 2.20: Predictions of the simple Jeans modelling for NGC 3706 for the major axis. The meaning of symbols is the same as in Fig. (2.9).

NGC 2434

In Fig. (2.20) we present our simple Jeans modelling results for the galaxy NGC 2434. One can see that interior to $\sim 1R_e$ the mass-to-light ratio, $\Upsilon_B = 7$ provides a satisfactory fit and that beyond $\sim 1R_e$ the total mass-to-light ratio appears to increase.

Between $\sim 1R_e$ and $\sim 2.5R_e$ the value of the mass-to-light ratio increases to $\Upsilon_B = 10$. Using 2I axisymmetric modelling Carollo et al. (1995) concluded that there must be dark matter in this galaxy. Rix et al. (1997) used spherical Schwarzschild modelling to conclude that there is dark matter in the outer regions of this galaxy. From our simple, spherical Jeans modelling, we can say that there is indeed an indication of the rise of the total mass-to-light ratio, but since $\Upsilon_B = 10$ provides a satisfactory fit to the observed velocity dispersion it appears that the contribution of dark matter is not significant and dark matter does not dominate luminous matter interior to $\sim 2.5R_e$ in NGC 2434.

NGC 3706

In Fig. (2.21) we present the observed declining trend in the velocity dispersion of the galaxy NGC 3706. It is hard to draw conclusions on the exact value of the mass-to-light ratio in this galaxy but it is obvious that $7 < \Upsilon_B < 10$ provides a good fit throughout the galaxy which means that dark matter does not dominate luminous matter interior to $\sim 3R_e$.

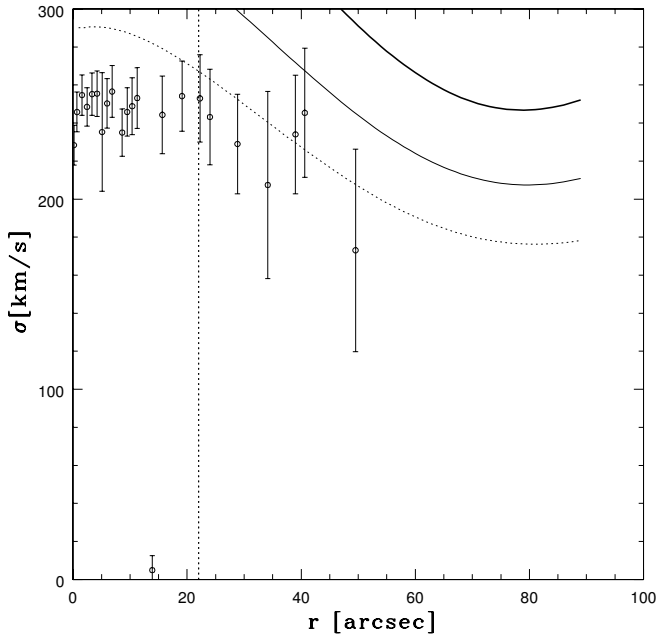

Figure 2.21: Predictions of the simple Jeans modelling for NGC 5018 for the major axis. The meaning of symbols is the same as in Fig. (2.9).

NGC 5018

In Fig. (2.22) we present the results of the simple Jeans modelling of the galaxy NGC 5018. Only one value of the tested mass-to-light ratio ($\Upsilon_B = 5$) can provide a fit to the observed velocity dispersion. In the inner regions (interior to $\sim 1R_e$) an even smaller value of the mass-to-light ratio would provide a fit to the observed data. One can therefore safely conclude, based on this simple Jeans modelling, that dark matter does not play an important role interior to the last observed point of NGC 5018 ($\sim 2R_e$).

2.2. THREE-INTEGRAL MODELLING

2.2.1. THEORETICAL INTRODUCTION

For axisymmetric potentials one can have orbits that have three integrals of motion: E, L_z and I_3. There is no general expression for the third integral, I_3. The assumption that the distribution has the form $f = f(E, L_z, I_3)$ broadens the range of possible axisymmetric motions (see Appendix 3 for details on orbits). Three-integral models are used for modelling of triaxial systems. Schwarzschild (1979) invented a very powerful method that can be used for the construction of axisymmetric and triaxial models of galaxies in equilibrium without explicit knowledge of the integrals of motion. The basic steps of this approach are the following: one specifies the mass model $\rho(r)$, finds its potential and then constructs a grid of cells in position space. Then initial conditions are chosen for a set of orbits and for every orbit one integrates the equations of motion for many orbital periods and measures how much time the orbit spends in each cell (that measures how much mass the orbit contributes to that cell). Finally, one needs to determine the non-negative weights for each orbit such that the summed mass in each cell is equal to the mass given by the original $\rho(r)$. For the last step one can use different methods; for example, Schwarzschild (1979) used linear programming. A non-negative least squares (NNLS) method (Lawson and Hanson 1974) was used in this work (see Appendix 2 for details on NNLS).

Schwarzschild's original idea has recently been further developed: namely, models are now made that match the bulk kinematics and LOSVD of observed galaxies. Rix et al. (1997) used such an approach to search for dark matter in elliptical galaxies. Cretton and van der Bosch (1999) used it to confirm the presence of nuclear black holes. Recently, Gebhardt et al. (2003) used the orbit superposition method for detection of central black holes in 12 galaxies. These works deal with axisymmetric modelling only. We have used the Rix et al. (1997) algorithm to build a new Schwarzschild modelling code that uses the so-called self-organizing maps (SOMs) (Kohonen 1997, Murtagh 1995) to extract velocity profiles from the large orbit library. The flowchart is presented in Fig. (2.22).

We made the orbit libraries using standard definitions for the orbits. Orbital starting conditions were given in the $(\mathbf{r}, \mathbf{v})$ phase space selected in such a way that the starting points were all equidistant points in both position and velocity with a given step (10 per cent of the outermost radial distance measured from the centre for the position and 10 per cent of the maximum velocity for the velocity) in a given re-

gion (from the center out to the last spectroscopically measured point). We did not attempt to analyze in detail the orbital structure of our models because it is beyond the scope of this book. However, we are aware that among orbits which we generated there were chaotic orbits: these orbits were dealt with as regular orbits, i.e., they were included together with the regular ones in our orbit library.

The details of the modelling procedure are given in Rix et al. (1997). We explain here several important steps. Note that in the paper of Rix et al. (1997) there are numerous unfortunate (uncorrected) typographical errors that are absent from the preprint version of this paper (available through LANL as `astro-ph/9702126`). Namely, in equations (4), (5), (7), (8), (9), (11) and (12) the sign ">" should be omi-

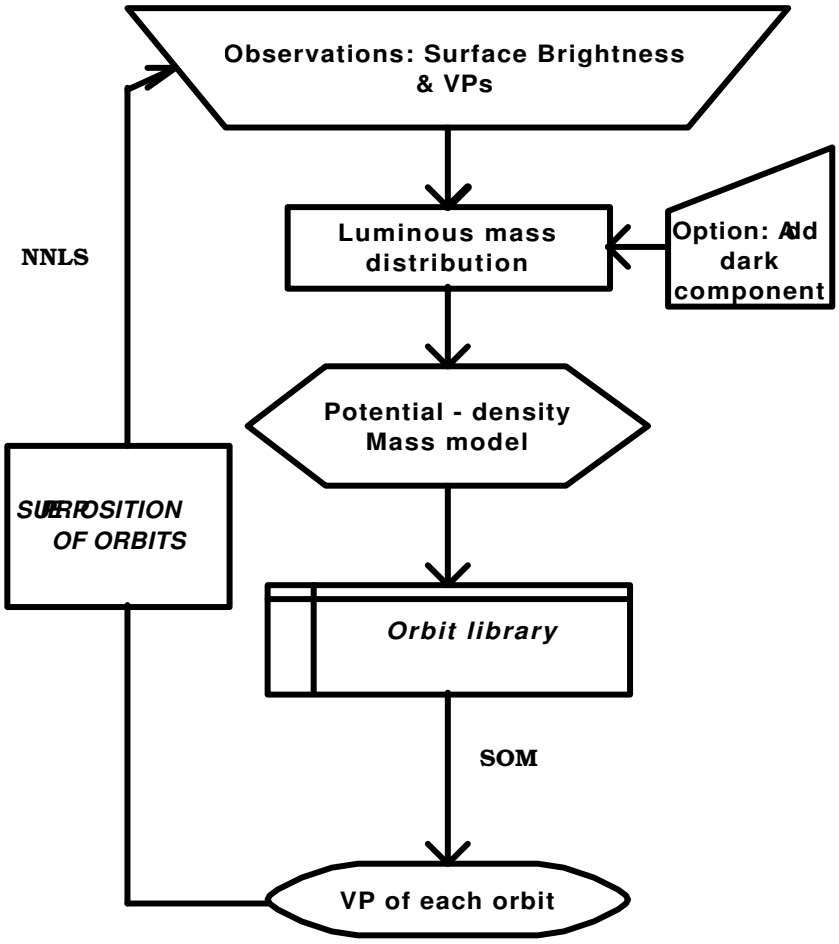

Figure 2.22: Flowchart of three-integral modelling procedure. (SOM stands for self-organizing maps; see Appendix 4 for details on SOMs, NNLS stands for non-negative least squares; see Appendix 2 for details on NNLS).

tted. In equation (13) the comma sign (",") in the second term on the right hand side should be omitted and, finally, in equation (14) N_e in a matrix on the left hand side should read N_c, $\gamma N0$ in the vector on the left hand side should read γ_{N0} and N_e in the vector on the right hand side should read N_c.

The details of the modelling procedure are given in Rix et al. (1997) and here we explain only several important steps and present corrected formulas. We generated orbits in different potentials using a leapfrog integrator. As in Rix et al. (1997) the energy fractional conservation was at least 10^{-5} over the whole integration. We tested two groups of potentials (using different input parameters, such as flattening of the potential, total mass, core radius): spherical constant mass-to-light ratio models based on the Hernquist (1990) potential which is given in Eq. (2.12). We also used the logarithmic potentials (both axisymmetric and triaxial) (e.g., Binney and Tremaine 1987, Chapters 2.2.2 and 2.3.2). The axisymmetric logarithmic potential is given as:

$$\Phi(x,y,z) = \frac{1}{2}v_0^2 \ln\left(R_c^2 + R^2 + \frac{z^2}{q^2}\right),$$

and the triaxial logarithmic potential is given as:

$$\Phi(x,y,z) = \frac{1}{2}v_0^2 \ln\left(R_c^2 + x^2 + \frac{y^2}{p^2} + \frac{z^2}{q^2}\right),$$

where in both cases velocity, v_0 and core radius, R_c, are constants and p and q represent flattenings of the potential: in the triaxial case, for example, $p = b/a$ and $q = c/a$ are axis ratios of the potential, where a is the long axis, b is intermediate and c is the short axis.

As already mentioned, details of orbit calculations are given in Appendix 3. Here we note that it is important to have the projected properties of orbits in order to compare them with the observations. As given in Cretton, Rix, and de Zeeuw (1999) only three coordinates in the phase space are available for comparison with the observations: the projected positions x', y' (that are chosen to be aligned with the photometric major and minor axis), and the line-of-sight velocity, $v_{\rm los}$ ($\equiv v_{z'}$). If the inclination angle is i (for edge-on galaxy $i = 90°$, see Introduction), these coordinates are related to the cylindrical coordinates (R, z, ϕ) as:

$$x' = R\sin\phi, \tag{2.18}$$

$$y' = -R\cos i\cos\phi + z\sin i, \tag{2.19}$$

and

$$v_{\rm los} = (v_R\cos\phi - v_\phi\sin\phi)\sin i + v_z\cos i. \tag{2.20}$$

One can assign to each orbit in the library an index k, with $k = 1, \ldots, N_0$, where N_0 is the total number of orbits (in this book $N_0 = 729$). The *occupation weight* of the orbit k in the storage cube cell that is centered on (x, y, v) is denoted as w^k_{xyv}. The occupation weights for each orbit are normalized to unit mass:

$$\sum_{xyv} w^k_{xyv} = 1, \quad \forall k. \tag{2.21}$$

After the calculation of the k-th orbit, one can proceed with the modelling with the direct comparison with the observational constraints. These constraints are taken at different constraint positions on the projected face of the galaxy. One can again use the photometric and kinematic data as in the case of the 2I modelling. The constraint positions are labeled by l, with $l = 1, \ldots, N_c$. As in Rix et al. (1997) one can denote by $f_{xy,l}$ the fraction of the area of the storage cube cell centered on the grid point (x, y) that is contained within the constraint area l.

Let M_l^k be the fraction of the total mass in orbit k that contributes to constraint area l. This mass fraction is obtained by summing over the storage cube for the given orbit:

$$M_l^k = \sum_{xyv} f_{xy,l}\, w_{xyv}^k. \tag{2.22}$$

To calculate a dynamical model one needs to estimate its *orbital weights* γ_k, which measure the fraction of the total mass of the system that resides in each orbit k. The total mass fraction M_l of the model that contributes to constraint area l is then obtained as a sum over all orbits:

$$M_l = \sum_k \gamma_k\, M_l^k. \tag{2.23}$$

Under the assumption that the stellar population has the same mass-to-light ratio everywhere in the galaxy one can obtain the observed mass fractions $M_l^{\rm obs}$ at the constraint positions l from the observed surface brightnesses $\mu_l^{\rm obs}$ as:

$$M_l^{\rm obs} = \mu_l^{\rm obs}\, A_l / L_{\rm tot}, \tag{2.24}$$

A_l is the area of constraint position l, and $L_{\rm tot}$ is the total observed luminosity. When one wants to fit the predicted mass fractions M_l to the observed mass fractions $M_l^{\rm obs}$ one encounters a linear superposition problem for the γ_k.

For this kind of modelling one must be sure that the contributions of individual orbits to all kinematic constraints add up linearly. This can be achieved if one chooses the Gauss-Hermite coefficients h_m $(m = 1, \ldots, M)$ to describe the shape of the VP. The normalized VP contributed by orbit k to constraint position l is

$$\mathrm{VP}_{l,v}^k = \frac{1}{M_l^k} \sum_{xy} f_{xy,l}\, w_{xyv}^k. \tag{2.25}$$

When one performs the sum over all orbits one obtains the total normalized VP at the constraint position l:

$$\mathrm{VP}_{l,v} = \frac{1}{M_l} \sum_k \gamma_k\, M_l^k\, \mathrm{VP}_{l,v}^k. \tag{2.26}$$

The Gauss-Hermite moment $h_{m,l}$ of order m at constraint position l is defined as an integral over $\mathrm{VP}_l(v)$:

$$h_{m,l} = 2\sqrt{\pi} \int_{-\infty}^{\infty} \mathrm{VP}_l(v)\, \alpha(w_l)\, H_m(w_l)\, \mathrm{d}v. \tag{2.27}$$

The function α is a Gaussian weighting function:

$$\alpha(w_l) \equiv \frac{1}{\sqrt{2\pi}} \exp\left[-\frac{1}{2} w_l^2\right]. \tag{2.28}$$

Here, w_l is defined as $w_l \equiv (v - V_l)/\sigma_l$, where the velocity V_l and dispersion σ_l are free parameters. The $H_m(w_l)$ are Hermite polynomials that were defined previously. In a similar manner one can define the Gauss-Hermite moment $h^k_{m,l}$ of orbit k and order m for constraint position l, as an integral over $\mathrm{VP}^k_l(v)$ (of which $\mathrm{VP}^k_{l,v}$ is the discrete representation). When one chooses the free parameters V_l and σ_l to be the same for each orbit k, it follows that

$$M_l\, h_{m,l} = \sum_k \gamma_k\, M^k_l\, h^k_{m,l}. \tag{2.29}$$

Therefore, fitting the observed Gauss-Hermite moments $h^{\mathrm{obs}}_{m,l}$ through the combination $M^{\mathrm{obs}}_l\, h^{\mathrm{obs}}_{m,l}$ is also a linear superposition problem for the γ_k.

In practice one chooses V_l and σ_l equal to the parameters of the best-fitting Gaussian to the observed VP at constraint position l, which are the observationally determined quantities. This implies $h^{\mathrm{obs}}_{1,l} = h^{\mathrm{obs}}_{2,l} = 0$ for the first- and second-order observed Gauss-Hermite moments. When one requires that the predicted moments $h_{1,l}$ and $h_{2,l}$ should reproduce this, the model VP automatically has the correct mean velocity and velocity dispersion (as determined through a Gaussian fit). So these latter quantities need not be fitted separately. As for the errors $\Delta h^{\mathrm{obs}}_{1,l}$ and $\Delta h^{\mathrm{obs}}_{2,l}$ that correspond to the observationally quoted errors ΔV in V_l and $\Delta\sigma$ in σ_l, one can obtain them using the following equations:

$$\Delta h_1 = -\frac{1}{2}\sqrt{2}\, \Delta V/\sigma, \qquad \Delta h_2 = -\frac{1}{2}\sqrt{2}\, \Delta\sigma/\sigma. \tag{2.30}$$

The question of the zeroth-order moment h_0 is resolved by not including this quantity in the fit, because it is not accessible observationally. It determines the unknown difference in the line strength between the galaxy spectrum and the template spectrum. In practice one can safely use the assumption $h_0 = 1$.

After the calculation of the properties of all the orbits is finished for all constraint positions one proceeds with the evaluation of the non-negative superposition of orbital weights γ_k that best matches the observational constraints within the error bars. When the observational errors are normally distributed, the quality of the fit to the data is determined by the χ^2 statistic:

$$\chi^2 \equiv \sum_{l=1}^{N_{\mathrm{p}}} \left(\frac{M^{\mathrm{obs}}_l - \sum \gamma_k M^k_l}{\Delta M^{\mathrm{obs}}_l} \right)^2 + \sum_{l=N_{\mathrm{p}}+1}^{N_{\mathrm{c}}} \sum_{m=1}^{M} \left(\frac{M^{\mathrm{obs}}_l h^{\mathrm{obs}}_{m,l} - \sum \gamma_k M^k_l h^k_{m,l}}{\Delta (M^{\mathrm{obs}}_l h^{\mathrm{obs}}_{m,l})} \right)^2. \tag{2.31}$$

Here, N_p are photometric constraints and $N_{\mathrm{k}} = N_c - N_p$ are kinematic constraints (N_c is the number of constraint positions). We have chosen the number M of Gauss-Hermite moments that can be extracted from spectroscopic observations to be $M = 4$,

since the kinematic parameters extracted from spectra are v, σ, h_3 and h_4. Therefore when higher order moments can be routinely extracted from spectra it will be straightforward to include them in the fitting procedure also.

When one divides all quantities by their observational uncertainties, e.g., $M_1^{\rm obs} \to M_1^{\rm obs}/\Delta M_1^{\rm obs}$, $M_1^1 h_{1,1}^1 \to M_1^1 h_{1,1}^1/\Delta(M_1^{\rm obs} h_{1,1}^{\rm obs})$, etc., the χ^2 minimization is converted into a least squares problem:

$$\begin{bmatrix} M_1^1 & \dots & \dots & M_1^{N_0} \\ M_2^1 & \dots & \dots & M_2^{N_0} \\ \vdots & \vdots & \vdots & \vdots \\ M_{N_p}^1 & \dots & \dots & M_{N_p}^{N_0} \\ M_{Np+1}^1 h_{1,N_p+1}^1 & \dots & \dots & M_{Np+1}^{N_0} h_{1,N_p+1}^{N_0} \\ \vdots & \vdots & \vdots & \vdots \\ M_{N_c}^1 h_{1,N_c}^1 & \dots & \dots & M_{N_c}^{N_0} h_{1,N_c}^{N_0} \\ \vdots & \vdots & \vdots & \vdots \\ \vdots & \vdots & \vdots & \vdots \\ M_{Np+1}^1 h_{M,N_p+1}^1 & \dots & \dots & M_{Np+1}^{N_0} h_{M,N_p+1}^{N_0} \\ \vdots & \vdots & \vdots & \vdots \\ M_{N_c}^1 h_{M,N_c}^1 & \dots & \dots & M_{N_c}^{N_0} h_{M,N_c}^{N_0} \end{bmatrix} \begin{bmatrix} \gamma_1 \\ \vdots \\ \vdots \\ \gamma_{N_o} \end{bmatrix} = \begin{bmatrix} M_1^{\rm obs} \\ M_2^{\rm obs} \\ \vdots \\ M_{N_p}^{\rm obs} \\ M_{Np+1}^{\rm obs} h_{1,N_p+1}^{\rm obs} \\ \vdots \\ M_{N_c}^{\rm obs} h_{1,N_c}^{\rm obs} \\ \vdots \\ \vdots \\ M_{Np+1}^{\rm obs} h_{M,N_p+1}^{\rm obs} \\ \vdots \\ M_{N_c}^{\rm obs} h_{M,N_c}^{\rm obs} \end{bmatrix} \tag{2.32}$$

Here, M denotes mass fractions, "obs" is related to the observed quantities. The total number of orbits is N_0 (we used 729, and Rix et al. used 420 orbits). This least squares problem has to be solved for the occupation vector $(\gamma_1, ..., \gamma_{N_0})$, with the constraints $\gamma_k \geq 0$, for $k = 1, \dots, N_0$ for $m = 1, 2, 3, 4$. We have used, as did Rix et al. (1997), a non-negative least-squares (NNLS) procedure described in Appendix 2. The dimension of the vector on the right hand side of the equation is 500. One hundred points belong to the photometric data and 400 points belong to kinematical data: 200 are zeros related to velocity and velocity dispersion, 100 points are related to h_3 parameter and 100 points are related to h_4 parameter. Since the extraction of the kinematical parameters provides smaller number of non-equidistant points, we made a fit to the observational data using Chebishev polynomials to get a hundred equidistant points that are then included in the vector on the right hand side (similar procedure is also applied on the photometric data). Obviously, the same grid used in this fitting is also used when obtaining data on the left hand side of the equation. Therefore, in the case of 729 orbits and 500 constraints, the dimension of the matrix on the left hand side is 729×500, the dimension of the vector on the left hand side is 729, and the dimension of the vector on the right hand side is 500. Since this is an ill-posed problem, the regularization procedure has to be applied (in Appendix 1 we present the details of the procedure).

For the purpose of the 3I modelling of both galaxies we generated orbit libraries of 729 orbits in the following way: for the constant mass-to-light potentials and

axisymmetric logarithmic potentials we used tube orbits and in the case of the triaxial logarithmic potential we used a mixture of tube and box orbits with both familes giving the equal contribution. In the case of the logarithmic potentials, tests were done using $p = 0.8$, $q = 0.7$ in the case of the triaxial potential and $q = 0.8$ in the case of the axisymmetric potential, where p is the flattening of the potential on the y axis and q represents the flattening of the potential on the z axis. We checked the existence of the third integral visually following the prescription of Binney and Tremaine (Chap. 3.2.2) in the (R, V_R) plane. Our procedure differs from that of Rix et al. in that we used also axisymmetric and triaxial potentials (as described above) in addition to spherical models, we used the SOMs for a quick extraction of velocity profiles from the orbit libraries and we also model velocity and the h_3 parameter. We are aware that other dynamical modelling procedures are possible which include different dark matter profiles, but since in our two cases we did not find much evidence for dark matter (based on the declining velocity dispersion profile and the 2I dynamical modelling) we restricted our 3I modelling to the simple logarithmic potentials; we, however, do not exclude application of more complex dark matter models in future work.

The code that we have created was used for testing several astrophysically important potentials (details in Appendix 3) for the different samples of galaxies that we had. Results and discussion are given below.

2.2.2. MODELLING RESULTS

Using the three-integral modelling procedure we analyzed the galaxies which belong to Sample 1. We again assume symmetry about the y-axis and therefore we folded all the observational data taking into account that velocity and h_3 are odd functions of the radius, and that velocity dispersion and h_4 are even functions of the radius.

Sample 1

IC 3370

Fig. (2.23) shows several examples of the modelling of IC 3370 for the major axis (left) and the minor axis (right). The inclination angle of 50° was used in all the cases. Again, as in the case of IC 1459, in the discussion that follows we address only the major axis case, because for the minor axis all the models tested tend to give very similar results. We note that our 3I modelling package is suitable for the fast extraction of kinematical parameters for major and minor axis, and therefore we did not model the intermediate axis.

Again two examples of modelling using a constant mass-to-light ratio are given: a case with $M/L_B = 7$ is now plotted using a thick solid line, and a case with a larger $M/L_B = 10$ is plotted using a thin solid line. We can exclude the $M/L_B = 10$ case because it does not provide a good fit to the h_3 parameter and it provides a worse fit to the h_4 parameter with respect to to the $M/L_B = 7$ case. In all the cases the values of the $\chi^2/N_{\rm dof}$ was typically $0.5 \lesssim \chi^2/N_{\rm dof} \lesssim 1$ except for the h_3 parameter for the $M/L_B = 10$ for which we found $\chi^2/N_{\rm dof} \sim 4$. Tests with the logarithmic potentials were made using a constant circular velocity of 125 km s^{-1} and the core radius of 10

arcsec because it was found that these values provided the best fit to the observed rotation curve of IC 3370. We again present two different tests made using logarithmic potentials: now the dotted line represents the axisymmetric logarithmic potential and the dot-dashed line is for the triaxial logarithmic potential. Both logarithmic potentials provide similar (good) fit to observed kinematics. Therefore, using a 3I modelling we can conclude that dark matter is not dominant within $\sim 3R_e$ because a satisfactory fit can be obtained using a constant mass-to-light potential ($M/L_B \sim 7$). However, we note that a logarithmic potential can also provide a good fit to the data.

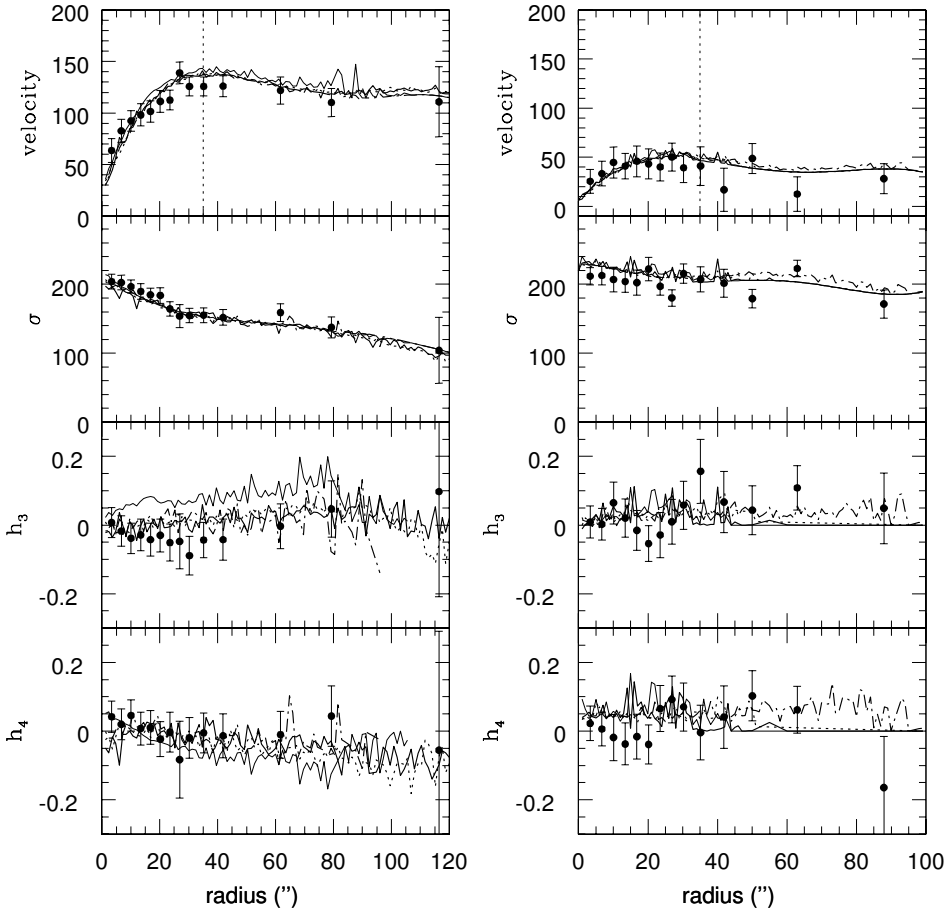

Figure 2.23: Predictions of the three-integral models for IC 3370. Inclination angle used was 50° in all the cases. Thick solid line: constant mass-to-light ratio, $M/L_B = 7$. Thin solid line: constant mass-to-light ratio, $M/L_B = 10$. Dot-dashed line: triaxial logarithmic potential with flattening $q = 0.8$, $q = 0.7$. Dotted line: axisymmetric logarithmic potential with flattening $p = 0.8$. One effective radius is given as a vertical dotted line. *Left*: major axis predictions. *Right*: minor axis predictions.

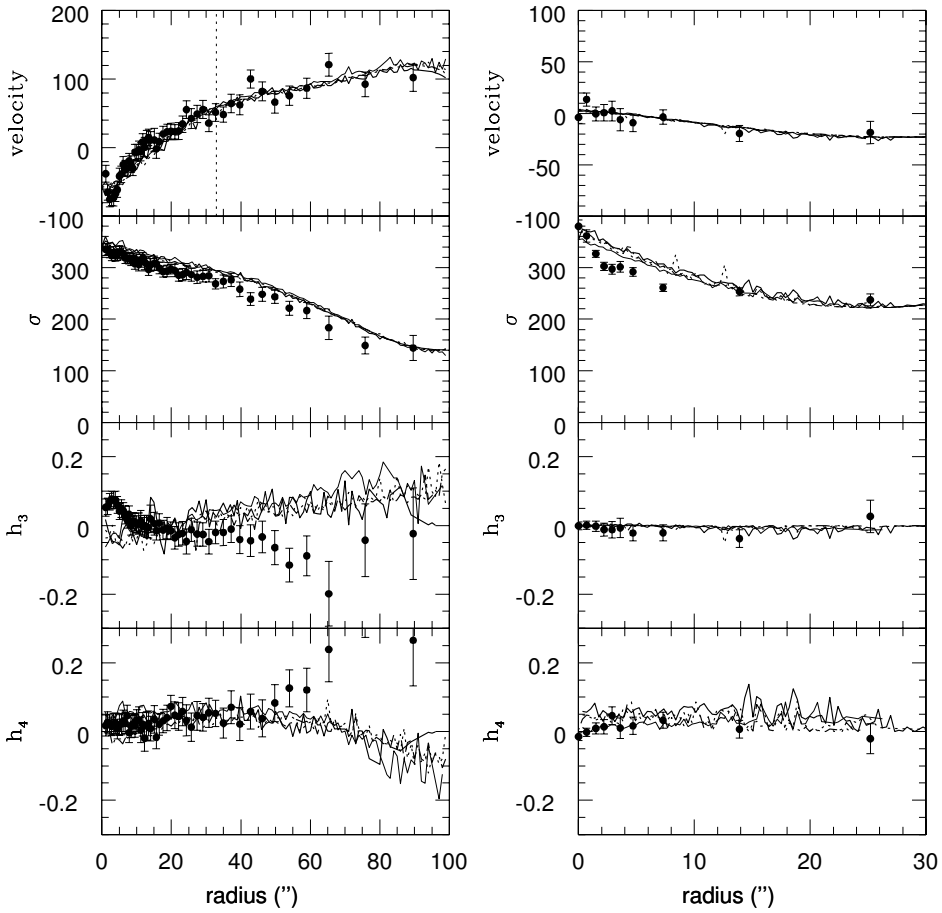

Figure 2.24: Predictions of the three-integral models for IC 1459. Inclination angle used was 65° in all the cases. Dotted line: constant mass-to-light ratio, $M/L_B = 7$. Dot-dashed line: constant mass-to-light ratio, $M/L_B = 10$. Thin solid line: axisymmetric logarithmic potential with flattening $q = 0.8$. Thick solid line: triaxial logarithmic potential with flattening $p = 0.8$, $q = 0.7$. One effective radius is given as a vertical dotted line (only in the case of the major axis). *Left*: major axis predictions. *Right*: minor axis predictions.

IC 1459

In Fig. (2.24) we present several examples of the modelling of IC 1459 for the major axis (left) and the minor axis (right). They were all made with the inclination angle of 65°. In the discussion below we address only the major axis case, because for the minor axis models tend to give very similar results (note again that for the minor axis the data which we had extend only to 30 arcsec).

Two examples of modelling using a constant mass-to-light ratio are given: a case with $M/L_B = 7$ is plotted using a dotted line, a case with a larger $M/L_B = 10$ is plotted using a dot-dashed line. Tests with the logarithmic potentials were done using a constant circular velocity of 110 km s^{-1} and the core radius of 50 arcsec because it was found that these values provided the best-fitting to the observed rotation curve of IC 1459 beyond 20 arcsec. We present two different tests made using logarithmic potentials: the thick solid line represents the triaxial logarithmic potential and the thin solid line is for the axisymmetric logarithmic potential. The h_3 parameter can be fitted throughout the whole galaxy, but the obtained fit for is however not particularly good (typical value of the $\chi^2/N_{\rm dof} \sim 5$). None of these potentials could provide a good fit to the h_4 parameter beyond $\sim 2R_e$. In addition to the tests shown here we performed numerous other tests with different combinations of parameters (adding, for example, more mass): none of the models tested could produce significant positive values of h_4. The $\chi^2/N_{\rm dof}$ interior to ~ 50 arcsec is ~ 1.1, while throughout the whole galaxy its value is typically ~ 2.1. Therefore, in the case of IC 1459 it is difficult to draw a conclusion concerning the existence of dark matter judging from the 3I modelling alone.

2.3. SUMMARY OF THE DYNAMICAL MODELLING

In this Chapter we performed different kinds of the dynamical modelling of elliptical galaxies based on the integrated stellar spectra. First, we used the two-integral (2I) models based on the solving of the Jeans equation. Two different approaches were performed: the axisymmetric one which we called detailed Jeans modelling which takes into full kinematic profile (velocity, velocity dispersion, h_3 and h_4 parameters) and the spherical one which we called simple Jeans modelling which provides predictions of the velocity dispersion only (but takes into account the anisotropies given with the h_4 parameter). Second, we used the three-integral (3I) modelling technique based on the Schwarzschild approach which is based on the calculation of the stellar orbits in axisymmetric and triaxial potentials. Our results – based on the observations which we had at our disposal and which include galaxies in different environments – strongly suggest that dark matter does not dominate interior to $\sim 3R_e$ (IC 3370 and IC 1459: the galaxies for which we had the best observational data which extend out to $\sim 3R_e$) although there are indications that the mass-to-light ratio does have a tendency of increase beyond $\sim 1-2R_e$ in some cases (NGC 1339, NGC 1373 and NGC 2434). The most important conclusion of this Chapter is that beyond $\sim 3R_e$ we might expect that dark matter starts to dominate and it is therefore only natural to ask what is the mass-to-light ratio beyond this galactocentric distance: unfortunately because of the reasons given in Introduction the integrated stellar spectra are not suitable for this purpose. However, in Chapters 3 and 5 we use other mass tracers and give the answer to this question. We anticipate that the influence of dark matter becomes stronger beyond $\sim 3R_e$ and that at larger distances from the center (for example at $\sim 8R_e$ for the galaxy NGC 1399 already discussed in this Chapter) dark matter dominates luminous matter.

Chapter 3
GALAXIES WITH X-RAY HALOES

3.1. BASIC CONCEPTS

It is known that massive haloes of hot plasma exist around some, but not all elliptical galaxies (see, for example, Sansom et al. 2006). In the sample of galaxies that we analyzed using our reduced integrated stellar spectra (Samples 1, 2 and 3)[5] and several galaxies are catalogued as X-ray sources: IC 1459, NGC 1399, NGC 1404, NGC 4105 and NGC 3379. The galaxy NGC 5128 will be analyzed in Chapter 5 using X-rays, planetary nebulae (PNe) and globular clusters (GCs). X-rays are important for the early-type galaxies because they can provide independent constraints on the masses and mass-to-light ratios out to large radii (for a review see Danziger 1997, Mathews and Brighenti 2003a, hereafter MB03). Some of the results presented here are given in Samurović and Danziger (2005).

The EINSTEIN OBSERVATORY detected X-ray haloes around these galaxies, and the mass of the hot gas was estimated to be equal $\sim 10^{10}\ M_{\odot}$. Originally, Fabricant, Lecar and Gorenstein (1980) found that the mass of the dark halo of M87 lies between $1.7 \times 10^{13}\,\mathrm{M}_{\odot}$ and $4.0 \times 10^{13}\,\mathrm{M}_{\odot}$, and that the dark halo extends out to 50 arcsec (or 230 kpc). Therefore, an M/L ratio of 180 can be estimated from these data. The basics for the mass calculations inferred from X-rays were given in this paper, and we here only briefly present basic assumptions and formulas. One assumes that spherical symmetry holds, and that the condition of hydrostatic equilibrium is valid:

$$\frac{dP_{\mathrm{gas}}}{dr} = -\frac{GM(r)\rho_{\mathrm{gas}}}{r^2}, \tag{3.1}$$

where $M(r)$ is the mass interior to the radius r, and the gas obeys the perfect gas law:

$$P_{\mathrm{gas}} = \frac{\rho_{\mathrm{gas}} k T_{\mathrm{gas}}}{\mu m_H}, \tag{3.2}$$

where μ is the mean molecular weight for full ionization (taken to be 0.61), and m_H is the mass of the hydrogen atom. From these two equations one can give the expression

[5]Note that the galaxies NGC 2434 and NGC 5018, from Sample 4, which we took from the literature (Carollo et al. 1995) also possess an X-ray halo, see, for example, Diehl and Statler (2006) and Fukazawa et al. (2006).

for the gravitating mass interior to radius r (e.g. Danziger 1997):

$$M(r) = -\frac{kT_{\rm gas}r}{G\mu m_p}\left(\frac{d\ln\rho}{d\ln r} + \frac{d\ln T_{\rm gas}}{d\ln r}\right). \tag{3.3}$$

In the parenthesis on the right-hand-side one can add a term related to an additional nonthermal turbulent, magnetic, or cosmic ray pressure $P_{\rm nt}$ (e.g. MB03), so that the previous formula would read:

$$M(r) = -\frac{kT_{\rm gas}r}{G\mu m_p}\left(\frac{d\ln\rho}{d\ln r} + \frac{d\ln T_{\rm gas}}{d\ln r} + \frac{P_{\rm nt}}{P_{\rm gas}}\frac{d\ln P_{\rm nt}}{d\ln r}\right). \tag{3.4}$$

Although in early-type galaxies that contain strong radio sources one can estimate the pressure $P_{\rm nt}$ (MB03) this pressure is usually ignored in mass determinations of these galaxies, so we will neglect it in this book.

Hot gas in early-type galaxies derives from two sources: internal and external. *Internal sources* are evolving stars that continuously eject gas at a rate of $\sim 1.3[L_B/(10^{11}\ L_{B,\odot})]\ M_\odot\ {\rm yr}^{-1}$, where L_B is luminosity in the B-band. As noted by MB03 it is generally assumed that gas ejected by orbiting red giant stars passes through shocks and is raised to the stellar kinematic temperature:

$$T_* \approx T_{vir} \approx \mu m_p \sigma^2/k \sim 10^7\ {\rm K} \sim 1\ {\rm keV}, \tag{3.5}$$

where σ is the stellar velocity dispersion. Also, type Ia supernovae can provide some additional heating. For some massive galaxies in our sample large X-ray luminosities of $L_{\rm x} \sim 10^{40} - 10^{43}$ ergs s^{-1} for $L_B > 3\times10^{10}\ L_{B,\odot}$, are detected (see TABLE 3-1). This indicates that most of the internally produced gas is currently trapped in the galactic or group potential. At times when most of the galactic stars were forming, type II supernovae were driving winds of metal-enriched gas into the inter-galactic environment. The gas that was expelled in this way enriched the hot gas in the outer regions of the early-type galaxies. Later, some of this local gas fell back into the central galaxy, thus providing an *external source* of gas. An additional source of external gas was provided by a continued accretion from the ambient cosmological flow that was gravitationally bound to the group or cluster (MB03). The diffuse external gas that arrived after having fallen through the deeper potential well of the surrounding group (cluster), was shock-heated to the virial temperature of the galaxy group (cluster). This more distant accreted and shocked gas is hotter than gas virialized to T_* deeper in the stellar potential of the early-type galaxy. These two together form an outwardly increasing gas temperature that is observed (see Fig. (3.1), right). Fig. (3.1) was taken from MB03 and it shows the dependence $\rho_* \propto n_e^2$ that was found in the early-type galaxies. It is obvious that relation $n_e \propto \rho_*^{\frac{1}{2}}$ holds over a wide range in galactic radius. Here, n_e is the electron density of the hot gas. In giant elliptical galaxies it is typically $n_e(0) \sim 0.1$ cm^{-3} at the center and declines with radius as $n_e \propto r^{-1.25\pm0.25}$.

The total mass of hot gas in massive elliptical galaxies is roughly several times 10^{10} $M_\odot$ (about $\lesssim 1$ percent of the total stellar mass). This number depends on the extent of the given galaxy.

If one wants to calculate the mass and mass-to-light ratio of elliptical galaxy based upon X-ray observations one can use the following approach (which was used in Kim and Fabbiano (1995), hereafter KF95, for NGC 507 and NGC 499): one assumes circular symmetry and derives a radial profile of the X-ray surface brightness measured in concentric rings centered on the X-ray centroid. In a given range one then fits the analytic King approximation model:

$$\Sigma_{\rm X} \sim \left[1 + \left(\frac{r}{a}\right)^2\right]^{-3\beta+0.5} \tag{3.6}$$

(for details see KF95). Here a is the core radius (the radius where the surface brightness falls to half of its central value), and slope β. If the temperature of the X-ray emitting gas does not change much as a function of radius one can assume isothermality – in all cases in this book this assumption is valid because we have dealt mostly with the internal parts of galaxies (inside at most 3 effective radii, except for NGC 1399 for which we present the results out to $\sim 13R_e$ because this galaxy will be also studied in Chapter 5 using globular clusters). Now using this assumption together with the formula for $n_e \propto r^{-3\beta}$ (KF95) (see above) one can estimate the total gravitational mass at a given radius r (assuming hydrostatic equilibrium) in a convenient form (Kim and Fabbiano (1995)):

$$M_T = 1.8 \times 10^{12}(3\beta + \alpha)\left(\frac{T}{1\mathrm{keV}}\right)\left(\frac{r}{10^3\,\mathrm{arcsec}}\right)\left(\frac{d}{10\,\mathrm{Mpc}}\right)\mathrm{M}_\odot, \tag{3.7}$$

here the exponent α is related to the temperature ($T \sim r^{-\alpha}$) and is taken to be zero in all cases below. This formula is valid outside the core region.

The mass-to-light ratio (in the B-band) can be expressed as a function of radius r:

$$\frac{M_T}{L_B} = 1.16 \times 10^{-2} 10^{\frac{B}{2.5}}(3\beta + \alpha)\left(\frac{T}{1\mathrm{keV}}\right)\left(\frac{r}{10^3\,\mathrm{arcsec}}\right)\left(\frac{d}{10\,\mathrm{Mpc}}\right)^{-1}, \tag{3.8}$$

where B is the B magnitude of galaxy inside radius r (Kim and Fabbiano 1995). It is important to stress that the estimate of the total mass (and the total mass-to-light ratio) of a given galaxy estimated using the X-rays is not plagued with the uncertainties in the orbits (the well known mass-anisotropy degeneracy, see Introduction).

We present the results for our sample of galaxies with X-ray haloes below, taking $\beta = 0.5$, except for the faint X-ray galaxy NGC 3379 where $\beta = 0.64$ (result taken from Brown and Bregman 2001). In TABLE 3-1 we present estimated masses and mass-to-light ratios for the galaxies within the radius for which we had the long-slit spectra. The data sources are given at the bottom of TABLE 3-1.

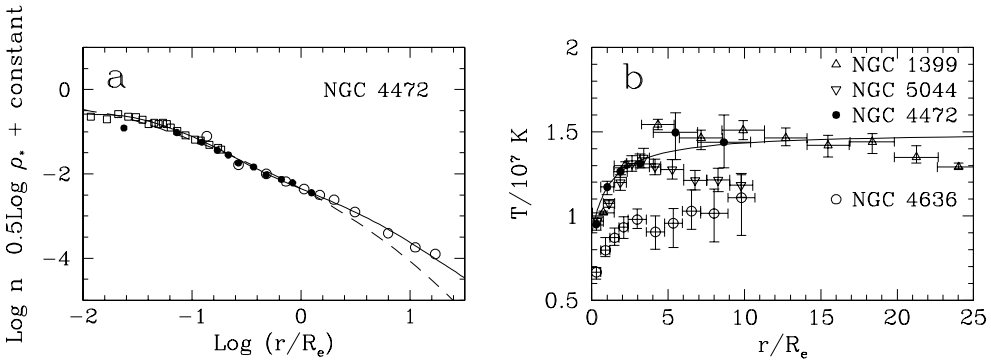

Figure 3.1: Taken from MB03 (their Figure 2). Left panel: The observed and azimuthally averaged electron density profile $n(r)$ in NGC 4472 is shown as a function of radius normalized to the effective radius $R_e = 8.57$ kpc at distance $d = 17$ Mpc. The observations are from EINSTEIN (Trinchieri, Fabbiano, and Canizares 1986) (*filled circles*) and ROSAT (Irwin and Sarazin 1996) (*open circles*); for the inner region MB03 have Abel-inverted CHANDRA surface brightness data from Loewenstein et al. (2001) (*open squares*) and normalized them to previous observations. The solid line is an analytic fit to the observations. The dashed line is the square root of the stellar density $\rho_*^{1/2}(r)$ normalized to n at $r = R_e$. Right panel: Typical temperature profiles for several bright E galaxies, taken from Brighenti and Mathews (1997), based on the following sources: NGC 1399: ROSAT PSPC from Jones et al. (1997); NGC 5044: ROSAT PSPC from David et al. (1994); NGC 4636: ROSAT PSPC from Trinchieri et al. (1994); NGC 4472: ROSAT HRI and PSPC from Irwin and Sarazin (1996). The solid line is an approximate analytic fit to $T(r)$ for NGC 4472. Note that galaxy NGC 1399 is present in our sample and will be analyzed later.

Using Eq. (3.3) one can estimate the total integrated mass $M(r)$ within a given radius. Loewenstein and White (1999) using the relationship between the X-ray temperatures and stellar velocity dispersions (the $T-\sigma$ relation: $< T > \propto < \sigma >^{1.45}$, where $< ... >$ denotes mean value) found that minimum values of dark matter core radii scale as $r_{\rm DM} > 4.6(L_V/3L_*)^{3/4}\ h_{70}^{-1}$ kpc and that the minimum dark matter mass fraction is $\gtrsim$20 % within one optical effective radius $r_{\rm eff}$ and is between $\gtrsim$39 per cent and 85 per cent within 6 $r_{\rm eff}$, depending on the stellar density profile and observed value of $\beta_{\rm spec}$. Here,

$$\beta_{\rm spec} \equiv \frac{\mu m_p < \sigma >^2}{k < T >}. \tag{3.9}$$

When dark matter dominates the gravitational potential on large scales, then $< T >$ is a measure of the dark matter content within the extraction radii (in this case 6 $r_{\rm eff}$ (Loewenstein and White (1999)). The Fundamental plane (FP)[6] provides a link between the velocity dispersion and the global luminosity and therefore $\beta_{\rm spec}$ is a good

[6]Elliptical galaxies populate a two-dimensional manifold in the space of their observable quantities: effective radius, $r_{\rm eff}$, effective surface brightness (mean surface brightness within $r_{\rm eff}$), and central velocity dispersion σ. This manifold was named fundamental plane (FP), cf. Djorgovski

quantity for establishing the dark-to-luminous matter ratio within the optical radius. One can also use temperature profiles as an additional constraint on dark matter; unfortunately, these profiles are available only for galaxies that are very bright in X-rays.

3.2. ANALYSIS OF ELLIPTICAL GALAXIES WITH X-RAY HALOES

3.2.1. BASIC DATA AND MASS ESTIMATES

Some of the results presented in this Section were published in Samurović and Danziger (2005). Here we update some of the figures and add some new ones to include new galaxies which were analyzed since this paper was published.

TABLE 3-1

X-RAY AND MASS PROPERTIES OF GALAXIES WITH X-RAY HALOES

Name	r ($''$)	r (kpc)	$r/r_{\rm eff}$	B	$\log L_X$ (erg s^{-1})	T (keV)	D (Mpc)	M ($10^{11} M_\odot$)	$(\frac{M}{L})_B$
IC 1459	100	11.7	2.86	11.13	41.19[1]	0.60[2,3]	24.16	3.91	15.53
NGC 1399	70	6.91	1.67	10.25	41.44[1]	1.08[3]	20.36	4.16	8.13
NGC 1404	80	10.79	3.08	10.82	41.27[1]	0.62[3]	27.81	3.72	6.60
NGC 3379	80	5.04	1.45	10.10	39.78[1]	0.26[4]	13.01	0.92	3.86
NGC 4105	30	4.02	0.86	11.26	41.94[5]	0.76[3]	27.66	1.70	4.58

NOTE: References: (1) Brown and Bregman (1998), (2) Fabbiano et al. (2003), (3) Davis and White (1996), (4) Brown and Bregman (2001), (5) Fabbiano, Kim and Trinchieri (1992)

In TABLE 3-1 we give a list of galaxies from different samples that posses X-ray haloes. The second and third columns give the radius for each galaxy out to which long-slit spectra extend to (in arcsecs and kiloparsecs, respectively). The fourth column expresses this in units of effective radii. Total B-magnitudes in the fifth column were taken from the LEDA catalog. In the sixth column are the data for X-ray luminosities that were collected from the literature (see the notes to TABLE 3-1). Temperatures in the seventh column were collected from the paper by Davis and White (1996), except in the case of NGC 3379 for which the temperature is taken from the Brown and Bregman (2001) paper that deals with emission mechanisms in X-ray faint galaxies. In the case of IC 1459 there is also a recent estimate by Fabbiano

and Davis (1987), Dressler (1987), see also Binney and Merrifield (1998). Borriello, Salucci and Danese (2003) showed that the small scatter around the FP of massive ellipticals can be used to infer important properties about their dark and luminous matter.

et al. (2003) that agrees well with Davis and White (1996). Distances in the eighth column are calculated using the Hubble parameter $h = 0.7$ (using heliocentric radial velocities form the NED archive). In the ninth column the mass of each galaxy in units of $10^{11} M_{\odot}$ is estimated using Eq. (3.7) for a radius given in the second column, and finally, in the tenth column the estimate of the mass-to-light ratio for each galaxy is given using Eq. (3.8) again for the radius in the second column. It is important to repeat that in the approximation which we have made in all cases the temperature is taken to be constant in the given region so α parameter from Eq. (3.7) and Eq. (3.8) is taken to be zero.

In Figs. (3.2) – (3.6) are presented graphical estimates of the mass-to-light ratios (in the B-band) for the galaxies from our samples. Shaded regions with indicated lower and upper limits provide estimates obtained using the value of T_{σ} for the lower limit and $T_{\rm X} = 1.5 T\sigma$ for the upper limit, because Brown and Bregman (1998) for objects with few counts assumed this latter limit (for example in the cases of NGC 1399 and NGC 1404). For several galaxies they found that $T_{\rm X} \approx 2T_{\sigma}$: this relation was used only in the case of NGC 3379 (for which they do not provide the estimate of $T_{\rm X}$) thus giving a corresponding upper limit. The case for which $T_{\rm X} = 1.5 T\sigma$ is also plotted as a thick dotted line in Fig. (3.5). T_{σ} expressed in keV is calculated using Eq. (3.5) which after insertion of appropriate values becomes:

$$kT_{\sigma} = 6.367 \times 10^{-6} \sigma^2 \tag{3.10}$$

where σ is expressed in $\mathrm{km\,s^{-1}}$. Estimates from two-integral (2I) modelling are also included.

Fukazawa et al. (2006) have recently investigated the dynamical structure of 53 elliptical galaxies using the CHANDRA archival X-ray data. They assumed the hypothesis of hydrostatic equilibrium and derived the total masses (and the mass-to-light ratios) for the galaxies in the sample. In some cases their inferred masses are in a disagreement with the results obtained in this book and also with the results found in the literature (see below when each galaxy is discussed). Humphrey et al. (2006) also used the CHANDRA archive to study the mass profiles of 7 elliptical galaxies. They measured approximately flat mass-to-light profile within an optical effective radius which rises by an order of magnitude at $\sim 10 R_e$ which confirms the presence of dark matter in the outer regions of ellipticals. Unfortunately, the galaxies in their sample were the different ones with respect to the galaxies which we analyze, so the comparison of the results was not possible.

IC 1459 (Fig. (3.2))

The stripe related to the X-rays is determined using the paper by Davis and White (1996) who found $T = 0.60^{+0.12}_{-0.13}$. This is in agreement with Fabbiano et al. (2003) who estimated $T = 0.5$-0.6 keV. We have also added a line which corresponds to $T = 0.4$ keV and which provides the best fit to the 2I modelling. Using virial assumption, Eq. (3.10), one gets $T_{\sigma} = 0.73$ keV. Only in the case of $T = 0.50 - 0.60$ keV do we have a marginal agreement (in region $1.0 < r < 2R_e$) with results obtained using 2I modelling techniques.

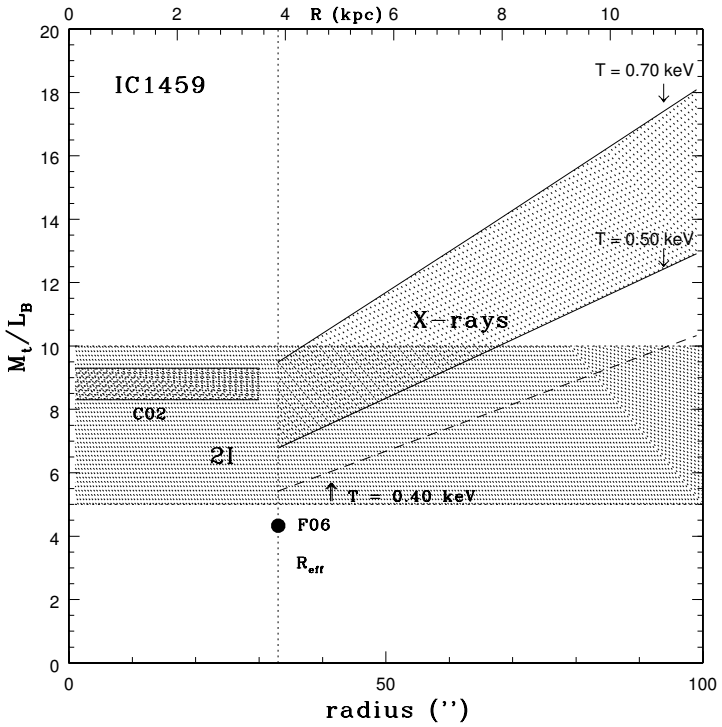

Figure 3.2: Cumulative mass-to-light ratio of IC 1459 in the B-band as a function of radius. The scale of the lower x-axis is given in arc seconds and the upper x-axis is in kiloparsecs. The effective radius is plotted as a dashed vertical line. Limits on the mass based on the X-rays are given using lower and upper limits obtained using Davis and White (1996): $T = 0.60 \pm 0.10$ keV. "2I" refers to two-integral modelling: the stripe in the 2I case provides the limits within which the kinematics can be fitted (see text for details). One additional line (see text for details) was also added to the plot: dashed line is for the case for which T =0.4 keV. The stripe labelled with C02 corresponds to the estimate obtained by Cappellari et al. (2002) of the M/L ratio which is, after the conversion to the B-band and the distance used in our paper, $M/L_B = 8.8 \pm 0.5$. Filled circle labelled with F06 is the result from the paper by Fukazawa et al. (2006).

This may mean that:

(i) the 2I integral models systematically underestimate the mass-to-light ratio value. This is possible but not probable since the estimated values of the mass-to-light ratio (M/L_B was found to be between ~ 6 and ~ 10, see the stripe in Fig. (3.2)) are in good agreement with the mean value found in the sample of van der Marel (1991) which after rescaling to the Hubble constant of 70 km s^{-1} Mpc^{-1} becomes $M/L_B = 8.33 \pm 0.35$. This type of modelling precludes the possibility that with an observed decreased velocity dispersion one could have a dark matter halo with a consequent increase of a mass-to-light ratio;

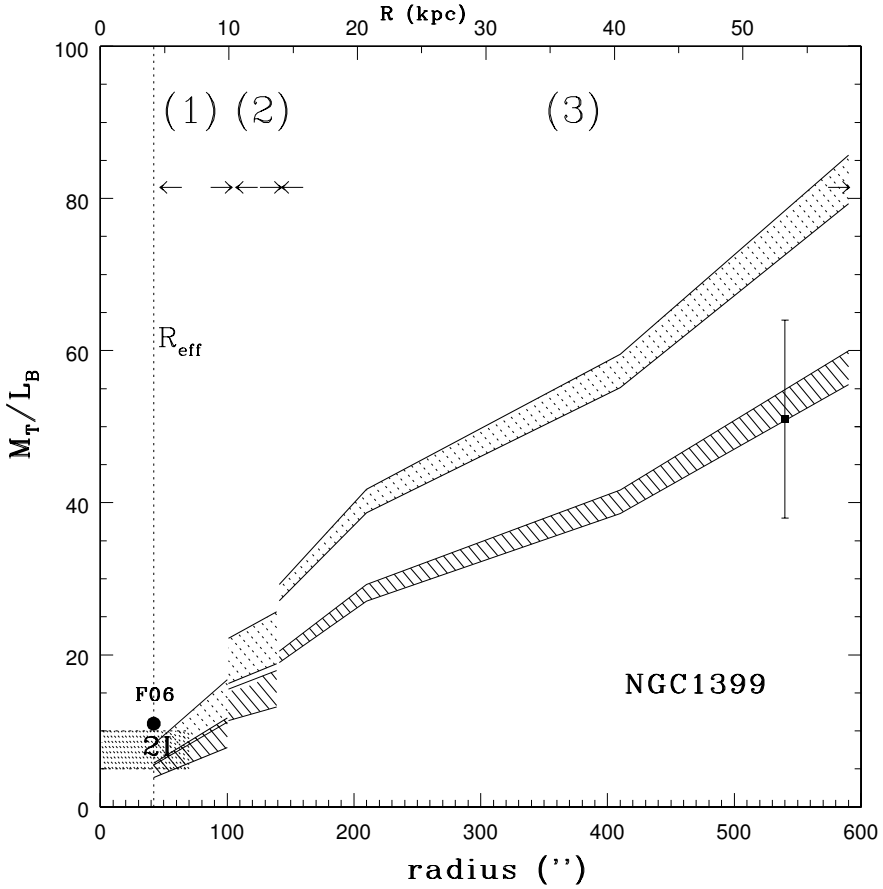

Figure 3.3: Estimates of the total mass-to-light ratio in the B-band in the solar units using X-rays assuming hydrostatic equilibrium and isotropic velocity distribution presented with three shaded regions. Three different regions of the constant temperature were used beyond one effective radius: region (1) is between 40 and 100 arcsec, region (2) is between 100 and 140 arcsec and the region (3) is between 140 and $\sim$ 600 arcsec. (1): the shaded regions interior to 100 arcsec cover the temperatures between 0.61 and 0.92 keV as estimated in Brown and Bregman (1998). (2): shaded regions between 100 and 140 arcsec have for a lower value $T \sim 0.88$ keV and for an upper value $T \sim 1.2$ keV as estimated from the paper of Jones et al. (1997) (their fig. 3). (3): beyond 140 arcsec $T = 1.30 \pm 0.05$ was used as estimated by Jones et al. (1997). With a filled square we presented the mass-to-light ratio found by Grillmair et al. (1994) ($M_T/L_B = 51 \pm 13$). Vertical dotted line is one effective radius. The regions shaded with dots are for the case for which $\beta = 0.50$ (Paolillo et al. 2002) and the regions shaded with lines are for the case for which $\beta = 0.35$ (Jones et al. 1997). The result based on the 2I modelling is given with a shaded region which extends out to 70 arcsec: these are the limits within which the kinematics can be fitted (see text for details). Filled circle labelled with "F06" is the result from the paper by Fukazawa et al. (2006).

(ii) the temperature estimates used above are not correct - note, however, that if we adopt a lower temperature, e.g. $T \sim 0.5$ keV (still allowed by the measurements of Fabbiano et al. 2003 and Davis and White 1996) a better agreement can be obtained; the strong rising trend of the mass-to- light ratio will persist making this new estimate again larger in the outer part of the galaxy. Only $T \sim 0.4$ keV (as calculated in the paper by Brown and Bregman 1998) would provide an agreement within the whole region (beyond $\sim\ 1R_e$) for which we have the 2I mass-to-light ratio estimate;

(iii) the assumption of the hydrostatic equilibrium for IC 1459 is not correct, so the usage of Eq. (3.1) is inappropriate which makes Eq. (3.8) inapplicable in this case. We here refer the reader to a recent important work by Ciotti and Pellegrini (2004) which investigates the effects of deviations from equilibrium on the mass of ellipticals (see also the discussion on NGC 3379 below).

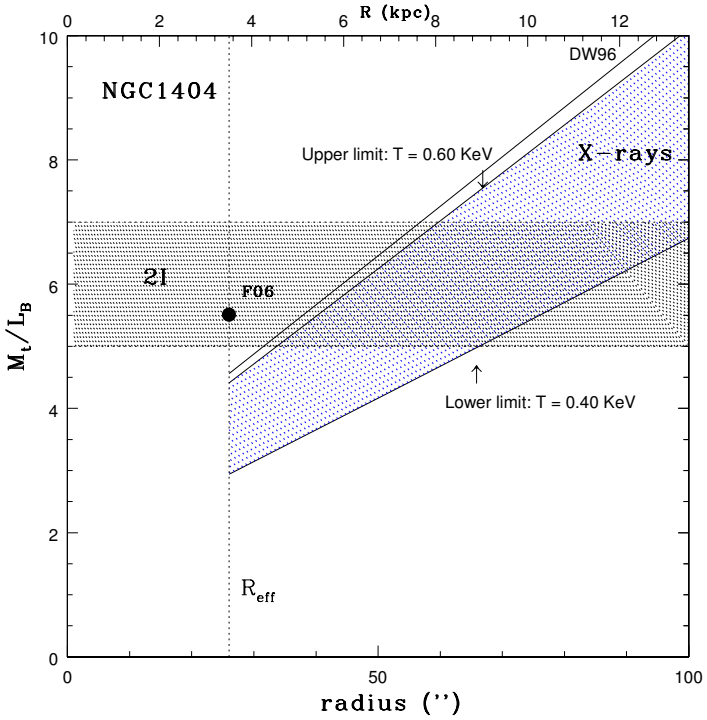

Figure 3.4: Cumulative mass-to-light ratio of NGC 1404 in the B-band as a function of radius. The scale of the lower x-axis is given in arc seconds and the upper x-axis is in kiloparsecs. The effective radius is plotted as a dashed vertical line. The upper limit given as "DW96" is based on the paper by Davis and White (1996). Limits on the mass based on the X-rays are given using lower and upper limits obtained using Davis and White (1996): $T \approx 0.62$ keV. The other limits are given by: the value of T_σ is for the lower limit and $T_{\rm X} = 1.5T\sigma$ is for the upper limit. "2I" refers to two-integral modelling: the stripe in the 2I case provides the limits within which the kinematics can be fitted (see text for details). Filled circle labelled with "F06" is the result from the paper by Fukazawa et al. (2006).

NGC 1399 (Fig. (3.3))

The plot in Fig. (3.3) gives the dependence of the mass-to-light ratio in the B-band using different estimates of the temperature in different regions (see caption of Fig. (3.3) for details). The problem of the mass-to-light ratio in this galaxy will be discussed in more detail in Chapter 5 when we compare the results of different techniques. Here we only note that in the inner region inside $\sim 3R_e$ there is no need for dark matter because the mass-to-light ratio reaches at most $M/L \approx 10$ (in the B-band). The estimate based on the X-rays interior to $\sim 1.7R_e$ is in agreement with that based on the 2I modelling. Note that the value of the mass-to-light ratio at $1R_e$ of Fukazawa et al. (2006) ($M/L_B = 10.95$, no errors given) is somewhat higher than our estimate (this is similar to what they inferred for NGC 3379, for a possible reason for discrepancy see below).

NGC 1404 (Fig. (3.4))

The case of the galaxy NGC 1404 is an interesting one: beyond $\sim 1R_e$ all the different estimates are in agreement: both 2I and X-ray predict the mass-to-light ratio which is in agreement with the lack of dark matter out to $\sim 3R_e$. The value given by Fukazawa et al. (2006), $M/L_B = 5.51$ (at $1R_e$) is in agreement with the results found in this book.

NGC 3379 (Fig. (3.5))

In the case of NGC 3379 we provide a lower value of the X-ray estimate on the mass-to-light ratio using $T = 0.26$ keV. Two upper limits are given: $T_X = 1.5T_\sigma$ represented by a thick dotted line, and one for which $T_X = 2T_\sigma$ as a solid line. In all these cases $\beta = 0.64$ (from Brown and Bregman 2001) is taken. One additional line is also given: the dashed line is for $T = 0.26$ and used a generic value of the β parameter, $\beta = 0.50$. To make a comparison with different mass tracers we also plotted available results on the mass-to-light ratio that were obtained using PNe (Ciardullo et al. 1993 (C93), Romanowsky et al. 2003 (R03) and Sluis and Williams 2006 (SW06)). It should be noted however that the methodology of the PNe and GCs does not provide measures of h_3 and h_4 parameters as tests of the models (see the discussion in Chapter 5).

The estimates from 2I modelling are in an agreement with the X-ray estimates. Our M/L ratios are similar to those obtained for PNe albeit at larger radii. We note that beyond 120 arcsec ($\sim 2.2R_e$) a discrepancy between PNe estimates and X-ray estimate occurs. If we reduce the value of the β parameter from 0.64 to 0.5 we obtain a good agreement with the data between $\sim 1R_e$ and $\sim 1.5R_e$; between ~ 1.5 and $\sim 3.5R_e$ the mass-to-light ratio in the B-band varies between 5.5 and 9.5. In Fig. (3.5) we also plotted a point (at $1R_e$) and a stripe based on the paper by Gebhardt et al. (2000) which is calculated using their 3I modelling procedure.

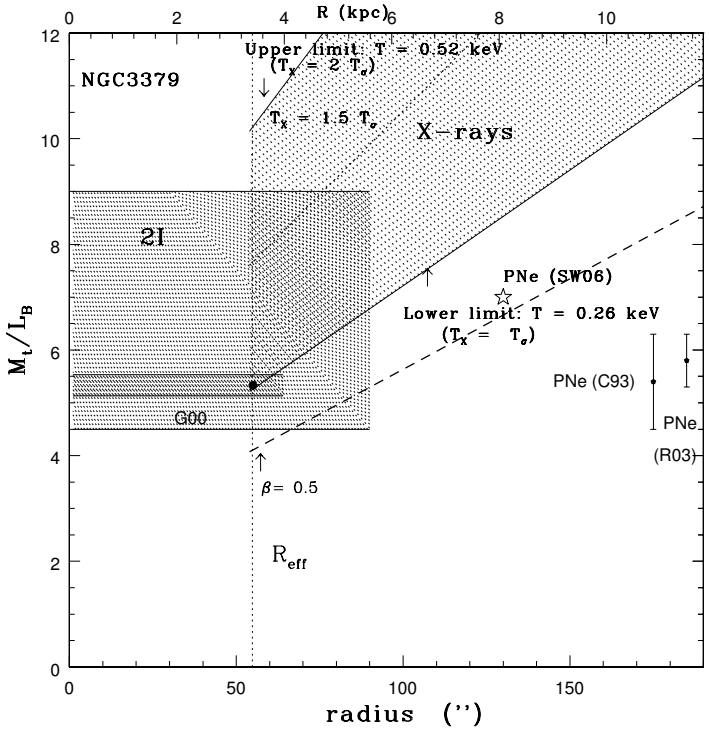

Figure 3.5: Cumulative mass-to-light ratio of NGC 3379 in the B-band as a function of radius. The meaning of the symbols is the same as in Fig. (3.2). Three additional points based on the PNe are given in the plot: "R03" refers to Romanowsky et al. (2003), "C93" to Ciardullo et al. (1993) and "SW06" to Sluis and Williams (2006). Two upper limits are given: one for $T_{\rm X} = 1.5T_\sigma$ represented by a thick dotted line, and one for which $T_{\rm X} = 2T_\sigma$ as a solid line. The dashed line is for the case for which $T_{\rm X} = 0.26$ keV and $\beta = 0.5$. The point labelled G00 and corresponding stripe are based on the result from the 3I modelling of Gebhardt et al. (2000); it has been obtained for the B-band and at the distance of 13 Mpc.

Pierce et al. (2006) very recently found at ~ 200 arcsec the mass-to-light ratio in the V-band: $M/L_V = 18 - 30$ (which in the B-band becomes $M/L_B \sim 24 - 40$; see also discussion below). These high values seem to favour higher values of the temperature (see Fig. (3.5), the upper limit for $T = 0.52$ keV). Very recently, Pellegrini and Ciotti (2006) attempted to reconcile the optical and X-ray mass using NGC 3379: they found that a possible discrepancy at large radii of ~ 2 can be explained by deviations from hydrostatic equilibrium of the hot gas (see also Ciotti and Pellegrini 2004).

Finally, we mention the recent paper by Fukazawa et al. (2006) who gives the following estimate of at $1R_e$: $\Upsilon_B = 13.93$. This is much higher than all the previous estimates. To address this issue we quote Pierce et al. (2006): "The XMM-Newton data analyzed by Fukazawa et al. (2006) are limited to the inner 17 arcsec; only 25 per cent of the X-ray luminosity is in the thermal component of the spectrum. The

authors [Fukazawa et al.] point out that the data constrain the properties of the interstellar medium but not the mass profile. Hence, their estimate of $\Upsilon_B = 13.93$ cannot be considered to be very robust." Note also that Sluis and Williams (2006) performed recently a search for PNe with the Rutgers Fabry-Pérot in NGC 3379. They "found a remarkably constant mass-to-light ratio" within $\sim 3R_e$ (if one takes the true value of the effective radius, 55 arcsec) with an overall $\Upsilon_B \approx 5$.

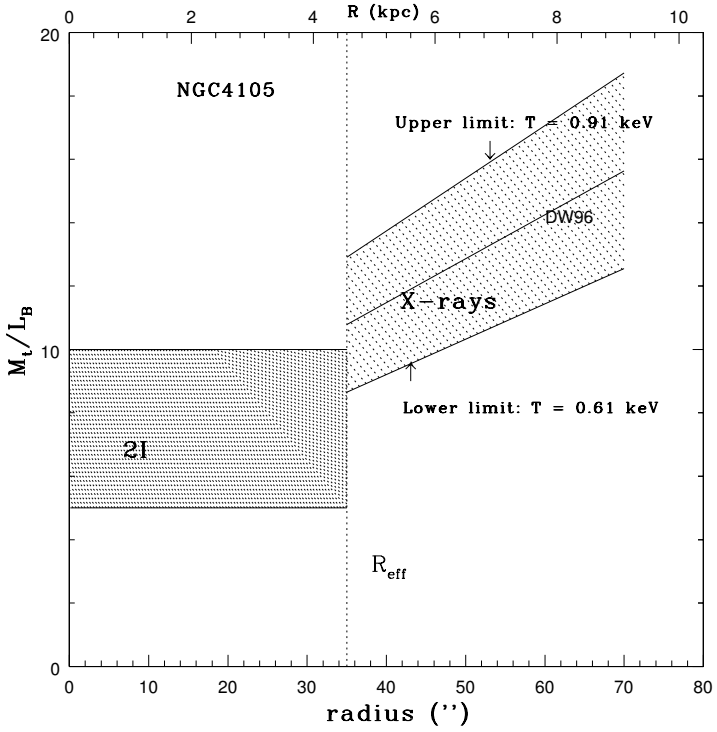

Figure 3.6: Cumulative mass-to-light ratio of NGC 4105 in the B-band as a function of radius. The meaning of the symbols is the same as in Fig. (3.2). The following limits are given: the upper one for $T_{\rm X} = 2T_\sigma$, and the lower one for which $T_{\rm X} = 1.5T_\sigma$ as a solid line. The line given as "DW96" is based on the paper by Davis and White (1996), $T \approx 0.76$ keV.

NGC 4105 (Fig. (3.6))

Since in the case of this galaxy our data extend only out to $\sim 1R_e$ the comparison of the X-ray predictions with the results of the 2I modelling interior to this point could not be done. It is however obvious that if one assumes that the constant mass-to-light ratio inferred from the 2I modelling is valid beyond 1 R_e there is a clear discrepancy between the predictions of the two methodologies (for $0.6 < T < 0.7$ keV): the value

of the mass-to-light ratio from the X-rays is higher (at $\sim 2R_e$ $M/L_B \sim 12-18$) than that obtained using the 2I modelling (assumed to be between ~ 5 and ~ 7). The reason for this discrepancy could be the lack of hydrostatic equilibrium (Ciotti and Pellegrini 2004). We did not have data related to other mass tracers, so further comparisons were not possible.

3.2.2. SIMPLE JEANS MODELLING

The modelling performed in this subsection is based on the solving of the Jeans equation which was explained in Section 2.1.1.2. The mass which is included in the Jeans equation is calculated in Eq. (3.7). When we speak of the correction for the velocity dispersion we assume the correction based on the non-zero value of the h_4 parameter (see Chapter 2):

$$\sigma_{\rm corr} = \sigma_{\rm GH}(1 + \sqrt{6}(h_4)_{\rm GH}). \tag{3.11}$$

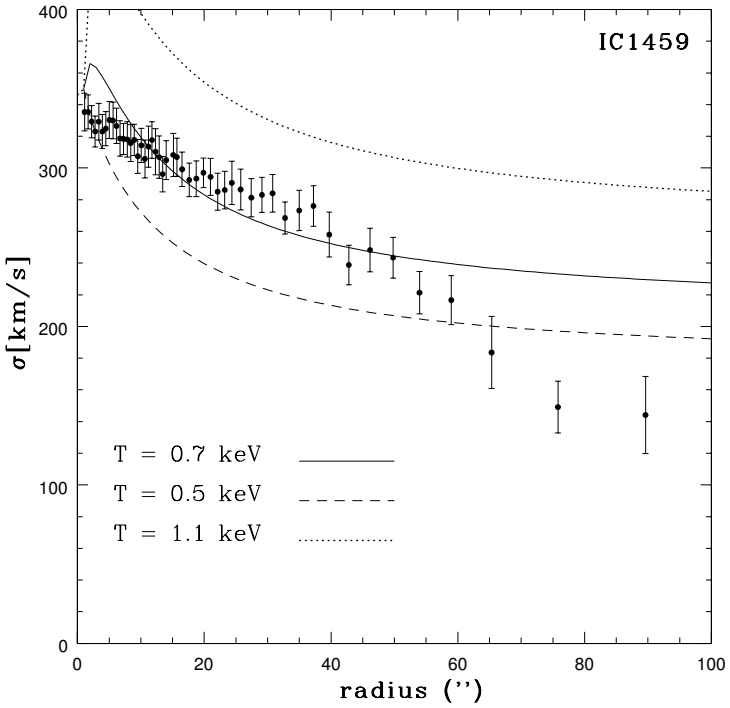

Figure 3.7: Dynamical modelling of the *uncorrected* velocity dispersion of IC 1459 using X-ray data. The modelling lines based on different masses which correspond to different temperatures are the following: the case of $T = 0.7$ keV is given with a solid line, the case of $T = 0.5$ keV is given with a dashed line and the case of $T = 1.1$ keV is given with a dotted line. In all cases spherical isotropy ($\beta_* = 0$) and hydrostatic equilibrium are assumed.

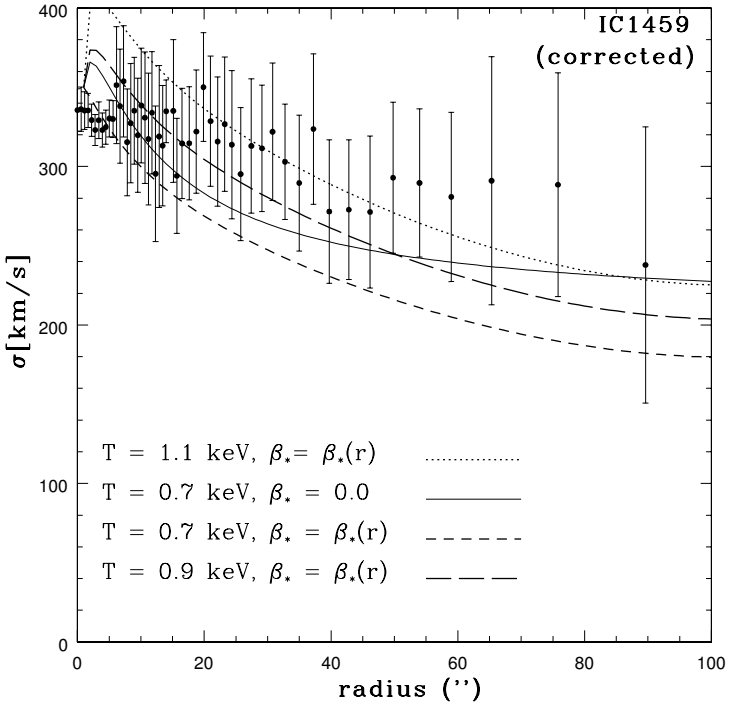

Figure 3.8: Dynamical modelling of the velocity dispersion corrected for non-zero values of the h_4 parameter of IC 1459 using X-ray data. The modelling lines based on different masses which correspond to different temperatures are the following: the case of $T = 0.7$ keV is again given with a solid line ($\beta_* = 0$) and a short dashed line is for the case of $T = 0.7$ keV ($\beta_* = \beta_*(r)$). The case of $T = 0.9$ keV and $\beta = \beta_*(r)$ is given with a long dashed line and the case of $T = 1.1$ keV and $\beta = \beta_*(r)$ is given with a dotted line. Again, in all cases hydrostatic equilibrium is assumed.

IC 1459 (Fig. (3.7), Fig. (3.8))

First, we tested a spherical isotropic model ($\beta_* = 0$) using different estimates for the temperature: $T = 0.7$ keV (solid line), $T = 0.5$ keV (dashed line) and $T = 1.1$ keV (dotted line). In all three cases spherical isotropy ($\beta_* = 0$) and validity of hydrostatic equilibrium were assumed and the values of the velocity dispersion were uncorrected (the values of the h_4 parameter were not taken into account, see Chapter 2). Only the case for which $T = 0.7$ keV can provide a good fit to the observed data out to ~ 50 arcsec. In the outer regions the *observed* velocity dispersion tends to decrease and none of the fits is successful. This best-fitting value of $T = 0.7$ keV is, as expected, in an excellent agreement with the value found using a virial assumption (see Eq. (3.10)). This value, however, is somewhat higher than our preferred value of $T = 0.4 - 0.6$ keV found with the 2I modelling, thus implying a higher X-ray based mass-to-light ratio than one inferred from stellar dynamics (as shown in Fig. (3.2)).

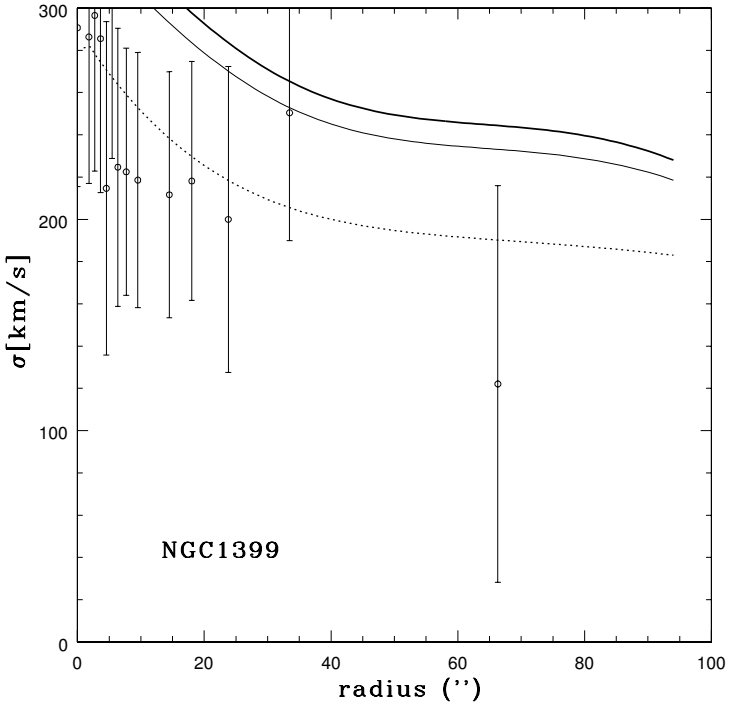

Figure 3.9: Dynamical modelling of the velocity dispersion NGC 1399 using X-ray data. For all the tests: $\beta_* = 0$. Solid line is for the case for which $T = 1.08$ keV (from Davis and White 1996), the dashed line is for the case for which $T = 0.98$ keV and the dotted line is for the case for which $T = 0.65$ keV.

Second, since for IC 1459 (see Chapter 2) we have departures from zero of the h_4 which imply that radial orbits dominate ($h_4 > 0$ beyond ~ 20 arcsec) we have also modelled the corrected values of the velocity dispersion (see Eq. (3.11)). For the relations between h_4 and β_* see van der Marel and Franx (1993) and Gerhard (1993). The fit which uses $T = 0.7$ keV and $\beta_* = 0$ (the same as in Fig. (3.7) repeated here again with solid line) can produce a reasonable agreement with the data. If we now allow anisotropies ($\beta_* = \beta(r)$) based on our observed $h_4(r)$ values as given above we can see that $T = 0.7$ keV, except for the central parts (interior to ~ 20 arcsec) this fit given with the short dashed line fails to fit the corrected velocity dispersion. We assume that $h_4 \sim 0$ ($\beta_* \sim 0$) in the inner regions of the galaxy and in the outer parts at $\sim 3R_e$ h_4 is ~ 0.2 ($\beta \sim 1$). A slightly higher value of the temperature of $T = 0.9$ KeV, taken together with the same anisotropies ($\beta_* = \beta(r)$) provides a better fit especially in the intermediate region (between ~ 10 and ~ 50 arcsec). Finally, a fit which used $T = 1.1$ KeV and $\beta_* = \beta(r)$ provides the best fit (among the ones tested) in the region between ~ 20 and ~ 100 arcsec. Again, in the case of the modelling of the corrected velocity dispersion data the value of the temperature based on the X-rays is higher than that inferred from stellar dynamics ($T \sim 0.4 - 0.5$ keV): the

preferred value of $T = 1.1$ keV is higher than that in the uncorrected case ($T = 0.7$ keV). The reason for this discrepancy could be due to the inherent assumptions of the two methodologies (such as the validity of hydrostatic equilibrium and constant value of the temperature in the case of the X-rays and mass profile used in the case of the detailed Jeans modelling; see also the discussion about the mass-to-light ratio of IC 1459 earlier in this Section). It is important to stress that before we can use the X-ray temperatures to model the velocity dispersion we need to understand the reasons for the differences which might be due to different types of mass profiles and/or problems with the 2I models.

NGC 1399 (Fig. (3.9))

When we modelled the corrected values of the velocity dispersion of NGC 1399 we again applied the hypothesis of isotropy ($\beta_* = 0$, based on the h_4 parameter consistent with zero throughout the galaxy). The best agreement with the observed data is attained when $T = 0.65$ keV (this corresponds to a lower mass-to-light ratio, $M/L_B \approx 4 - 7$). If one adopts this value of the temperature, this would mean that out to $\sim 1.7R_e$ (the distance out to which we have long-slit observations) dark matter does not play an important role.

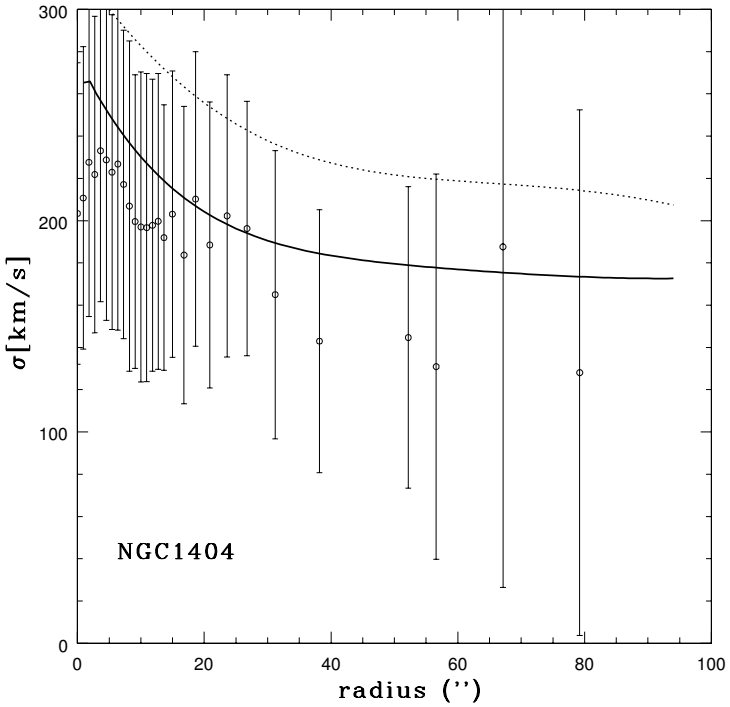

Figure 3.10: Dynamical modelling of the velocity dispersion NGC 1404 using X-ray data. For all the tests: $\beta_* = 0$. Solid line is for the case for which $T = 0.40$ keV and the dotted line is for the case for which $T = 0.62$ keV (from Davis and White 1996).

NGC 1404 (Fig. (3.10))

Because of the huge error bars taken into account when the corrected values of the velocity dispersion are plotted the simple Jeans modelling of NGC 1404 cannot tell us much. It is however obvious that for the isotropic modelling ($\beta_* = 0$, based on the h_4 parameter consistent with zero throughout the galaxy) the lower value of the temperature ($T = 0.40$ keV) is preferred. We remind the reader that both quoted low value and the high value ($T = 0.62$ keV) of the temperature were permitted when we compared the X-ray estimates of the total mass-to-light ratio to those based on the 2I modelling (see Fig. (3.4)).

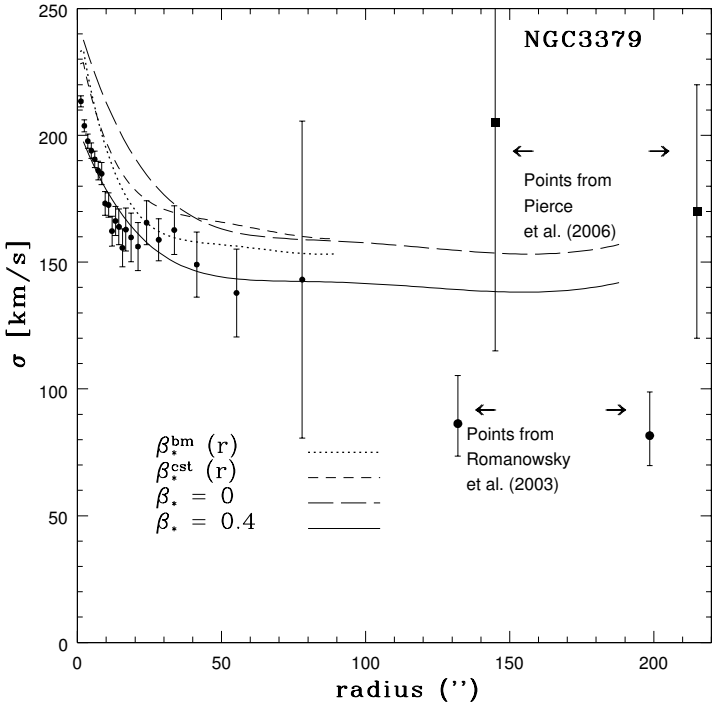

Figure 3.11: Dynamical modelling of the velocity dispersion of NGC 3379 using X-ray data. Observational points are folded about y-axis and are taken from Statler and Smecker-Hane (1999). Long dashed line is the spherical isotropic case ($\beta_* = 0$), when hydrostatic equilibrium is assumed. Thin solid line is for the case when hydrostatic equilibrium is assumed for which radial orbits dominate ($\beta_* = 0.4$). The short dashed line is based on the estimate of the β_*-parameter obtained for the constant mass-to-light ratio model ("cst" model) of Kronawitter et al. (2000) and the dotted line is based on the estimate of the β_*-parameter obtained for the "best model" ("bm") of Kronawitter et al. (2000): they extend only interior to ~ 100 arcsec. Two outermost points given as filled circles taken from Romanowsky et al. (2003) are based on PNe and two outermost points given as filled squares are taken from Pierce et al. (2006) and are based on GCs.

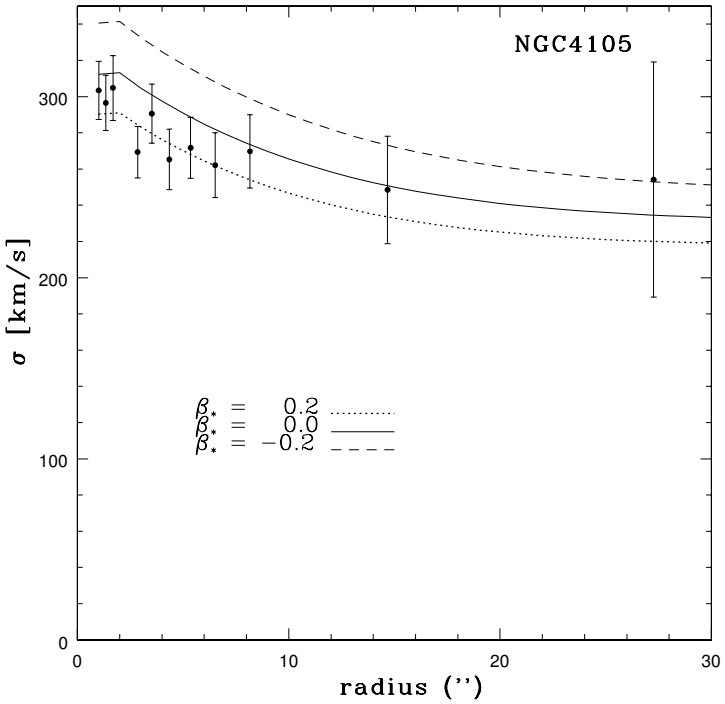

Figure 3.12: Dynamical modelling of the velocity dispersion NGC 4105 using X-ray data. Solid line is for the spherical isotropic case ($\beta_* = 0$), the dashed line is for the case of $\beta_* = -0.2$ (predominantly tangential orbits) and the dotted line is for the case of $\beta_* = 0.2$ (predominantly radial orbits).

NGC 3379 (Fig. (3.11))

Here we modelled uncorrected values of the velocity dispersion because the departures of the h_4 parameter are only marginally inconsistent with zero. In our modelling we have used the temperature $T = 0.26$ keV, as given in TABLE 3-1. A spherical isotropic model ($\beta_* = 0$) is excluded: in this case the model is completely inconsistent with the observed data. Two models based on the paper by Kronawitter et al. (2000) do not provide a good fit to the data either: the case of the "best model" (dark matter implied: $0 < \beta_* < 0.3$) provides marginally better fit than that of the constant M/L ratio ($0 < \beta_* < 0.2$). After a failure to obtain a successful fit using β_* values taken from the literature we experimented with different (positive and constant) values of β_*: the case of $\beta_* = 0.4$ provides a very good fit to the data. Thus we can conclude that using the approach based on the X-rays (two-integral approach) we can say that for NGC 3379 the dark matter is not dynamically dominant to $\sim 1.5R_e$ because at $\sim 1.5R_e$ one can get the same cumulative mass-to-light ratio as it is obtained using stellar dynamical modelling. Note that the gradient of the mass seen in the X-rays

is not consistent with the constant mass-to-light ratio. However, as in Mathews and Brighenti (2003b) the value of the β_* parameter is larger than that obtained using stellar dynamics although not much. Note that in our 2I dynamical modelling we have used the h_4 parameter to describe the anisotropies and not β_*. We find that the positive value of the β_* parameter ($\beta_* \sim 0.4$) is in agreement with the positive values of the h_4 parameters ($h_4 \sim 0.05$) extracted from the observations and indicating radial anisotropies in the outer parts of NGC 3379 (for the relations between h_4 and β_* see van der Marel and Franx 1993, Gerhard 1993).

In a recent paper Pierce et al. (2006) studied Gemini/GMOS spectra for 22 globular clusters associated with NGC 3379. Their results for the velocity dispersion are incompatible with those of Romanowsky et al (2003), but are in agreement with the predictions based on the X-rays found in this book (paragraph above; also published in Samurović and Danziger 2005). Both our isotropic ($\beta_* = 0$) and radially anisotropic ($\beta_* = 0.4$) predictions are in agreement with the results obtained by Pierce and collaborators. It is however interesting to note that at larger distances from the center isotropic case provides better agreement with the observed data. One of the consequences of the results of Pierce et al. (2006) is the increasing mass-to-light ratio in the outer regions of NGC 3379: they found at ~ 200 arcsec that $M/L_B = 24 - 40$ (in the B-band). The reason for the discrepancy with the results of Romanowsky et al. (2003) is unclear because the modelling techniques used in two works are different[7]; as stated by Pierce et al.: "For detailed comparison to such a model [Romanowsky et al.], the dynamical characteristics and projection effects for both GCs and PNe would need to be taken into account, which is beyond the scope of this work".

A conclusion which emerges from different studies (some from this book and some found in the literature) is the following: interior to $\sim 3R_e$ (≈ 170 arcsec, that is ≈ 10 kpc) dark matter does not dominate because the total mass-to-light ratio in the B-band is $\Upsilon_B \approx 5$. Beyond $\sim 3R_e$ the influence of dark matter starts to increase, and most probably, at these higher radii it starts to dominate. More detailed studies of different mass tracers (PNe and/or GCs) together with the X-rays studies will hopefully clarify this.

NGC 4105 (Fig. (3.11))

In the modelling which we performed we have used the temperature $T = 0.76$ keV, as given in TABLE 3-1. A spherical isotropic model ($\beta_* = 0$) provides a good fit to the observed data (note that we again neglected possible influence of NGC 4106). We have also tested a case with $\beta_* = 0.2$ (predominantly radial orbits) which provides a reasonable fit to the observed velocity dispersion and a case with ($\beta_* = -0.2$) (predominantly tangential orbits) which does not provide a good fit to the data. Note that in the case of NGC 4105 the error bars for the temperature of the X-ray halo given by Davis and White (1996) are huge (especially the upper one): $T_X = 0.76^{+4.40}_{-0.69}$ keV. However, as can be seen in Fig. (3.6) the value $T_X = 0.76$ keV falls just in the middle between the upper and lower limit as obtained from the stellar velocity dispersion which justifies its usage in the dynamical modelling which we performed.

[7]See the discussion on NGC 3379 above for a possible reasons for a discrepancy.

As a side note, we stress that with the upper limit of $T_X = 0.76 + 4.40 = 5.16$ keV no fit could be obtained to the velocity dispersion even in the case when the maximum allowed value of $\beta_* = 1$ was used: velocity dispersion values were always grossly exaggerated: $\sigma > 450$ km s^{-1} throughout the whole galaxy.

3.3. SUMMARY OF THE GALAXIES WITH X-RAY HALOES

In this Section we presented the X-ray data and modelling of the galaxies from our sample which possess an X-ray halo. A detailed stellar dynamical modelling of these galaxies was given in Chapter 2 of this book. Here we note that Figures (3.2) – (3.6) show in graphical form how X-rays can be used as an independent tracer of the mass of the early-type galaxy: they show an overlapping (in some cases good, in other cases poor) of X-ray data with the estimates obtained using stellar dynamical models.

A careful inspection of Figures (3.2) – (3.5) shows that there is an overlapping of the mass-to-light ratio predictions based on the X-rays calculations and those based using other methods (2I modelling, PNe, GCs). From the Figures presented in this Chapter one can see that agreement between 2I modelling and other tracers and X-ray estimates is: poor/good for IC 1459 and very good for NGC 1399, NGC 1404 and NGC 3379. Here we obviously excluded the galaxy NGC 4105 for which our long-slit data extended to only $\sim 1R_e$.

The case of IC 1459 (the galaxy with the counterrotating core) is the only one for which there is a strong discrepancy between the X-ray and stellar dynamics estimate. The reason for a poor agreement in the case of IC 1459 may lie in the temperature determination in the inner parts of the galaxy (inside 3 R_e): lower temperature ($T \sim 0.6$ keV, taken from Davis and White 1996) does provide at least a marginal concordance with the 2I modelling; the estimate based on T_σ (Eq. (3.10)) is large which is a consequence of the large central velocity dispersion of this galaxy.

Using the PNe observations that provide mass-to-light ratio estimates out to much larger radii, one can see that the conclusions based on the X-rays for NGC 3379 are inconsistent with the observations (see Fig. (3.5)) beyond $3R_e$. The behaviour of the mass-to-light ratio in this galaxy based on the GCs is in agreement with the X-ray estimates.

Using these findings, together with the result of Peng et al. (2003) who have found that for NGC 5128 at 15 R_e the mass-to-light ratio is only 13 (in the B-band) (much lower than the value expected from the X-rays analysis: $M/L_B \sim 112 \pm 28$, cf. Bahcall, Lubin and Dorman 1995), one can infer that there is a discrepancy between the mass-to-light ratios calculated using X-rays and PNe techniques at the large radii (beyond $3R_e$) from the center (see the discussion in Chapter 5 for more details). One possible reason could be that the initial assumptions about the hot gas are not correct. In a recent review Bosma (2004) writes: "Yet the new CHANDRA and XMM data show a wealth of detail in the images of the X-ray gas of individual galaxies, so much that one can question the validity of the hydrostatic equilibrium equation used to evaluate masses". Bosma (2004) notes that another complication related to the mass determinations based on the X-rays is the contribution to the X-ray flux of low mass X-ray binaries, which presumably occur in globular clusters and in the

field. Ciotti and Pellegrini (2004) and Pellegrini and Ciotti (2006) also question the existence of hydrostatic equilibrium in elliptical galaxies and discuss the influence of departures from equilibrium on the estimate of the mass in these galaxies. Diehl and Statler (2006) used a sample of 54 normal ellipticals from the CHANDRA archive and found that there is no correlation between optical and X-ray ellipticity as would be expected had the gas settled into hydrostatic equilibrium with a given gravitational potential (see also Chapter 5 when we discuss the galaxy NGC 5128). Their analysis lead them to conclude that, in the sample which they studied, "the gas appears to be very disturbed and that the general perception of normal elliptical galaxies hosting calm, hydrostatic gas has to be revised."

Chapter 4
LINE STRENGTH INDICES

In this Section we define spectral indices and present their measurements for the galaxies from our samples. We then compare the results from the up-to-date chemical evolution models with measurements in order to gain insights about the existence of dark matter in the objects which we analyzed.

4.1. MEASUREMENTS

Sandra Faber initiated in 1972 a long-term spectroscopic project that was aimed at the study of the stellar populations in globular clusters and early-type galaxies. For this purpose the IMAGE DISSECTOR SCANNER (IDS) on the Shane 3m telescope of Lick Observatory was used. Faber and her collaborators observed a large number of galaxies, and stars of all types, field and cluster giants, subgiants and dwarfs in the spectral range from $\sim$ 4000 Åto $\sim$ 6200 Åwith a $\sim$ 8.6 ÅFWHM resolution. The Lick group defined and measured 21 indices to monitor the strength of spectral features in stars and galaxies (see Gonzalez 1993).

Spectral indices were defined in Faber et al. (1985) and reprinted in Binney and Merrifield (1998)[8]. Note, however, that since the early papers of the Lick group the wavelength accuracy has improved and new definitions are now valid. All of our calculations were based on the updated version of the indices table taken from the WWW site of G. Worthey[9].

In order to define an index one should define a central band of width Δ_0 and two side bands. The "side-band level" I_s is defined to be the mean intensity over the two side bands, and the intensity of the central feature I_c is the mean intensity in the central band. There are two groups of indices: one is measured as an equivalent width (for example iron indices):

$$w = \left(1 - \frac{I_c}{I_s}\right) \Delta_0$$

and the other is measured in magnitudes (for example Mg_2):

$$w = -2.5 \log\left(1 - \frac{I_c}{I_s}\right).$$

[8]Note the misprint in the book of Binney and Merrifield, for the Mg_2 index the central band should read: 515.600–519.725 nm instead of 515.600–519.750 nm, cf. Faber et al. (1985).

[9]`http://astro.wsu.edu/worthey/html/index.table.html`.

The spectra that we had were centered to be near the Mg_2 feature ($\sim$ 5150 Å). For the comparison with the models we will use Mg_2 and iron indices and their definitions are given in TABLE 4-1 (for a full list of definitions see WWW site of G. Worthey).

TABLE 4-1

DEFINITIONS OF INDICES USED IN THIS BOOK

Name	Index band		blue continuum		red continuum		Units
Mg_2	5154.125	5196.625	4895.125	4957.625	5301.125	5366.125	mag
Fe5270	5245.650	5285.650	5233.150	5248.150	5285.650	5318.150	ang
Fe5335	5312.125	5352.125	5304.625	5315.875	5353.375	5363.375	ang

NOTE: Units: "mag" refers to the index measured in magnitudes, and "ang" refers to the index measure in Angstroems.

For the purpose of measuring of the line strength indices we have written a set of routines in `FORTRAN` that we embedded in the `MIDAS` scripts in order to extract indices from the long-slit spectra. We relied on the `AVINT` routine by Davis and Rabinowitz (1984) that was included in the SLATEC library of programs[10]. This routine, based on overlapping parabolas, calculates the integral

$$\int_a^b f(x)dx$$

when $f(x)$ is tabulated in nonequally spaced abscissas – this is the most general case: in our calculations abscissas were equally spaced. We tested the routine using some elementary functions and also some standard spectra obtained from the site of G. Worthey and the agreement was excellent with the elementary functions and very good in the case of the Worthey's spectra.

We performed two tests to verify the accuracy of our spectral indices calculations. The first test is an example (p. 61) from Chapter 2.3 of Davis and Rabinowitz (1984): integrals of four functions given in TABLE 4-2 over [0,1] are calculated using the `AVINT` algorithm. The functions are calculated at $x = 0.00$, 0.10, 0.15, 0.20, 0.23, 0.25, 0.30, 0.40, 0.45, 0.48, 0.53, 0.62, 0.78, 0.82, 0.89, 0.92 and 1.00. The agreement with both theoretical and values calculated by Davis and Rabinowitz is extremely good. In the second test we calculated the aforementioned three indices for all seven IDS stars whose spectra and indices are given on the WWW site of G. Worthey (see TABLE 4-3). The agreement, is typically very good, although we note that in the case of a very low Mg_2 (HYA VB 95) and a very low Fe5335 (HYA VB 103_R) there are some discrepancies. We also note the discrepancy with the Worthey's calculations in the case of HR 6770 (in iron indices). As an additional test we will compare our results with the results of other authors when such data exist for the internal parts of early-type galaxies.

[10] `http://www.netlib.org/slatec/src`.

TABLE 4-2

COMPARISON OF CALCULATIONS OF INTEGRALS OF ANALYTIC FUNCTIONS

function	exact	this book	Davis and Rabinowitz
$x^{1/2}$	0.6666 6667	0.6634 2467	0.6634 2607
$x^{1/4}$	0.8000 0000	0.7883 1637	0.7883 1842
$x^{1/8}$	0.8888 8889	0.8676 3126	0.8676 3089
$x^{1/16}$	0.9411 7647	0.9126 5356	0.9126 5294

TABLE 4-3

COMPARISON WITH THE WORTHEY'S CALCULATIONS

Name	calc.	Mg_2	Fe5270	Fe5335
HYA VB 111	(W)	0.0294	1.2326	0.5729
HYA VB 111	(S)	0.0296	1.2866	0.6132
HYA VB 112	(W)	0.0368	0.9764	0.7577
HYA VB 112	(S)	0.0367	0.9562	0.7827
HYA VB 103_R	(W)	0.0264	2.3431	-0.1757
HYA VB 103_R	(S)	0.0267	2.2108	-0.0804
HYA VB 103_{R+L}	(W)	0.0298	1.3770	0.3774
HYA VB 103_{R+L}	(S)	0.0300	1.3709	0.4655
HYA VB 95	(W)	0.0181	0.3502	0.2472
HYA VB 95	(S)	-0.0082	0.3585	0.5283
HR 6770	(W)	0.1490	3.4392	2.5624
HR 6770	(S)	0.1371	2.4596	0.8761
HR 7429	(W)	0.3599	3.6879	3.5034
HR 7429	(S)	0.3613	3.8625	3.5029

NOTE: Letter "W" refers to the calculations of Worthey, and letter "S" refers to the results obtained using AVINT routine in this book. Note that in the case of HYA VB 103 two different spectra were given.

The routines that we have written were used on the deredshifted spectra, and measurements were standardized to a Lick system. Two steps were necessary to transform the spectra into the Lick system (see for example Halliday 1998):

1. correction to zero velocity dispersion, and
2. correction to the Lick IDS spectral resolution ($\sim$ 8.2Åat $\sim$ 5200 Å).

The correction for the effects of the velocity dispersion included the following steps: different stellar spectra were smoothed by Gaussians of various widths that correspond to measurements of $\sigma = 0 - 400$ km s^{-1} in the intervals of 35 km s^{-1}. The smoothing was done using `IRAF` task `gauss`. Then a correction factor is calculated by a comparison of the each smoothed spectrum with a measurement for the original unsmoothed stellar spectrum. In the case of the molecular index Mg_2 the correction factor is defined as a difference between the measurement of the original unbrodened stellar spectrum and that of the spectrum broadened to a particular velocity dispersion:

$$C(\sigma) = I_{\rm orig} - I_\sigma.$$

For the atomic indices (Fe5270 (often abbreviated to Fe1), Fe5335 (often abbreviated to Fe2))[11] correction factor is defined as the ratio between the original and the smoothed line indices:

$$C(\sigma) = I_{\rm orig}/I_\sigma.$$

Because the bands are wide, the corrections for Mg_2 are very small, so we do not apply them. On the contrary, the corrections for the iron indices can be significant, and we present in Fig. (4.1) the calculated values of the corrections for the iron indices in the case of IC 3370.

The second correction is related to the different spectral resolution of our observations and those of the Lick IDS. The spectra of the calibration lamps (for example Helium-Argon) were inspected to measure the instrumental resolution and then the galaxy frames were broadened so as to match the Lick spectral resolution (~ 8.2Åat ~ 5200 Å).

Following the paper of Carollo, Danziger and Buson (1993) the estimate of the errors for the indices was calculated using:

$$\epsilon_i = \frac{\sqrt{\rm OBJ + 2 \times DK + \left(1 + \frac{1}{N_{\rm rows}}\right) \times SKY + ron^2}}{\rm OBJ},$$

where OBJ is the total count in the object, SKY is the total count in the sky, DK is the total count in dark, and ron is the read-out noise of the CCD. The term $\frac{1}{N_{\rm rows}}$ comes from a subtraction of a sky averaged on $N_{\rm rows}(=30)$ rows from the galactic spectra. One can now define the error on the line-strength index:

$$\epsilon = {\rm coeff} \times \sqrt{\sum_{i=c1,c2,b} \epsilon_i^2},$$

where $c1$, $c2$ and b indicate respectively the two continua and the index band. The coefficient is equal to $1.08(= -2.5\log e)$ for the Mg_2 index (and is mentioned here only for the sake of completeness, because the Mg_2 correction was not applied), and to $\frac{(C_{\rm feat} \times W_{\rm pix})}{C_{\rm cont}}$ for the iron indices ($C_{\rm feat}$ is the total count in the feature, $W_{\rm pix}$ is the pixel width in Å, and $C_{\rm cont}$ is the average continuum).

[11] As usual, one defines $< {\rm Fe} >= \frac{\rm Fe5270+Fe5335}{2}$.

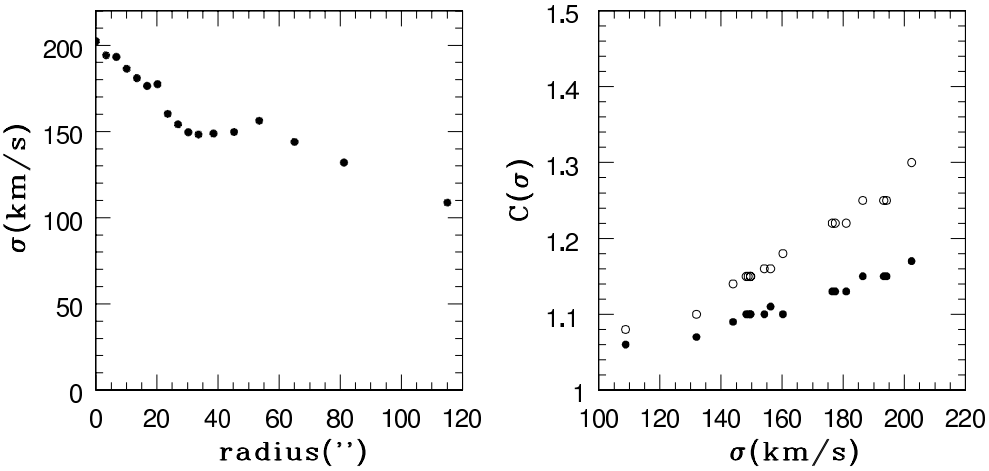

Figure 4.1: The corrections for the iron indices for IC 3370. *Left*: Dependence of the velocity dispersion on the radius. *Right*: Values of the corrections of the iron indices: black circles denote Fe5270 and open circles denote Fe5335.

In the case of Sample 2 (Fornax galaxies) we had spectra of three template stars: HD4188, HD26846 and HD4128. Since for HD4188 the calculated Mg_2 index was negative, for HD26846 Fe5335 was negative and for HD4128 both Mg_2 and Fe5335 were negative, no reliable corrections could have been obtained and therefore for this Sample we do not present result of calculations of indices. The stellar populations of early-type galaxies in the Fornax cluster are given in detail in Kuntschner (2000).

The results which we obtained are in good agreement with these of Carollo, Danziger and Buson (1993) for IC 1459 (Mg_2 is in an excellent agreement, Fe5270 that we obtained is somewhat higher ~ 3.8 in the center whereas they obtained ~ 3.4) and IC 3370 (Mg_2 in an excellent agreement, iron indices for IC 3370 are not given in Carollo, Danziger and Buson 1993). For NGC 3379 both Mg_2 and iron indices that we obtained are in a very good agreement with these obtained by Kuntschner et al. (2001). Finally, for NGC 4105 the central value for Mg_2 that we obtained (~ 0.26) is a bit lower than that given by Davies et al. (1987) (~ 0.3). Iron indices were not compared for NGC 4105 because they are not given in Davis et al. (1987).

4.2. MODELLING

The modelling of the indices in this book was based on the Pipino and Matteucci (2003) paper and the models were calculated by A. Pipino. Here, we briefly present the basics of the model.

This is a multi-zone photo-chemical evolution model for elliptical galaxies that takes into account detailed nucleosynthetic yields, feedback from supernovae and an initial infall episode. Its basic prediction is that for galaxies with higher mass the infall and the star formation timescales are shorter: the most massive objects are older than the less massive ones (the larger galaxies stop forming stars at earlier times). According

to this scenario, the galaxies are created outside-in: the outermost regions accrete gas, form stars and develop a galactic wind very quickly, whereas in the central core the star formation can last up to ~ 1.3 Gyr.

This monolithic collapse model in which ellipticals formed relatively quickly and at high redshifts is opposed to the hierarchical clustering model according to which ellipticals form over a large redshift interval. An evidence in favour of the monolithic collapse (for a full list see e.g. Calura 2004) is the increase in the strength of the metal metal absorption lines (Mass-metallicity relation) with the velocity dispersion (see Fig. (4.9)). The sample of five galaxies (especially galaxies with different peculiarities, such as counterrotating core, isophotal twisting, possible lack of dark matter) is of course too small to draw statistically significant conclusions, but the trend of increasing strength with the velocity dispersion is obvious.

Several different models were run with a calibration derived in the Pipino and Matteucci (2003) paper that uses calibration relations of Worthey (1994). This calibration is derived for a 12 Gyr old simple stellar population (SSP) with solar abundance ratios and [Fe/H]> -0.5 and the relations are:

$$\mathrm{Mg_2} = 0.187 \cdot [\mathrm{Fe/H}] + 0.263,$$

$$< \mathrm{Fe} >= 1.74 \cdot [\mathrm{Fe/H}] + 2.97,$$

where notation [Fe/H] is defined to be:

$$[\mathrm{Fe/H}] \equiv \log_{10}\left(\frac{\mathrm{n(Fe)}}{\mathrm{n(H)}}\right)_{\mathrm{galaxy}} - \log_{10}\left(\frac{\mathrm{n(Fe)}}{\mathrm{n(H)}}\right)_{\odot},$$

where n(Fe)/n(H) is the abundance (by number) of iron relative to hydrogen.

There exists a significantly different calibration based on the synthetic indices by Tantalo et al. (1998). At present the quality of fit with this calibration is not good, especially for the $\mathrm{Mg_2}$ index where unphysical results occur. One suspects that this calibration needs to be revised.

Results of different runs are given in Figs. (4.10)–(4.13). In several runs a dark matter halo was included for which the profile was taken from Bertin et al. (1992). The assumption that was made in this case is that the total mass of the dark component is ten times larger than that of the luminous one. Dark halo has a scale radius of 10 R_e. Because of the fact that no significant amount of dark matter was found in this book from the dynamical modelling, several runs were made without the dark matter component. Physically, the lack of the dark matter means that the galactic wind in a given galaxy stars earlier at a given radial distance from the center but does not affect the chemical evolution. These runs seem to provide a better agreement with the observed data (see below).

An important conclusion from the paper of Pipino and Matteucci (2003) is that the variations of $\mathrm{Mg_2}$ depend on the radial gradients in [Fe/H] and [Mg/Fe] (see Fig. 7 in their paper), while the predicted <Fe> gradient reflects instead the variation of the real abundance, [Fe/H], as a function of galactic radius (see their Fig. 8). Therefore, one can conclude that the modelling of the iron indices is more reliable in establishing the real variation of the metallicity with the radius.

The results of the modelling are as follows. Two cases for which we had the spectra that extend out to large radial distances are especially difficult ones: IC 1459 (with a counterrotating core) and IC 3370 (with the large isophotal twisting). The calibration based on Worthey (1994) provided various degrees of fit to the observed data. Several tests were done for each galaxy, and only the best fits to the observed values were plotted. The masses that were used are given in captions of Figs. (4.10)–(4.13). Different input parameters are given in Pipino and Matteucci (2003): the best model "IIb" was used. For IC 3370 (see Fig. (4.10)) the model with dark matter can provide a good fit for the iron index, but fails for Mg_2, whereas the test done without the dark matter provides better agreement for Mg_2 throughout the whole galaxy. None of the computed models could provide a good fit for Mg_2 index of IC 1459 (see Fig. (4.11)). The model which is devoid of dark matter provides better agreement in the outer parts of IC 1459 (beyond $1R_e$). The observational results for NGC 3379 (see Fig. (4.12)) unfortunately do not extend out to a large radial distance and firm conclusions cannot be drawn. Finally, in the case of NGC 4105 (see Fig. (4.13)) the models provide an excellent fit to the Mg_2 index (again for the test done without the dark matter); none of the models run could fit the iron index.

As we have shown, the approach of Pipino and Matteucci can provide satisfactory fits in several difficult cases with the assumption of the absence of the dark halo in the given galaxy. One may argue that the changes of different input parameters to the model could improve the fit for a given galaxy without depriving it of its dark matter content. Several such tests were run: (i) the efficiency of star formation (ν) was varied but without a significant improvement of the fit (in the case of IC 3370, for example), (ii) the infall timescale (τ) was varied but again without a significant improvement of the fit (again for IC 3370). Only the exclusion of the dark matter halo could improve the fit to the data. It is probably premature to draw a conclusion about the dark matter content in early-type galaxies based on this kind of modelling (certainly, more tests are needed on a larger sample), but this approach in combination with the dynamical analyses could provide some insights into the chemo-dynamical properties and history of these galaxies.

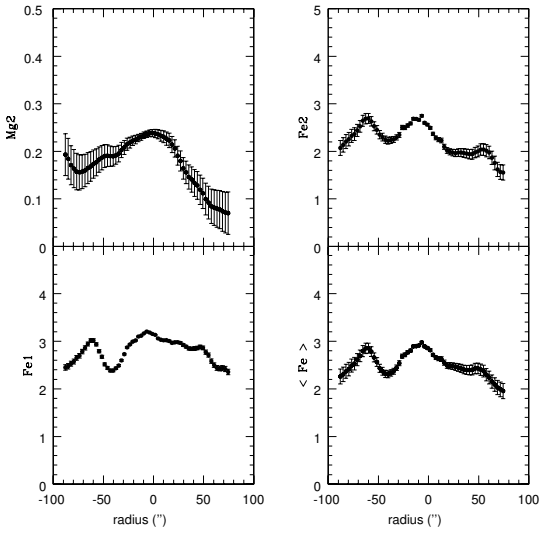

Figure 4.2: Mg_2 and iron indices (Fe5270, Fe5335, and <Fe>) for the major axis of IC 3370.

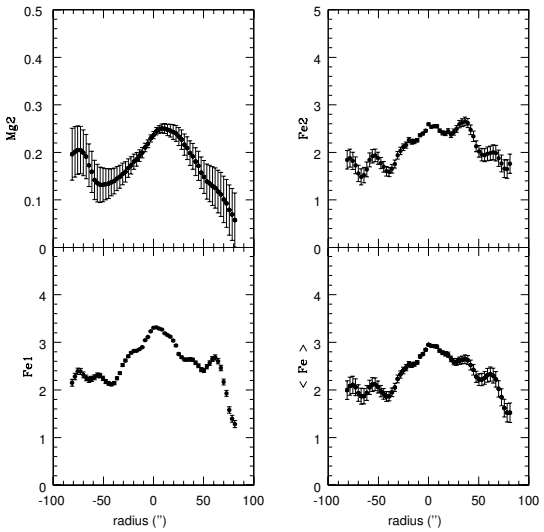

Figure 4.3: Mg_2 and iron indices (Fe5270, Fe5335, and <Fe>) for the minor axis of IC 3370.

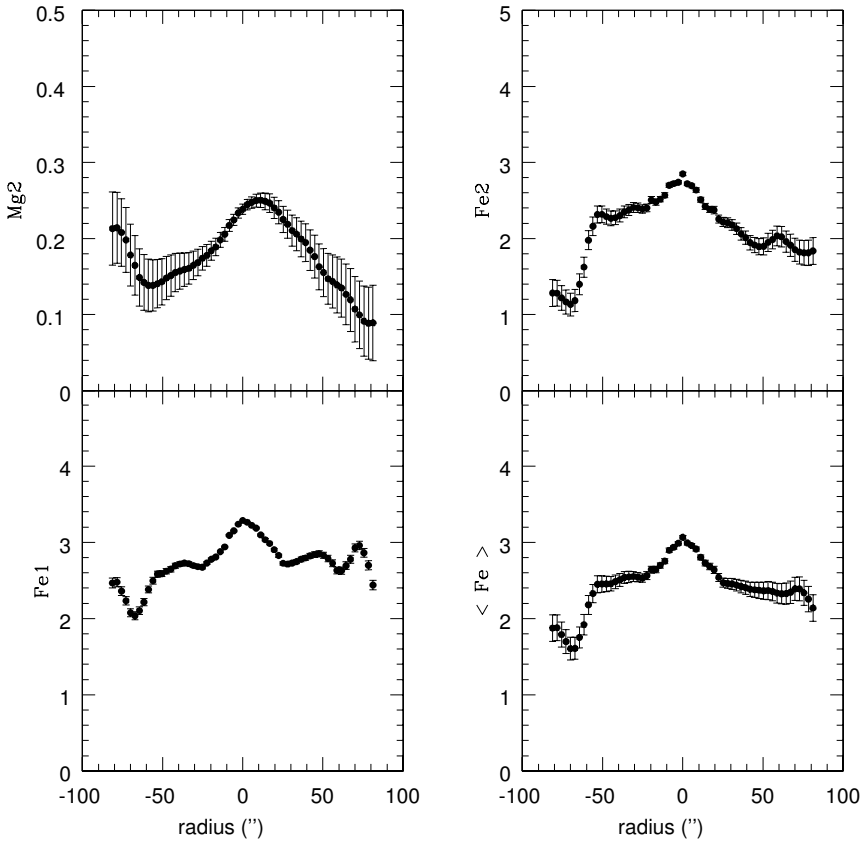

Figure 4.4: Mg_2 and iron indices (Fe5270, Fe5335, and <Fe>) for the intermediate axis of IC 3370.

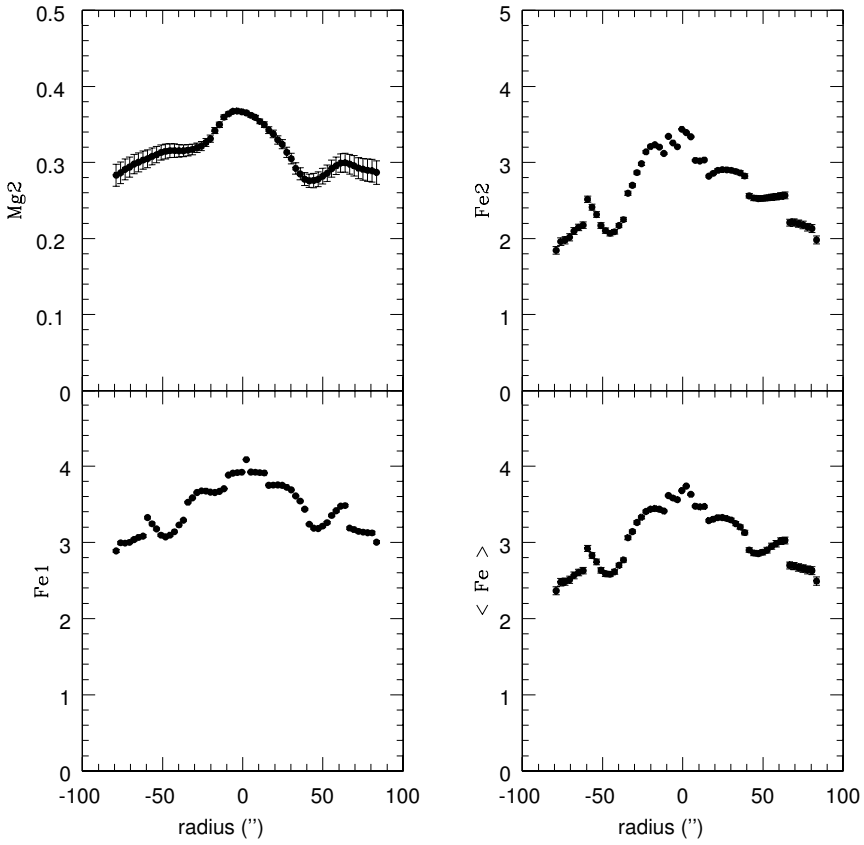

Figure 4.5: Mg_2 and iron indices (Fe5270, Fe5335, and <Fe>) for the major axis of IC 1459.

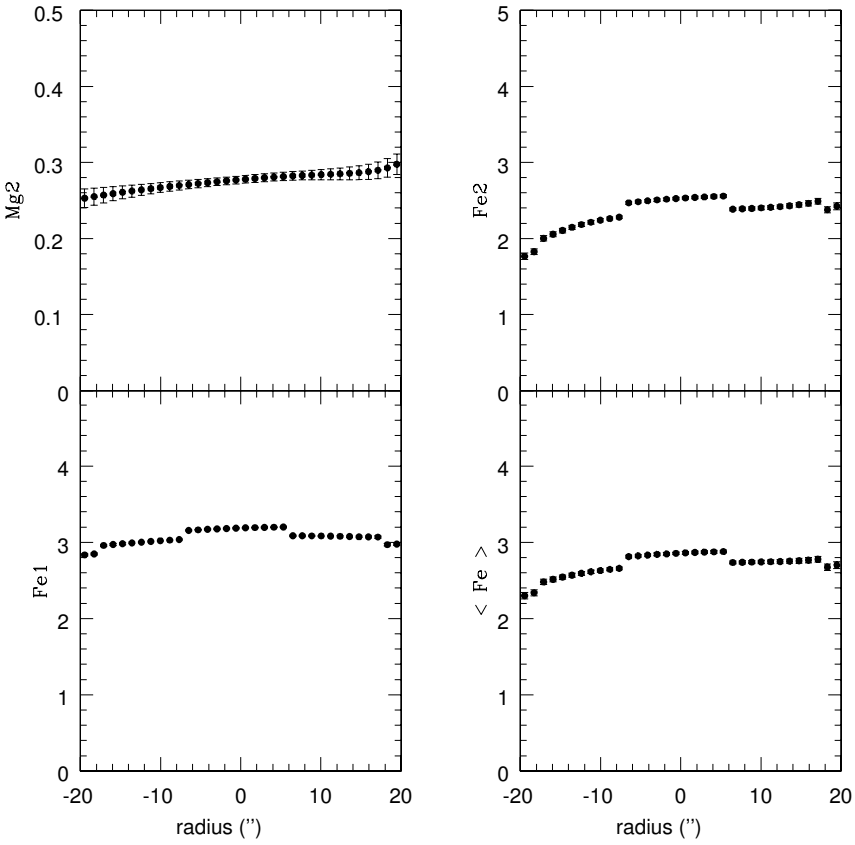

Figure 4.6: Mg_2 and iron indices (Fe5270, Fe5335, and <Fe>) for the major axis of NGC 3379.

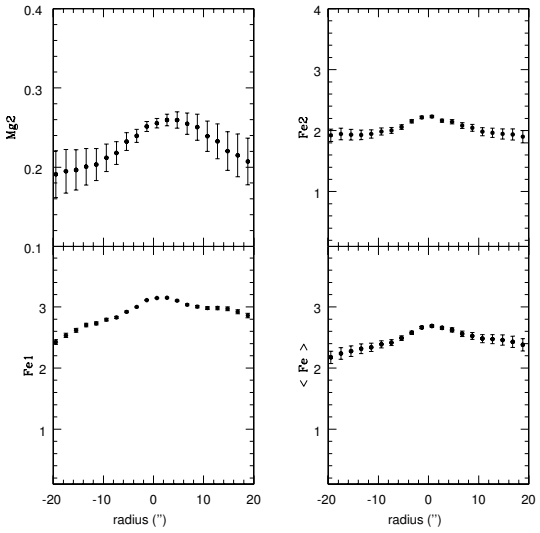

Figure 4.7: Mg_2 and iron indices (Fe5270, Fe5335, and <Fe>) for the major axis of NGC 4105.

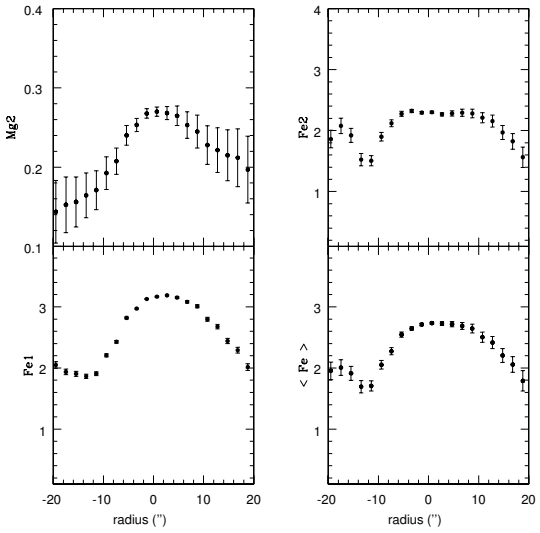

Figure 4.8: Mg_2 and iron indices (Fe5270, Fe5335, and <Fe>) for the minor axis of NGC 4105.

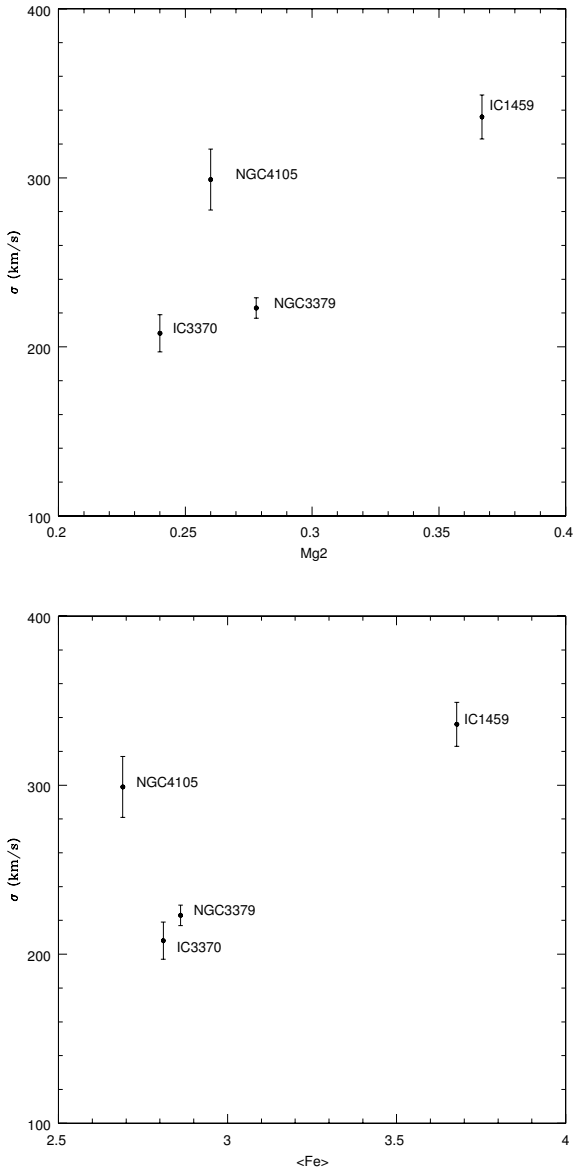

Figure 4.9: Mass-metallicity relation for the galaxies in our samples. *Top*: Mg_2 index (in magnitudes) vs. velocity dispersion (in km s^{-1}). *Bottom*: <Fe> index (in Å) vs. velocity dispersion (in km s^{-1}).

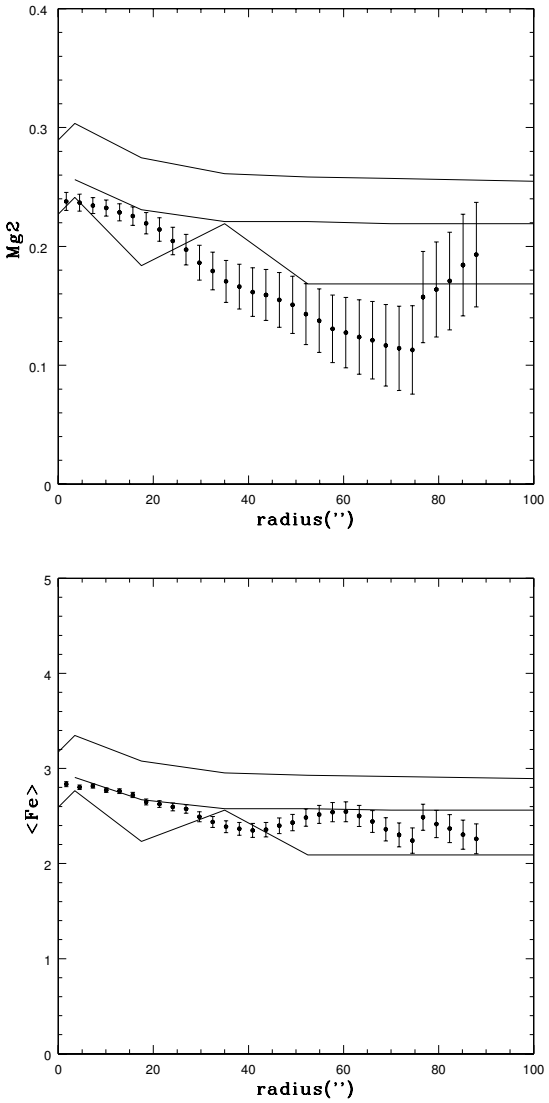

Figure 4.10: Modelling of Mg_2 index (above) and <Fe> (below) for IC 3370 using model of Pipino and Matteucci (2003). Thin solid lines are for the case for which the total mass is $1.15 \times 10^{11} M_{\odot}$, with dark matter, thicker solid lines are for the case for which the total mass is $4.00 \times 10^{11} M_{\odot}$, with dark matter, and finally, the thickest solid lines are for the case for which the total mass is $1.15 \times 10^{11} M_{\odot}$ and *without* dark matter.

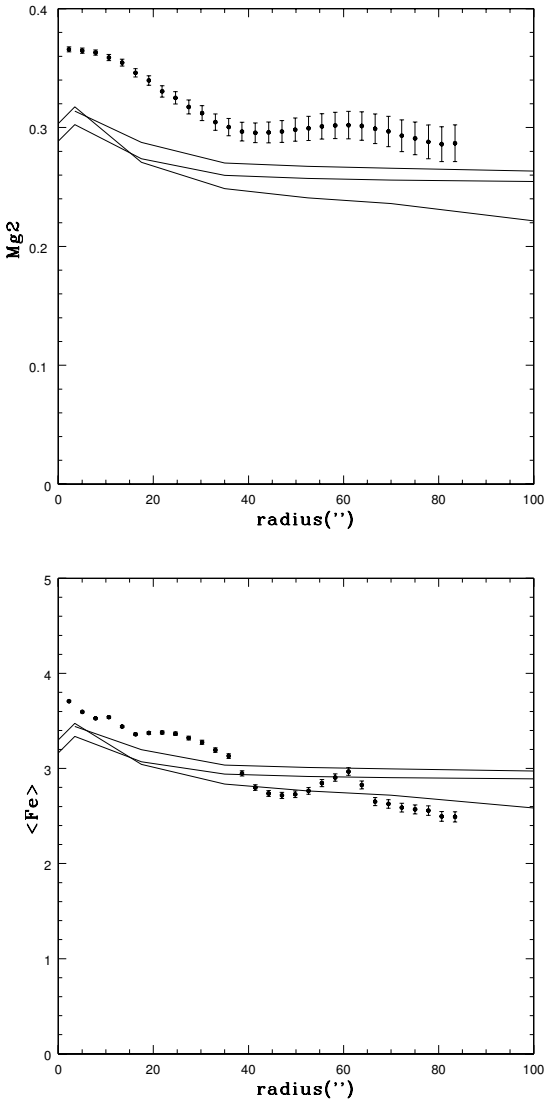

Figure 4.11: Modelling of Mg_2 index (above) and <Fe> (below) for IC 1459 using model of Pipino and Matteucci (2003). Thin solid lines are for the case for which the total mass is $6.00 \times 10^{11} M_{\odot}$, with dark matter, thicker solid lines are for the case for which the total mass is $2.38 \times 10^{11} M_{\odot}$, with dark matter, and finally, the thickest solid lines are for the case for which the total mass is $6.00 \times 10^{11} M_{\odot}$ and *without* dark matter.

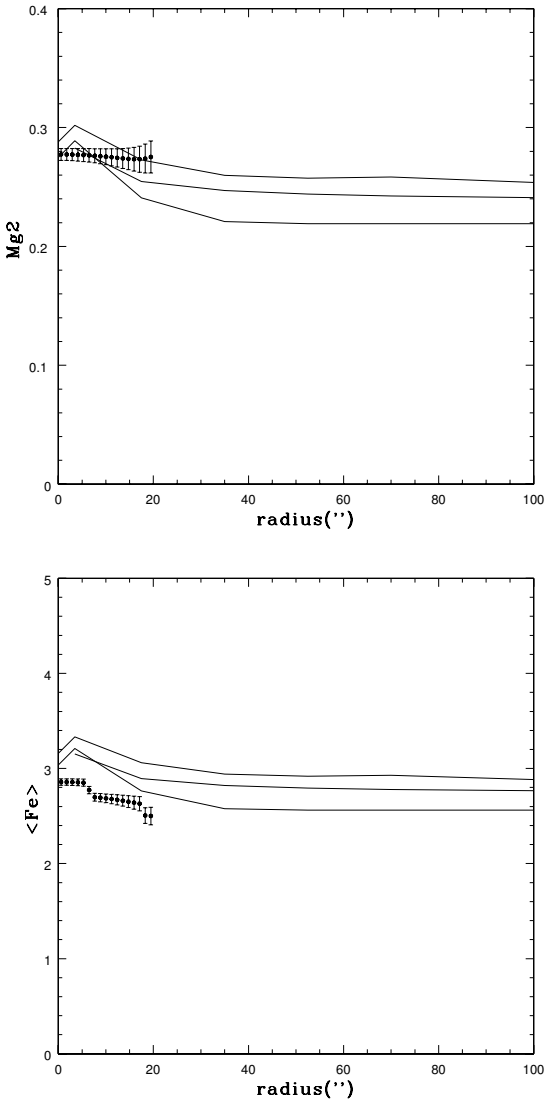

Figure 4.12: Modelling of Mg_2 index (above) and <Fe> (below) for NGC 3379 using model of Pipino and Matteucci (2003). Thin solid lines are for the case for which the total mass is $1.00 \times 10^{11} M_{\odot}$, with dark matter, thicker solid lines are for the case for which the total mass is $1.82 \times 10^{11} M_{\odot}$, with dark matter, and finally, the thickest solid lines are for the case for which the total mass is $1.00 \times 10^{11} M_{\odot}$ and *without* dark matter.

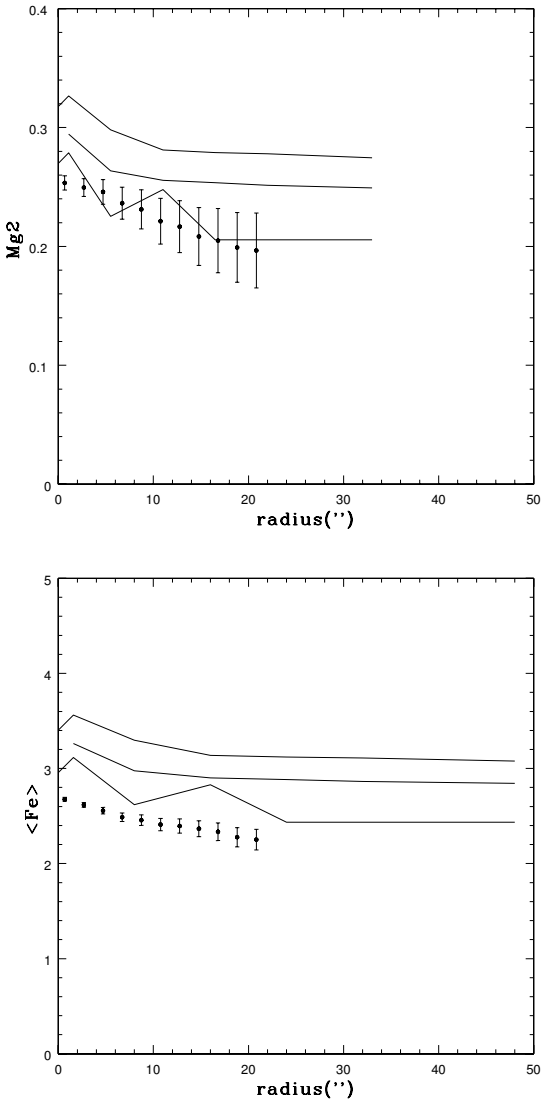

Figure 4.13: Modelling of Mg_2 index (above) and <Fe> (below) for NGC 4105 using model of Pipino and Matteucci (2003). Thin solid lines are for the case for which the total mass is $5.00 \times 10^{10} M_{\odot}$, with dark matter, thicker solid lines are for the case for which the total mass is $2.00 \times 10^{11} M_{\odot}$, with dark matter, and finally, the thickest solid lines are for the case for which the total mass is $5.00 \times 10^{10} M_{\odot}$ and *without* dark matter.

Chapter 5
MASS ESTIMATES BASED ON PLANETARY NEBULAE AND GLOBULAR CLUSTERS

As already mentioned in Introduction (Sec. I.2b) planetary nebulae (PNe) and globular clusters (GCs) represent very important tracers of the total mass of a given elliptical galaxy at large radii from the center. The case of the galaxy NGC 3379 already mentioned in the previous Chapters is an interesting one: integrated stellar spectra interior to $\sim 1.5R_e$ suggest the lack of dark matter there. Ciardullo, Jacoby and Dejonghe (1993) used 29 PNe to infer that there was no dark matter within $\sim 3.5R_e$ (R_e was taken to be ~ 55 arcsec). Ten years later a paper by Romanowsky et al. (2003) attracted a lot of attention in the scientific community interested in dark matter because it claimed that in the sample studied which consisted of three early–type galaxies (NGC 821 out to $\sim 3.5R_e$, NGC 3379 out to $\sim 5.5R_e$[12] and NGC 4494 out to $\sim 3R_e$) there was no need for dark matter because of declining trend in the velocity dispersion of the observed galaxies. Very recently, Pierce et al. (2006) have obtained Gemini/GMOS spectra for 22 GCs associated with NGC 3379 and found that, in contrast to the results of Romanowsky et al. (2003), their results suggest a constant value of the velocity dispersion (out to ~ 200 arcsec) which imply a normal–sized dark matter halo. They do note, however, that due to possible anisotropies (see below) they could not rigorously determine the dark halo mass. The result by Pierce et al. (2006) is the confirmation of the trend in the velocity dispersion obtained using solving the Jeans equation based on the X–ray observations in Chapter 3 (see also Samurović and Danziger 2005). Throughout this section it is assumed, as previously, the following value of the Hubble constant: $h_0 = 0.70$.

In this Chapter some basic concepts regarding calculation of the basic quantities (such as velocity dispersion and total mass) will be given. Later in the Chapter this formalism will be applied to two large ellipticals: NGC 1399 (central galaxy of the Fornax galaxy cluster, already discussed using integrated stellar spectra in Chapters 2 and 3) and NGC 5128 (also known as the radio source Centaurus A). Since both of these galaxies possess an X–ray halo, the comparison with the results based on the X–ray methodology will also be given. In the case of NGC 5128, the Jeans modelling of the velocity dispersion will also be presented. The results from this Chapter are

[12]Note that Romanowsky et al. used $R_e = 35$ arcsec; the last observed point is thus observed at $\sim 3.5R_e$ which is the same distance found in Ciardullo et al. (1993). It is also worth noting that Romanowsky et al. observed 109 PNe.

given in Samurović and Danziger (2006, for NGC 1399) and Samurović (2006, for NGC 5128).

5.1. MATHEMATICAL BACKGROUND

5.1.1. VELOCITY DISPERSION

The most important quantity that is calculated from both GCs and PNe radial velocity observations is the velocity dispersion. Frequently authors do not explicitly state how they obtained their estimates of this quantity, so one is led to the conclusion that the adopted velocity distribution is purely Gaussian or that the authors have used a simple statistical definition of the standard deviation to calculate it. For example, in a recent series of papers Dirsch et al. (2003), Richtler et al. (2004) and Dirsch et al. (2004) analyzed the GC system of the galaxy NGC 1399, the central galaxy of the Fornax cluster. They used 468 radial velocities assuming a pure Gaussian distribution to conclude that the velocity dispersion of this galaxy remains approximately constant between 2 and 9 arcmin, corresponding to 12 kpc to 54 kpc, which corresponds to approximately 2.86 and 12.86 R_e, under the assumption that one effective radius is 42 arcsec. This value of the effective radius comes from the RC3 catalog (de Vaucouleurs et al. (1991)) and we verified it using the growth curve of NGC 1399.

When dealing with the velocities related to the GCs and/or PNe one usually assumes a pure Gaussian velocity distribution: for example, Grillmair et al. (1994) analyzed 47 GCs within 9 arcmin in NGC 1399 using the methodology developed by Morrison et al. (1990) to calculate a velocity dispersion ($\sigma = 388 \pm 54$ km s^{-1}) and a mass-to-light ratio in the B-band ($M/L_B = 79 \pm 20$, interior to 9 arcmin). This technique uses a maximum likelihood approach and, Morrison et al. state that since this technique is model–dependent slightly non–Gaussian distributions can have significant effects on the performance of estimators resulting in the possibility that this model dependence may be important and should be recognized. Richtler et al. (2004) used the maximum likelihood dispersion estimator given in Pryor and Meylan (1993). The Gaussian estimator can be expressed as:

$$f_G(v_i) = \frac{1}{\sqrt{2\pi(\sigma^2 + \delta_i^2)}} \exp\left(-\frac{(v_i - \overline{v})^2}{2(\sigma^2 + \delta_i^2)}\right), \tag{5.1}$$

where σ is the velocity dispersion, and it is assumed that each velocity v_i (the GC velocity from which the systemic velocity, $v_{\rm sys}$, is subtracted — in the case of NGC 1399 $v_{\rm sys}$ is fixed to 1441 km s^{-1} and in the case of NGC 5128 is fixed to 541 km s^{-1}) is drawn from the normal, Gaussian, distribution. $\overline{v}$ is the mean velocity and δ_i is a known measurement uncertainty of v_i.

The maximum likelihood function is then given as

$$L_{\rm G} = \prod_i \frac{1}{\sqrt{2\pi(\sigma^2 + \delta_i^2)}} \exp\left(-\frac{(v_i - \overline{v})^2}{2(\sigma^2 + \delta_i^2)}\right). \tag{5.2}$$

Taking the logarithm of Eq. (5.2) and finding

$$\frac{\partial \ln L_{\rm G}}{\partial \sigma} = 0, \tag{5.3}$$

one can calculate the velocity dispersion using an iteration procedure as:

$$\sum_i \frac{(v_i - \overline{v})^2}{(\sigma^2 + \delta_i^2)^2} = \sum_i \frac{1}{\sigma^2 + \delta_i^2}, \tag{5.4}$$

where the sum includes all the velocities in a given bin. In all our calculations below we always have $\overline{v} = 0$. Using expressions given in Pryor and Meylan (1993) one can then calculate uncertainty of the resulting velocity dispersion.

5.1.2. MASS ESTIMATES

Evans et al. (2003) introduced a new "tracer mass estimator" which provides an estimate of the enclosed mass from the projected positions and line–of–sight velocities of a given tracer population (such as GCs and PNe). One can assume that the tracer population is spherically symmetric and has a number density which obeys a power law:

$$\rho(r) = \rho_0 \left(\frac{a}{r}\right)^\gamma \tag{5.5}$$

where a is constant, and radius r ranges between $r_{\rm in}$ and $r_{\rm out}$, inner and outer points of the given population (in this case GCs and PNe), respectively. The parameter γ can be determined using the surface density of the tracer population between $r_{\rm in}$ and $r_{\rm out}$. Evans et al. provide the following formula for the mass enclosed within $r_{\rm in}$ and $r_{\rm out}$ for the isotropic ("iso" in the formulas below) case ("los" stands for line–of–sight):

$$M = \frac{C_{\rm iso}}{GN} \sum_i v_{{\rm los}\,i}^2 R_i, \tag{5.6}$$

where constant $C_{\rm iso}$ is given as:

$$C_{\rm iso} = \frac{4(\alpha+\gamma)}{\pi} \frac{4-\alpha-\gamma}{3-\gamma} \frac{1-(r_{\rm in}/r_{\rm out})^{3-\gamma}}{1-(r_{\rm in}/r_{\rm out})^{4-\alpha-\gamma}}. \tag{5.7}$$

The parameter α for an isothermal potential is equal to zero and this value was taken in all the calculations which we performed below. This is a reasonable assumption (see Evans et al. 2003 for details). In this book we dealt with the isotropic case, because of the hint of the small departures from the Gaussian distribution (as given by the s_3 and s_4 parameters, see below). The isothermal potential predicts a quasi–constant velocity dispersion profile and this is applicable in the cases of NGC 1399 and NGC 5128 (see below). Note that the formalism of Evans et al. (2003) permits one to perform calculations related to an anisotropic case: in such a case the coefficient $C_{\rm iso}$ will be modified. These authors however strongly recommend the usage of the isotropic case "unless there are compelling reasons to the contrary (e.g., a highly flattened system supported by an anisotropic velocity dispersion)".

5.2. NGC 1399

5.2.1. KINEMATICS OF GCs OF NGC 1399

The basic data related to the early–type galaxy NGC 1399 were given in Chapter 1 and this Section we only presented the data and analysis related to its GCs. The already obtained results from the X–rays methodology (from Chapter 3) will be used for comparison.

The globular cluster system of NGC 1399 was presented in Dirsch et al. (2003, wide–field photometry), Richtler et al. (2004, kinematics) and Dirsch et al. (2004, spectroscopy and database). In our analysis, we use the set of 445 GCs for which the estimated uncertainties are $\delta_i < 60$ km s^{-1}. This selection enabled us to have a sufficiently large number of clusters in each chosen radial bin and it was also useful in the construction of the bins given in TABLE 5-2, which contain approximately 50 clusters each. We took as a center of NGC 1399 the coordinates (J2000.0) given in the NED database: $\alpha = 03^{\rm h}38^{\rm m}29\overset{\rm s}{.}08$ and $\delta = -35°27'02\overset{''}{.}7$. In Fig. (5.1) we present the comparison of our results (open circles) with those of Richtler et al. (2004) (filled circles; the second column of their Table 2, no selection was performed). In this case a pure Gaussian distribution is assumed and the agreement is very good. In Fig. (5.2) we present the comparison of our results (open symbols) with those of Richtler et al. (2004) (filled symbols) for red ($C-R > 1.6$) and blue ($C-R < 1.6$) clusters using the Richtler et al. bins (see also TABLE 5-1 (where the data for Washington C and Kron–Cousins R are taken from Dirsch et al. 2004). Our total number of red and blue clusters used in this comparison is 412: we have taken into account all the clusters for which we had colours and for which $\delta_i < 60$ km s^{-1}. A pure Gaussian distribution is assumed. If we place all GCs of a given colour in one bin our results are in very good agreement with those of Richtler et al. : for red GCs we found $\sigma_{\rm red} = 259 \pm 11$ km s^{-1} and they found $\sigma_{\rm red} = 255 \pm 13$ km s^{-1}, and for blue GCs we found $\sigma_{\rm blue} = 295 \pm 12$ km s^{-1} and they found $\sigma_{\rm blue} = 291 \pm 14$ km s^{-1}. However, there are discrepancies related to the individual bins for the velocity dispersion values of Richtler et al. which we may attribute to our selection criterion: we took only GCs for which $\delta_i < 60$ km s^{-1}.

In TABLE 5-1 we list our results for the projected velocity dispersion in the case of the pure Gaussian velocity distribution (with $\delta_i < 60$ km s^{-1}) for the total sample of clusters. In this Table we also give our results for blue and red clusters. We have used the bins defined in the Richtler et al. (2004) paper: as can be seen from Fig. (5.3) with these bins the velocity dispersion remains approximately constant throughout the galaxy. Errors were calculated using the lengthy expressions of Pryor and Meylan (1993). With Richtler et al. binning of the data there exists a significant overlap of the bins: that is, there are many of the same clusters present in two different bins. Therefore, we bin the data taking approximately 50 GCs in each separate bin (see TABLE 5-2): using this approach and assuming a Gaussian distribution we see a decreasing trend in the velocity dispersion between ~ 3 and ~ 7 arcmin (see also Fig. (5.4); more details are given below in this Section). We checked the projected velocity dispersion for the cases of departure from a pure Gaussian velocity distribution using s_3 and s_4 parameters presented in TABLE 5-2 and we did not find

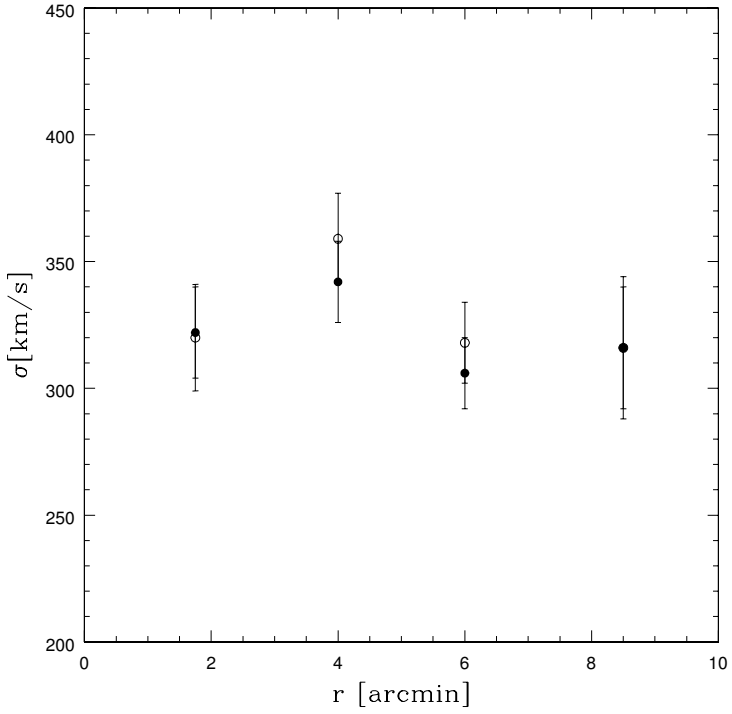

Figure 5.1: Comparison between our calculation of the velocity dispersion of NGC 1399 (open circles) and calculations of Richtler et al. (2004) (filled circles), when a pure Gaussian distribution is assumed. Note that for the outermost point the two values overlap.

large differences: the calculated values thus obtained are equal to the ones obtained using a pure Gaussian within the error bars.

For example, using large (Richtler et al.) bins the last measured point was calculated for *all* GCs beyond 6.5 arcmin and some clusters (73 clusters between 6.5 and 7.5 arcmin) were already taken into account in a preceding bin. For all the given bins we calculated the velocity dispersion and the skewness and kurtosis parameters, s_3 and s_4, using standard definitions and the NAG routine `G01AAF` (see TABLE 5-2 in which we present the results based on the maximum likelihood function and, for comparison, the result obtained using the standard statistical definition). We are not trying to reconstruct the full line–of–sight velocity distribution, because it is known (see Merritt 1997) that for small samples such as ours which contain less than a few hundred objects per bin this is not possible — we simply calculate skewness and kurtosis parameters (we do not attribute much of significance to the numerical values of these parameters) in order to determine whether in some bin a significant departure from a Gaussian distribution exists. The parameter s_3 corresponds to h_3 and s_4 corresponds to h_4 where h_3 and h_4 are quantities extracted from integrated stellar

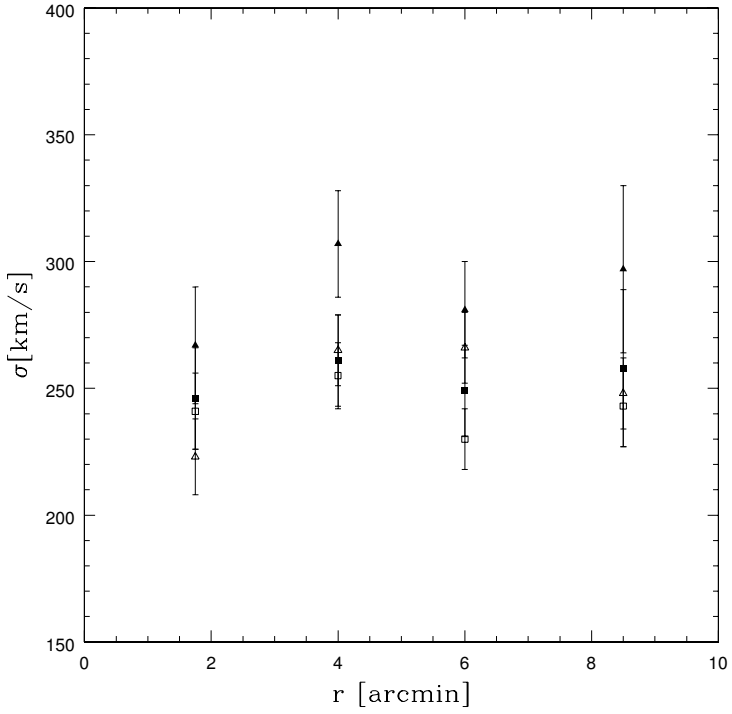

Figure 5.2: Comparison between our calculation of the velocity dispersion of NGC 1399 for red (open rectangles) and blue clusters (open triangles) and calculations of Richtler et al. (2004) for red (filled rectangles) and blue clusters (filled triangles). In all the cases we assumed a pure Gaussian distribution.

spectra, as shown in Chapter 1. This is similar to the approach applied by Teodorescu et al. (2005) in their Figure 18. The results are graphically presented in Fig. (5.3) (left). The results based on the maximum likelihood function and those based on the standard statistical method are in very good agreement. In order to test whether differences in binning affect our calculations we also performed the calculations using different binning with variable numbers of the GCs within a bin of fixed length (2 arcmin) without overlap of the bins. In Tables 5-3 and 5-4 we present the results for the blue and red clusters, respectively. Here we have used a bin width of 2 arcmin in order to include in each bin a statistically significant number of clusters. In Tables 5-5 and 5-6 we present two different types of binnings for which the center of each bin is placed on odd and even values of the radius, respectively (the obvious exceptions are the first and the last bin in Table 5-6). Table 5-7 presents the results of one additional binning check for which each bin contains approximately 75 clusters (instead of 50). The results for the blue, red and the total sample (which includes both blue and red clusters) given in Tables 5-3 – 5-7 were obtained using the same

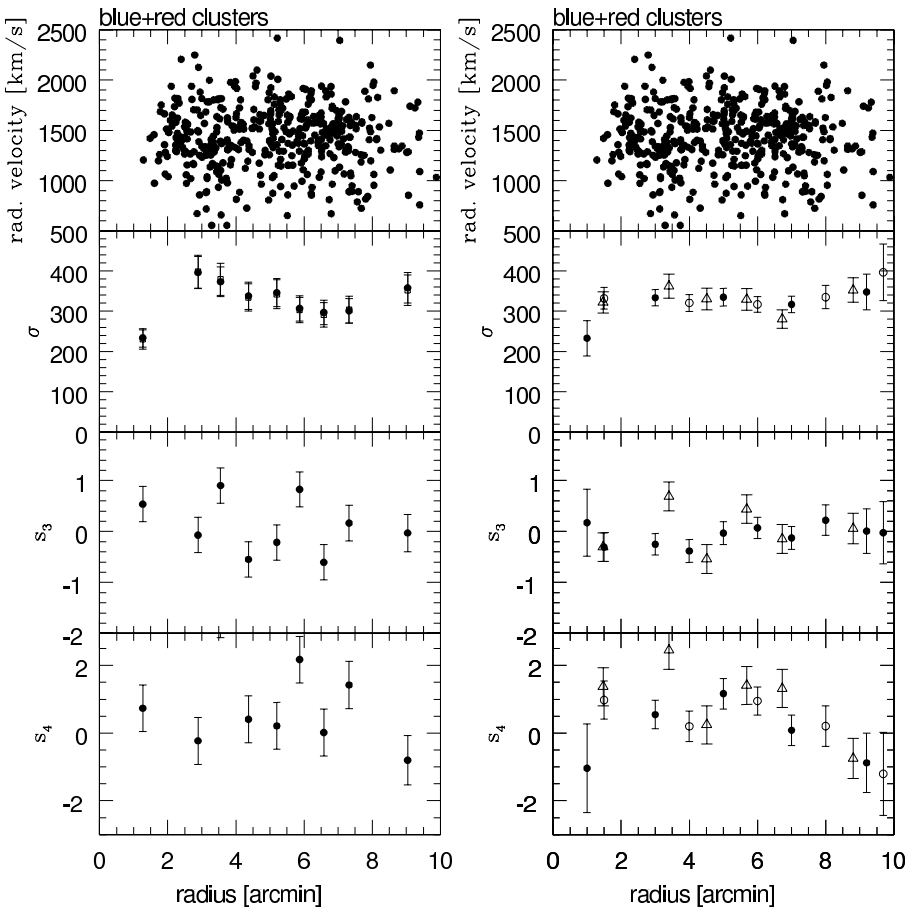

Figure 5.3: Kinematics of NGC 1399 based on the total sample of red and blue GCs. *Left*: From top to bottom: radial velocity of the GCs in km s^{-1}, velocity dispersion calculated in a given bin using a maximum likelihood method (open squares) and using standard statistical procedures (filled circles), s_3 and s_4 parameters. In all the bins the total number of clusters per bin was approximately 50. *Right*: The meaning of the data on the ordinate is the same as in the left panel. It combines results for binning methods given as follows: filled circles represent the data in TABLE 5-5, open circles are for the data given in TABLE 5-6 and open triangles are for the data from TABLE 5-7.

standard statistical procedure based on the same NAG routine; they are graphically presented in Fig. (5.3) (right) and Fig. (5.4). Although in Fig. (5.3) (left) we can see a declining trend in the velocity dispersion, the reduced χ^2 value is low for a constant velocity dispersion of 330 km s^{-1} and is equal to 1.1 (the best fit case, when the first point is excluded). The constant value of the velocity dispersion that ranges between 320 and 330 km s^{-1} provides the best fit case when $N = 75$ (the right hand panel of Fig. (5.3)), but then $\chi^2 \approx 1.3$ (all points are included in the fit).

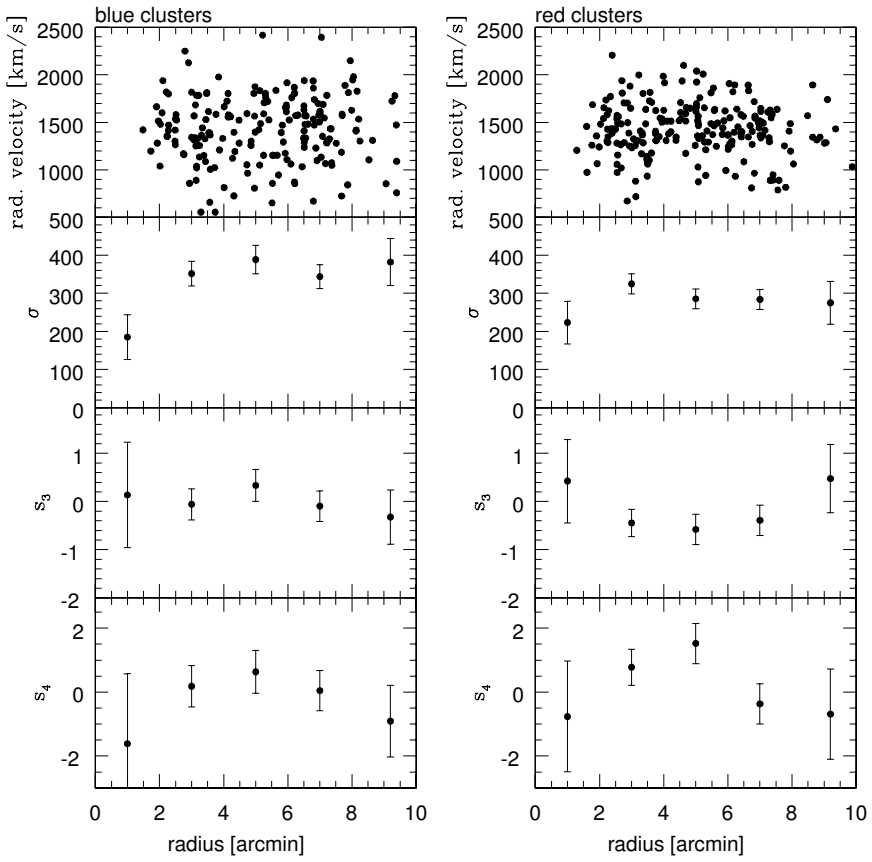

Figure 5.4: Kinematics of NGC 1399 based on the total sample of blue (left) and red (right) GCs. From top to bottom: radial velocity of the GCs in km s^{-1}, velocity dispersion, s_3 and s_4 parameters calculated in a given bin from TABLES 5-3 AND 5-4.

For the total sample of clusters (Fig. (5.3)) we see a low velocity dispersion in the inner region (interior to $\sim$ 2 arcmin), a higher value of the velocity dispersion (beyond $\sim$ 2 arcmin) and a decrease of the velocity dispersion between $\sim$ 3 and $\sim$ 7 arcmin (more evident in the left panel of Fig. (5.3), because of the binning applied). Beyond $\sim$ 8 arcmin we notice an increase in the velocity dispersion. We confirm the finding of Richtler et al. (2004) regarding the innermost point ($<$ 2 arcmin). Beyond $\sim$ 2 arcmin our results differ somewhat from those by Richtler et al. because of the binning and selection criteria used.

The red clusters show a lower velocity dispersion than the blue clusters (see Fig. (5.4)) and for a possible explanation we refer the reader to §4 of the paper by Richtler et al. (2004). Although both s_3 and s_4 parameters are small we see that while the calculated s_3 parameters for blue clusters differ from those for red clusters, the s_4

parameters for both classes are very similar. The binning in both cases was such that we kept the bin width constant and equal to 2 arcmin in order to have enough clusters per bin.

Forte et al. (2005) state there are indications (albeit not conclusive) that there could be an association between the red GCs and the stellar component and that blue GCs show a spatial distribution which is similar to that inferred for dark matter. However any attempt to draw conclusions from this is outside the province of this book.

As an additional test we also calculated the velocity dispersion in the inner part of NGC 1399 (interior to ~ 2 arcmin) in which we have 14 GCs (the innermost at ~ 1.3 arcmin and the outermost at ~ 2 arcmin). We calculated that for the total sample of blue and red clusters the velocity dispersion is 232 ± 62 km s^{-1}. We note that this result is in agreement with the integrated stellar light observations thus giving credence to the feasibility of calculating galaxy kinematics even with the small number of mass tracers in a given bin.

5.2.2. X–RAY MODELLING OF NGC 1399

The reader is referred to Chapter 3 of this book for the details regarding the X–ray properties of NGC 1399. Here we note that although the X–ray data suggest that beyond $\sim 3R_e$ in NGC 1399 there should be a significant amount of dark matter, we note, however, that since NGC 1399 is a central galaxy of the Fornax cluster, the confinement of the hot gas may be assisted by the external pressure of the intercluster medium (ICM) and is not wholly due to the gravitational field of NGC 1399 (Bertin 2000).

5.2.3. MASS ESTIMATES OF NGC 1399 BASED ON GCs

For the application of Eq. (5.6) we split the total sample of GCs into 5 bins: each bin (except the first one which is 2 arcmin wide) contains the previous one in addition to a fixed width of 2 arcmin. Our results (for mass and mass-to-light ratios) for the isotropic case are given in TABLE 5-8. In this Table for comparison we also provide estimates for mass and mass-to-light ratio obtained using X–ray methodology in the same bins. The errors for the estimates based on the X–rays reflect uncertainty in the temperature. In the calculation of the mass (and mass-to-light ratios) based on the GCs we used $\gamma = 1.54$ which was derived using a least–squares fit applied to the data published by Dirsch et al. (2003) for *all* the clusters in the sample. The outermost point at 10 arcmin was taken. The data from the TABLE 5-8 are graphically presented in Fig. (5.5). The large box contains estimates for the total mass-to-light ratio (open and filled triangles are for the determination based on the X–ray technique assuming hydrostatic equilibrium (open triangles are for $\beta = 0.35$ and filled triangles are for $\beta = 0.50$) and open circles are for the estimate based on GCs assuming isotropy. In the estimates of the mass-to-light ratio based on the X–rays we take $T = 1$ keV in the first bin, and $T = 1.30$ keV in all the other bins. In a small inserted box we plot the estimates for the mass: the symbols have the same meaning as in the large box. In the inner regions (interior to ~ 6 arcmin) of NGC 1399 we have good agreement between the two techniques. At ~ 6 arcmin and beyond the estimate of the mass

(and the mass-to-light ratio) based on $\beta = 0.50$ starts to diverge from the estimate based on the GCs, whereas the estimate based on $\beta = 0.35$ is consistent with it up to 8 arcmin. Note also that the estimate of Grillmair et al. (1994) is consistent with both results based on the GCs and X–rays ($\beta = 0.35$ case).

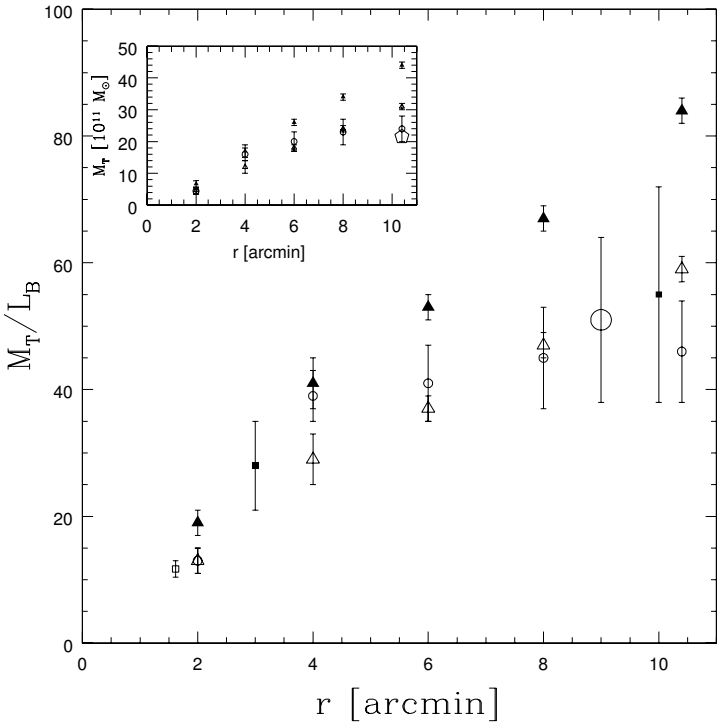

Figure 5.5: Mass estimates using the GCs and X–ray methodology for NGC 1399. *Large box*: estimates for the total mass-to-light ratio in the B-band in the solar units as a function of radius; the triangles are for the determination based on the X–ray technique assuming hydrostatic equilibrium (the open triangles for $\beta = 0.35$ and the filled triangles for $\beta = 0.50$), the open circles are for the estimate based on GCs assuming isotropy. The large open circle is the value obtained in the paper by Grillmair et al. (1994) scaled to the distance used in this book (see text for details). The open square is the value obtained in the paper by Saglia et al. (2000) scaled to the distance used in this book. The filled square is the value obtained in the paper by Jones et al. (1997) scaled to the distance used in this book. The temperature is taken to be 1 keV in the first bin and 1.30 keV in all the other bins. *Small inserted box*: estimates of the total mass in units of $10^{11} M_\odot$ as a function of radius; the symbols have the same meaning as in the large box. The large open pentagon in the small box is for the estimates of Richtler et al. (2004) for the mass based on the Navarro, Frenk and White profile and the logarithmic potential.

The only point for which there seems to be a discrepancy between the X–ray and the GC estimates is the one at 10 arcmin: the X–rays (with $\beta = 0.35$) predict the mass-to-light ratio of 59 ± 2 whereas the estimate based on the GCs gives 46 ± 8. There may be two possible sources of this discrepancy:

(i) The errors given in the X–ray case should be understood as minimal, because in these estimates we took into account only the uncertainty in temperature ($T = 1.30 \pm 0.05$) keV. Note that Jones et al. (1997) at 10 arcmin calculated $M/L_B = 55 \pm 17$ (scaled to the distance used in this book; see their Fig. 7 – in our Fig. (5.5) we plotted the points at 3 and 10 arcmin based on their plot); note also that at ~ 10 arcmin their best fit for the temperature is 1.22 keV which is somewhat lower than the value we took thus implying a lower mass-to-light ratio which is closer to that obtained using GC methodology.

(ii) The discrepancy between the two results may be real and might be attributed to the effect of a contribution to the X–ray gas pressure by the ICM referred to above, i.e. the assumption of hydrostatic equilibrium fails in this case. As it is shown below for the galaxy NGC 5128, the data based on the GCs and PNe that between 50 and 80 kpc $M/L_B \sim 11 - 14$ which suggests even smaller amounts of dark matter in the outer parts of this galaxy.

Different cosmological models and their predictions for the mass may in principle be tested. Richtler et al. (2004) (references therein) tested among others, logarithmic potentials and Navarro, Frenk and White (NFW) (1996) mass profiles. With the data which extend out to ~ 10 arcmin it is difficult to draw firm conclusions; the mass predicted by both NFW profile and the logarithmic potential is closer to the mass based on GCs and X–rays for which $\beta = 0.35$ than to the X–rays for which $\beta = 0.50$: $M \sim 2.15 \times 10^{12} M_{\odot}$ at ~ 10 arcmin (scaled to the distance used in this book; see the large open pentagon in the small inserted box of Fig. (5.5)).

We see in Fig. (5.5) that there is agreement between the following four different estimates of the total mass-to-light ratio: (i) our estimate based on the GCs, (ii) our estimate based on the X–rays (the case with $\beta = 0.35$), (iii) the estimate based on the Grillmair et al. (1994) paper based on the GCs and (iv) the estimate based on the NFW approach (this last one is given only in the small inserted box of Fig. (5.5)).

TABLE 5-1

PROJECTED VELOCITY DISPERSION MEASUREMENTS OF NGC 1399 FOR A GAUSSIAN DISTRIBUTION ($\delta_i < 60$ km s^{-1})

radial bin (arcmin) (1)	$< r >$ (arcmin) (2)	$\sigma_{\rm tot}$ (km s^{-1}) (3)	$N_{\rm tot}$ (4)	$\sigma_{\rm blue}$ (km s^{-1}) (5)	$N_{\rm blue}$ (6)	$\sigma_{\rm red}$ (km s^{-1}) (7)	$N_{\rm red}$ (8)
All r	–	331 ± 11	445	295 ± 12	196	259 ± 11	216
$r < 3.5$	1.75	320 ± 21	124	223 ± 15	51	241 ± 15	66
$2.5 < r < 5.5$	4.00	359 ± 18	201	265 ± 14	80	255 ± 13	107
$4.5 < r < 7.5$	6.00	315 ± 16	209	266 ± 14	90	230 ± 12	103
$r > 6.5$	8.50	316 ± 28	127	248 ± 14	67	243 ± 16	53

NOTES – Col. (1): radial bin. Col. (2): central point for a given bin. Col. (3): velocity dispersion with the estimated uncertainty for a total sample of clusters. Col. (4): number of objects in a given bin for a total sample of clusters. Col. (5): velocity dispersion with the estimated uncertainty for blue clusters. Col. (6): number of objects in a given bin for blue clusters. Col. (7): velocity dispersion with the estimated uncertainty for red clusters. Col. (8): number of objects in a given bin for red clusters.

TABLE 5-2

PROJECTED VELOCITY DISPERSION MEASUREMENTS OF NGC 1399 FOR A GAUSSIAN DISTRIBUTION WITH A FIXED NUMBER OF CLUSTERS PER BIN ($\delta_i < 60$ km s^{-1}, $N \approx 50$)

radial bin (arcmin) (1)	$< r >$ (arcmin) (2)	$\sigma_{\rm ML}$ (km s^{-1}) (3)	err_$\sigma_{\rm ML}$ (km s^{-1}) (4)	$\sigma_{\rm stat}$ (km s^{-1}) (5)	err_$\sigma_{\rm stat}$ (km s^{-1}) (6)	s_3 (7)	err_s_3 (8)	s_4 (9)	err_s_4 (10)	N (11)
$0.000 < r < 2.543$	1.27	230	24	234	23	0.54	0.35	0.74	0.48	50
$2.543 \leq r < 3.240$	2.89	398	41	396	40	-0.07	0.35	-0.23	0.48	50
$3.240 \leq r < 3.860$	3.55	379	40	373	37	0.90	0.35	3.51	0.48	50
$3.860 \leq r < 4.880$	4.37	334	34	338	34	-0.55	0.35	0.41	0.48	50
$4.880 \leq r < 5.528$	5.20	342	36	346	35	-0.21	0.35	0.21	0.48	50
$5.528 \leq r < 6.214$	5.87	303	31	307	30	0.83	0.34	2.17	0.47	51
$6.214 \leq r < 6.950$	6.58	291	30	297	30	-0.60	0.35	0.02	0.48	50
$6.950 \leq r < 7.690$	7.32	304	33	301	30	0.17	0.35	1.42	0.49	49
$7.690 \leq r < 10.380$	9.04	352	38	358	38	-0.03	0.37	-0.80	0.53	45

NOTES – Col. (1): radial bin. Col. (2): central point for a given bin. Col. (3): velocity dispersion for a Gaussian distribution. Col. (4): formal errors for the velocity dispersion. Col. (5): velocity dispersion obtained using the standard statistical definition. Col. (6): formal errors for the velocity dispersion obtained using standard statistical definitions. Col. (7): s_3 parameter. Col. (8): formal errors for the s_3 parameter. Col. (9): s_4 parameter. Col. (10): formal errors for the s_4 parameter. Col. (11): number of clusters in a given bin.

TABLE 5-3

KINEMATICS DATA FOR NGC 1399 FOR THE BLUE CLUSTERS

radial bin (arcmin) (1)	$\sigma_{\rm blue}$ (km s^{-1}) (2)	err_$\sigma_{\rm blue}$ (km s^{-1}) (3)	$s_{3\rm blue}$ (4)	err_$s_{3\rm blue}$ (5)	$s_{4\rm blue}$ (6)	err_$s_{4\rm blue}$ (7)	N (8)
1	185	59	0.14	1.10	-1.60	4.80	5
3	352	33	-0.07	0.32	0.20	0.41	58
5	389	38	0.35	0.33	0.60	0.44	54
7	344	31	-0.07	0.32	0.00	0.40	60
9.2	382	62	-0.35	0.56	-0.80	1.26	19

NOTES – Col. (1): central point for a given bin. Col. (2): velocity dispersion for the blue clusters. Col. (3): formal errors for the velocity dispersion of the blue clusters. Col. (4): s_3 parameter for the blue clusters. Col. (5): formal errors for the s_3 parameter for the blue clusters. Col. (6): s_4 parameter for the blue clusters. Col. (7): formal errors for the s_4 parameter for the blue clusters. Col. (8): number of clusters in a given bin. In all the cases $\delta_i < 60$ km s^{-1}.

TABLE 5-4

KINEMATICS DATA FOR NGC 1399 FOR THE RED CLUSTERS

radial bin (arcmin) (1)	$\sigma_{\rm red}$ (km s^{-1}) (2)	err_$\sigma_{\rm red}$ (km s^{-1}) (3)	$s_{3\rm red}$ (4)	err_$s_{3\rm red}$ (5)	$s_{4\rm red}$ (6)	err_$s_{4\rm red}$ (7)	N (8)
1	223	56	0.42	0.87	-0.80	3.00	8
3	325	27	-0.42	0.28	0.80	0.32	75
5	286	26	-0.56	0.31	1.60	0.39	61
7	284	26	-0.42	0.32	-0.40	0.40	60
9.2	275	56	0.49	0.71	-0.60	2.00	12

NOTES – The same as in TABLE 5-3 but for the red clusters.

TABLE 5-5

KINEMATICS DATA FOR NGC 1399 FOR THE TOTAL SAMPLE OF BLUE AND RED CLUSTERS (PART 1)

radial bin (arcmin) (1)	$\sigma_{\rm total1}$ (km s^{-1}) (2)	err_$\sigma_{\rm total1}$ (km s^{-1}) (3)	$s_{3\rm total1}$ (4)	err_$s_{3\rm total1}$ (5)	$s_{4\rm total1}$ (6)	err_$s_{4\rm total1}$ (7)	N (8)
1	233	44	0.14	0.65	-1.00	1.71	14
3	334	20	-0.28	0.21	0.60	0.18	135
5	335	22	0.00	0.23	1.20	0.21	117
7	317	20	-0.14	0.22	0.00	0.20	120
9.2	348	44	0.00	0.44	-0.80	0.77	31

NOTES – The same as in TABLE 5-3 but for the total sample of blue and red clusters (bins centered on odd values of radius, see text for details)

TABLE 5-6

KINEMATICS DATA FOR NGC 1399 FOR THE TOTAL SAMPLE OF BLUE AND RED CLUSTERS (PART 2)

radial bin (arcmin) (1)	$\sigma_{\rm total2}$ (km s^{-1}) (2)	err_$\sigma_{\rm total2}$ (km s^{-1}) (3)	$s_{3\rm total2}$ (4)	err_$s_{3\rm total2}$ (5)	$s_{4\rm total2}$ (6)	err_$s_{4\rm total2}$ (7)	N (8)
1.5	332	27	-0.28	0.28	1.00	0.32	76
4	321	21	-0.42	0.22	0.20	0.20	119
6	317	19	0.07	0.21	1.00	0.17	139
8	335	29	0.21	0.30	0.20	0.36	67
9.69	396	70	0.00	0.61	-1.20	1.50	16

NOTES – The same as in TABLE 5-3 but for the total sample of blue and red clusters (bins centered on even values of radius, see text for details)

TABLE 5-7
KINEMATICS DATA FOR NGC 1399 FOR THE TOTAL SAMPLE OF BLUE AND RED CLUSTERS (PART 3)

radial bin (arcmin) (1)	$\sigma_{\rm total3}$ (km s^{-1}) (2)	err_$\sigma_{\rm total3}$ (km s^{-1}) (3)	$s_{3\rm total3}$ (4)	err_$s_{3\rm total3}$ (5)	$s_{4\rm total3}$ (6)	err_$s_{4\rm total3}$ (7)	N (8)
1.47	322	26	-0.28	0.28	1.40	0.32	75
3.40	362	30	0.69	0.28	2.40	0.32	75
4.51	330	27	-0.56	0.28	0.20	0.32	75
5.68	329	27	0.42	0.28	1.40	0.32	76
6.73	281	23	-0.14	0.28	1.40	0.32	75
8.81	352	30	0.07	0.30	-0.80	0.35	68

NOTES – The same as in TABLE 5-3 but for the total sample of blue and red clusters. The number of clusters per bin is approximately 75, see text for details.

TABLE 5-8
MASS ESTIMATES OF NGC 1399 USING GLOBULAR CLUSTERS AND X–RAYS

Radius (arcmin) (1)	$M_{\rm tot}^{\rm xray,\beta=0.35}$ $10^{11}M_\odot$ (2)	$M^{\rm xray}/L_B$ $M_\odot/L_\odot$ (3)	$M_{\rm tot}^{\rm xray,\beta=0.50}$ $10^{11}M_\odot$ (4)	$M^{\rm xray}/L_B$ $M_\odot/L_\odot$ (5)	$M^{\rm GC,iso}{}_{\rm tot}$ $10^{11}M_\odot$ (6)	$M^{\rm GC,iso}/L_B$ $M_\odot/L_\odot$ (7)	N (8)
<2	4.7 ± 1	13 ± 2	6.7 ± 1	19 ± 2	4.4 ± 1	13 ± 2	14
<4	12 ± 2	29 ± 4	17 ± 2	41 ± 4	16 ± 2	39 ± 4	157
<6	18 ± 1	37 ± 2	26 ± 1	53 ± 2	20 ± 3	41 ± 6	283
<8	24 ± 1	47 ± 2	34 ± 1	67 ± 2	23 ± 4	45 ± 8	413
<10.4	31 ± 1	59 ± 2	44 ± 1	84 ± 2	24 ± 4	46 ± 8	445

NOTES – Col. (1): radius interior to which a given quantity is calculated. Col. (2): estimate of the total mass based on the X–ray methodology expressed in units of $10^{11}M_\odot$ for $\beta = 0.35$ (the temperature was taken to be 1 keV in the first bin and 1.30 keV in all the other bins). Col. (3): mass-to-light ratio based on the X–ray methodology in the B-band in solar units for $\beta = 0.35$. Col. (4): estimate of the total mass based on the X–ray methodology expressed in units of $10^{11}M_\odot$ for $\beta = 0.50$ (the temperature was taken to be 1 keV in the first bin and 1.30 keV in all the other bins). Col. (5): mass-to-light ratio based on the X–ray methodology in the B-band in solar units for $\beta = 0.50$. Col. (6): estimate of the total mass based on the GCs assuming isotropy (see text for details). Col. (7): mass-to-light ratio based on the GCs assuming isotropy in solar units (see text for details). Col. (8): the number of clusters in a given bin.

5.2.4. SUMMARY OF THE RESULTS RELATED TO NGC 1399

The summary of the results related to the galaxy NGC 1399 is as follows.

(1) We show that the departures from the Gaussian distribution (given by the skewness and kurtosis parameters, s_3 and s_4, estimated from the radial velocities) are not large and that the estimates of the velocity dispersion calculated using standard statistical procedures and the maximum likelihood approach do not differ much. Using different binning we showed that slightly different trends in the velocity dispersion profile might be inferred.

(2) We find that inside $\sim 2.5R_e$ the mass is not dominated by dark matter (only for the case for which $\beta = 0.50$ and $T \sim 0.92$ keV might one infer dark matter in this region). However, beyond $\sim 3R_e$ the high velocity dispersion and the X–rays indicate the presence of dark matter. This is not inconsistent with the results results obtained so far in this book for 2 early–type galaxies (IC 1459, IC 3370) for which dark matter interior to $\sim 3R_e$ did not appear to dominate (Samurović and Danziger 2005). Our estimates of the total mass (and mass-to-light ratio) based on the X–ray and GC methodology imply $\beta = 0.35$ – this is in agreement with the value found in the paper by Jones et al. (1997). Beyond 8 arcmin there seems to be a discrepancy between the two methodologies: the GC data imply a smaller total mass than that obtained using X–rays; it is not clear whether this discrepancy lies within the uncertainties or not.

(3) Using the new "tracer mass estimator" of Evans et al. (2003) we find that the increase of the total mass of NGC 1399 beyond ~ 4 arcmin has a slow rise. At ~ 10 arcmin we calculated, for an isotropic case, $M/L_B = 46 \pm 8$. In spite of the hint of the decreasing velocity dispersion in NGC 1399 (between ~ 3 and ~ 7 arcmin) the observations show evidence of dark matter in the outer parts of this galaxy. The procedure outlined in this book provides a means of comparison between different calculations of the total mass of an early–type galaxy without resorting to much more complex and computationally intensive superposition of orbits required in the Schwarzschild (1979) modelling.

(4) It is difficult to draw general conclusions regarding anisotropies in the outer parts of early–type galaxies at this point because the sample of galaxies is still too small and there are problems regarding the small number of observed clusters per galaxy. Judging from the sample of clusters used in this book we did not find large departures from a Gaussian distribution. In the Chapter 1 of this book in the case of IC 1459 (beyond $\sim 2R_e$) and NGC 3379 (beyond $\sim 1.4R_e$) we found a hint of radial anisotropies. Dekel et al. (2005) using numerical simulations of disc–galaxy mergers recently found that for early–type galaxies the stellar orbits in their outer parts are very elongated. Teodorescu et al. (2005) found that for PNe in the flattened early–type galaxy NGC 1344 the departures from a Gaussian distribution are small but they did not quantify them (see their Figure 18).

(5) Given the fact that the full LOSVD profile of a given early–type galaxy obtained from integrated stellar light is typically based on the integrated spectra of several million stars and the velocity dispersion based on GCs (and PNe) is based on at most several hundred objects, it is obvious that for more accurate kinematics of

early–type galaxies at large radial distances an increased number of observed GCs (and PNe) is highly desirable.

5.3. NGC 5128

5.3.1. BASIC DATA

NGC 5128 (also known as the radio source Centaurus A) is the nearest large elliptical galaxy. The value of the distance used in this book, $D = 3.84 \pm 0.35$ Mpc is taken from the paper by Rejkuba (2004) and is in agreement with other estimates found in the literature (such as Hui et al. 1993). At this distance $1' \approx 1$ kpc. NGC 5128 is the only early–type member of the Centaurus group. In this book the adopted center of the galaxy is $(13^{\rm h}25^{\rm m}27\overset{\rm s}{.}72, -43°01'05\overset{''}{.}8$,J2000). The effective radius is $R_e = 5.3$ kpc and the systemic velocity is $v_{\rm syst} = 541$ km s^{-1}. The B-band luminosity of the stellar component NGC 5128 is $L_B = 3.98 \times 10^{10} L_\odot$. The complete review of this galaxy can be found in the paper by Israel (1998) Because of its proximity and interesting features (observational evidence of one or more major merging events) NGC 5128 is an excellent target for a detailed study: a large number of papers with a wealth of observational data is available which makes it possible to investigate its properties by comparing different observations (in this book, GCs, PNe and X–rays).

5.3.2. KINEMATICS OF GCs OF NGC 5128

The sample which was used in this book was built using two different samples: (i) the first one is taken from the paper by Peng et al. (2004a) who conducted an optical and spectroscopic survey for GCs across $\sim 1°$ of sky around NGC 5128 and includes 215 clusters: their whole sample was taken and (ii) the second one is taken from the paper by Woodley, Harris and Harris (2005) who measured radial velocities for 74 GCs: in this case 31 GCs not present in the previous sample were taken. In total we use 246 clusters which extend out to 42.44 kpc ($= 8R_e$). The kinematics of NGC 5128 based on the GCs is given in TABLE 5-9 and also in Fig. (5.6) (left): from the top to the bottom we plot as a function of radius, radial velocity, velocity dispersion, s_3 and s_4 parameters.[13]

5.3.3. KINEMATICS OF PNe OF NGC 5128

The sample of PNe used in this book comes from the paper by Peng et al. (2004b) and contains 780 PNe. The kinematics of NGC 5128 based on the PNe is given in TABLE 5-10 and also in Fig. (5.6) (right) (the meaning of symbols is the same as in the case of GCs). Note that error bars are not plotted in the case of radial velocities: as given in Peng et al. (2004b) they are taken to be 20 km s^{-1} in the calculations below. The data for the PNe extend out to 78 arcmin ($= 14.7R_e$).

5.3.4. X–RAY DATA FOR NGC 5128

The analysis of NGC 5128 based on the results from two CHANDRA/ACIS-I observations and one XMM-Newton observation of X-ray emission from the interstellar

[13]The parameters s_3 and s_4 are explained in Section 5.2.1.

medium (ISM) is given in Kraft et al. (2003). It was found that the ISM has an average radial surface brightness profile that is well described by a β-model profile with index $\beta = 0.40 \pm 0.04$ and a temperature of $k_B T_{\rm ISM} = 0.29$ keV beyond 2 kpc from the galactic nucleus. These data will be used below when we calculate the total mass and the total mass-to-light ratio of NGC 5128.

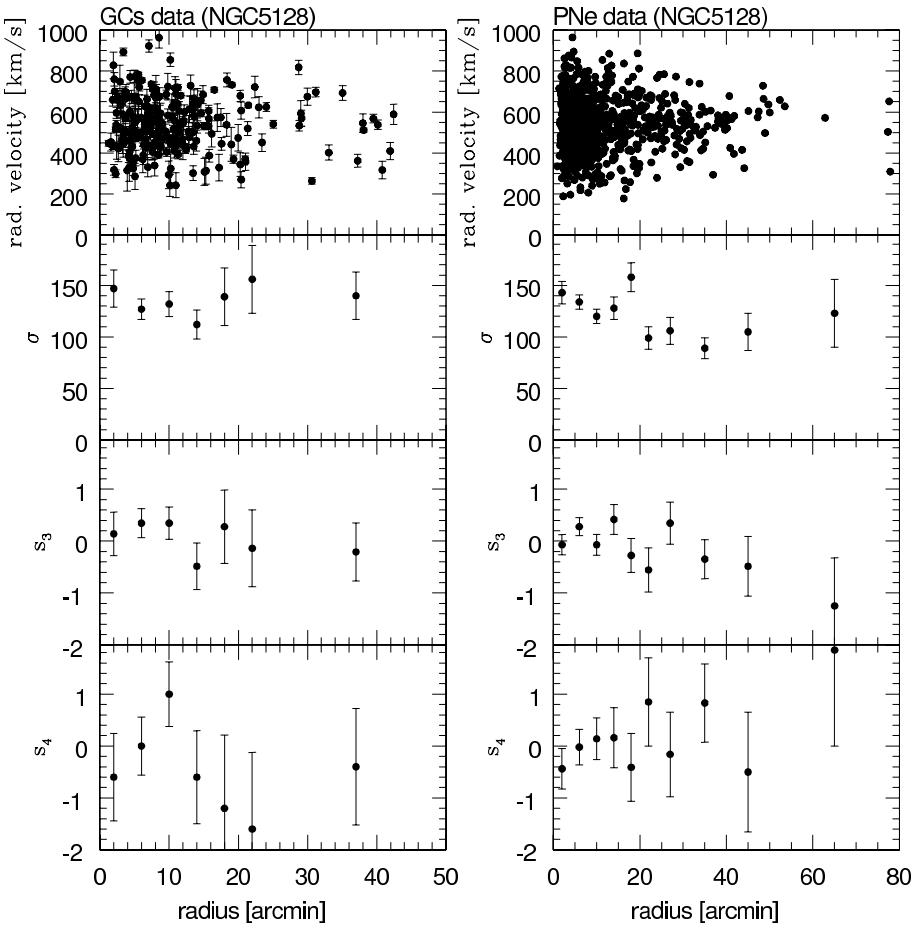

Figure 5.6: *Left:* Globular clusters kinematics of NGC 5128. From top to bottom: radial velocities of the GCs as a function of radius, velocity dispersion as a function of radius, asymmetric (s_3) and symmetric departures (s_4) from Gaussian as a function of radius. *Right:* Planetary nebulae kinematics of NGC 5128. The meaning of symbols is the same as on the left. Error bars for the radial velocities are not plotted (see text for details). Note the different scale with respect to the plot on the left hand side of the Figure.

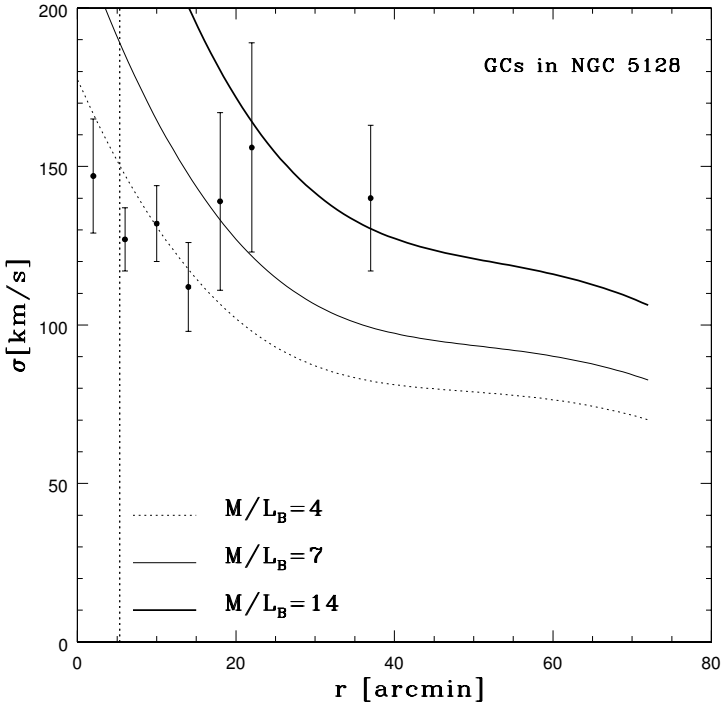

Figure 5.7: Jeans modelling of the globular clusters of NGC 5128. Dotted line is used for the modelling for which $M/L_B = 4$, thin solid line is for $M/L_B = 7$ and thick solid line is for $M/L_B = 14$. Note that the same scale as in Fig. (5.8) is used for the sake of comparison. Vertical dotted line represents one effective radius.

5.3.5. X–RAY AND JEANS MODELLING

For the details concerning the Jeans and X–ray modelling the reader is referred to Chapter 2 and 3 of this book, respectively. Some details for the sake of clarity will be repetead below.

If we accept to a first order approximation that the X–ray results are realistic we solve the Jeans equation which provides the connection between the anisotropy and the temperature of the hot interstellar gas through which the stars move (Binney and Tremaine 1987):

$$\frac{1}{\ell_*}\frac{\mathrm{d}(\ell_*\sigma_r^2)}{\mathrm{d}r} + \frac{2\beta_*\sigma_r^2}{r} = -\frac{GM(r)}{r^2} + \frac{v_{\rm rot}^2}{r} \qquad (5.8)$$

where σ_r is the radial stellar velocity dispersion, ℓ_* is the stellar luminosity density which corresponds to the radial (σ_r) and transverse (σ_t) stellar velocity dispersions. Here, $v_{\rm rot}$ is the rotational speed (see Hui et al. 1995). A parameter β_* is introduced

to describe the nonspherical nature of the stellar velocity dispersion:

$$\beta_* = 1 - \overline{v_\theta^2}/\sigma_r^2, \tag{5.9}$$

where $\overline{v_\theta^2} = \overline{v_\theta}^2 + \sigma_\theta^2$. For $0 < \beta_* < 1$ the orbits are predominantly radial, in this case the line of sight velocity profile is more strongly peaked than a Gaussian profile (positive s_4 parameter), and for $-\infty \leq \beta_* < 0$ the orbits are mostly tangential, so the profile is more flat–topped than a Gaussian (negative s_4 parameter) (Gerhard 1993). For the stellar luminosity density we adopted the Hernquist (1990) profile:

$$\ell_* = \frac{L}{2\pi}\frac{a}{r}\left(\frac{1}{r+a}\right)^3 \tag{5.10}$$

where $R_e = 1.8153a$. The projected line–of–sight velocity dispersion is calculated as (e.g. Binney and Mamon 1982, Mathews and Brighenti 2003a):

$$\sigma^2(R) = \frac{\int_R^{r_t} \sigma_r^2(r)\left[1-(R/r)^2\beta_*\right] \times \ell_*(r)(r^2-R^2)^{-1/2}\, r\mathrm{d}r}{\int_R^{r_t} \ell_*(r)(r^2-R^2)^{-1/2}\, r\mathrm{d}r} \tag{5.11}$$

where the truncation radius, r_t, extends to a large distance: in this work it was 50 arcmin ($= 9.4R_e$, for GCs) and 80 arcmin ($= 15R_e$ for PNe).

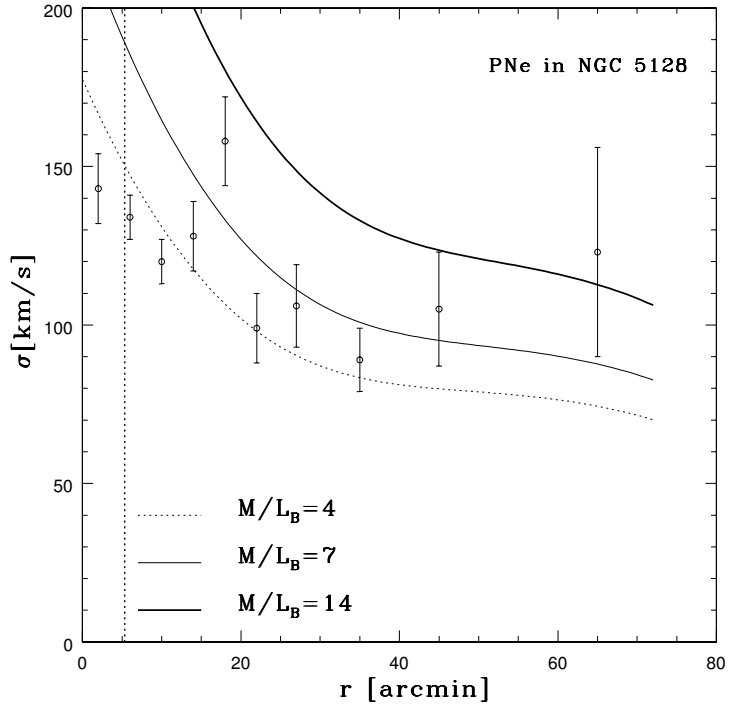

Figure 5.8: Jeans modelling of the planetary nebulae of NGC 5128. The same modelling was used as in Fig. (5.7).

The results of this kind of modelling are given in Fig. (5.7) (for the GCs) and Fig. (5.8) (for the PNe). For the sake of comparison both Figures have the same scales. Since both tracers have similar surface density (see below) the same modelling is given in both Fig. (5.7) and Fig. (5.8). One can see that a low constant mass-to-light ratio ($M_T/L_B = 4$) can provide a successful fit (interior to ~ 15 arcmin for GCs and interior to ~ 30 arcmin for PNe). An intermediate constant mass-to-light ratio ($M_T/L_B = 7$) can provide a good fit (between ~ 15 and ~ 25 arcmin for GCs and between ~ 30 and ~ 45 arcmin for PNe). A high constant mass-to-light ratio ($M_T/L_B = 14$) provides a good fit in the outer part of the galaxy (beyond ~ 30 arcmin for GCs and beyond ~ 45 arcmin for PNe). This kind of modelling is in agreement with both X-ray estimates and the estimates based on different tracers (see below for details regarding these tracers; see TABLE 5-12 for a comparison of the mass-to-light ratios at different radii). The high value of the total mass-to-light ratio implies the existence of dark matter in the outer regions of the galaxy.

5.3.6. MASS ESTIMATES OF NGC 5128 BASED ON GCs AND PNe

The methodology for the calculation of the mass using GCs and PNe was given in Sec. 5.1.2 and it was applied in the case of the galaxy NGC 5128.

As it was argued in Evans et al. (2003) the mass estimator which they derived only calculates the contribution of random motion to the mass. The galaxy NGC 5128 has a large rotational component which is added to the mass calculated using the tracers. Because the rotation curve flattens at ~ 100 km s^{-1} (see Peng et al. 2004b, their figure 10) this value of the rotation speed $v_{\rm rot}$ was used when the calculation of the rotational component was calculated: $M_{\rm rot}(r) =< v_{\rm rot} >^2 r/G$.

Peng et al. (2004c,b) calculated the value for the γ parameter for both GCs and PNe and these values were used in this book: for GCs they found $\gamma = 2.72$ (for *all*, blue and red clusters in the sample, Peng et al. 2004c) and for PNe they found $\gamma = 2.54$. Note that we have used the same value as Peng et al. for the GCs although our sample differs for additional 31 clusters from Woodley et al. (2005). The reason for this is that Peng et al. calculated the value for the γ parameter between ~ 6 and ~ 18 arcmin because this region is less affected by incompleteness and the GCs from Woodley et al. sample are found between ~ 17.5 and ~ 20.3 arcmin.

Using the methodology of Evans et al. (2003) and the estimates by Peng et al. (2004b,c) our calculated mass estimates as function of radius are given in TABLE 5-11 and our calculated mass-to-light ratio (in solar units in the B-band) are given in TABLE 5-12. If one compares the results for the estimates based on GCs and PNe one can see that both tracers predict very similar values of the mass interior to a given radius which may mean that the orbital anisotropies of these two different populations are very similar (noted also in Fig. (5.6), especially interior to 20 arcmin where the most of the tracers are present and the estimate of the anisotropies given by the s_3 and s_4 parameters is more accurate). When compared with the results obtained using different techniques found in the literature, the agreement is very good. For example, Kraft et al. (2003) using X–rays found that the total mass interior to 15 arcmin is $M_T = 2 \times 10^{11} M_\odot$ (and $M_T/L_B = 6.64$): this result is represented with the cross symbol in Fig. (5.9). Peng et al. (2004c) found using GCs that interior to 40 arcmin

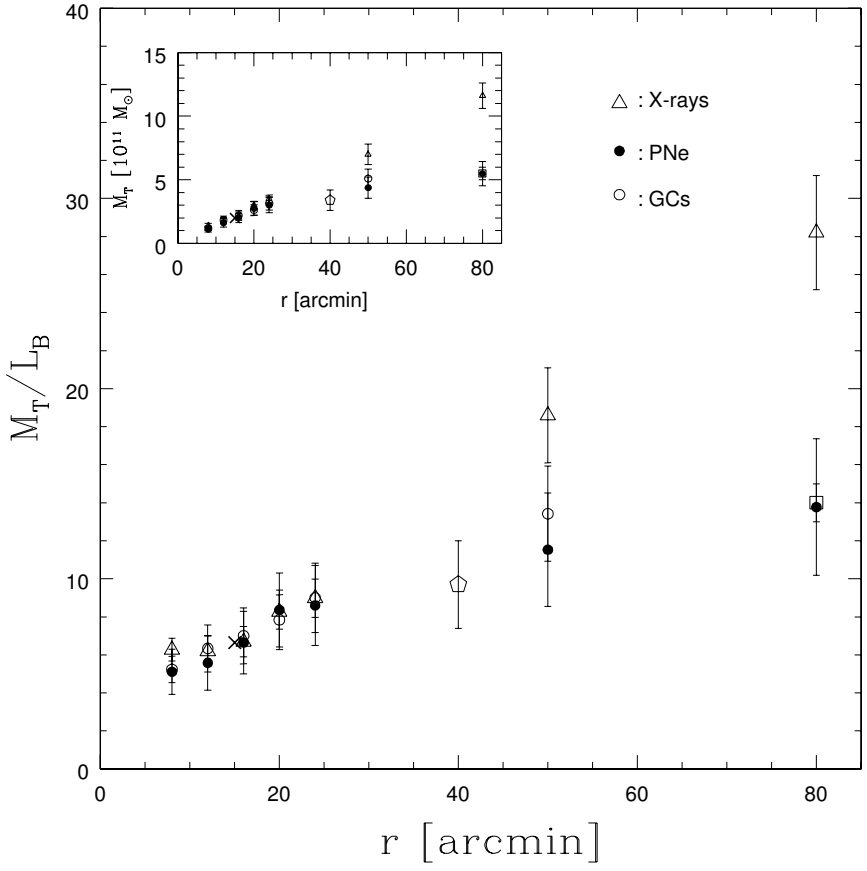

Figure 5.9: Mass and mass-to-light ratio of NGC 5128 using different techniques. *Large box:* mass-to-light ratio in the B-band expressed in solar units as a function of radius. *Small inserted box:* Total mass as a function of radius expressed in $10^{11} M_\odot$. Open triangles are for the estimates based on the X–ray methodology, filled circles are for the results based on the PNe and opened circles are for the data based on the GCs. Point represented with cross is a result based on the X–rays from Kraft et al. (2003), diamond is a result from Peng et al. (2004c) based on the GCs and open rectangle is from Peng et al (2004b) based on the PNe.

$M_T = (3.4 \pm 0.8) \times 10^{11} M_\odot$ ($M_T/L_B = 9.7 \pm 2.3$) which is again in agreement with the results found in this book. Note again, that our two samples differ because we included 31 clusters from Woodley et al. (2005). Finally, Peng et al. (2004b) found for PNe interior to 80 arcmin $M_T = 5 - 6 \times 10^{11} M_\odot$ ($M_T/L_B = 13 - 15$) (open rectangle in Fig. (5.9)). Note that there is a slight difference between Peng et al. and our estimates of the mass interior to 80 arcmin. Although we used the same Evans et

al. (2003) technique we did not have error bars for the radial velocity ($\Delta v = 20$ km s^{-1} was taken in all the cases) and this fact produced this minor difference.

We can see in Fig. (5.9) that dark matter does not dominate interior to ~ 25 arcmin ($\sim 5R_e$) because the total mass-to-light ratio is less that 10. Beyond ~ 25 arcmin the amount of dark matter starts to increase, so at 80 arcmin the mass-to-light ratio of NGC 5128 becomes ~ 14. This is *much* lower than expected: Bahcall, Lubin and Dorman (1995) found a relation based on the compilation of the data from the literature that for elliptical galaxies $M_T/L_B = (200 \pm 50)h_0 \times (R/100\text{kpc})$, which becomes for the adopted $h_0 = 0.70$ at $R = 80$ kpc, $M_T/L_B = 112 \pm 28$.

If we now compare the results for the estimates of the total mass interior to a given radius using both X–rays and the "tracer mass estimator" we can see that interior to ~ 30 arcmin both techniques agree very well. Beyond ~ 30 arcmin the X–rays tend to predict higher inferred mass, so that at 80 kpc the discrepancy between the two becomes significant: X–rays predict $M_X = (11.6 \pm 1.00) \times 10^{11} M_\odot$ whereas the estimate based on the PNe gives $M_T(\text{PNe}) = (5.48 \pm 0.98) \times 10^{11} M_\odot$. A similar discrepancy was noted earlier in this Chapter in the case of the early–type galaxy NGC 1399: it was argued that this may be the effect of a contribution of the X–ray gas pressure by the intercluster medium (ICM) (Bertin 2000). However, NGC 5128 does not belong to a cluster and the solution to this problem may be different: the lack of the assumed hydrostatic equilibrium. Very recently, two papers by Humphrey et al. (2006) and Fukazawa et al. (2006) analyzed two samples made using CHANDRA observations assuming hypothesis that hydrostatic equilibrium holds. However, Diehl and Statler (2006) using a sample of 54 normal ellipticals from the CHANDRA archive found that there is no correlation between optical and X–ray ellipticity as would be expected had the gas settled into hydrostatic equilibrium with a given gravitational potential. They found that the hot gas appears to be very disturbed and that the concept of normal ellipticals which host calm, hydrostatic gas needs a revision and argue that X–ray derived radial mass profiles may be in error by a factor of a few. Pellegrini and Ciotti (2006) very recently attempted to reconcile the optical and X–ray mass using the case of the early–type galaxy NGC 3379 (see also this Chapter, Sec. 5.2.3) and found that a discrepancy of ~ 2 can be explained by deviations from hydrostatic equilibrium of the hot gas (see also Ciotti and Pellegrini 2004). This may well be the case in the example of NGC 5128 but further detailed analysis is necessary; the attempt in this book presents only a first step which quantifies the discrepancy between the X–ray and optical mass.

TABLE 5-9

PROJECTED VELOCITY DISPERSION MEASUREMENTS OF GCS IN NGC 5128.

r (arcmin) (1)	σ (km s^{-1}) (2)	err_σ (km s^{-1}) (3)	s_3 (4)	err_s_3 (km s^{-1}) (5)	s_4 (6)	err_s_4 (7)	N (8)
2	147	18	0.15	0.42	-0.68	0.84	34
6	127	10	0.36	0.28	-0.01	0.56	77
10	132	12	0.32	0.31	0.91	0.62	62
14	112	14	-0.48	0.45	-0.52	0.89	30
18	139	28	0.27	0.71	-1.18	1.41	12
22	156	33	-0.11	0.74	-1.59	1.48	11
37	140	23	-0.21	0.56	-0.47	1.12	19

NOTES – Col. (1): radial bin. Col. (2): velocity dispersion. Col. (3): formal errors for the velocity dispersion. Col. (4): s_3 parameter. Col. (5): formal errors for the s_3 parameter. Col. (6): s_4 parameter. Col. (7): formal errors for the s_4 parameter. Col. (8): number of GCs in a given bin.

TABLE 5-10

PROJECTED VELOCITY DISPERSION MEASUREMENTS OF PNE IN NGC 5128.

r (arcmin) (1)	σ (km s^{-1}) (2)	err_σ (km s^{-1}) (3)	s_3 (4)	err_s_3 (km s^{-1}) (5)	s_4 (6)	err_s_4 (7)	N (8)
2	143	11	-0.07	0.19	-0.44	0.39	158
6	134	07	0.29	0.17	-0.02	0.34	204
10	120	07	-0.06	0.20	0.14	0.40	147
14	128	11	0.44	0.29	0.16	0.58	72
18	158	14	-0.26	0.33	-0.41	0.65	56
22	99	11	-0.56	0.43	0.85	0.85	33
27	106	13	0.33	0.41	-0.16	0.82	36
35	89	10	-0.31	0.38	0.83	0.76	42
45	105	18	-0.48	0.58	-0.50	1.15	18
65	123	33	-1.25	0.93	1.85	1.85	7

NOTES – Col. (1): radial bin. Col. (2): velocity dispersion. Col. (3): formal errors for the velocity dispersion. Col. (4): s_3 parameter. Col. (5): formal errors for the s_3 parameter. Col. (6): s_4 parameter. Col. (7): formal errors for the s_4 parameter. Col. (8): number of PNe in a given bin.

TABLE 5-11

MASS ESTIMATES OF NGC 5128 USING GCS, PNE AND X–RAYS.

r (arcmin) (1)	$M_{\rm GCs}$ ($10^{11}M_{\odot}$) (2)	err$M_{\rm GCs}$ ($10^{11}M_{\odot}$) (3)	$M_{\rm PNe}$ ($10^{11}M_{\odot}$) (4)	err$M_{\rm PNe}$ ($10^{11}M_{\odot}$) (5)	$M_{\rm rot}$ ($10^{11}M_{\odot}$) (6)	$M_{\rm X}$ ($10^{11}M_{\odot}$) (7)	err$M_{\rm X}$ ($10^{11}M_{\odot}$) (8)
8	0.99	0.14	0.96	0.24	0.18	1.4	0.18
12	1.57	0.30	1.35	0.34	0.27	1.8	0.22
16	1.84	0.38	1.70	0.42	0.36	2.1	0.25
20	2.17	0.43	2.31	0.54	0.45	3.0	0.27
24	2.61	0.52	2.47	0.59	0.54	3.5	0.30
50	3.97	0.74	3.25	0.84	1.13	7.0	0.80
80	—	—	3.68	0.96	1.80	11.6	1.00

NOTES – Col. (1): radius interior to which a given mass is calculated. Col. (2): estimate of the total mass based on the GCs expressed in units of $10^{11}M_{\odot}$. Col. (3): error for the quantity in Col. (2) expressed in the same units. Col. (4): estimate of the total mass based on the PNe expressed in units of $10^{11}M_{\odot}$. Col. (5): error for the quantity in Col. (4) expressed in the same units. Col. (6): estimate of the total mass based on the rotation of NGC 5128 expressed in units of $10^{11}M_{\odot}$. Col. (7): estimate of the total mass based on the X–ray methodology expressed in units of $10^{11}M_{\odot}$ for $\beta = 0.40$ and $T = 0.29$ keV. Col. (8): error for the quantity in Col. (7) expressed in the same units. The total mass is obtained by summing: $M_{T\,(\rm GCs,PNe)} = M_{\rm GCs,PNe} + M_{\rm rot}$ (see text for details).

TABLE 5-12

MASS-TO-LIGHT RATIO IN THE B-BAND ESTIMATES OF NGC 5128 USING GCS, PNE AND X–RAYS EXPRESSED IN SOLAR UNITS.

r (arcmin) (1)	$M/L_{\rm GCs}$ ($M_{\odot}/L^{B}_{\odot}$) (2)	err$M/L_{\rm GCs}$ ($M_{\odot}/L^{B}_{\odot}$) (3)	$M/L_{\rm PNe}$ ($M_{\odot}/L^{B}_{\odot}$) (4)	err$M/L_{\rm PNe}$ ($M_{\odot}/L^{B}_{\odot}$) (5)	$M/L_{\rm X}$ ($M_{\odot}/L^{B}_{\odot}$) (6)	err$M/L_{\rm X}$ ($M_{\odot}/L^{B}_{\odot}$) (7)
8	5.24	1.19	5.11	1.19	6.28	0.6
12	6.34	1.44	5.58	1.44	6.20	0.8
16	7.00	1.64	6.65	1.64	6.69	0.8
20	7.84	1.95	8.36	1.95	8.26	0.9
24	9.00	2.10	8.60	2.10	8.98	1.0
50	13.42	2.98	11.53	2.98	18.6	2.5
80	—	—	13.77	3.59	28.2	3.0

NOTES – Col. (1): radius interior to which a given mass-to-light ratio is calculated. Col. (2): estimate of the mass-to-light ratio in the B-band based on the GCs expressed in solar units. Col. (3): error for the quantity in Col. (2) expressed in the same units. Col. (4): estimate of the mass-to-light ratio in the B-band based on the PNe expressed in solar units. Col. (5): error for the quantity in Col. (4) expressed in the same units. Col. (6): estimate of the mass-to-light ratio in the B-band based on the X–rays expressed in solar units. Col. (7): error for the quantity in Col. (6) expressed in the same units.

5.3.7. SUMMARY OF THE RESULTS RELATED TO NGC 5128

In this Section we investigated the kinematics calculated from the observations of GCs (Peng et al. (2004a) and Woodley et al. (2005)) and PNe (by Peng et al. 2004b) in the early–type galaxy NGC 5128. From the observational data we calculated velocity dispersions and skewness and kurtosis parameters using standard statistical procedures. We performed an X–ray modelling assuming the hypothesis of hydrostatic equilibrium. Using mass obtained in such a way, we performed the Jeans modelling and compared the modelling results with the observational ones. We also calculated the total mass (and the total mass-to-light ratio) of NGC 5128 using X–ray methodology and a new "tracer mass estimator" in order to compare these estimates.

Our conclusions are as follows.

(1) We show that the departures from the Gaussian (given with the skewness and kurtosis parameters, s_3 and s_4, estimated from the radial velocities) are not large. The similar values of the calculated mass of NGC 5128 at different radii using different tracers suggest that the orbital anisotropies of these two different populations are very similar and small.

(2) We have performed an X–ray modelling of NGC 5128 and solved the Jeans equation. It was found that interior to ~ 25 arcmin ($\sim 5R_e$) the mass is not dominated by dark matter. This is not inconsistent with the previous results (see Chapter 2) for 2 early–type galaxies (IC 1459, IC 3370) for which dark matter interior to $\sim 3R_e$ did not appear to dominate. The mass-to-light ratio which we inferred (in the B-band and in solar units) ranges from 4 in the inner regions to 14 in the outer parts of NGC 5128.

(3) Using a new "tracer mass estimator" of Evans et al. (2003) we find that the increase of the total mass of NGC 5128 beyond ~ 25 arcmin ($\sim 5R_e$) implies the existence of dark matter: the total mass rises from $\sim 3 \times 10^{11} M_\odot$ (corresponds the mass-to-light ratio in the B-band of ~ 9) at $\sim 5R_e$ to $\sim 5.5 \times 10^{11} M_\odot$ (corresponds the mass-to-light ratio in the B-band of ~ 14). This amount of dark matter (in agreement with Peng et al. 2004c) is lower than expected (see, for example, Bahcall et al. 1995).

(4) We found that, assuming hydrostatic equilibrium, the total mass of NGC 5128 measured at the last observed point, obtained using the X–rays is equal to $11.6 \times 10^{11} M_\odot$ which is ~ 2 times higher than that found using a "tracer mass estimator". A possible solution to this problem may be the lack of hydrostatic equilibrium in the outer parts of the galaxy, as suggested by Pellegini and Ciotti (2006) and Diehl and Statler (2006).

(5) It remains difficult to draw general conclusions regarding anisotropies in the outer parts of early–type galaxies in general at this point because the sample of galaxies is still too small. Also, in the case of NGC 5128 there are problems regarding small number of observed clusters per galaxy. Judging from the sample of clusters which we used in this book we did not find large departures from the Gaussian. The similarities of the mass estimates mentioned in the item (1) seem to imply that for NGC 5128 anisotropies are small. As it was shown in Chapter 2, for the ellipticals IC 1459 (beyond $\sim 2R_e$) and NGC 3379 (beyond $\sim 1.4R_e$) there is a hint for

radial anisotropies. Dekel et al. (2005) recently found, using numerical simulations of disc–galaxy mergers, that for the early–type galaxies the stellar orbits in their outer parts are very elongated. Also, very recently, Teodorescu et al. (2005) found that for PNe in the flattened early–type galaxy NGC 1344 the departures from the Gaussian are small (see their figure 18).

At the time of this writing (September 2006) a preprint of the accepted paper by Woodley (2006) appeared in which a much higher mass was claimed based on the new (but still unpublished) sample of GCs of NGC 5128. For example, Woodley finds within $\sim$ 15 kpc the total mass of $4 \times 10^{11} M_{\odot}$. In this book, as well as in the aforementioned Peng et al. papers, the total mass within $\sim$ 15 kpc is $\sim 2 \times 10^{11} M_{\odot}$. The reason for this discrepancy lies in the parameter γ (Woodley, private communication): in this book $\gamma_{\rm GC} = 2.72$ was used and Woodley used $\gamma_{\rm GC} = 3.65$. Woodley (private communication) claims that Peng et al. (2004b,c) erroneously used surface density slope instead of the volume density slope. Note however, that using completely different technique, such as the X–ray methodology (Kraft et al. 2003) half of this higher mass is obtained: $\sim 2 \times 10^{11} M_{\odot}$ within $\sim$ 15 kpc. At $\sim$ 50 kpc Woodley (2006) finds the total mass equal to $1.3 \pm 0.5 \times 10^{12} M_{\odot}$ which is again not consistent with the estimate based on X–rays which is equal to $7.0 \pm 0.8 \times 10^{11} M_{\odot}$. As one can see from Fig. (5.9) the X-ray mass is in very good agreement with that obtained TME interior to $\sim$ 50 kpc. This shows that the variations in the γ parameter may cause significant discrepancies. It is worth noting that both Peng et al. (2004b,c) and Woodley (2006) calculated the γ parameter outside of 5 kpc because of the incompleteness; this may have influenced the true value of the γ parameter. That is why we decided to calculate the total mass of this galaxy using another estimator which uses point tracers (such as GCs and PNe) but *does not* depend on the density slope. Bahcall and Tremaine (1979) give the following formula (which uses the same notation as previously in this book) for the isotropic case:

$$M = \frac{16}{GN} \sum_i v_{{\rm los}\,i}^2 R_i. \tag{5.12}$$

Using this formula we found, for example, that interior to $\sim$ 16 kpc the total mass obtained in this way using GCs is equal to $\sim 1.8 \times 10^{11} M_{\odot}$ which is very close to the value obtained using the Evans et al. TME ($M_{\rm GCs} = 1.84 \times 10^{11} M_{\odot}$, see TABLE 5-11). Within $\sim$ 50 kpc using the formula from Bahcall and Tremaine (1979) and the sample of GCs the mass becomes equal to $\sim 3.3 \times 10^{11} M_{\odot}$ again very close to the estimate based on the Evans et al. TME ($M_{\rm GCs} = 3.97 \times 10^{11} M_{\odot}$, see TABLE 5-11). These two estimates at two different radii are based only on the *random* motions and the rotational part was not taken into account. Therefore, for the estimate of the total mass the appropriate values from the column (6) found in the TABLE 5-11 must be added. It is also important to inspect Fig. (5.7) and Fig. (5.8) in which the Jeans modelling was presented: it is obvious that much higher masses can not provide a satisfactory fit to the observed velocity dispersion (the Jeans modelling is not present in Woodley 2006). The mass-to-light ratio in the B-band between $\sim$ 4 and $\sim$ 14 provides a good fit to the mass-to-light ratio for both GCs and PNe. The

mass-to-light ratio in the B-band inferred by Woodley (2006) which is equal to 52 (interior to 50 kpc) seems to be too high.

As a final attempt to calculate the total mass of NGC 5128 we decided to use the formula which comes from the paper by Bertin et al. (2002) and is valid for a stationary stellar system for which the scalar virial theorem can be written as:

$$\frac{G\Upsilon L_*}{R_e} = K_V \sigma_0^2,$$

where Υ is the ***stellar*** mass-to-light ratio in the given band, R_e is the effective radius and σ_0 is the central velocity dispersion referred to an aperture radius of $R_e/8$. K_V is the so-called "virial coefficient" which takes into account the projection effects. It was shown recently by Cappellari et al. (2006) that $K_V = 5 \pm 0.1$ for a sample of early-type galaxies at redshift $z \sim 0$. From this equation the total dynamical mass is:

$$M_{\rm dyn} = K_V \frac{\sigma_0^2 R_e}{G}.$$

Inserting the aforementioned value for $K_V = 5$, $\sigma_0 = 150$km s^{-1}, and $R_e = 5.3$ kpc one obtains the total mass dynamical mass of NGC 5128: $M_{\rm dyn} = 1.34 \times 10^{11} M_\odot$. This value takes into account only ***random*** motions and it does not take into account the rotational support so it is necessarily lower than the true value. Taking into account $M_{\rm rot}$ from TABLE 5-11 one gets the total mass of $\sim 3 \times 10^{11} M_\odot$ which is lower (but not much) than the value obtained using GCs and PNe, but is ***much*** lower than the value inferred by Woodley (2006).

To summarize, one can conclude that the results for the total mass (and the mass-to-light ratio) of NGC 5128 obtained in this book are robust, because the results obtained using different techniques are consistent (except for the last measured point, but this may be due to some real physical effect as said in the item 4 above). Also, the results of the Jeans modelling provide an important additional evidence to the robustness of the results presented in this book.

It is certain that the galaxy NGC 5128 will be studied in more detail in the years to come and the question of its total mass will be addressed using more sophisticated observations and models therefore removing the discrepancies found in the literature present at this stage.

Chapter 6
CONCLUSIONS

In this book the problem of dark matter in elliptical galaxies was carefully analyzed using different observational and modelling techniques. The conclusions are as follows.

The *first conclusion* is that the former point of view (cf. Binney and Merrifield 1998) is still valid: it remains very difficult to establish unambiguously the existence of dark haloes in elliptical galaxies (at least out to a given distance from the center; most probably out to $\sim 3R_e$). Small values of the $|h_4|$ parameter at large radial distances from the center of a given galaxy can mean that there is no significant orbital anisotropy and that a slow decline (or even increase) of the velocity dispersion is due to the existence of a dark halo. However, as we have shown in the case of the two galaxies, for which the spectra extend to $\sim 3R_e$ (IC 1459, IC 3370), and at least for two other cases which are well studied in literature (NGC 5128 out to $\sim 15R_e$ and NGC 3379 out to $\sim 3.5R_e$) the velocity dispersion does not show such a slow decline (even if the h_4 parameter does show a non-zero value at $\sim 3R_e$ in the case of IC 1459). In principle, it is incorrect to draw conclusions about dark matter in a given galaxy judging only from the behaviour of the velocity dispersion, if the h_4 parameter is not known. Therefore, all statements in literature when there is claim about the existence of dark matter in a given galaxy, but without providing the information about h_4 should be taken with caution, and the data should be, if possible, reanalyzed. A question that one naturally poses is: "how can one establish whether the decline is 'slow'?", or, more precisely, "what is the criterion for the behaviour of the velocity dispersion in the absence of a dark halo?".

These coupled questions lead to the *second conclusion*, also recognized earlier (cf. Binney and Merrifield 1998): for a confirmation of the existence of dark matter in elliptical galaxies detailed modelling is needed. As shown in the previous Chapters, one can use two- and three-integral modelling techniques. Each one has its own merits and shortcomings. Two-integral modelling (which we called detailed Jeans modelling, see Binney, Davies, and Illingworth 1990; this was done for the galaxies for which we had at least major and minor axis spectroscopic data) gives a prediction of the velocity dispersion behaviour and sometimes it might be enough to perform only this analysis: this would be an ideal case of an axisymmetric galaxy in which there are only two integrals of motion. It is not an easy task to find a priori a galaxy which simultaneously possesses these two features: of the four galaxies studied in this book using a two-integral approach and applying detailed Jeans modelling

(IC 1459, IC 3370, NGC 3379, NGC 4105), none of them fulfilled both of these two requirements. It is however interesting to see how they differ with respect to these given requirements: the best fit to the whole observed velocity profile was found in the case of NGC 3379; beyond $\sim 20''$ (the region where this galaxy is axisymmetric) the whole velocity profile can be fitted for both major and minor axis, thus leading to the conclusion that the dark halo is not necessary at least out to $\sim 2-3R_e$. This result is in agreement with the recent studies of Romanowsky et al. (2003) and Sluis and Williams (2006) who studied this galaxy using planetary nebulae (PNe). The problem with PNe (and GCs) is the lack of knowledge of anisotropies at this stage. For IC 1459 and NGC 4105 the velocity dispersion declines again in an agreement with the no dark matter hypothesis, but since the two-integral modelling cannot provide a simultaneous fit to velocity and velocity dispersion one can conclude that the motion in these two galaxies depends on three integrals of motion. Note also that since IC 1459 possesses a stellar counter-rotating core, two-integral modelling based on photometry, fails in the inner regions of this galaxy. The case of IC 3370 was particularly difficult to model because this galaxy shows a large isophotal twist, indicating triaxiality. Still, using the two-integral approach, the fit to the velocity dispersion was obtained without the introduction of a dark halo. Regardless of the fact that the two-integral modelling is not suitable when there are strong departures from axisymmetry and when the motion depends on the third integral, this method is very convenient for establishing the possible range of the mass-to-light ratio of a given galaxy. Its application gave results that are in agreement with the results obtained using other methods: for example, for IC 1459 the estimated mass-to-light ratio ($6 \lesssim M/L_B \lesssim 10$) is in a rough agreement with the value found using X-ray data, while for NGC 3379 the obtained mass-to-light ratio ($5 \lesssim M/L_B \lesssim 9$) is in a better agreement with the values found using X-ray data, PNe, and globular clusters, GCs (out to $\sim 2R_e$; beyond this region the discrepancies with GCs start to occur). It is important to note that a constant mass-to-light ratio *does not exclude* the presence of a dark halo: if the dark matter has the same profile as the stars, the derived mass-to-light ratio will be constant with radius, but of course, it will be higher than that produced by the stars alone (cf. Ashman 1992). But if the mass-to-light ratio of a given galaxy is not significantly different from the result obtained by van der Marel (1991): $M/L_B = 8.33 \pm 0.35$ (for $h = 0.70$ used in this book), one can claim that no significant amount of the dark matter is present. An additional clue related to the two-integral modelling is that there is a tendency for a slight increase of the mass-to-light ratio in the outer parts of the elliptical galaxies which we studied. Applying the simple Jeans modelling (when we model only the velocity dispersion) we could get insights about the matter content in the galaxies for which we had only major axis spectroscopic data. The conclusions do not differ much from what we obtained in the case of the detailed Jeans modelling: only in the case of two galaxies did we have a hint of the existence of dark matter beyond $\sim 1R_e$ which came from the increase of the velocity dispersion (NGC 1339 and NGC 1373). Note, however, that the quality of the data related to these two galaxies is lower than that related to the galaxies analyzed using the detailed Jeans modelling.

The existence of the triaxiality and the existence of the third integral of motion in the elliptical galaxies initiated the development of the three-integral techniques based on the Schwarzschild's (1979) orbit superposition method. The *third conclusion* is related to the three-integral modelling in general: using the three-integral modelling technique one can obtain better fits to the observed galaxy kinematics but the price that one has to pay is rather high. This method is very CPU intensive and requires large disk storage and therefore its application is rather difficult which is the reason why so far only a fairly small number of galaxies has been analyzed in such a way: according to one of the latest reviews which dealt with this issue (Gebhardt 2004) only 17 galaxies were analyzed using three different codes[14] for the orbit superpositions (none of them is freely available), and the analyses mainly dealt with the inner parts, i.e. central massive black holes. Gebhard (2004) however warns: "With so few groups using orbit-based codes, we must be certain that the immense freedom allowed by these codes does not bias the results due to some feature of an individual code." Therefore, one may conclude that the interpretation of the results obtained using the orbit superposition method must be taken with the greatest caution and used (wherever possible) in combination with the results obtained using other methods. The "immense freedom" inherent in these models (choice of orbits, choice of potential, features of the potential, number of orbits, etc) still permits some conclusions related to the "features of an individual code" and the properties of galaxies to be drawn. In our implementation (which makes the second code to be added to the Gebhard's list) orbit superposition method provided hints about the applicability of a given potential. It also gave a possibility to test different features of a given potential (flattening, different mass-to-light ratios, for example). Since this method (Rix et al. 1997 implementation) forces the fit of the velocity and the velocity dispersion, one has to study carefully the modelling of the Gauss-Hermite parameters. We found that in the very difficult case of IC 3370 the constant mass-to-light ratio potential provides a better fit to h_3 and h_4 interior to $2R_e$ (see Fig. (23) in Chapter 2) and that inside this region dark matter is not required. Another example, IC 1459 (see Fig. (24) from Chapter 2), shows how difficult it is to discriminate between different potentials using orbit superposition techniques. Beyond $\sim 1R_e$ both mass-to-light ratio potentials (for $M/L_B \sim 7$ and ~ 10) seem to provide similar fits. None of the potentials used managed to fit satisfactorily the h_4 parameter in the outer parts, therefore making it difficult to draw conclusions about the dark matter content in IC 1459. The overall conclusion is that the three-integral modelling, in our implementation, can only provide a useful hint about applicability of a given potential for a given set of orbits. Given the "immense freedom" of this kind of modelling, this method should (or better, must) be used in combination with other approaches to infer the existence of dark haloes.

[14]Here, we add the code of Romanowsky and Kochanek (2001) that was applied in the Romanowsky et al. (2003) paper.

TABLE 6-1

RESULTS OF DARK MATTER RESEARCH IN ELLIPTICAL GALAXIES USING DIFFERENT METHODOLOGIES

Method	Radius	M/L_B	Reference
Hot gas/X–rays	$13-15R_e$	$\sim 28-60$	This book
Warm gas	$1\ R_e$	~ 5	Pizzella et al. (1997)
Cold gas	$6\ R_e$	~ 18	Oosterloo et al. (2002)
PNe	$15\ R_e$	~ 14	This book
GCs	$8-13R_e$	$\sim 13-24$	This book
Integrated stellar spectra	$1-3R_e$	5-10	This book
Lensing	$5R_e$	~ 8	Treu & Koopmans (2002)

The problems that arose in the three-integral method which show that different approaches have to be applied to a given galaxy in order to determine the existence of the dark halo lead to a *fourth conclusion*: discrepancies between the results of different methodologies have to be studied very carefully because they may indicate that some of the fundamental physical assumptions are not valid and need to be revised and/or some new assumptions should be taken into account. To illustrate the present doubts we compiled the TABLE 5-1 which shows state-of-the-art results in dark matter research. In the first column we put the method of research. The second column is the radius out to which a given method is being applied (it is given in units of effective radius), the third column presents the mass-to-light ratio obtained with a given method at the radius given in the third column (note that it is given in the B-band; we converted the data originally given in other bands to the B-band for the sake of comparison). Finally, in the fourth column are the references.[15] One can see that methods based on gas (hot gas from X-ray observations) and cold gas (from neutral hydrogen observations) give large mass-to-light ratios. It is of interest to note that especially X-ray analyses strongly suggest very large mass-to-light ratios in the outer parts of elliptical galaxies, which has not been confirmed recently using other methods (such as PNe or globular clusters (GCs)). Of course, one should be cautious about these two new techniques when drawing conclusions, because the number of analyzed galaxies is still very small. However, some of the two basic postulates of this method: (i) the fact that the gas obeys the perfect gas low and (ii) the fact that the condition of hydrostatic equilibrium holds, may not be valid (see the discussion in Chapter 3). In the case of the mass-to-light ratio estimate based on the cold gas the basic assumptions are (cf. Oosterloo et al. 2002): (i) spherical mass distribution and (ii) circular orbits of the gas, which may not be true. Also, since the cold gas is not frequent in the early-type galaxies this method is unsuitable for larger surveys in the future. One may notice that in this book strong evidence for dark haloes in the

[15]If a given methodology is discussed in this book, the reference is "This book" is given and the reader is invited to check the related Chapters.

elliptical galaxies was not found inside $\sim 3R_e$. The reasons for this could be (i): our results are biased because our sample included only galaxies that do not have much dark matter, (ii) the modelling that we used was not suitable for the detection of the dark matter. The first of this statements could be true, but one should bear in mind that we analyzed galaxies that are isolated (field), that belong to some group and that belong to the Fornax cluster. The samples of galaxies included both bright and intermediate luminosity galaxies. A bigger sample would, of course, be useful, but even the present one should be large enough to provide some conclusions that might be indicative of the existence of dark matter in the elliptical galaxies. The second statement could also be true, but again, one should take into account that given the "immense liberty" (at least in the three-integral modelling case) such an outcome was one of the possible ones. Therefore, in order to see the convergence of results for a given galaxy (observations plus modelling for every given method), a combination of different methodologies is necessary. The lensing technique, another promising new method, can provide useful insights about the dark matter in distant elliptical galaxies ($z \sim 1$), especially about the evolution of the stellar mass-to-light ratio with redshift. Results obtained so far strongly suggest the existence of large amounts of dark matter ($> 50\%$ of the mass inside the Einstein radius) in the elliptical galaxies. Probably, the best way to study the dark haloes in the near future would be by using PNe and GCs in combination with the integrated spectra data: stellar spectra should provide reliable estimates of the velocity profiles out to $\sim 3R_e$ and PNe and/or GCs in the outer parts. For example, Bridges et al. (2003) obtained (but has not published) results for GCs of, among other galaxies, IC 1459 — it will be of interest to compare their findings with the results obtained in this book.

A *fifth conclusion* is related to the relationship between the X-ray haloes and dark haloes. The X–rays predict an increase of the total mass (and the mass-to-light ratio) with the radius. In general (inside $\sim 3R_e$, region inside which we had long-slit spectra data) there is good agreement between integrated stellar spectra and X–ray estimates. Beyond $\sim 3R_e$ the X-rays predict the existence of larger amounts of dark matter. However, there are discrepancies beyond $\sim 8R_e$ between X–rays and GCs/PNe (see the next conclusion). The reason for this as mentioned earlier (the fourth conclusion) could be due to the lack of hydrostatic equilibrium in these regions. This however remains an open question at this stage.

The *sixth conclusion* is related to the estimates of the total mass (and the mass-to-light ratio) inferred from the studies of the planetary nebulae and globular clusters: in this book we have studied two ellipticals, NGC 1399 and NGC 5128, for which a database of both PNe and GCs exists. The departures from the Gaussian (given with the skewness and kurtosis parameter) are not large although more detailed studies are needed in order to establish them accurately. Since both of these galaxies posses an X–ray halo it was possible to compare the results of different mass tracers: (i) For NGC 1399 the estimates of the total mass based on the GCs and X–rays are in good agreement out to $\sim 10R_e$ and beyond this region they diverge, i.e., X–rays predict a higher mass. Inside $\sim 3R_e$ there is no need for dark matter. At $\sim 10R_e$ the total mass-to-light ratio rises to ~ 45 (in the B-band) implying significant amount of dark matter there. (ii) For NGC 5128 the estimates of the total mass based on

both GCs and PNe agree well with the estimates based on the X–rays out to $\sim 8R_e$. Beyond this radius again the X–ray estimate is the largest one. The estimate for the total mass-to-light ratio in the B-band is ~ 10 which is rather low and is consistent with a low amount of the dark matter there. At $\sim 15R_e$ the estimate based on the PNe is ~ 14 which implies that the amount of dark matter increases between 10 and 15 R_e (the estimate based on the X–rays is even higher, $M/L_B \sim 28$). The overall impression is that dark matter starts to increase its contribution beyond $\sim 3R_e$ and at higher radii it starts to completely dominate.

Given the problems in establishing the very existence of the dark matter haloes at different radii in the elliptical galaxies the *seventh conclusion* comes as no surprise: one cannot say much about the nature of the dark matter content of these galaxies, for example, whether it is baryonic or non-baryonic.

The final, *eighth conclusion* is related to the modelling of the line strength indices: it was shown that in several cases (most notably of IC 1459 and IC 3370) a better fit to the observed values is obtained without dark matter out to $\sim 3R_e$ (the radii out to which we had the observational data).

PROSPECTS FOR THE FUTURE

If we want to establish unambiguously the existence of dark haloes in elliptical galaxies we need to perform more accurate studies involving different interconnected branches of astrophysics. To date, different important aspects (for example, stellar dynamics, X-ray haloes and other mass tracers, chemical evolution) have been studied in detail, but much is left to be done, especially observationally, always bearing in mind the theoretical assumptions which have to be constantly questioned. First of all, it is absolutely necessary to enlarge the sample of integrated stellar spectra of elliptical galaxies observed out to at least three effective radii. For all the existing observations a critical reanalysis that takes into account the full line-of-sight velocity distribution is needed (when such data exist). On the basis of the results from this book, a good way to proceed would be to choose several elliptical galaxies which should be isolated, which should exhibit axisymmetry and are devoid of peculiarities (such as counterrotating core), which should possess an X-ray halo, and preferably have other possible mass tracers (for example, PNe and/or GCs) in order to perform a detailed stellar kinematic modelling (inside $\sim 3R_e$) and an X-ray study (beyond $1R_e$). This is, of course, an ambitious undertaking – a search for such candidates is already a demanding task. Other mass tracers will have to be studied and the results should be confronted with the previous two analyses. Detailed chemical evolution modelling should also be performed. Only in this way can we expect that the dark matter problem in elliptical galaxies will be fully understood.

Appendix 1
ILL-POSED PROBLEMS AND REGULARIZATION

A1.1. BASIC CONCEPTS

The solution of the system of equations given in eq. (14) of Rix et al. (1997) gives the orbital weights γ_k. Non-negative least square (NNLS) fit always gives a formally unique solution (more about NNLS in a separate appendix). However, this solution will in principle be very irregular in phase space which is physically implausible. Non-negativity is the only physical constraint on the distribution function (DF).

The study of the extremely simple worked example (from Hansen (2001)) provides a description of the problems that one faces when encountered with an ill-posed problem such as the one mentioned above. One can consider the following least-squares problem:

$$\min_{\mathbf{x}} \parallel A\mathbf{x} - \mathbf{b} \parallel_2 . \tag{A1.1}$$

Here, coefficient matrix A and right-hand side (RHS) vector b are given by:

$$A = \begin{pmatrix} 0.16 & 0.10 \\ 0.17 & 0.11 \\ 2.02 & 1.29 \end{pmatrix} \tag{A1.2}$$

and

$$\mathbf{b} = \begin{pmatrix} 0.27 \\ 0.25 \\ 3.33 \end{pmatrix} \quad . \tag{A1.3}$$

In this case the RHS vector $\mathbf{b}$ is generated by simply adding a small perturbation to an exact RHS that corresponds to the exact solution

$$\mathbf{x} = \begin{pmatrix} 1.00 \\ 1.00 \end{pmatrix} \quad :$$

$$\mathbf{b} = \begin{pmatrix} 0.16 & 0.10 \\ 0.17 & 0.11 \\ 2.02 & 1.29 \end{pmatrix} \times \begin{pmatrix} 1.00 \\ 1.00 \end{pmatrix} + \begin{pmatrix} 0.01 \\ -0.03 \\ 0.02 \end{pmatrix} \quad . \tag{A1.4}$$

The problem with this least-squares problem is that the matrix A is ill-conditioned. Namely, since its condition number[16] is equal to 1.0975×10^3 (using MATLAB `cond` routine), this means that the computed solution will be very sensitive to perturbations of the data. If now one calculates the ordinary least-squares (LSQ) solution by means of QR factorization (using, for example, NAG routine `F08AEF`) one obtains the solution:

$$\mathbf{x}_{\mathrm{LSQ}} = \begin{pmatrix} 7.01 \\ -8.40 \end{pmatrix} \quad . \tag{A1.5}$$

It is quite obvious that this solution is worthless. One therefore must try to apply some procedure in order to get a better approximation to the exact solution: $\bar{\mathbf{x}}^T = (1 \;\; 1)$.

The very large condition number implies that the columns of the matrix A are nearly linearly dependent. Therefore one could try to replace the ill-conditioned matrix $A = (\mathbf{a_1} \;\; \mathbf{a_2})$ with either $(\mathbf{a_1} \;\; \mathbf{0})$ or $(\mathbf{0} \;\; \mathbf{a_2})$, both of each are well conditioned. Thus one gets two so-called basic solutions:

$$\mathbf{x}^1_{\mathrm{B}} = \begin{pmatrix} 1.65 \\ 0.00 \end{pmatrix} \quad , \quad \mathbf{x}^2_{\mathrm{B}} = \begin{pmatrix} 0.00 \\ 2.58 \end{pmatrix} \quad . \tag{A1.6}$$

The corresponding residual norms are both small:

$$\| A\mathbf{x}^{(1)}_B - \mathbf{b} \|_2 = 0.031, \quad \| A\mathbf{x}^{(2)}_B - \mathbf{b} \|_2 = 0.036, \tag{A1.7}$$

and these solutions are much less sensitive to perturbations of the data. However, as can be seen these solutions are again not good and they have nothing in common with the exact solution: $\bar{\mathbf{x}}^T = (1 \;\; 1)$.

When one tries to find the ordinary least-squares solution, $\mathbf{x}_{\mathrm{LSQ}}$ one can encounter a major difficulty that its norm is much greater than the norm of the exact solution. Therefore, one can try to add some side constraint that the solution norm must not exceed a certain value α:

$$\min_{\mathbf{x}} \| A\mathbf{x} - \mathbf{b} \|_2 \quad \text{subject to} \quad \| \mathbf{x} \| \leq \alpha. \tag{A1.8}$$

For a set of different α's (α =0.1, 1.0, 1.385, 10) one obtains:

$$\mathbf{x}_{0.1} = \begin{pmatrix} 0.08 \\ 0.05 \end{pmatrix} , \; \mathbf{x}_{1.0} = \begin{pmatrix} 0.84 \\ 0.54 \end{pmatrix} , \; \mathbf{x}_{1.385} = \begin{pmatrix} 1.17 \\ 0.74 \end{pmatrix} , \; \mathbf{x}_{1.385} = \begin{pmatrix} 6.51 \\ -7.60 \end{pmatrix} . \tag{A1.9}$$

It is obvious that if one sets the value of α properly (for example, in this case, α = 1.385), one can obtain the solution that is rather close to the exact one: $\bar{\mathbf{x}}^T = (1 \;\; 1)$. However, one must take care when choosing α, and the proper choice is not obvious.

[16]The condition number of a matrix A is a measure of the sensitivity of the solution of a system of linear equations to errors in the data. It also gives an indication of the accuracy of the results from matrix inversion and the linear equation solution. If the condition number of A is large, A is said to be ill-conditioned. A value near 1 indicates a well-conditioned matrix. The condition number is the ratio of the largest singular value of A to the smallest.

The example given above is a very small one but it provides an idea of problems that one encounters when dealing with large matrices and vectors: in this book when we solve the NNLS problems we use 729 orbits and 500 constraints that leads to matrices whose dimensions are 729×500. The problems are the following:

- The condition number of the matrix A is large.
- Replacement of A by a well-conditioned matrix derived from A does not necessarily lead to a useful solution.
- One must take care when imposing additional constraints.

To overcome these problems numerical regularization theory is used in order to provide efficient and numerically stable methods for inclusion of proper side constraints that lead to useful stabilized solutions. These methods also provide robust ways for choosing the optimal weight given to the side constraints such that the regularized solution is a good approximation to the desired unknown solution.

A good introduction to the regularization can be found in the book ***Numerical Recipes in Fortran*** (Press et al. 1994). In our implementation of the regularization we have relied on the functions written in MATLAB by P.C. Hansen (descriptions are given in a manual ***Regularization Tools. A Matlab Package for Analysis and Solution of Discrete Ill-Posed Problems*** (Hansen 2001)).

A1.2. DISCRETE ILL-POSED PROBLEMS

The definition of the ill-posed problem due to J. Hadamard states that the problem is ill-posed if the solution is not unique or if it is not a continuos function of the data –i.e., if an arbitrarily small perturbation of the data can cause an arbitrarily large perturbation of the solution. As a side note, Hadamard believed (beginning of the 20th century) that ill-posed problems were "artificial" in that they would not describe physical systems (for applications in astronomy see Craig and Brown 1986).

Certain finite-dimensional discrete problems have properties that are very similar to those of ill-posed problems [17] (for example, being highly sensitive to high-frequency perturbations), so it is common to associate the term ***discrete ill-posed problems*** with these problems. For linear systems of equations:

$$A\mathbf{x} = \mathbf{b}, \qquad A \in \Re^{m \times n} \tag{A1.10}$$

and linear least-squares problems

$$\min_{\mathbf{x}} \| A\mathbf{x} - \mathbf{b} \|_2, \qquad A \in \Re^{m \times n}, \qquad m > n, \tag{A1.11}$$

one can say that these are discrete ill-posed problems if both of these two criteria are met: (i) the singular values of A decay gradually to zero and (ii) the ratio between the largest and the smallest nonzero singular values is large. The first criterion implies that there is no "nearby" problem with a well-conditioned coefficient matrix and with well-determined numerical rank (see below). The routines used in MATLAB environment require singular value decomposition (SVD) so this will be discussed in more detail later. The second criterion implies that the matrix A is ill-conditioned.

[17] Ill-posed problems must be infinite dimensional (see Hansen 2001).

A1.3. TIKHONOV REGULARIZATION

The most common and most widely used form of regularization is the so-called Tikhonov regularization. The basic idea is to define a regularized solution $\mathbf{x}_\lambda$ as the minimizer of the following weighted combination of the residual norm and the side constraint:

$$\mathbf{x}_\lambda = \text{argmin}\left\{ \parallel A\mathbf{x} - \mathbf{b} \parallel_2^2 + \lambda^2 \parallel L(\mathbf{x} - \mathbf{x}^*) \parallel_2^2 \right\}, \tag{A1.12}$$

where the regularization parameter λ controls the weight given to minimization of the side constraint relative to minimization of the residual norm. Here, $\mathbf{x}^*$ is an initial estimate of the solution, and L is typically either the identity matrix I_n or a $p \times n$ discrete approximation of the $(n-p)$-th derivative operator. It is obvious that a large value of λ (large amount of regularization) favors a small solution seminorm at the cost of a large residual norm, while a small value of λ (small amount of regularization) has the opposite effect. The regularization parameter λ thus controls the properties of the regularized solution and should be chosen with care.

One should stress that there are many other regularization methods apart from Tikhonov regularization: (i) direct regularization methods are: least-squares with a quadratic constraint, damped SVD/GSVD (generalized SVD), truncated SVD (TSVD), truncated GSVD (TGSVD), maximum entropy regularization, and (ii) iterative regularization methods are: conjugate gradients and LSQR, bidiagonalization with regularization, ν method.

A1.4. SVD AND GENERALIZED SVD

Some useful tools in analyses of ill-posed problems are the singular value decomposition (SVD) and its generalization to two matrices, the generalized singular value decomposition (GSVD) of the matrix pair (A, L). Let $A \in \Re^{\mathrm{m}\times\mathrm{n}}$ be a rectangular matrix with $m \geq n$. Then the SVD of the matrix A is a decomposition of the form:

$$A = U\Sigma V^T = \sum_{i=1}^{n} \mathbf{u}_i \sigma_i \mathbf{v}_i^T, \tag{A1.13}$$

where $U = (\mathbf{u}_1, ..., \mathbf{u}_n)$ and $V = (\mathbf{v}_1, ..., \mathbf{v}_n)$ are the matrices with orthonormal columns, $U^T U = V^T V = I_n$, and $\Sigma = \text{diag}(\sigma_1, ..., \sigma_n)$ has non-negative diagonal elements appearing in non-increasing order such that:

$$\sigma_1 \geq \sigma_2 \geq ... \geq \sigma_n \geq 0. \tag{A1.14}$$

The numbers σ_i are the singular values of the matrix A (see the definition of the condition number above). The vectors $\mathbf{u}_i$ and $\mathbf{v}_i$ are the left and right singular vectors of A. respectively. According to the definition, the condition number of A is equal to:

$$\text{cond}(A) = \frac{\sigma_1}{\sigma_n}. \tag{A1.15}$$

The GSVD of the matrix pair (A, L) is a generalization of the SVD of A in the sense that the generalized singular values of (A, L) are the square roots of the generalized

eigenvalues of the matrix pair (A^TA, L^TL). The dimension of $A \in \Re^{\mathrm{m}\times\mathrm{n}}$ and $L \in \Re^{\mathrm{p}\times\mathrm{n}}$ satisfy $m \geq n \geq p$ (this is always fulfilled in the case of the ill-posed problems). The GSVD is the decomposition of A and L in the form:

$$a = \begin{pmatrix} \Sigma & 0 \\ 0 & I_{n-p} \end{pmatrix} \quad X^{-1}, \qquad L = V(M, 0)X^{-1}, \tag{A1.16}$$

where the columns of $U \in \Re^{\mathrm{m}\times\mathrm{n}}$ and $V \in \Re^{\mathrm{p}\times\mathrm{p}}$ are orthonormal, $X \in \Re^{n\times n}$ is nonsingular, and Σ and M are $p \times p$ matrices: $\Sigma = \mathrm{diag}(\sigma_1, \ldots, \sigma_p)$, $M = \mathrm{diag}(\mu_1, \ldots, \mu_p)$. The diagonal values of Σ and M are non-negative and ordered in the following manner:

$$0 \leq \sigma_1 \leq \ldots \sigma_p \leq 1, \quad 1 \geq \mu_1 \geq \ldots \mu_p > 0, \tag{A1.17}$$

and are normalized such that:

$$\sigma_i^2 + \mu_i^2 = 1, \qquad i = 1, \ldots, p. \tag{A1.18}$$

Now one can define the generalized singular values γ_i of (A, L) as the ratios:

$$\gamma_i = \frac{\sigma_i}{\mu_i}, \qquad i = 1, \ldots, p. \tag{A1.19}$$

A1.5. THE L-CURVE

The so-called L-curve is a very convenient graphical tool for analysis of discrete ill-posed problems. It is a plot for all valid regularization parameters of the (semi)norm $\| L\mathbf{x}_{\mathrm{reg}} \|_2$ of the regularized solution versus the corresponding residual norm $\| A\mathbf{x}_{\mathrm{reg}} - \mathbf{b} \|_2$ (see Fig. (A1.1)). Thus, the L-curve displays the compromise between the minimization of these quantities (see also Fig. 18.4.1. from Press et al. (1994)). Its name came from the fact that for discrete ill-posed problems the L-curve (when plotted in log-log scale), almost always has a characteristic L-shaped form (more or less deformed). There is a distinct corner that separates vertical and horizontal parts of the curve.

For a general-form regularization ($L \neq I_n$) the following equation holds that gives the expression for error in $\mathbf{x}_{\mathrm{reg}}$:

$$\mathbf{x}_{\mathrm{reg}} - \bar{\mathbf{x}} = \left(\sum_{i=1}^{p} f_i \frac{\mathbf{u}^T\mathbf{e}}{\sigma_i}\mathbf{x}_i + \sum_{i=p+1}^{n} (\mathbf{u}^T\mathbf{e})\mathbf{x}_i \right) + \sum_{i=p+1}^{n} (f_i - 1)\frac{\mathbf{u}^T\bar{\mathbf{b}}}{\sigma_i}\mathbf{x}_i. \tag{A1.20}$$

Here, $\mathbf{x}_{\mathrm{reg}}$ is a regularized solution, the term in parenthesis denotes the perturbation error due to the perturbation $\mathbf{e}$, and the second term is the regularization error that is caused by regularization of the unperturbed component $\bar{\mathbf{x}}$. Filter factors for the Tikhonov regularization are given as:

$$f_i = \frac{\sigma_i^2}{(\sigma_i^2 + \lambda^2)} \quad \text{for} \quad L = I_n \tag{A1.21}$$

and

$$f_i = \frac{\gamma_i^2}{(\gamma_i^2 + \lambda^2)} \quad \text{for} \quad L \neq I_n \tag{A1.22}$$

When one introduces only little regularization, most of the filter factors f_i are approximately one and the error $\mathbf{x}_{\text{reg}} - \bar{\mathbf{x}}$ is dominated by the perturbation error. On the contrary, if one introduces plenty of regularization, most filter factors are small ($f_i \ll 1$, and $\mathbf{x}_{\text{reg}} - \bar{\mathbf{x}}$ is dominated by the regularization errors.

In the case of the Tikhonov regularization the L-curve divides the first quadrant into two regions: any regularized solution must lie on or above this curve (see Fig. (A1.1)). Thus the solution obtained using the Tikhonov regularization is optimal in the sense that for a given residual norm there does not exist a solution with smaller seminorm than the Tikhonov solution (the same also holds when one interchanges the roles of the norms). When one locates the corner of the L-curve one can compute an approximation to the optimal regularization parameter that leads to a computation of regularized solution with a good balance between two error types. The definition of the L-curve's corner is the point with the maximum curvature in log-log scale.

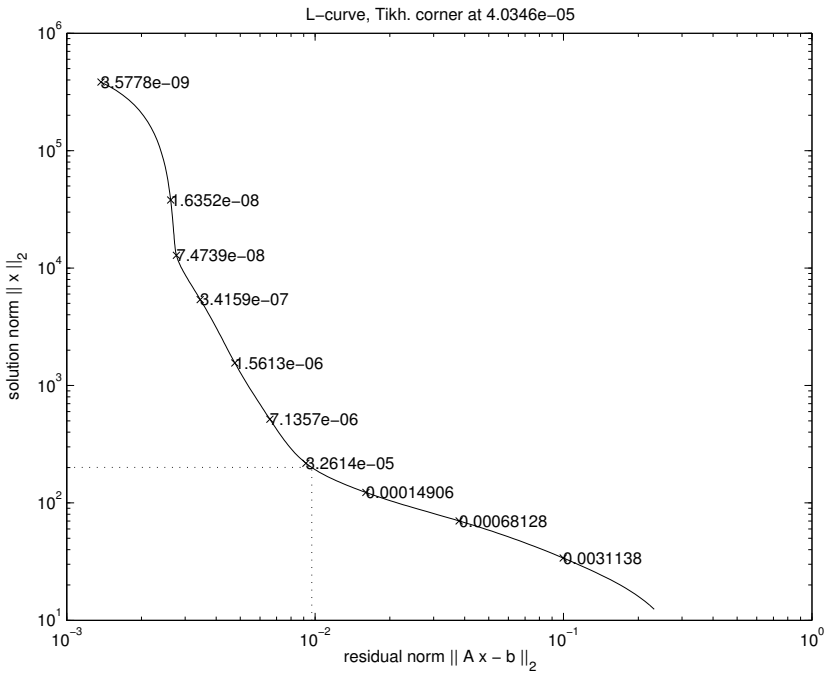

Figure A1.1: L-curve in case of orbits in triaxial logarithmic potential for which $p = q = 0.9$. Inclination is 40° and box orbits are used.

A1.6. TIKHONOV REGULARIZATION

Tikhonov regularization is a direct method because the regularized solution $\mathbf{x}_\lambda$ (defined in eq. Eq. (A1.12)) is the solution to the following least-squares problem:

$$\mathbf{b} = \min \left\| \begin{pmatrix} A \\ \lambda L \end{pmatrix} \mathbf{x} - \begin{pmatrix} \mathbf{b} \\ \lambda L \mathbf{x}^* \end{pmatrix} \right\|_2 \quad . \tag{A1.23}$$

This problem is then solved taking into account the non-negativity of the orbital weights (see Appendix 2 for more details about NNLS).

A1.7. CHOICE OF THE REGULARIZATION PARAMETER

The appropriate choice of the regularization parameter means a good balance between the perturbation error and the regularization error in the regularized solution. There are two approaches: (1) methods based on knowledge, or a good estimate of $\| \mathbf{e} \|_2$ (the norm of the perturbation of the RHS) and (2) methods that do not require the knowledge of $\| \mathbf{e} \|_2$, but extract the necessary information from the given RHS. We have used the L-curve criterion that belongs to the second class using Hansen (2001) routines written in MATLAB. For a continuous regularization parameter λ, we compute the curvature of the curve $(\log \| \mathrm{A}\mathbf{x}_\lambda - \mathbf{b} \|_2, \log \| \mathrm{L}\mathbf{x}_\lambda \|_2)$, where λ is curve's parameter and then search for a point with maximum curvature: this point then can be defined as the L-curve corner. In a similar manner, when the regularization parameter is discrete one can approximate the discrete L-curve in log-log scale by a two-dimensional spline curve, compute the point on the spline curve with maximum curvature and define the corner of the discrete L-curve as the point which is closest to the corner of the spline curve.

Appendix 2
NNLS (NON-NEGATIVE LEAST SQUARES)

As it is shown in Chapter 2 and in Appendix 1, in solving the least-squares problem (Rix et al. 1997, eq. (14)) there is a constraint that for the occupation vector $(\gamma_1, \ldots, \gamma_{N_0})$, the following relation holds: $\gamma_k \geq 0$, for $k = 1, \ldots, N_0$ (N_0 is the number of orbits). This is the non-negative least squares (NNLS) problem to be solved after the regularization procedure has been performed:

$$\textit{Minimize} \parallel Ex - f \parallel \textit{subject to } x \geq 0.$$

The standard algorithm for this is given by Lawson and Hanson (1974) and the following discussion relies on this book.

Initially one takes the matrix E (matrix on the left hand side of eq. (14) from Rix et al). Its dimension is $m_2 \times n$ (in our case, $m_2 = 500$ and $n = 729$)[18] so the dimension is 500×729, because we used 500 observational constraints and 729 orbits). The vector that consists of observational points on the right hand side of this equation has the dimension $m_2 = 500$. Finally, the unknown vector x has the dimension $n = 729$. Auxiliary n-vectors w and z provide a working space. Index sets $\mathcal{P}$ and $\mathcal{Z}$ are defined and modified in the course of execution of the algorithm. Variables indexed in the set $\mathcal{Z}$ are held at the value zero. Variables indexed in the set $\mathcal{P}$ will be free to take values different from zero. If such a variable takes a non-positive value, the algorithm will either move the variable to a positive value or else set the variable to zero and move its index from from set $\mathcal{P}$ to set $\mathcal{Z}$. The solution vector x is given as an output.

The following steps are contained in the NNLS algorithm:

Step 1 Set $\mathcal{P} :=$ NULL, $\mathcal{Z} := \{1, 2, \ldots, n\}$, and $x := 0$.

Step 2 Compute the n-vector $w := E^T(f - Ex)$

Step 3 If the set $\mathcal{Z}$ is empty or if $w_j \leq 0$ for all $j \in \mathcal{Z}$, go to *Step 12*.

Step 4 Find an index $t \in \mathcal{Z}$ such that $w_t = \max\{w_j : j \in \mathcal{Z}\}$.

Step 5 Move the index t from set $\mathcal{Z}$ to set $\mathcal{P}$.

Step 6 Let $E_{\mathcal{P}}$ denote the $m_2 \times n$ matrix defined by:

$$\text{Column } j \text{ of } E_{\mathcal{P}} := \begin{cases} \text{column } j \text{ of } E \text{ if } j \in \mathcal{P} \\ 0 \text{ if } j \in \mathcal{Z} \end{cases}$$

[18] In the batch procedure that we have written these two numbers are free parameters and can have whatever positive value, but for the sake of comparison between different potentials and orbits we use one fixed combination: 500×729.

Compute the n-vector z as a solution of the least-squares problem $E_{\mathcal{P}} z \cong f$. Only the components $z_j, j \in \mathcal{P}$ are determined by this problem. Define: $z_j := 0$ for $j \in \mathcal{Z}$.

Step 7 If $z_j > 0$ for all $j \in \mathcal{P}$, set $x := z$ and go to *Step 2*.

Step 8 Find an index $q \in \mathcal{P}$ such that $x_q/(x_q - z_q) = \min\{x_j/(x_j - z_j) : z_j \leq 0, j \in \mathcal{P}\}$.

Step 9 Set $\alpha := x_q/(x_q - z_q)$.

Step 10 Set $x := x + \alpha(z - x)$.

Step 11 Move from set $\mathcal{P}$ to set $\mathcal{Z}$ all indices $j \in \mathcal{P}$ for which $x_j = 0$. Go to *Step 6*.

Step 12 The end of computation.

The solution vector x as a final result of this algorithm satisfies:

$$x_j > 0, \quad j \in \mathcal{P}$$

and

$$x_j = 0, \quad j \in \mathcal{Z}.$$

Appendix 3
ORBITS

In this Appendix we will present some necessary details connected with the orbits of individual stars in a given potential. The fundamental approximation is valid: forces from individual stars are neglected and only large-scale forces from the overall mass distribution (made up of billions of stars) is considered (cf. Binney and Tremaine 1997, hereafter BT87). Small-scale irregularities due to individual stars or objects like globular clusters and molecular clouds are ignored.

A3.1. GRAVITATIONAL POTENTIALS

A3.1.1. ORBITS IN SPHERICAL POTENTIALS

The gravitational potential, $\Phi(\mathbf{x})$ for an arbitrary mass density $\rho(\mathbf{x})$ is given as (see, for example, Barnes (2006)):

$$\Phi(\mathbf{x}) = -G \int d^3\mathbf{x}' \frac{\rho(\mathbf{x}')}{|\mathbf{x} - \mathbf{x}'|} \tag{A3.1}$$

where G is the gravitational constant and the integral is taken over all space.

The potential energy of a test mass m is given as:

$$U = m\Phi(\mathbf{x}). \tag{A3.2}$$

Using Poisson's equation one can establish the relationship between density and potential:

$$\nabla^2\Phi = 4\pi G\rho, \tag{A3.3}$$

from which it is obvious that linearity holds: if ρ_1 generates potential Φ_1 and ρ_2 generates Φ_2 then the sum $\rho_1 + \rho_2$ generates the sum $\Phi_1 + \Phi_2$.

If one considers a spherical shell of mass m, Newton's first and second theorems state:

1. the gravitational force inside a spherical shell of matter vanishes and
2. the gravitational force on a body that lies outside a closed spherical shell of matter is the same as it would be if all the shell's matter were concentrated into a point at its center.

The potential of an arbitrary spherical mass distribution is:

$$\Phi(r) = -\int_{r0}^{r} dx \;\; a(x) = G\int_{r0}^{r} dx \frac{M(x)}{x^2}, \tag{A3.4}$$

the mass that is enclosed is given as:

$$M(r) = 4\pi \int_{0}^{r} dx \;\; x^2 \rho(x). \tag{A3.5}$$

A3.1.2. EXAMPLES

For a point of mass M a Keplerian potential is given as:

$$\Phi(r) = -G\frac{M}{r}. \tag{A3.6}$$

Orbits in this potential obey the three Kepler's laws. A circular orbit at radius r has velocity: $v_c(r) = \sqrt{GM/r}$. A circular velocity that declines with increasing radius like $r^{\frac{1}{2}}$ is therefore called Keplerian. Kepler was the first to understand that in the Solar system $v_c \propto r^{\frac{1}{2}}$.

For a uniform sphere of mass M and radius a the potential is:

$$\Phi(r) = \begin{cases} -2\pi G\rho(a^2 - r^2/3), & r < a \\ -Gm/r, & r > a \end{cases} \tag{A3.7}$$

where ρ is the mass density.

For a singular isothermal sphere that has a density profile: $\rho(r) = \rho_0(r/r_0)^{-2}$ the potential is:

$$\Phi(r) = 4\pi G\rho_0 r_0^2 \ln(r/r_0). \tag{A3.8}$$

The circular velocity is constant with radius: $v_c = \sqrt{4\pi G\rho_0 r_0^2}$. In case of galaxies with flat rotation curves this potential can be used as a valid approximation, but some outer cut-off must be imposed to obtain a finite total mass.

A3.1.3. POTENTIAL-DENSITY PAIRS

Using Poisson's equation one can obtain pairs of functions (potentials and density) characterized by a total mass M and a length scale a. A very short list is given in TABLE A3-1 (for a detailed list, see Ciotti 2001):

TABLE A3-1

POTENTIAL DENSITY PAIRS FOR SPHERICAL POTENTIALS

Name	$\Phi(r)$	$\rho(r)$
Plummer	$-G\frac{M}{\sqrt{r^2+a^2}}$	$\frac{3M}{4\pi a^3}\left(1+(r^2/a^2)\right)^{-5/2}$
Hernquist	$-G\frac{M}{r+a}$	$\frac{M}{2\pi}\frac{a}{r(r+a)^3}$
Jaffe	$-G\frac{M}{a}\ln\left(\frac{a}{r+a}\right)$	$\frac{M}{4\pi}\frac{a}{r^2(r+a)^2}$

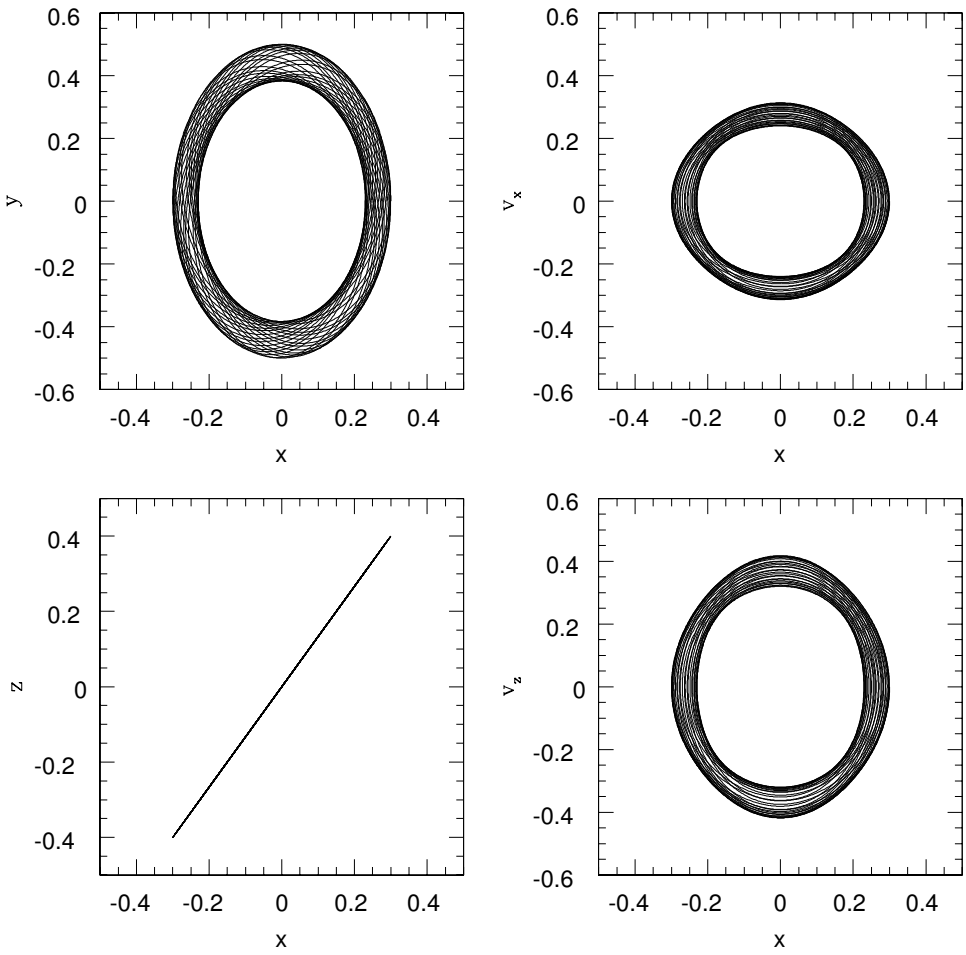

Figure A3.1: Example of an orbit in the Hernquist potential. Clockwise from the top left corner: dependence of y coordinate on x coordinate, dependence of v_x component of the velocity $\mathbf{v}$ on x coordinate, dependence of v_z component of the velocity $\mathbf{v}$ on x coordinate and dependence of z coordinate on x coordinate. See text for details.

A3.1.4. AN EXAMPLE

An example of an orbit generated in the Hernquist spherical potential (initial conditions were: $x_0 = 0.3$, $y_0 = 0.0$, $z_0 = 0.4$, $v_x = 0.0$, $v_y = 0.4$, and $v_z = 0.0$ is given in Fig. (A3.1). Radial length scale was 0.1. The number of time steps in this case, as well as in all other cases that follow, was 16384. Here, $L_z = 0.12$. From the z-x plot it is obvious that the motion is confined to two dimensions.

A3.1.5. CONSTANTS AND INTEGRALS OF MOTION

The constants of motion are functions of phase-space coordinates and time which are constant along orbits:

$$C(\mathbf{r}(t), \mathbf{v}(t), t) = \text{const.} \tag{A3.9}$$

Here, $\mathbf{r}(t)$ and $\mathbf{v}(t) = d\mathbf{r}/dt$ are a solution to the equations of motion. The function $C(\mathbf{r}, \mathbf{v}, t)$ must be constant along every orbit (its value depends on the orbit). If the phase-space has $2n$ dimensions, there are always $2n$ independent constants of motion.

Integrals of motion are functions of phase-space coordinates alone which are constant along orbits:

$$I(\mathbf{r}(t), \mathbf{v}(t)) = \text{const.} \tag{A3.10}$$

It can be seen that an integral of motion cannot depend on time, so all integrals are constants of motion but the opposite is not valid, not all constants are integrals of motion. There are two kinds of integrals (cf. classic paper of Henon and Heiles 1964): non-isolating and isolating. For a non-isolating integral the corresponding hypersurface consists of an infinity of sheets that fill the phase space densely, so that the equation

$$I_j = C_j \qquad (j = 1, \ldots, 5) \tag{A3.11}$$

does not give any information and is equivalent to no condition at all. Therefore, physically, nonisolating integrals do not have significance (integrals I_4 and I_5 are generally nonisolating). Isolating integrals (usually called simply "integrals") are important and they constrain the shapes of orbits. In a phase-space of $2n$ dimensions, an isolating integral defines a hypersurface of $2n - 1$ dimensions. Regular orbits are those that have $N = n$ isolating integrals. In such cases each orbit is confined to a hypersurface of $2n - N$ dimensions.

A3.1.6. AXISYMMETRIC POTENTIALS

In the case of the axisymmetric potentials one works in a cylindrical coordinate system (R, ϕ, z) that is centered on the galactic nucleus. The galaxy's symmetry axis is aligned with the z-axis. In this case the mass distribution is a function of two variables: cylindrical radius, R, and height z. We will not include potentials related to axisymmetric disks (see Ciotti 2001) because they are important in the context of spiral galaxies. For a flattened system we list two potential-density pairs:

TABLE A3-2

POTENTIAL DENSITY PAIRS FOR FLATTENED POTENTIALS

Name	$\Phi(r)$	$\rho(R,z)$
Miyamoto-Nagai (MN)	$-\frac{GM}{\sqrt{R^2+(a+\sqrt{b^2+z^2})^2}}$	$\left(\frac{b^2M}{4\pi}\right)\frac{aR^2+(a+3\sqrt{z^2+b^2})(a+\sqrt{z^2+b^2})^2}{[R^2+(a+\sqrt{z^2+b^2})]^{5/2}(z^2+b^2)^{3/2}}$
Logarithmic	$\frac{1}{2}v_0^2\ln(R_c^2+R^2+z^2/q)$	$\left(\frac{v_0^2}{4\pi Gq^2}\right)\frac{(2q^2+1)R_c^2+R^2+(2-q^{-2})z^2}{(R_c^2+R^2+z^2q^{-2})^2}$

The logarithmic potential is used in this book in several of its variants. Its importance comes from the fact that it can describe galaxies with approximately flat rotation curves: for the $z = 0$ plane the circular velocity $v_c = v_0 R/\sqrt{R_c^2 + R^2}$ rises linearly for $R \ll R_c$ and is approximately constant for large R. As one can see from the potential-density pairs from TABLE A3-2 (density is obtained using Poisson's equation), the density in the case of the logarithmic potential is "dimpled" at the poles (see Fig. 2.8 of BT87). Namely, for $q^2 < \frac{1}{2}$ the density along the z-axis is negative, which is obviously unphysical.

The stars which have motion in the equatorial plane in the axisymmetric potential can be reduced to a two-dimensional problem using the conservation of the z-component of angular momentum of any star. If the symmetric potential (symmetric about the plane $z = 0$) is $\Phi(R, z)$ the general equation of motion of the star is:

$$\frac{d^2\mathbf{r}}{dt^2} = -\nabla\Phi(R, z). \tag{A3.12}$$

In the cylindrical coordinates the following relations hold:

$$\mathbf{r} = R\mathbf{e}_R + z\mathbf{e}_z \tag{A3.13}$$

(where $\mathbf{e}_R$ and $\mathbf{e}_z$ are unit vectors, as well as $\mathbf{e}_\phi$). Now one can write the acceleration in the cylindrical coordinates (cf. BT87, p. 114, and their equation 1B-24):

$$\ddot{R} - R\dot{\phi}^2 = -\frac{\partial\Phi}{\partial R} \tag{A3.14}$$

$$\frac{d}{dt}\left(R^2\dot{\phi}\right) = 0 \tag{A3.15}$$

$$\ddot{z} = -\frac{\partial\Phi}{\partial z} \tag{A3.16}$$

The second of these equations (Eq. (A3.15)) describes the conservation of the component of angular momentum about the z-axis, $L_z = R^2\dot{\phi}$, and the remaining two describe the coupled oscillations of the star in the R and z-directions. From Eq. (A3.14) one can eliminate $\dot{\phi}$ to obtain equations for the evolution of R and z:

$$\ddot{R} = -\frac{\partial\Phi_{\text{eff}}}{\partial R} \quad ; \quad \ddot{z} = -\frac{\partial\Phi_{\text{eff}}}{\partial R} \quad ; \tag{A3.17}$$

where the effective potential has been introduced:

$$\Phi_{\text{eff}} \equiv \Phi(R, z) + \frac{L_z^2}{2R^2}. \tag{A3.18}$$

Therefore the three-dimensional motion of a star in an axisymmetric potential $\Phi(R, z)$ can be reduced to the motion of the star in the plane (see Fig. (A3.2)). This non-uniformly rotating plane with coordinates (R, z) is often called the meridional plane. Effective potential governs the star's motion in the meridional plane, which rotates

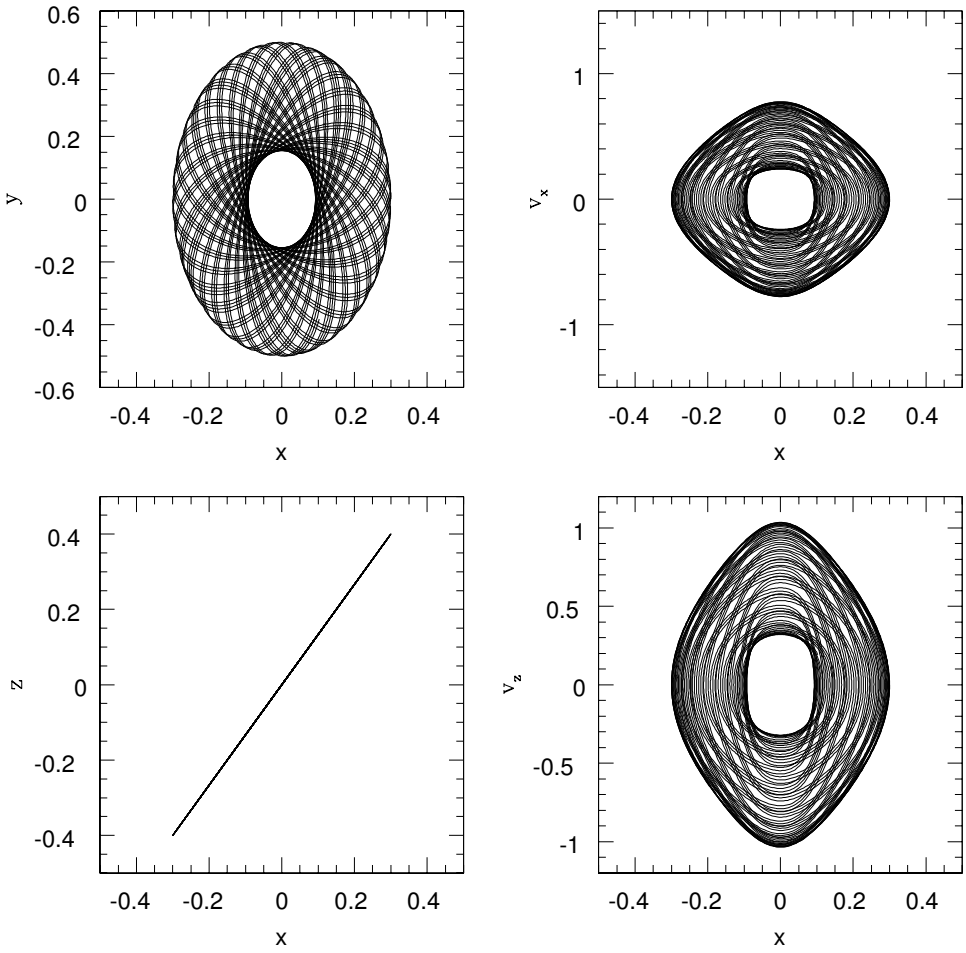

Figure A3.2: Example of an orbit in the logarithmic axisymmetric potential. Clockwise from the top left corner: dependence of y coordinate on x coordinate, dependence of v_x component of the velocity $\mathbf{v}$ on x coordinate, dependence of v_z component of the velocity $\mathbf{v}$ on x coordinate and dependence of z coordinate on x coordinate. See text for details.

about the z-axis with angular velocity L_z/R^2. On the meridional plane the effective potential has a minimum at $R > 0$ and $z = 0$ and a steep angular momentum barrier as $R \to 0$ (BT87, Figure 3-2). If the motion of a star in this plane is constrained only by the energy E (see the formula below) a star should travel everywhere inside within a closed contour of constant $\Phi_{\rm eff}$. This is, however, not always observed: it can happen that stars launched from rest at different points along a contour of constant $\Phi_{\rm eff}$ follow distinct trajectories. This is a consequence of the existence of a third integral, for which, however, general expression does not exist (as in the case

of two classic integrals given in equations for energy E, and a z-component of the angular momentum ($L_z = Rv_\phi$)). The existence of the third integral implies that a star's orbit is a combination of three period motions: radial, azimuthal, and vertical. The orbit can thus be represented as a path on an invariant 3-torus. In the case of some axisymmetric potentials orbits can go everywhere energetically permitted on the meridional plane. These orbits do not permit the description in terms of motion on an invariant 3-torus. These are irregular, or stochastic orbits in an axisymmetric potential that respect only two classical integrals: E and J_z.

The energy E of a star that is moving in an arbitrary axisymmetric potential Φ is given as:

$$E = \frac{1}{2}\left[\dot{R}^2 + (R\dot{\phi})^2 + \dot{z}^2\right] + \Phi = \frac{1}{2}(\dot{R}^2 + \dot{z}^2) + \left(\Phi + \frac{L_z^2}{2R^2}\right) \tag{A3.19}$$

that is

$$E = \frac{1}{2}(\dot{R}^2 + \dot{z}^2) + \Phi_{\text{eff}}. \tag{A3.20}$$

One can see that the effective potential Φ_{eff} is the sum of the gravitational potential energy of the orbiting star and the kinetic energy associated with its motion in the ϕ-direction. The difference between Φ_{eff} and E is the kinetic energy of the motion in the (R, z) plane. Kinetic energy is non-negative, and therefore the orbit is restricted to the area of the meridional plane that satisfies the relation: $E \geq \Phi_{\text{eff}}$. The curve that bounds this area is called the zero-velocity curve, because the orbit can only reach this curve if its velocity is instantaneously zero.

As noted in BT87 (p. 117) eq. (14) cannot be solved analytically, unless the gravitational potential Φ is of some special form. However, one can follow the evolution of $R(t)$ and $z(t)$ by integrating the equations of motion numerically, starting with some initial conditions.

The motion of the representative point is in the four-dimensional phase space $(R, z, \dot{R}, \dot{z})$. This is complicated to visualize, so one can study orbits in (R, z) plane using a simple techique of the surface of section (see Richstone 1982). Because the energy $E(R, z, \dot{R}, \dot{z})$ is conserved, one can plot the motion of the representative point in a three-dimensional space (for example, $(R, z, \dot{R})$ and then determine $\dot{z}$ to within a sign by the known value of E). Further on, one can decide to plot the points by choosing the moment when the representative point of the star crosses some plane (say $z = 0$ plane) in the phase space. Therefore, one can plot $(R, \dot{R})$ only when $\dot{z} > 0$ to remove the ambiguity due to the sign of $\dot{z}$: one can plot the values of R and $\dot{R}$ every time that the star crosses the equator going upward. These plots are called surfaces of section and were first used by Poincaré (see Fig. (A3.3)).

If one now supposes that the star's motion in (R, z) plane respects an additional isolating integral, I, the trajectory of its phase point in the three-dimensional space with coordinates $(R, z, \dot{R})$ is restricted by the condition $I =$ const. to a two-dimensional region, which must cut the plane $z = 0$ through $(R, z, \dot{R})$ space in a curve, called the orbit's invariant curve. Therefore, if I exists for any orbit, the points that are generated by that orbit in the surface of section must lie on a curve. If, however, the only isolating integral admitted by motion in the $(R, \dot{R})$ plane is E, the points generated

by each orbit will fill one or more areas in the surface of section (see Fig. (A3.3)). In Fig. (A3.5) one can see the example that the points lie on the smooth curve in the $(R, \dot{R})$ surface of section, so it seems that some isolating integral, I is respected by this orbit. This is the example of the third integral.

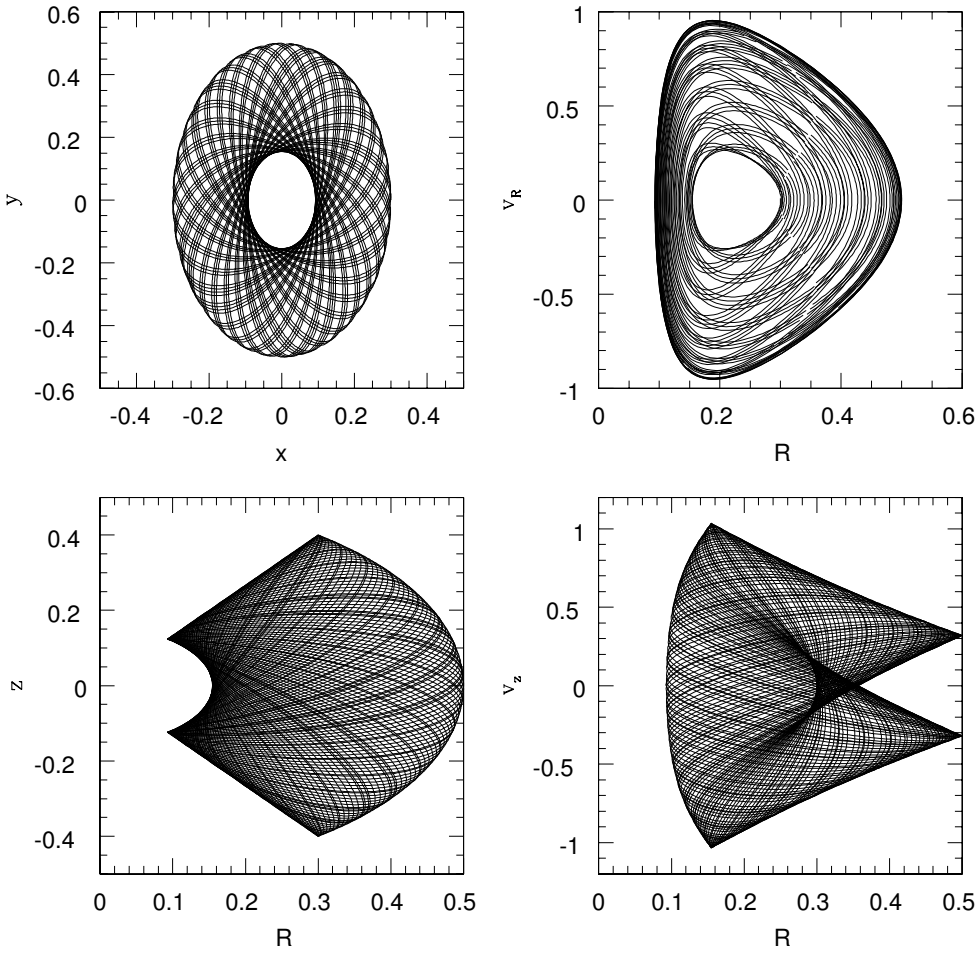

Figure A3.3: Example of an orbit in the logarithmic axisymmetric potential (same orbit as in Fig. (A3.2) but using cylindrical coordinates). Clockwise from the top left corner: dependence of y coordinate on x coordinate (same plot as in Fig. (A3.2)), dependence of v_R component of the velocity $\mathbf{v}$ on R coordinate, dependence of v_z component of the velocity $\mathbf{v}$ on R coordinate and dependence of z coordinate on R coordinate.

A3.1.7. AN EXAMPLE

An example of an orbit generated in the axisymmetric logarithmic potential (initial conditions were: $x_0 = 0.3$, $y_0 = 0.0$, $z_0 = 0.4$, $v_x = 0.0$, $v_y = 0.4$, and $v_z = 0.0$ is given in Fig. (A3.2) and Fig. (A3.3). Here, $L_z = 0.12$. Potential velocity scale was 1.0, the value of the core radius was $R_c = 0.2$, and the flattening of the potential was $q = 0.8$. From the z-x plot it is again obvious that the motion is confined to two dimensions.

A3.1.8. TRIAXIAL POTENTIALS

In the construction of the triaxial potentials, the first step is to generalize an infinitely thin spherical shell into an infinitely thin homeoid (a shell bounded by two similar ellipsoids having a constant ratio of axes) which has constant density between surfaces m^2 and $m^2 + dm^2$, where:

$$m^2 = x^2 + \frac{y^2}{b^2} + \frac{z^2}{c^2}. \tag{A3.21}$$

The acceleration inside the shell vanishes (in a similar way like in the spherical case). Therefore one can write $\Phi = \text{const.}$ inside the shell and on its surface. Outside the shell, the potential is stratified on ellipsoidal surfaces that are defined by:

$$m^2 = \frac{x^2}{1+\tau} + \frac{y^2}{1+\tau} + \frac{z^2}{1+\tau}, \tag{A3.22}$$

where parameter $\tau > 0$ labels the surface. In two extreme cases: (i) $\tau = 0$ the isopotential surface coincides with the homeoid, and (ii) when $\tau \to \infty$ the isopotential surfaces become spherical.

Making a superposition of a series of thin homeoids one can obtain a triaxial mass distribution with $\rho = \rho(m^2)$. The acceleration at a given point (x_0, y_0, z_0) is generated by the mass within $m^2 < m_0^2 = x_0^2 + y_0^2/b^2 + z_0^2/c^2$. This is again similar to the situation that one encounters in the case of a spherical system where the acceleration at distance r is only due to the mass within that radius, r.

Finally, one can write the expression for the logarithmic potential in the triaxial case:

$$\Phi(x, y, z) = \frac{1}{2} v_0^2 \ln\left(R_c^2 + x^2 + \frac{y^2}{b^2} + \frac{z^2}{c^2}\right). \tag{A3.23}$$

Again, as is in the aforementioned two-dimensional case it is not guaranteed that the corresponding density will be positive if the potential is too strongly flattened.

A3.1.9. ORBITS IN NON-AXISYMMETRIC POTENTIALS

Non-axisymmetric potentials with $\Phi = \Phi(x, y)$ or $\Phi = \Phi(x, y, z)$ admit a richer variety of orbits. In this case, the only classical integral of motion in such a potential is the energy given as:

$$E = \frac{1}{2}|\mathbf{v}|^2 + \Phi(\mathbf{r}). \tag{A3.24}$$

Some potentials permit other integrals of motion; in such potentials regular orbits may be mapped onto invariant tori. However, not all regular orbits can be continuously deformed into one another. Therefore, orbits can be grouped into topologically

distinct orbit families. Each orbit family requires in principle a different invariant torus.

A3.1.10. SEPARABLE POTENTIALS

In case of separable potentials all orbits are regular and the mapping to the invariant tori can be constructed analytically and all integrals of motion are known. This is a special case, and real galaxies do not have such a potential, but it has been shown in numerical experiments that non-axisymmetric galaxy models with finite cores or shallow cusps usually generate potentials that resemble separable potentials.

The orbits in a separable potential can be classified into different families. In two-dimensions there are two types of closed, stable orbits: (1) loop orbits that loop around the center, and (2) box orbits that oscillate back and forth along the major axis (cf. BT87, Chapter 3.3.1). In three dimensions, a separable potential permits four orbit families: (1) box orbits, (2) short-axis tube orbits (loop around the short (minor) axis), (3) inner long-axis tube orbits and (4) outer long-axis tube orbits . Two families of long axis-tube orbits that orbit around the long (major) axis come from different closed stable orbits and explore different regions of space (BT87, Figure 3-20, also Statler (1987)). Schwarzschild (1979) in his seminal paper defined box orbits as orbits for which one may choose a starting point in space but a definite velocity, namely zero. X-tube orbits are defined as orbits for which one may choose as starting conditions arbitrary x and z coordinates and and arbitrary y velocity component; other three phase-space coordinates are set to zero. There is no intermediate-axis tube because closed orbits that loop around the intermediate axis are unstable.

A3.1.11. AN EXAMPLE

An example of an orbit generated in the triaxial logarithmic potential (initial conditions were: $x_0 = 0.5$, $y_0 = 0.3$, $z_0 = 0.7$, $v_x = 0.0$, $v_y = 0.0$, and $v_z = 0.0$) is given in Fig. (A3.4) and Fig. (A3.5). Here $L_z = 0$, flattening of the potential $p = q = 0.9$ and the core radius $R_c = 0.3$. Note the difference in the z-x plot with respect to Fig. (A3.1) and Fig. (A3.2). Also, note the difference in $R - v_R$ plot with respect to Fig. (A3.3). Because the initial velocity $\mathbf{v} = 0$, the motion is again in two dimensions.

A3.2. LEAPFROG INTEGRATOR

In this book we generated orbits using a leapfrog integrator. This scheme is useful when one deals with the second-order problems and Newtonian equations of motion are second-order in time (see for example, Barnes 2006). Both positions and velocities are needed to specify the dynamical state of the system.

From classical mechanics it is known that one can obtain the equations of motion in an arbitrary coordinate system using a function called Lagrangian that depends on the generalized coordinates, generalized velocities and possibly the time. The equations of motion can be obtained using the principle of least action. The Lagrangian is:

$$L(x, \dot{x}, t) = T - U = \frac{1}{2} m \dot{x}^2 - U(x, t) \tag{A3.25}$$

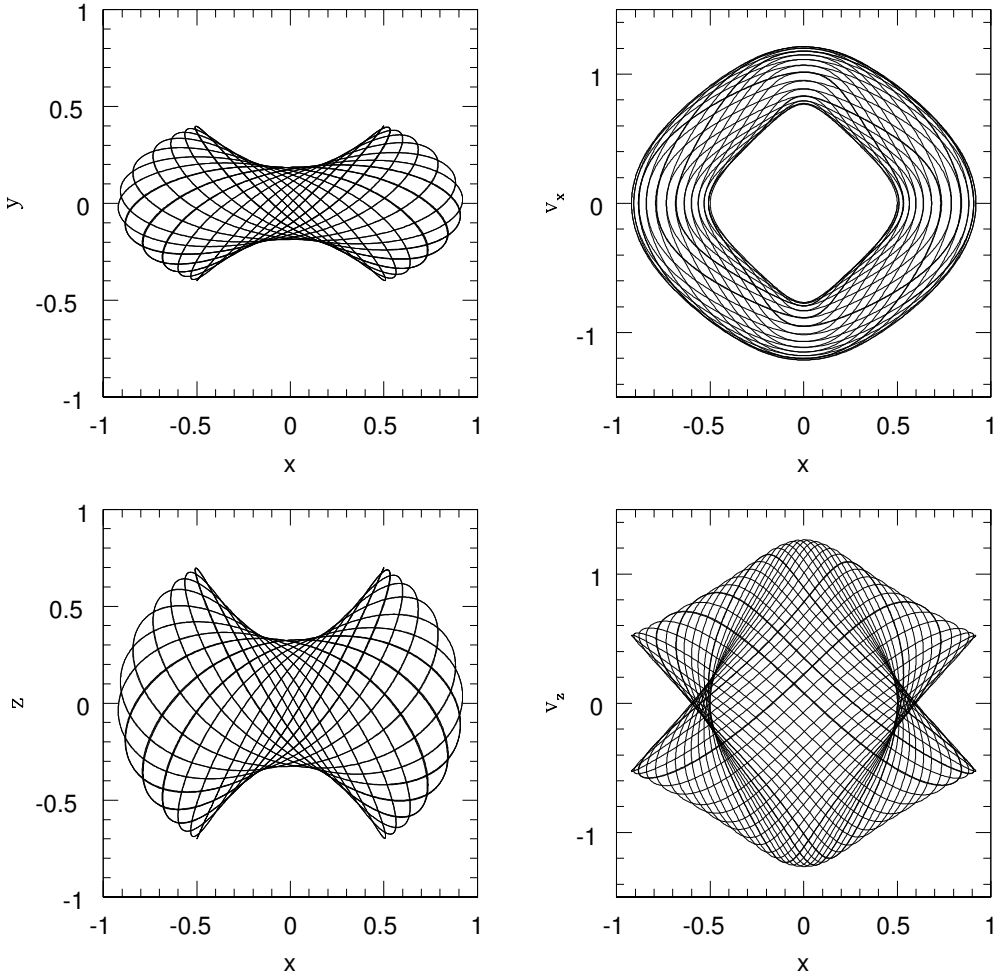

Figure A3.4: Example of an orbit in the logarithmic triaxial potential ($p = q = 0.9$). Clockwise from the top left corner: dependence of y coordinate on x coordinate, dependence of v_x component of the velocity $\mathbf{v}$ on x coordinate, dependence of v_z component of the velocity $\mathbf{v}$ on x coordinate and dependence of z coordinate on x coordinate. See text for details.

where x is the generalized coordinate, and $\dot{x}$ is the generalized velocity. Using the Euler-Lagrange equation one can find the trajectory $x(t)$:

$$\frac{d}{dt}\frac{\partial L}{\partial \dot{x}} - \frac{\partial L}{\partial x} = 0. \tag{A3.26}$$

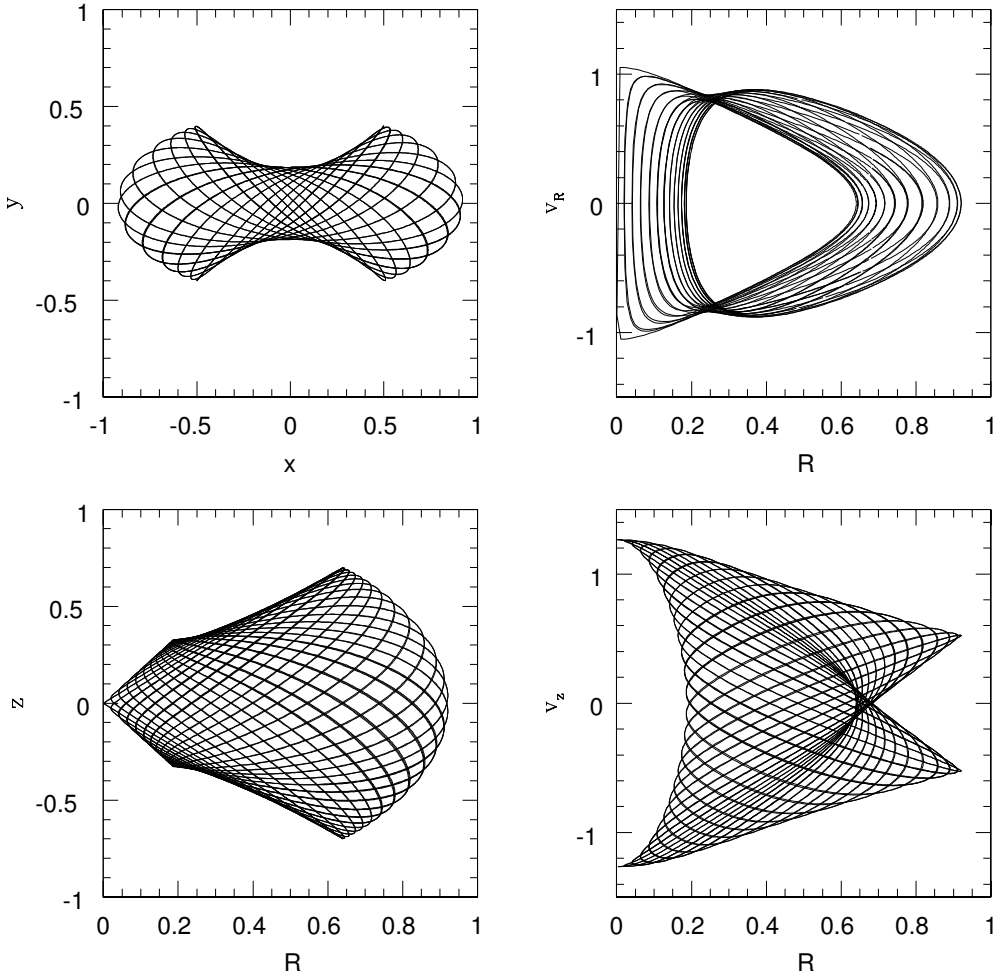

Figure A3.5: Example of an orbit in the logarithmic triaxial potential (same orbit as in Fig. (A3.4) but using cylindrical coordinates). Clockwise from the top left corner: dependence of y coordinate on x coordinate (same plot as in Fig. (A3.2)), dependence of v_R component of the velocity $\mathbf{v}$ on R coordinate, dependence of v_z component of the velocity $\mathbf{v}$ on R coordinate and dependence of z coordinate on R coordinate.

From these two equations it follows:

$$\frac{d}{dt}(m\dot{x}) + \frac{dU}{dx} = 0 \tag{A3.27}$$

which is in fact the Newton's law of motion usually expressed as:

$$m\frac{d^2x}{dt^2} = f(x). \tag{A3.28}$$

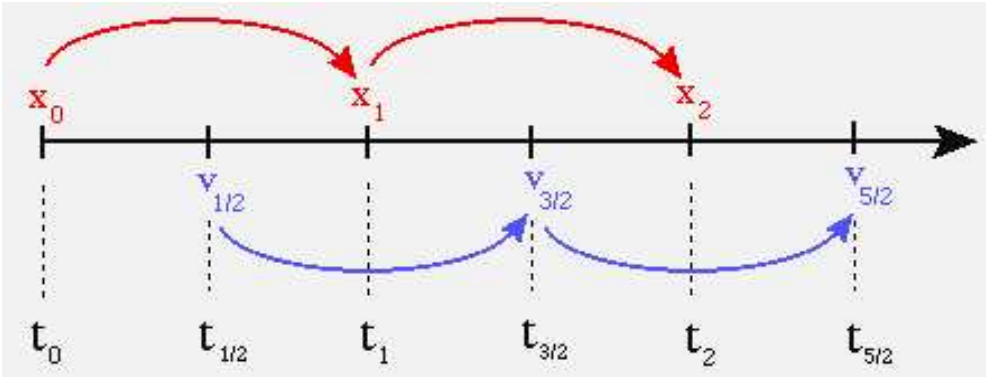

Figure A3.6: Scheme of leapfrog integration

In a similar manner, one can use the generalized momentum

$$p = \frac{dL}{d\dot{x}} = m\dot{x} \tag{A3.29}$$

define the Hamiltonian function as:

$$H(x,p) = p\dot{x} - L(x,\dot{x},t) = \frac{1}{2}m\dot{x}^2 + U(x,t) = \frac{1}{2m}p^2 + U(x,t), \tag{A3.30}$$

which is numerically equal to the total energy.

Now one can write the equations of motion:

$$\frac{dp}{dt} = -\frac{\partial H}{\partial x}, \quad \frac{dx}{dt} = \frac{\partial H}{\partial p} \tag{A3.31}$$

which after using the definition of the Hamiltonian becomes:

$$\frac{dp}{dt} = -\frac{dU}{dx}, \quad \frac{dx}{dt} = \frac{p}{m} \tag{A3.32}$$

that are identical to the familiar form:

$$\frac{dx}{dt} = v, \quad m\frac{dv}{dt} = f(x). \tag{A3.33}$$

There are different numerical integrators for solving a system of coupled ordinary differential equations but not all respect the symmetric structure in Eq. (A3.25). The time-centered leapfrog integrator does respect this structure. In second-order systems it is useful to define the velocities at the mid-points of the intervals – it is said that the velocities are staggered with respect to the positions x. If $x[k] = x(kh)$ is the position at time $t = kh$, where k is the step number and h is the time-step. Velocity $v[k + 1/2] = v([k + 1/2]h)$ is the velocity a half-step later (see Fig. (A3.6)). The leapfrog step is:

$$x[k+1] = x[k] + hv[k+1/2] \tag{A3.34}$$

$$v[k+3/2] = v[k+1/2] + ha(x[k+1]), \tag{A3.35}$$

where $a(x) = -(1/m)\partial U/dx$ is the acceleration. In this scheme both x and v are treated symmetrically: they are both reversible. The leapfrog scheme is time reversible and that is important because it guarantees conservation of energy, angular momentum and any other conserved quantity. The problem of the leapfrog integrator is the need to offset the position and velocity variables by half a timestep. One can do the split of the velocity step:

$$v[k+1/2] = v[k] + (h/2)a(x[k]), \tag{A3.36}$$

$$x[k+1] = x[k] + hv[k+1/2], \tag{A3.37}$$

$$v[k+1] = v[k+1/2] + (h/2)a(x[k+1]). \tag{A3.38}$$

This is equivalent to Eqs. (A3.34) and (A3.35). When used as a mapping from time kh to time $(k+1)h$ Eqs. (A3.37) and (A3.38) are equivalent to starting Eqs. (A3.36) through (A3.38) with the linear approximation:

$$v[1/2] = v[0] + (h/2)a(x[0]) + \mathcal{O}(h^2). \tag{A3.39}$$

The solution jump-starts from a phase-space point offset in velocity by $\mathcal{O}(h^2)$ from specified $v[0]$ and similar errors are made in extracting $v[k]$ at later times. The leapfrog method is only second-order accurate, but it is very stable.

Appendix 4
SELF-ORGANIZING MAPS (SOMs)

A4.1. BASIC CONCEPTS

The self-organizing map (SOM) method invented by T. Kohonen (Kohonen 1997) is a neural network method. The Kohonen (1997) definition states: "SOM [is a] result of a nonparametric regression process that is mainly used to represent high-dimensional, nonlinearly related data items in an illustrative, often two-dimensional display, and to perform unsupervised classification and clustering". Thus it is closely related to cluster analysis (partitioning) and other methods of data analysis (cf. Murtagh and Hernandez-Pajeres 1995).

The SOM method includes a set of iterative procedures for associating a finite number of object vectors (inputs) with a finite number of representational points (that should be viewed as bins or clusters). These representational points should respect the proximity relations between the inputs, and can be arranged, for example, in a planar grid. It is important to note that the SOM approach is representative of an *unsupervised learning* approach: cluster properties are estimated or learned without usage of prior information.

The SOM method can be condensed in the following three points (Murtagh 1995):

1. Each item in a multidimensional input data set is assigned to a cluster center.
2. The cluster centers are themselves ordered by their proximities.
3. The cluster centers are arranged in some specific output representational structure, for example a regularly spaced grid.

The output representational grid of cluster centers $\mathbf{w}_i$ (that are initially randomly valued) is structured through the imposing of neighborhood relations (Murtagh 1995, Murtagh and Hernandez-Pajeres 1995):

Step 1 Set $t = 0$. Consider an input vector $\mathbf{x}$ from the set of inputs.

Step 2 Determine the cluster center $c = i$ such that $\| \mathbf{x} - \mathbf{w}_i^{(t)} \|$ is minimum over all i.

Step 3 For all clusters centers i:

$$\mathbf{w}_i^{(t+1)} = \begin{cases} \mathbf{w}_i^{(t)} + \alpha^{(t)}(\mathbf{x} - \mathbf{w}_i^{(t)}) & \text{if } \; i \in N_c(t) \\ \mathbf{w}_i^{(t)} & \text{if } \; i \notin N_c(t) \end{cases}$$

Step 4 Increment t. Go to *Step 1*, unless a stopping condition is reached.

An iteration in this algorithm is the assignment (or re-assignment) of an input vector to a cluster center. An epoch is the assignment (or re-assignment) of all inputs. Murtagh (1995) found that 5 or 6 epochs are enough to attain convergence. After some testing, in the code that we have applied we decided to use 10 epochs as a reasonable number that provides a balance between the time needed for one orbit SOM extraction and the quality of the extraction. Here, $\alpha^{(t)}$ is a small fraction that is used for controlling convergence, $N_c(t)$ is the neighborhood of the lattice element c. The weight vector $\mathbf{w}_i^{(t)}$ is calculated for a lattice element i at iteration number t. The neighborhood is made to decrease with iterations, towards the best "winner" (defined in *Step 2*) cluster center. Note that the initial cluster centers are randomly valued and are of the same dimensionality as the input data vectors.

A4.2. APPLICATION

We have applied the aforementioned algorithm and wrote a FORTRAN program based on Murtagh and Hernandez-Pajeres (1995) that extracts positions and velocities from the orbit libraries that we had previously generated (for calculation of orbits see Appendix 3). As an input to the SOM routine for every calculated orbit we have a file that includes projected radius (r, through x and y coordinate) and line-of-sight velocity and as an output the following is calculated: for a selected number of points on the grid, projected radius (r, through x and y coordinate), line-of-sight velocity and the occupation weight (using notation of Rix et al. (1997): w_{xyv}, for which the following normalization is valid ($\sum_{xyv} w_{xyv} = 1$)).

In the following several plots we provide examples of calculated orbits and the SOM reconstruction. These examples were done using a tube orbit but similar results are obtained for a box orbit. Fig. (A4.2) gives the tube orbit (presented in Fig. (A4.1)) projected using inclination angle of 50°. To show the SOM extraction of occupation weights from this plot, we presented in Fig. (A4.3) numbers representing occupation weight at each given point. Note that the total number of points is 15,000. It is obvious that the SOM method manages to extract orbital weights successfully in 10 epochs. Using SOMs the storage of the necessary data is drastically reduced making them easily accessible for further calculations. Needless to say, one orbit library, with appropriate scaling, can be used in multiple cases after a projection procedure for a desired inclination angle.

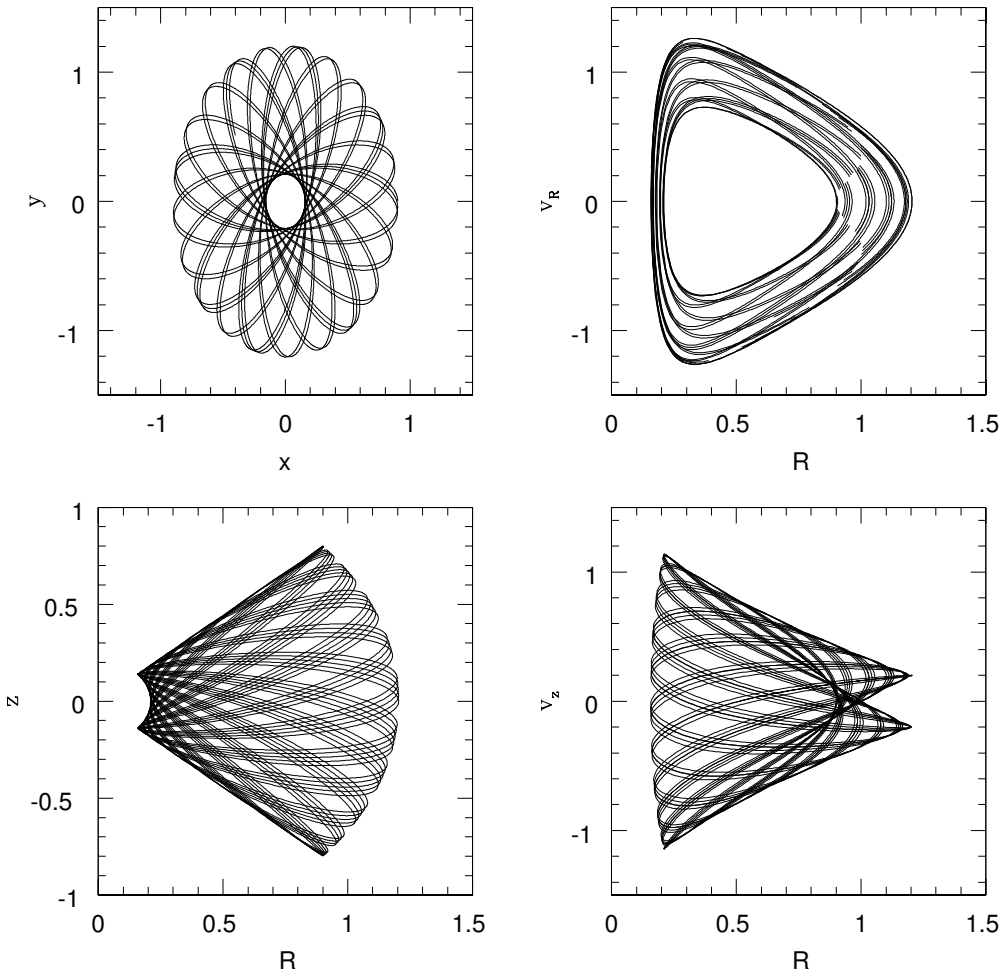

Figure A4.1: Tube orbit calculated in the axisymmetric logarithmic potential. Initial conditions were: $x = 0.9$, $y = 0.0$, $z = 0.8$, $v_x = 0.0$, $v_y = 0.3$, and $v_z = 0.0$. Potential velocity scale was 1.0, the value of the core radius was $R_c = 0.2$, and the flattening of the potential was $q = 0.9$. Note that the orbit extends out to larger radius with respect to the orbit plotted in Figure 3 (from Appendix 3), because of different initial conditions. Clockwise from the top left corner: dependence of y coordinate on x coordinate, dependence of v_R component of the velocity $\mathbf{v}$ on R coordinate, dependence of v_z component of the velocity $\mathbf{v}$ on R coordinate and dependence of z coordinate on R coordinate. Discontinuities in $v_R - R$ plot are due to the fact that values in the plot are taken only in the case when $\dot{z} > 0$. Without this condition the whole region of surface of section will be filled (see Chapter A3.1.6).

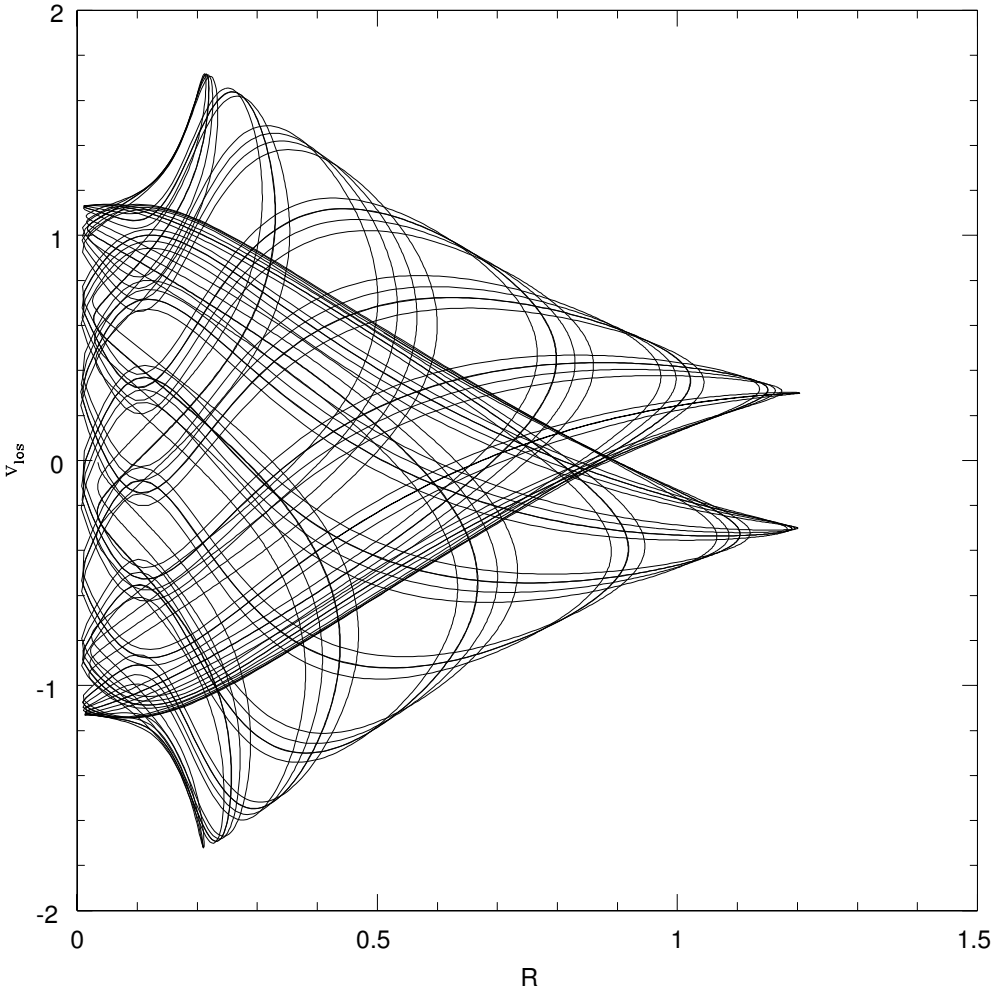

Figure A4.2: Tube orbit calculated in the axisymmetric logarithmic potential. x-axis in now R coordinate and y-axis is the velocity along the line-of-sight ($v_{\rm los}$). Inclination is 50°.

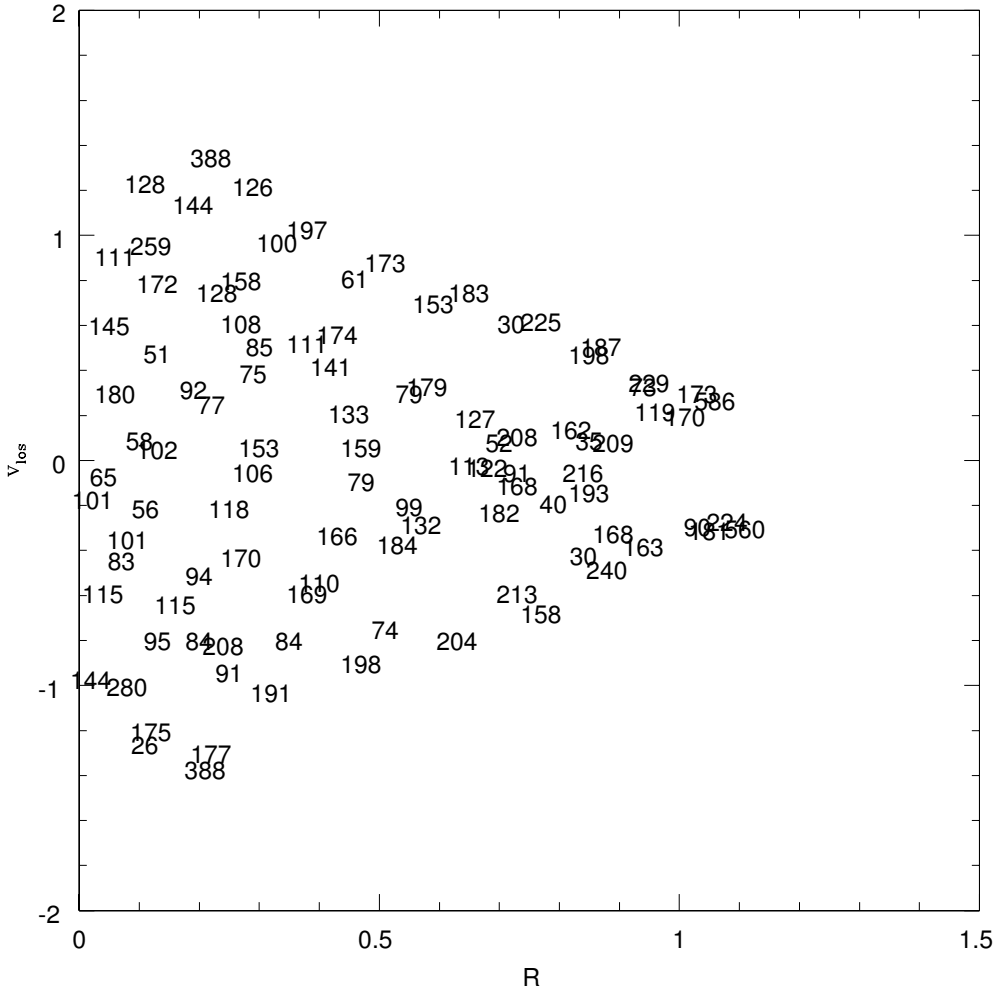

Figure A4.3: SOM reconstruction of the orbit from Fig. (A4.2). Occupation weights are given in plot as numbers.

Appendix 5
FRACTION OF THE TOTAL FLUX AS A FUNCTION OF RADIUS

One effective radius, as said in Introduction encompasses half the total luminosity of the given galaxy. But what is the fraction of the total light contained at, say, 5 effective radii (R_e)? Which radius contain the totality of the galactic light? The first question is asked when we want to calculate the mass–to–light ratio in a given galaxy at a given radius (*not* for the *whole* galaxy). However the answers to these questions are unfortunately not readily available as one might expect. This is the reason for inclusion of TABLE A5-1 and Fig. (A5.1) given below in this Appendix.

To calculate the fraction of the total light at a given radius we start by writing the expression for the modified de Vaucouleurs (Sersic) law (see Introduction of this book):

$$I(R) = I_e \mathrm{e}^{\{-b_n[(R/R_e)^{1/n}-1]\}}. \tag{A5.1}$$

We remind the reader that for the case for which $n = 4$ we have the de Vaucouleurs law according to which

$$I(R) = I_e \exp\{-7.67[(R/R_e)^{0.25} - 1]\}. \tag{A5.2}$$

Now we integrate over the surface brightness profile to get the flux interior to the radius R:

$$f(R) = \int_0^R 2\pi R' \mathrm{d}R' I_e \mathrm{e}^{\{-b_n[(R/R_e)^{1/n}-1]\}}. \tag{A5.3}$$

After the calculations one obtains the following expression:

$$f(R) = \frac{2\pi n \mathrm{e}^{b_n} I_e r_e^2}{b_n^{2n}} \Gamma\left[2n, b_n\left(\frac{r}{r_e}\right)^{1/n}\right], \tag{A5.4}$$

where $\Gamma(x, y)$ is the incomplete gamma function.

The fraction of the flux emitted within a given radius (we take $2R_e$ in an example below):

$$\beta = \frac{f(2R_e)}{f(\infty)} = \frac{\Gamma\left[2n, b_n 2^{1/n}\right]}{\Gamma\left[2n, \infty\right]}.$$

For the widely used de Vaucouleurs law one has $n = 4$ and $b_4 = 7.67$, and therefore the parameter β from the example above becomes:

$$\beta = \frac{\Gamma(8, 9.121)}{\Gamma(8)},$$

where $\Gamma(x)$ is the Euler gamma function.

The Table given below is calculated for $n = 4$ and $b_4 = 7.67$ (de Vaucouleurs law). It can be seen that within $1R_e$ (by definition) one half of the total light is emitted. To answer the question from the beginning of this Appendix: at $5R_e$ 89 per cent of the total light is encompassed. Starting with $\sim 16R_e$ one can see that $\sim$ 99 per cent of the total light is emitted and the increase beyond this radius is asymptotic never reaching full 100 per cent (as an extreme case we calculated that at $50R_e$ $\beta = 0.999402$). It is worth noting that modern mathematical packages (for example Wolfram's Mathematica) have a possibility to quickly calculate incomplete gamma function (command `Gamma[`α`, z]` in Mathematica) so if it is necessary one can calculate β at, say, $1.4R_e$ by using Eq. (A5.4). One can also experiment with different values of n (and b_n) in order to obtain the parameter β for such cases.

TABLE A5-1

FRACTION OF THE TOTAL FLUX AS FUNCTION OF RADIUS

R $[R_e]$	β
1	0.50
2	0.69
3	0.79
4	0.85
5	0.89
6	0.91
7	0.93
8	0.94
9	0.95
10	0.96
11	0.97
12	0.97
13	0.98
14	0.98
15	0.98
16	0.99
17	0.99
18	0.99
19	0.99
20	0.99

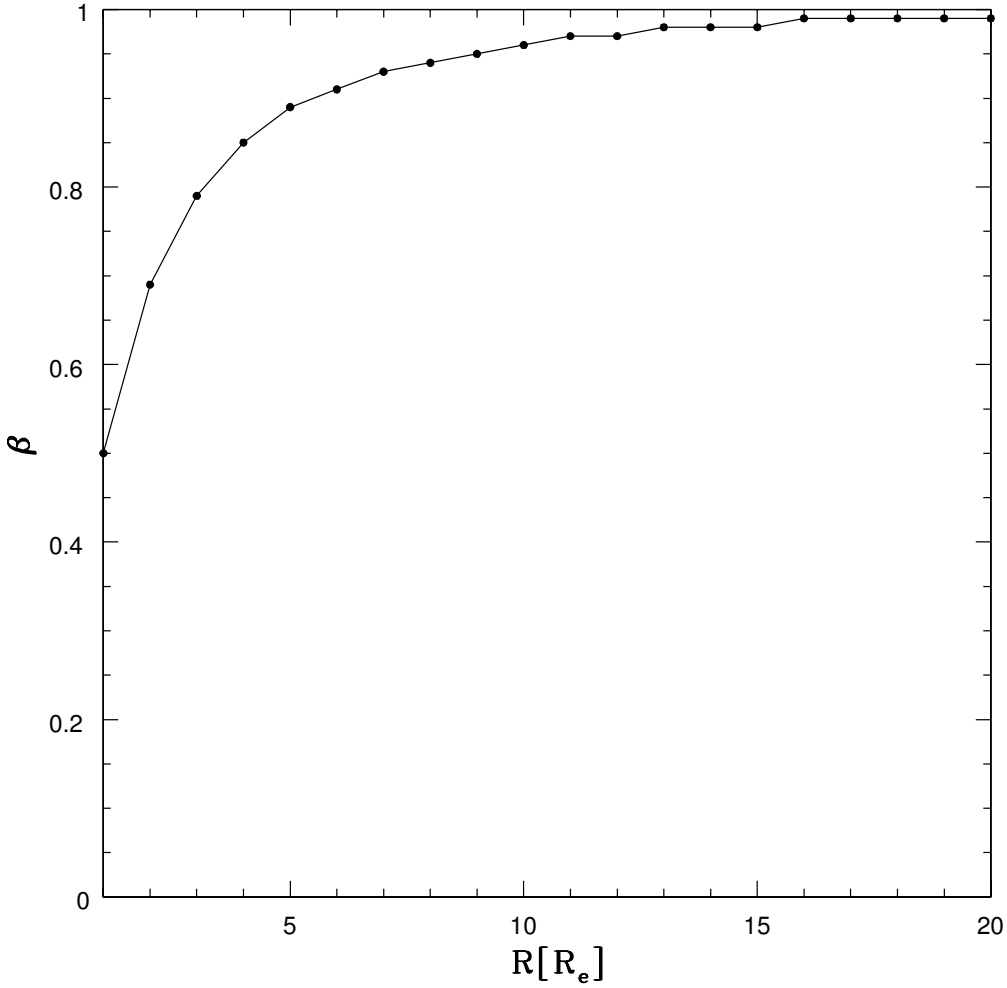

Figure A5.1: The fraction of the total light emitted in a galaxy, β as function of radius R. In TABLE A5-1 and in this Figure the radius R is expressed in the units of effective radius (R_e), and for the de Vaucouleurs law.

Appendix 6
TABLES

A6.1. STELLAR KINEMATICS

TABLE A6-1
IC 1459: MAJOR AXIS

r	velocity	err	σ	err	h_3	err	h_4	err
-89.608	95.698	25.135	169.480	24.391	-0.068	0.133	0.133	0.133
-75.794	102.597	19.720	163.257	16.297	-0.079	0.106	0.241	0.107
-65.327	121.165	17.883	183.567	22.703	-0.199	0.094	0.239	0.094
-58.974	76.006	16.481	234.049	15.407	-0.019	0.058	0.069	0.063
-53.963	61.948	14.635	241.966	13.329	0.007	0.049	0.075	0.054
-49.787	81.218	13.897	231.859	12.874	-0.032	0.050	0.075	0.054
-46.163	110.24	15.757	262.035	13.837	0.018	0.046	0.080	0.054
-42.810	124.364	13.676	242.944	12.458	-0.057	0.046	0.071	0.051
-39.725	66.984	13.232	255.728	14.135	0.024	0.041	-0.015	0.048
-37.223	67.771	14.594	278.077	12.821	0.028	0.039	0.076	0.048
-34.981	48.423	13.359	270.989	12.674	0.065	0.038	0.030	0.044
-32.739	56.906	10.967	258.893	10.091	0.005	0.033	0.058	0.038
-30.785	38.417	12.847	267.527	11.879	0.002	0.036	0.051	0.043
-29.112	69.605	12.108	268.088	10.983	0.024	0.034	0.060	0.040
-27.428	61.859	13.102	275.242	12.066	-0.010	0.035	0.050	0.042
-25.748	52.271	12.670	274.420	12.825	0.014	0.034	-0.001	0.041
-24.355	70.152	14.619	287.086	13.682	-0.003	0.037	0.040	0.045
-23.234	35.261	12.820	279.566	11.885	0.038	0.034	0.044	0.041
-22.114	20.275	11.958	266.581	11.656	0.003	0.034	0.024	0.040
-20.994	19.439	12.491	280.641	11.685	-0.004	0.033	0.041	0.039
-19.873	21.448	10.453	291.712	9.357	0.024	0.026	0.066	0.032
-18.753	30.122	12.012	286.600	11.272	0.031	0.031	0.037	0.037
-17.634	36.696	10.995	283.593	10.608	0.017	0.028	0.022	0.034
-16.513	20.862	11.180	301.964	10.874	0.059	0.027	0.011	0.032
-15.680	12.527	12.161	308.807	12.062	0.020	0.027	0.008	0.033

IC 1459: MAJOR AXIS (CONTINUED)

r	velocity	err	σ	err	h_3	err	h_4	err
-15.120	18.488	13.908	302.048	13.638	0.063	0.033	0.005	0.040
-14.560	0.628	16.895	305.528	17.641	0.054	0.040	-0.037	0.048
-14.000	20.766	12.372	293.623	12.266	0.020	0.030	0.005	0.036
-13.440	22.538	11.843	289.379	11.235	0.027	0.030	0.031	0.036
-12.880	18.442	14.275	312.678	13.395	0.040	0.032	0.045	0.041
-12.320	13.073	13.877	309.492	14.580	0.026	0.031	-0.034	0.038
-11.760	20.24	12.140	318.476	11.560	0.042	0.026	0.039	0.034
-11.200	7.132	13.393	310.274	12.989	0.058	0.031	0.016	0.037
-10.640	11.204	12.971	308.312	11.974	0.075	0.031	0.044	0.038
-10.080	1.964	11.344	316.647	10.728	0.050	0.025	0.040	0.032
-9.520	14.763	11.508	308.410	10.749	0.042	0.026	0.045	0.033
-8.960	-11.319	10.450	307.970	9.865	0.065	0.024	0.032	0.030
-8.400	2.195	11.973	315.360	11.706	0.052	0.027	0.015	0.033
-7.840	-0.192	11.165	326.330	11.215	0.081	0.024	-0.011	0.029
-7.280	-11.324	10.741	315.678	9.805	0.053	0.024	0.063	0.031
-6.720	-14.223	11.613	322.202	11.122	0.093	0.026	0.018	0.031
-6.160	-18.614	11.714	341.184	11.177	0.067	0.024	0.052	0.031
-5.600	-19.66	12.040	338.357	11.596	0.091	0.026	0.029	0.031
-5.040	-32.463	11.824	341.004	11.608	0.077	0.024	0.025	0.030
-4.480	-44.091	11.259	338.169	10.803	0.104	0.025	0.023	0.029
-3.920	-50.476	11.266	334.689	10.751	0.097	0.025	0.029	0.030
-3.360	-51.924	11.881	338.544	11.498	0.089	0.025	0.027	0.031
-2.800	-59.817	10.187	330.681	9.706	0.104	0.023	0.022	0.027
-2.240	-56.934	10.723	341.247	10.165	0.117	0.024	0.027	0.028
-1.680	-56.246	11.498	346.636	10.854	0.101	0.024	0.048	0.030
-1.120	-34.563	12.155	343.103	11.845	0.076	0.025	0.034	0.031
-0.560	-11.207	13.910	341.779	13.939	0.077	0.029	0.009	0.034
0.000	0.000	13.584	335.607	13.451	0.059	0.028	0.021	0.035
0.560	64.773	13.550	330.543	13.831	-0.019	0.027	0.003	0.034
1.120	41.025	12.329	327.415	12.543	-0.029	0.025	0.001	0.031
1.680	72.978	12.977	324.131	13.110	-0.010	0.027	0.006	0.033
2.240	93.515	13.384	317.287	13.243	-0.022	0.029	0.014	0.036
2.800	88.161	12.975	315.420	12.818	-0.051	0.029	0.008	0.035
3.360	94.115	13.326	319.895	13.020	-0.059	0.029	0.017	0.036
3.920	83.247	13.626	311.288	13.196	-0.052	0.031	0.020	0.038
4.480	77.888	12.533	311.528	12.755	-0.016	0.028	-0.008	0.034
5.040	50.191	13.194	319.595	13.135	-0.006	0.028	0.013	0.035
5.600	57.395	13.182	321.551	13.124	-0.007	0.028	0.015	0.035
6.160	30.099	12.318	311.903	12.207	-0.018	0.027	0.010	0.034
6.720	45.402	11.682	315.057	11.229	0.031	0.026	0.032	0.032

IC 1459: MAJOR AXIS (CONTINUED)

r	velocity	err	σ	err	h_3	err	h_4	err
7.280	49.54	11.678	320.937	11.378	0.020	0.025	0.028	0.031
7.840	38.143	11.796	309.733	11.779	0.016	0.026	0.004	0.032
8.400	50.055	13.290	316.146	12.994	0.053	0.029	0.015	0.036
8.960	48.897	13.160	327.410	13.156	0.037	0.027	0.013	0.034
9.520	27.645	12.004	306.298	12.232	0.022	0.027	-0.012	0.033
10.080	14.984	11.952	311.881	11.556	0.043	0.027	0.023	0.033
10.640	17.1	11.947	303.106	11.402	0.063	0.028	0.023	0.034
11.200	18.861	11.859	316.752	12.039	0.033	0.026	-0.006	0.031
11.760	2.951	11.570	316.747	11.553	0.046	0.025	0.003	0.031
12.320	10.752	12.174	311.036	12.311	0.028	0.027	-0.005	0.033
12.880	-4.117	10.728	301.099	10.872	0.046	0.025	-0.013	0.031
13.440	-7.849	10.265	302.861	9.980	0.040	0.024	0.016	0.029
14.000	-1.452	12.259	316.277	12.168	0.020	0.026	0.012	0.033
14.560	-0.432	11.647	305.249	11.583	0.016	0.026	0.005	0.032
15.120	-3.782	13.528	314.441	12.288	0.052	0.031	0.066	0.040
15.680	15.954	10.125	304.898	10.658	0.050	0.024	-0.042	0.029
16.240	2.923	12.771	296.385	12.075	0.045	0.031	0.031	0.038
17.073	-3.435	10.380	301.319	9.704	0.043	0.025	0.040	0.030
18.194	-16.026	10.976	299.967	10.196	0.046	0.026	0.043	0.032
19.314	-26.115	10.609	302.258	9.316	0.055	0.026	0.080	0.033
20.436	-27.453	12.201	308.059	11.141	0.068	0.029	0.054	0.036
21.551	-28.393	12.007	303.493	10.798	0.055	0.029	0.064	0.036
22.674	-33.819	10.082	292.630	8.810	0.084	0.026	0.072	0.032
23.795	-41.113	11.382	294.164	10.656	0.090	0.029	0.025	0.034
24.915	-33.013	12.538	298.468	11.986	0.039	0.030	0.026	0.037
27.988	-36.619	12.789	287.368	11.879	0.040	0.033	0.042	0.039
29.669	-42.04	10.953	297.999	10.392	0.076	0.027	0.022	0.032
31.350	-33.386	11.511	300.428	10.263	0.096	0.029	0.058	0.035
33.303	-46.175	10.867	277.943	10.008	0.045	0.029	0.047	0.035
35.541	-48.5	12.146	275.367	11.475	0.106	0.036	0.019	0.040
37.782	-61.208	11.763	273.917	10.507	0.049	0.033	0.065	0.039
40.294	-57.907	12.915	260.229	11.573	0.106	0.041	0.058	0.045
43.106	-76.088	9.915	234.690	9.735	0.032	0.035	0.045	0.038
46.136	-54.036	11.510	234.418	12.348	0.085	0.043	-0.004	0.047
49.795	-51.694	13.862	255.001	11.893	0.097	0.045	0.091	0.051
53.928	-89.869	14.058	200.652	26.597	0.238	0.071	0.177	0.069
58.963	-97.594	15.891	199.162	27.492	0.158	0.075	0.173	0.075
65.327	-120.835	17.883	183.567	22.703	0.199	0.094	0.239	0.094
73.939	-82.389	23.726	135.026	32.675	0.007	0.142	0.522	0.148
86.244	-108.638	37.625	118.830	69.486	-0.020	0.247	0.398	0.234

TABLE A6-2

IC 3370: MAJOR AXIS

r	velocity	err	σ	err	h_3	err	h_4	err
-118.709	-97.283	33.982	108.359	47.825	-0.102	0.306	-0.009	0.346
-76.994	-98.17	13.729	149.995	15.174	-0.020	0.082	0.054	0.088
-58.261	-108.416	13.138	172.560	12.817	0.040	0.065	0.070	0.068
-46.710	-131.07	10.158	157.412	11.417	0.093	0.060	0.023	0.064
-38.513	-118.186	9.072	161.628	10.925	0.077	0.052	-0.015	0.058
-31.791	-111.942	9.111	152.370	10.386	0.086	0.056	0.027	0.059
-26.880	-148.232	10.553	138.989	16.823	0.072	0.080	-0.138	0.112
-23.520	-97.746	9.498	157.489	10.566	0.043	0.054	0.035	0.058
-20.160	-94.81	10.537	186.111	11.442	0.047	0.048	0.000	0.051
-16.800	-77.852	10.333	183.333	9.788	0.047	0.048	0.066	0.049
-13.440	-82.048	10.792	193.314	11.130	0.033	0.046	0.015	0.048
-10.080	-70.944	9.994	189.044	9.632	0.036	0.044	0.050	0.045
-6.720	-69.167	11.289	205.146	10.671	0.007	0.044	0.041	0.045
-3.360	-60.06	11.441	208.147	10.757	0.011	0.044	0.040	0.045
0.000	0.000	11.151	208.537	10.793	0.050	0.043	0.025	0.044
3.360	67.06	10.770	199.582	10.236	0.026	0.044	0.044	0.045
6.720	96.202	11.002	199.779	11.602	-0.028	0.045	-0.001	0.048
10.080	113.86	10.915	204.124	10.313	-0.041	0.043	0.041	0.044
13.440	114.294	9.822	185.917	10.724	-0.024	0.045	0.000	0.048
16.800	125.151	9.606	185.910	11.544	-0.038	0.045	-0.045	0.051
20.160	127.636	9.426	181.309	11.575	-0.013	0.045	-0.047	0.052
23.520	127.365	8.849	170.744	10.957	-0.059	0.047	-0.041	0.054
26.880	129.717	9.302	168.540	11.390	-0.023	0.049	-0.028	0.056
30.240	139.625	9.165	156.671	12.257	-0.092	0.058	-0.066	0.068
35.141	133.451	8.889	148.509	10.985	-0.010	0.055	0.005	0.062
41.864	121.188	8.819	146.365	12.311	0.008	0.057	-0.051	0.071
50.100	146.844	8.659	154.099	12.364	-0.034	0.054	-0.083	0.069
61.694	135.349	9.836	145.376	14.707	0.033	0.067	-0.091	0.088
79.294	122.278	12.685	124.982	15.916	0.073	0.097	0.033	0.104
116.432	124.591	18.182	99.847	30.532	0.093	0.184	-0.102	0.247

TABLE A6-3

IC 3370: MINOR AXIS

r	velocity	err	σ	err	h_3	err	h_4	err
-80.156	41.732	15.472	185.858	20.348	-0.170	0.103	-0.305	0.149
-61.574	30.78	17.496	233.660	11.910	-0.133	0.065	0.170	0.068
-50.043	54.865	15.371	183.722	13.351	-0.067	0.071	0.107	0.073
-41.662	1.02	21.828	201.291	20.062	-0.058	0.089	0.057	0.091
-35.373	29.818	19.630	232.101	18.222	-0.243	0.093	-0.038	0.080
-30.240	34.231	14.851	186.155	13.909	-0.105	0.070	0.062	0.070
-26.880	21.567	14.278	182.174	11.897	0.016	0.065	0.133	0.068
-23.520	40.021	14.302	183.965	12.714	0.056	0.066	0.096	0.067
-20.160	48.205	15.211	230.440	16.886	0.035	0.052	-0.050	0.057
-16.800	37.463	15.702	216.157	17.973	-0.020	0.058	-0.051	0.065
-13.440	35.915	13.037	205.530	15.336	-0.081	0.056	-0.064	0.061
-10.080	36.775	15.706	220.740	18.126	-0.078	0.061	-0.070	0.067
-6.720	34.023	12.548	216.791	13.353	0.033	0.046	-0.020	0.049
-3.360	35.387	12.093	206.551	12.634	0.025	0.047	-0.002	0.050
0.000	0.000	11.312	223.119	10.956	0.072	0.041	0.011	0.041
3.360	-15.449	11.714	216.859	10.655	0.043	0.043	0.047	0.044
6.720	-32.512	11.494	208.624	11.032	0.038	0.044	0.032	0.045
10.080	-52.446	10.533	193.031	10.462	0.051	0.046	0.033	0.047
13.440	-45.915	11.340	202.402	12.168	-0.040	0.046	-0.011	0.049
16.800	-54.17	11.744	188.615	12.172	-0.051	0.053	0.019	0.055
20.160	-38.137	14.072	213.722	15.152	-0.073	0.055	-0.028	0.057
23.520	-40.025	15.812	210.258	15.055	-0.002	0.060	0.035	0.062
26.880	-78.507	13.215	178.116	13.214	0.035	0.063	0.051	0.066
30.240	-44.075	21.753	245.018	17.623	0.011	0.067	0.079	0.070
35.131	-52.099	13.435	181.799	13.803	0.070	0.064	0.030	0.066
41.859	-32.566	14.869	201.688	14.593	0.076	0.062	0.025	0.063
50.024	-42.578	14.372	174.449	13.211	0.020	0.070	0.098	0.072
62.955	6.104	17.907	212.082	19.989	0.084	0.073	-0.046	0.077
87.898	-14.423	17.562	156.723	22.006	-0.072	0.106	-0.024	0.120

TABLE A6-4

IC 3370: INTERMEDIATE AXIS

r	velocity	err	σ	err	h_3	err	h_4	err
-59.788	-97.318	11.334	180.295	16.307	0.052	0.059	-0.142	0.082
-46.693	-103.027	9.992	133.376	11.399	0.006	0.068	0.069	0.072
-38.494	-103.169	10.171	147.593	14.390	-0.018	0.066	-0.062	0.083
-31.754	-100.368	9.884	157.162	12.581	0.079	0.060	-0.037	0.068
-26.880	-99.208	10.273	166.574	14.369	0.027	0.057	-0.095	0.074
-23.520	-102.625	10.907	156.696	13.198	0.038	0.063	-0.004	0.071
-20.160	-87.717	10.239	162.518	14.397	0.064	0.061	-0.100	0.077
-16.800	-84.928	10.636	174.007	14.551	0.078	0.059	-0.107	0.073
-13.440	-87.972	10.301	170.535	12.116	0.051	0.054	-0.016	0.059
-10.080	-81.43	9.921	169.085	11.912	0.061	0.053	-0.025	0.059
-6.720	-74.647	10.695	173.391	12.346	0.053	0.055	-0.012	0.060
-3.360	-47.07	11.336	190.177	12.093	0.047	0.050	0.002	0.053
0.000	0.000	11.413	198.156	12.091	0.077	0.049	-0.008	0.051
3.360	48.517	10.996	196.522	13.149	0.021	0.047	-0.053	0.054
6.720	94.703	10.941	188.287	12.965	-0.019	0.049	-0.040	0.056
10.080	107.835	10.712	183.460	13.909	-0.019	0.051	-0.078	0.063
13.440	115.963	10.342	185.005	13.115	-0.036	0.049	-0.069	0.058
16.800	132.163	9.937	176.510	13.251	-0.002	0.050	-0.082	0.063
20.160	133.392	9.804	175.128	13.410	-0.053	0.052	-0.100	0.066
23.520	129.282	9.888	169.665	14.142	-0.083	0.058	-0.134	0.076
26.880	128.456	9.650	169.223	14.866	-0.017	0.056	-0.177	0.084
31.771	139.59	9.432	159.740	14.169	-0.005	0.057	-0.129	0.080
38.494	139.441	9.034	142.028	11.807	-0.149	0.067	-0.047	0.074
46.683	140.017	10.226	150.049	14.515	-0.091	0.069	-0.089	0.086
59.581	134.721	12.377	163.816	15.429	-0.152	0.079	-0.067	0.085
84.130	115.096	12.181	144.219	17.536	-0.150	0.094	-0.128	0.116

TABLE A6-5

NGC 1336: MAJOR AXIS

r	velocity	err	σ	err	h_3	err	h_4	err
-16.735	-18.592	37.439	78.257	55.978	-0.109	0.440	-0.152	0.602
-6.386	-21.773	13.465	89.392	15.367	0.046	0.125	0.026	0.131
-2.617	-13.72	9.048	91.756	10.478	0.009	0.081	0.022	0.086
-0.910	-1.815	9.183	91.497	8.703	-0.002	0.081	0.113	0.082
0.000	0.000	10.134	100.126	10.012	0.021	0.084	0.086	0.083
0.910	-1.478	8.907	96.390	9.001	-0.026	0.076	0.078	0.076
2.249	-6.818	7.028	93.551	6.235	-0.002	0.061	0.144	0.062
4.440	3.631	7.727	76.800	7.871	-0.179	0.088	0.073	0.089
8.180	13.251	12.526	75.136	13.568	-0.177	0.146	0.041	0.154
19.703	51.156	63.643	40.820	141.717	-0.938	2.092	-0.175	2.480

TABLE A6-6

NGC 1339: MAJOR AXIS

r	velocity	err	σ	err	h_3	err	h_4	err
-25.742	-94.743	22.695	134.458	16.413	0.520	0.287	-0.476	0.303
-17.480	-111.953	12.207	75.172	11.303	-0.222	0.146	0.114	0.153
-13.053	-117.659	7.751	101.705	7.262	0.117	0.065	0.068	0.063
-9.929	-129.029	6.559	99.831	5.974	0.073	0.054	0.094	0.054
-7.699	-111.261	8.081	119.588	8.357	0.086	0.058	0.031	0.056
-5.868	-99.337	6.740	128.511	6.474	0.095	0.046	0.059	0.043
-4.550	-71.191	6.395	136.939	6.492	0.084	0.041	0.039	0.039
-3.640	-61.163	6.098	149.073	7.438	0.079	0.037	-0.037	0.039
-2.730	-48.896	7.170	157.476	9.638	-0.004	0.040	-0.072	0.048
-1.820	-38.789	6.579	165.892	8.376	0.043	0.035	-0.058	0.040
-0.910	-21.133	6.201	172.602	7.512	0.029	0.031	-0.038	0.034
0.000	0.000	5.861	174.987	7.127	0.008	0.028	-0.040	0.032
0.910	21.724	5.864	173.035	6.838	0.002	0.028	-0.021	0.031
1.820	39.686	5.531	166.422	6.791	-0.026	0.029	-0.039	0.032
2.730	57.038	6.473	156.475	7.520	-0.046	0.036	-0.012	0.037
3.640	72.192	5.589	145.910	6.245	-0.004	0.032	0.011	0.033
4.550	81.129	5.815	143.540	6.723	-0.041	0.035	-0.004	0.036
5.460	97.88	6.954	139.692	7.243	-0.108	0.045	0.022	0.043
6.776	106.814	5.935	121.410	6.198	-0.063	0.041	0.032	0.040
9.034	124.889	5.154	115.339	4.817	-0.115	0.039	0.066	0.037
12.161	122.955	7.434	120.445	6.607	-0.104	0.053	0.091	0.051
16.197	118.14	8.421	94.826	6.760	-0.059	0.072	0.172	0.077
22.679	131.216	13.618	127.333	10.591	-0.059	0.091	0.160	0.091
35.049	133.738	24.404	117.745	19.926	-0.120	0.180	0.129	0.175

TABLE A6-7

NGC 1373: MAJOR AXIS

r	velocity	err	σ	err	h_3	err	h_4	err
-32.824	7.214	52.102	106.468	37.297	-0.534	0.777	-0.433	0.784
-10.954	7.102	8.473	75.902	8.484	-0.059	0.090	0.102	0.101
-7.159	9.676	6.315	85.218	7.601	-0.021	0.060	-0.020	0.069
-4.945	17.341	5.729	91.327	6.227	0.017	0.050	0.025	0.053
-3.640	19.185	6.782	110.464	5.431	-0.020	0.050	0.156	0.052
-2.730	10.607	5.044	96.357	4.877	0.013	0.042	0.075	0.043
-1.820	9.967	5.050	97.436	5.202	-0.010	0.041	0.046	0.042
-0.910	7.414	4.732	94.230	5.345	0.021	0.040	0.006	0.043
0.000	0.000	3.485	90.562	3.795	0.004	0.031	0.025	0.033
0.910	-4.025	2.927	89.411	3.131	0.010	0.026	0.033	0.028
1.820	-5.595	2.680	88.067	2.942	0.015	0.024	0.022	0.026
2.730	-6.238	3.511	81.374	3.529	0.046	0.034	0.077	0.038
3.640	-10.881	4.108	80.626	4.403	-0.032	0.041	0.045	0.046
4.550	-7.639	6.087	85.431	6.176	-0.054	0.057	0.061	0.061
5.851	-12.728	6.517	88.276	7.788	-0.049	0.060	-0.022	0.067
8.064	-9.953	8.120	81.012	12.069	0.037	0.086	-0.144	0.125
11.834	-13.691	14.856	83.622	13.563	0.258	0.171	0.048	0.166
16.543	-27.347	48.526	145.338	32.566	-0.131	0.304	0.234	0.315

TABLE A6-8

NGC 1374: MAJOR AXIS

r	velocity	err	σ	err	h_3	err	h_4	err
-26.939	-57.611	30.424	114.178	37.117	0.169	0.268	-0.066	0.274
-17.962	-47.56	16.999	134.089	22.601	0.127	0.126	-0.082	0.142
-13.065	-43.008	11.989	143.066	13.917	0.056	0.074	0.008	0.077
-9.930	-55.522	10.645	157.363	11.902	0.057	0.059	0.014	0.061
-7.694	-56.133	9.601	163.833	9.097	0.118	0.053	0.070	0.051
-5.862	-46.672	8.958	159.571	8.335	0.067	0.048	0.090	0.048
-4.550	-63.018	9.524	162.250	9.163	0.125	0.053	0.062	0.052
-3.640	-64.943	10.422	188.411	9.097	0.060	0.046	0.098	0.047
-2.730	-52.424	11.462	202.537	9.629	0.044	0.046	0.106	0.048
-1.820	-40.744	10.421	187.258	9.232	0.055	0.047	0.092	0.047
-0.910	-20.41	11.040	201.617	10.030	0.056	0.045	0.070	0.046
0.000	0.000	10.103	184.430	10.135	0.008	0.046	0.043	0.047
0.910	27.026	9.453	174.201	10.318	-0.032	0.046	0.015	0.048
1.820	43.939	9.187	156.135	9.719	-0.051	0.051	0.039	0.052
2.730	48.49	8.751	151.891	9.321	-0.090	0.052	0.032	0.051
3.640	30.511	9.484	163.355	9.705	-0.044	0.050	0.049	0.050
4.550	40.101	9.607	160.424	9.248	-0.123	0.054	0.063	0.053
5.868	53.032	9.151	138.085	8.992	-0.030	0.057	0.081	0.056
7.699	43.762	9.707	135.940	8.344	0.037	0.061	0.140	0.060
9.937	54.533	10.305	149.730	10.522	-0.180	0.068	0.022	0.064
13.480	54.652	11.499	119.739	10.684	-0.131	0.086	0.092	0.081
19.154	44.85	19.196	109.795	17.579	-0.140	0.155	0.096	0.147
30.536	58.845	61.594	146.638	73.102	-0.102	0.500	-0.368	0.756

TABLE A6-9

NGC 1379: MAJOR AXIS

r	velocity	err	σ	err	h_3	err	h_4	err
-27.414	-37.638	26.266	84.144	29.456	0.193	0.294	-0.019	0.295
-17.864	-30.576	12.878	90.752	14.091	0.204	0.137	-0.021	0.133
-13.084	-35.328	9.933	77.046	11.534	-0.058	0.107	0.041	0.118
-9.935	-26.562	9.367	96.713	9.119	-0.103	0.083	0.088	0.081
-7.696	-36.17	9.835	118.130	9.880	0.045	0.071	0.078	0.071
-5.860	-25.16	8.067	103.744	7.898	0.009	0.065	0.095	0.065
-4.550	-23.787	8.249	109.633	8.732	-0.009	0.064	0.060	0.064
-3.640	-24.055	7.737	114.886	7.704	0.061	0.058	0.080	0.057
-2.730	-15.61	8.461	125.739	8.579	0.035	0.058	0.073	0.058
-1.820	-9.037	7.374	113.555	8.749	-0.002	0.056	0.014	0.059
-0.910	-5.116	7.489	111.421	7.633	0.011	0.057	0.075	0.057
0.000	0	8.205	99.870	8.156	-0.029	0.069	0.089	0.068
0.910	3.801	9.410	108.872	11.584	0.005	0.075	0.001	0.080
1.820	16.739	10.116	109.554	12.447	-0.004	0.080	0.001	0.086
3.138	19.829	10.067	111.362	9.526	0.067	0.077	0.103	0.076
4.970	28.732	9.627	99.779	11.808	-0.056	0.084	-0.004	0.089
7.210	8.949	9.837	95.435	9.048	0.010	0.085	0.129	0.085
10.355	10.738	10.791	84.713	10.734	-0.015	0.104	0.106	0.106
15.076	26.726	15.407	80.422	18.253	0.059	0.160	0.022	0.176
24.776	31.714	23.826	81.533	39.904	-0.050	0.275	-0.223	0.449
49.381	2.922	60.072	88.758	50.863	-0.091	0.562	0.179	0.568

TABLE A6-10

NGC 1399: MAJOR AXIS

r	velocity	err	σ	err	h_3	err	h_4	err
-57.866	-56.932	28.389	186.720	33.541	0.101	0.141	-0.037	0.150
-34.004	-44.194	21.697	263.389	20.368	-0.013	0.060	0.039	0.067
-23.828	-48.451	26.690	265.557	27.482	0.063	0.077	-0.014	0.082
-18.032	-31.729	18.278	210.741	17.697	0.018	0.070	0.048	0.075
-13.979	-33.779	17.142	243.371	19.832	0.081	0.059	-0.078	0.068
-10.848	-32.732	17.815	253.375	20.222	0.113	0.062	-0.094	0.069
-8.615	-23.84	18.614	240.227	19.851	0.079	0.063	-0.025	0.068
-6.793	-36.237	21.843	264.060	23.903	0.038	0.062	-0.041	0.069
-5.460	3.885	25.089	288.781	22.179	0.084	0.066	0.057	0.071
-4.550	-15.904	21.980	285.350	26.589	0.063	0.062	-0.156	0.085
-3.640	-43.939	24.524	278.302	24.373	-0.024	0.063	0.009	0.069
-2.730	-26.106	26.837	314.417	25.249	0.091	0.065	0.021	0.066
-1.820	-18.244	24.138	297.469	23.973	0.103	0.064	-0.012	0.063
-0.910	1.204	25.296	307.789	26.199	0.046	0.059	-0.015	0.061
0.000	0.000	26.829	318.740	29.269	0.017	0.059	-0.036	0.062
0.910	-14.935	27.587	314.022	29.412	0.047	0.063	-0.030	0.065
1.820	25.378	26.884	307.782	29.042	0.002	0.061	-0.032	0.065
2.730	20.336	27.599	291.960	29.897	0.042	0.069	-0.039	0.074
3.640	-2.417	25.858	299.042	27.112	-0.015	0.061	-0.018	0.065
4.550	7.407	22.832	278.705	24.721	0.044	0.060	-0.039	0.066
5.460	32.475	26.527	297.061	28.291	0.039	0.064	-0.030	0.068
6.370	-9.957	26.312	282.230	30.246	0.090	0.076	-0.104	0.087
7.702	18.435	20.548	242.598	22.727	0.051	0.067	-0.039	0.075
9.524	26.225	23.907	256.182	25.238	-0.056	0.072	-0.022	0.078
11.757	33.544	17.898	238.130	20.274	0.050	0.060	-0.049	0.068
14.500	33.286	19.607	252.804	21.725	0.029	0.059	-0.042	0.067
18.033	41.765	15.772	199.916	17.242	-0.029	0.066	0.003	0.071
23.805	21.854	17.721	237.931	22.407	0.069	0.065	-0.154	0.092
33.462	7.361	17.882	214.600	18.993	0.059	0.069	0.000	0.074
66.315	27.565	36.641	212.475	47.827	0.055	0.176	-0.280	0.310

TABLE A6-11

NGC 1404: MAJOR AXIS

r	velocity	err	σ	err	h_3	err	h_4	err
-79.230	-67.908	35.671	170.194	35.648	-0.292	0.257	-0.101	0.234
-67.148	-66.976	27.246	145.061	39.868	0.034	0.180	-0.181	0.275
-56.551	-85.784	22.325	179.746	26.729	-0.028	0.104	-0.040	0.115
-44.822	-78.145	17.516	166.335	20.560	0.157	0.106	-0.076	0.109
-34.710	-65.477	19.448	192.650	23.450	0.113	0.094	-0.082	0.103
-28.977	-63.873	19.392	194.510	20.242	0.047	0.081	0.006	0.084
-24.934	-76.662	19.792	204.481	23.400	0.025	0.079	-0.051	0.088
-21.787	-73.017	19.593	192.370	21.551	0.149	0.098	-0.050	0.097
-19.543	-88.97	21.312	193.010	22.469	0.084	0.094	-0.004	0.095
-17.723	-60.481	19.772	195.616	23.287	0.109	0.092	-0.069	0.099
-15.900	-62.848	22.611	219.149	23.825	0.070	0.084	-0.016	0.087
-14.077	-57.908	20.830	203.490	21.607	0.068	0.084	0.000	0.086
-12.740	-66.113	21.690	225.700	24.900	0.086	0.082	-0.066	0.089
-11.830	-60.627	20.810	219.085	23.730	0.112	0.085	-0.071	0.090
-10.920	-81.796	21.739	212.467	25.163	0.082	0.087	-0.059	0.095
-10.010	-74.736	22.695	231.514	25.583	0.119	0.088	-0.078	0.093
-9.100	-65.053	22.672	228.310	24.830	0.076	0.081	-0.040	0.086
-8.190	-70.622	24.176	242.353	27.892	0.078	0.082	-0.077	0.092
-7.280	-53.125	24.332	238.015	26.102	0.059	0.081	-0.031	0.085
-6.370	-41.985	24.883	241.758	27.432	0.070	0.083	-0.048	0.089
-5.460	-32.67	24.751	245.101	26.705	0.051	0.078	-0.035	0.084
-4.550	-26.696	25.522	247.036	26.909	0.070	0.082	-0.029	0.085
-3.640	-22.327	24.603	249.490	25.131	0.057	0.076	-0.012	0.079
-2.730	-19.154	24.786	242.072	26.857	0.041	0.079	-0.033	0.085
-1.820	-7.683	24.578	242.723	26.016	0.034	0.077	-0.022	0.082
-0.910	-1.999	23.345	232.569	25.728	0.030	0.078	-0.035	0.085
0.000	0.000	22.845	226.077	25.761	0.017	0.079	-0.041	0.087
0.910	-0.464	24.044	229.634	26.563	0.046	0.083	-0.037	0.089
1.820	3.951	25.089	238.422	26.493	0.051	0.082	-0.022	0.086
2.730	11.678	25.523	240.624	27.740	0.029	0.081	-0.033	0.088
3.640	30.664	25.167	243.186	27.373	-0.006	0.078	-0.032	0.085
4.550	41.524	25.382	239.067	26.887	-0.007	0.080	-0.019	0.086
5.460	32.838	26.256	241.279	28.648	-0.005	0.082	-0.033	0.090
6.370	46.561	25.360	243.891	25.980	0.005	0.078	-0.006	0.083
7.280	61.767	24.287	231.353	26.501	-0.031	0.081	-0.030	0.088
8.190	63.565	24.536	237.202	27.020	-0.005	0.079	-0.035	0.086
9.100	76.874	22.275	222.214	25.892	-0.020	0.079	-0.053	0.089
10.010	79.801	21.837	215.010	23.682	-0.010	0.080	-0.018	0.085
10.921	89.696	22.518	215.494	23.762	-0.034	0.082	-0.008	0.087

NGC 1404: MAJOR AXIS (CONTINUED)

r	velocity	err	σ	err	h_3	err	h_4	err
11.830	93.1	21.457	209.028	21.591	-0.079	0.085	0.008	0.085
12.740	90.926	20.635	204.205	21.075	-0.065	0.083	0.007	0.084
13.650	89.024	19.502	195.113	21.907	-0.070	0.084	-0.030	0.089
14.987	80.048	20.457	201.418	22.251	-0.023	0.081	-0.012	0.086
16.812	92.978	20.550	211.731	21.897	-0.038	0.077	-0.011	0.081
18.633	80.826	19.696	198.656	17.907	0.007	0.079	0.064	0.081
20.877	98.042	20.974	205.081	21.186	-0.080	0.085	0.008	0.085
23.609	86.675	20.127	196.115	18.547	0.028	0.082	0.059	0.084
26.751	77.569	18.888	189.532	19.628	-0.042	0.081	0.012	0.084
31.203	82.592	19.020	186.533	21.525	-0.056	0.086	-0.025	0.091
38.184	92.712	17.412	168.845	20.488	-0.102	0.094	-0.044	0.099
52.192	101.68	18.176	169.521	24.888	0.019	0.094	-0.100	0.121
67.123	241.99	42.197	207.255	27.489	0.080	0.178	0.234	0.197

TABLE A6-12

NGC 1419: MAJOR AXIS

r	velocity	err	σ	err	h_3	err	h_4	err
-6.521	0.024	17.809	113.962	25.817	-0.029	0.142	-0.069	0.173
-4.023	-15.093	13.940	110.476	10.743	0.173	0.114	0.193	0.112
-2.730	-16.604	12.411	122.926	12.931	0.028	0.087	0.064	0.087
-1.820	16.003	11.973	126.676	12.193	0.107	0.086	0.060	0.083
-0.910	-8.81	10.837	111.608	11.892	0.152	0.092	0.010	0.088
0.000	0.000	9.044	106.235	11.431	0.033	0.074	-0.011	0.080
0.910	5.598	9.235	104.526	11.035	-0.033	0.076	0.011	0.080
1.820	-9.225	9.446	114.905	12.436	0.013	0.073	-0.026	0.081
2.730	-5.819	11.340	107.952	16.569	0.026	0.095	-0.073	0.117
3.640	3.304	9.793	88.596	10.736	0.054	0.092	0.050	0.096
4.941	5.946	12.755	107.210	12.159	0.016	0.100	0.106	0.099
7.140	-3.687	21.883	107.995	27.116	-0.152	0.199	-0.054	0.205
10.857	-67.488	32.059	125.815	20.233	-0.376	0.279	0.295	0.279

TABLE A6-13

NGC 3379: MAJOR AXIS

r	velocity	err	σ	err	h_3	err	h_4	err
-25.879	63.194	8.513	162.073	7.368	-0.090	0.045	0.109	0.046
-14.051	68.302	7.637	179.704	7.898	-0.073	0.036	0.028	0.037
-8.753	56.908	4.830	176.622	5.180	-0.012	0.023	0.022	0.024
-6.255	52.234	5.303	183.786	5.603	0.015	0.024	0.024	0.025
-4.809	51.106	5.572	199.728	5.931	-0.015	0.023	0.014	0.024
-3.624	42.337	5.403	207.183	5.545	0.002	0.021	0.026	0.022
-2.773	45.139	5.834	214.089	5.978	-0.011	0.022	0.023	0.023
-2.183	39.724	5.935	219.934	5.964	-0.019	0.021	0.029	0.023
-1.593	35.234	5.928	225.600	6.096	-0.010	0.021	0.016	0.022
-1.003	29.393	5.767	224.304	5.916	-0.003	0.020	0.018	0.022
-0.413	19.156	5.681	217.610	5.945	0.016	0.021	0.012	0.022
-0.177	5.516	5.703	223.417	6.094	0.013	0.020	0.001	0.022
0.767	-3.167	5.601	217.749	5.619	0.016	0.020	0.030	0.022
1.357	-9.204	5.750	208.990	5.938	0.024	0.022	0.022	0.023
1.947	-11.184	6.080	203.897	6.422	0.040	0.024	0.013	0.026
2.798	-18.15	5.505	201.697	5.764	0.028	0.022	0.019	0.023
3.983	-24.77	5.559	196.204	5.828	0.032	0.023	0.021	0.024
5.428	-29.387	5.263	184.628	5.622	0.010	0.023	0.020	0.025
7.704	-30.205	4.881	175.466	5.150	0.025	0.023	0.028	0.024
12.261	-45.279	5.224	171.950	5.111	0.027	0.025	0.060	0.026
20.582	-60.748	7.666	155.531	8.560	0.033	0.042	0.011	0.043

TABLE A6-14

NGC 4105: MAJOR AXIS

r	velocity	err	σ	err	h_3	err	h_4	err
-22.585	31.695	62.504	260.281	84.348	0.134	0.246	-0.143	0.310
-14.673	4.87	33.698	234.433	42.807	0.095	0.136	-0.051	0.154
-10.619	35.136	23.159	253.402	27.209	0.072	0.081	-0.026	0.090
-8.165	12.979	19.660	259.904	21.912	0.069	0.066	-0.008	0.071
-6.519	24.065	17.210	262.390	18.105	0.016	0.055	0.020	0.058
-5.356	27.889	14.490	262.859	17.444	0.027	0.047	-0.039	0.055
-4.347	20.754	14.195	257.176	15.235	-0.010	0.047	0.017	0.050
-3.520	11.619	15.405	285.667	17.093	0.021	0.044	-0.021	0.049
-2.847	21.285	14.241	284.228	15.041	0.025	0.041	0.001	0.044
-2.173	15.245	14.320	283.497	14.142	0.027	0.041	0.031	0.043
-1.680	10.452	16.009	310.394	16.202	-0.001	0.040	0.004	0.044
-1.344	4.165	15.589	307.387	15.176	0.032	0.040	0.022	0.042
-1.008	3.815	16.464	298.603	18.045	0.055	0.045	-0.028	0.050
-0.672	7.031	16.050	298.183	16.030	-0.003	0.042	0.017	0.046
-0.336	15.546	14.806	304.751	16.300	-0.022	0.039	-0.030	0.044
0.000	0.000	14.837	298.764	18.337	-0.020	0.041	-0.079	0.051
0.336	1.583	17.086	313.825	18.558	-0.039	0.043	-0.031	0.049
0.672	-5.221	15.298	306.415	16.960	-0.044	0.040	-0.037	0.046
1.008	14.739	15.538	308.173	15.828	-0.067	0.041	-0.003	0.044
1.344	28.992	15.082	285.592	14.677	-0.013	0.042	0.036	0.045
1.680	28.555	15.058	299.200	17.439	-0.058	0.042	-0.054	0.049
2.016	4.331	16.399	301.758	18.116	-0.026	0.043	-0.030	0.049
2.352	50.178	14.001	278.795	16.299	0.001	0.042	-0.036	0.048
2.688	32.482	13.129	254.500	13.943	-0.020	0.044	0.023	0.046
3.181	38.352	13.591	277.016	14.385	0.043	0.041	0.004	0.044
3.855	21.539	14.533	295.552	16.118	-0.029	0.040	-0.028	0.045
4.528	28.619	14.184	273.435	16.533	-0.032	0.044	-0.034	0.050
5.356	41.094	15.362	280.693	16.450	-0.001	0.045	-0.001	0.049
6.516	26.132	14.800	261.816	17.802	0.032	0.049	-0.038	0.056
8.017	31.639	17.392	279.589	19.685	0.032	0.052	-0.026	0.058
9.996	31.828	18.018	262.988	21.318	0.045	0.059	-0.033	0.067
12.943	40.285	25.093	262.602	27.882	0.075	0.083	-0.010	0.089
18.002	66.794	33.495	249.708	45.852	0.014	0.120	-0.085	0.154
27.268	49.384	45.562	248.060	63.312	0.018	0.166	-0.092	0.216

TABLE A6-15

NGC 4105: MINOR AXIS

r	velocity	err	σ	err	h_3	err	h_4	err
-9.613	66.253	56.865	287.610	63.660	-0.164	0.240	-0.404	0.377
-6.800	-11.076	27.873	243.361	32.630	0.106	0.106	-0.024	0.114
-5.167	41.767	37.886	309.688	28.733	0.076	0.099	0.139	0.105
-4.009	22.206	24.338	283.535	34.077	0.001	0.075	-0.136	0.109
-3.180	9.865	28.872	315.807	26.594	0.044	0.071	0.041	0.075
-2.504	25.53	15.694	288.956	15.782	-0.036	0.044	0.018	0.047
-2.016	25.516	18.632	284.057	22.655	0.073	0.057	-0.070	0.068
-1.680	68.354	23.839	327.022	16.758	0.100	0.060	0.175	0.066
-1.344	2.133	16.576	303.480	16.686	-0.044	0.043	0.008	0.047
-1.008	11.083	18.115	317.555	19.687	0.075	0.046	-0.041	0.052
-0.672	14.812	14.372	288.949	13.448	-0.047	0.040	0.049	0.042
-0.336	-7.478	15.040	318.497	13.816	-0.052	0.037	0.040	0.039
0.000	0.000	14.757	303.940	15.209	0.015	0.038	0.000	0.042
0.336	-3.794	15.515	312.880	13.146	-0.034	0.039	0.082	0.041
0.672	-5.044	19.103	327.555	17.912	-0.008	0.044	0.030	0.048
1.008	-13.082	17.626	301.887	15.988	-0.019	0.046	0.057	0.048
1.344	-31.054	15.749	277.036	16.262	0.006	0.046	0.017	0.049
1.680	-30.863	17.706	305.189	19.507	0.005	0.046	-0.030	0.052
2.169	-7.328	24.048	292.992	18.893	-0.001	0.066	0.133	0.069
2.844	-55.537	53.998	238.476	26.755	0.057	0.277	0.760	0.297
3.668	-5.908	17.948	280.591	24.505	-0.008	0.055	-0.115	0.076
4.829	16.595	19.588	267.684	23.580	0.046	0.063	-0.045	0.073
6.466	58.218	30.208	278.722	34.763	-0.070	0.093	-0.039	0.104
9.289	14.762	67.459	223.187	108.529	0.019	0.327	-0.293	0.556
16.996	63.552	89.328	199.778	151.321	-0.076	0.487	-0.237	0.759

A6.2. LINE STRENGTH INDICES

TABLE A6-16

IC 1459: MAJOR AXIS

r	Mg2	err	Fe5270	err	Fe5335	err	<Fe>	err
-78.960	0.283	0.015	2.888	0.018	1.844	0.051	2.366	0.051
-76.160	0.286	0.014	2.994	0.018	1.960	0.050	2.477	0.050
-73.360	0.291	0.014	2.990	0.017	1.979	0.048	2.484	0.048
-70.560	0.294	0.013	3.000	0.017	2.017	0.046	2.508	0.046
-67.760	0.298	0.013	3.037	0.016	2.097	0.044	2.567	0.044
-64.960	0.300	0.012	3.065	0.016	2.146	0.043	2.605	0.043
-62.160	0.303	0.012	3.081	0.015	2.175	0.041	2.628	0.041
-59.360	0.305	0.012	3.324	0.015	2.515	0.040	2.920	0.040
-56.560	0.308	0.011	3.243	0.014	2.411	0.038	2.827	0.038
-53.760	0.310	0.011	3.175	0.014	2.314	0.037	2.745	0.037
-50.960	0.313	0.010	3.094	0.013	2.171	0.036	2.633	0.036
-48.160	0.315	0.010	3.072	0.013	2.103	0.034	2.588	0.034
-45.360	0.316	0.009	3.095	0.012	2.068	0.032	2.581	0.032
-42.560	0.316	0.009	3.139	0.011	2.089	0.031	2.614	0.031
-39.760	0.315	0.008	3.227	0.011	2.171	0.029	2.699	0.029
-36.960	0.315	0.008	3.290	0.010	2.248	0.028	2.769	0.028
-34.160	0.316	0.007	3.526	0.009	2.595	0.025	3.060	0.025
-31.360	0.317	0.007	3.584	0.009	2.699	0.024	3.141	0.024
-28.560	0.319	0.006	3.653	0.008	2.866	0.022	3.259	0.022
-25.760	0.321	0.006	3.675	0.007	2.983	0.020	3.329	0.020
-22.960	0.326	0.005	3.672	0.007	3.139	0.018	3.405	0.018
-20.160	0.331	0.005	3.658	0.006	3.209	0.016	3.434	0.016
-17.360	0.342	0.004	3.653	0.005	3.234	0.014	3.443	0.014
-14.560	0.350	0.004	3.668	0.004	3.201	0.012	3.435	0.012
-11.760	0.359	0.003	3.704	0.004	3.117	0.010	3.411	0.010
-8.960	0.364	0.003	3.883	0.003	3.343	0.009	3.613	0.009
-6.160	0.367	0.002	3.906	0.003	3.256	0.008	3.581	0.008
-3.360	0.367	0.002	3.914	0.003	3.206	0.007	3.560	0.007
-0.560	0.367	0.002	3.920	0.003	3.435	0.007	3.678	0.007
2.240	0.365	0.002	4.085	0.003	3.392	0.007	3.738	0.007
5.040	0.362	0.002	3.922	0.003	3.338	0.008	3.630	0.008
7.840	0.359	0.003	3.920	0.003	3.027	0.009	3.473	0.009
10.640	0.354	0.003	3.914	0.004	3.017	0.011	3.466	0.011
13.440	0.350	0.004	3.909	0.004	3.032	0.012	3.471	0.012
16.240	0.343	0.004	3.749	0.005	2.819	0.015	3.284	0.015
19.040	0.337	0.005	3.751	0.006	2.856	0.016	3.303	0.016
21.840	0.330	0.006	3.752	0.007	2.895	0.019	3.324	0.019

IC 1459: MAJOR AXIS (CONTINUED)

r	Mg2	err	Fe5270	err	Fe5335	err	<Fe>	err
24.640	0.324	0.006	3.747	0.007	2.905	0.021	3.326	0.021
27.440	0.313	0.007	3.722	0.008	2.902	0.023	3.312	0.023
30.240	0.305	0.007	3.688	0.009	2.896	0.024	3.292	0.024
33.040	0.292	0.008	3.609	0.010	2.881	0.026	3.245	0.026
35.840	0.285	0.008	3.541	0.010	2.863	0.027	3.202	0.027
38.640	0.278	0.008	3.435	0.011	2.820	0.029	3.128	0.029
41.440	0.276	0.009	3.237	0.011	2.561	0.031	2.899	0.031
44.240	0.276	0.009	3.187	0.012	2.533	0.033	2.860	0.033
47.040	0.278	0.010	3.181	0.012	2.525	0.034	2.853	0.034
49.840	0.282	0.010	3.213	0.013	2.528	0.036	2.870	0.036
52.640	0.286	0.011	3.259	0.014	2.534	0.037	2.896	0.037
55.440	0.292	0.011	3.352	0.014	2.544	0.039	2.948	0.039
58.240	0.296	0.012	3.414	0.015	2.550	0.040	2.982	0.040
61.040	0.299	0.012	3.474	0.015	2.559	0.042	3.016	0.042
63.840	0.300	0.013	3.482	0.016	2.567	0.043	3.024	0.043
66.640	0.298	0.013	3.187	0.016	2.209	0.045	2.698	0.045
69.440	0.296	0.013	3.167	0.017	2.209	0.046	2.688	0.046
72.240	0.292	0.014	3.144	0.018	2.196	0.048	2.670	0.048
75.040	0.291	0.014	3.134	0.018	2.178	0.049	2.656	0.049
77.840	0.290	0.015	3.126	0.019	2.149	0.051	2.638	0.051
80.640	0.289	0.015	3.123	0.019	2.132	0.052	2.627	0.052
83.440	0.287	0.016	3.002	0.020	1.981	0.054	2.492	0.054

TABLE A6-17

IC 3370: MAJOR AXIS

r	Mg2	err	Fe5270	err	Fe5335	err	<Fe>	err
-87.92	0.19	0.04	2.45	0.06	2.07	0.16	2.26	0.16
-85.12	0.18	0.04	2.47	0.06	2.14	0.15	2.30	0.15
-82.32	0.17	0.04	2.53	0.05	2.21	0.15	2.37	0.15
-79.52	0.16	0.04	2.57	0.05	2.26	0.14	2.42	0.14
-76.72	0.16	0.04	2.65	0.05	2.32	0.14	2.49	0.14
-73.92	0.16	0.04	2.70	0.05	2.36	0.13	2.53	0.13
-71.12	0.16	0.04	2.78	0.05	2.44	0.13	2.61	0.13
-68.32	0.16	0.03	2.86	0.04	2.53	0.12	2.69	0.12
-65.52	0.16	0.03	2.94	0.04	2.64	0.12	2.79	0.12
-62.72	0.17	0.03	3.01	0.04	2.69	0.11	2.85	0.11
-59.92	0.17	0.03	3.01	0.04	2.69	0.10	2.85	0.10
-57.12	0.18	0.03	2.93	0.04	2.63	0.10	2.78	0.10
-54.32	0.18	0.03	2.79	0.03	2.53	0.09	2.66	0.09
-51.52	0.19	0.03	2.67	0.03	2.45	0.09	2.56	0.09
-48.72	0.19	0.02	2.52	0.03	2.35	0.09	2.43	0.09
-45.92	0.19	0.02	2.44	0.03	2.30	0.08	2.37	0.08
-43.12	0.19	0.02	2.38	0.03	2.24	0.08	2.31	0.08
-40.32	0.19	0.02	2.39	0.03	2.22	0.07	2.30	0.07
-37.52	0.19	0.02	2.43	0.02	2.24	0.07	2.34	0.07
-34.72	0.20	0.02	2.49	0.02	2.25	0.06	2.37	0.06
-31.92	0.20	0.02	2.60	0.02	2.29	0.06	2.45	0.06
-29.12	0.21	0.01	2.73	0.02	2.35	0.05	2.54	0.05
-26.32	0.21	0.01	2.87	0.02	2.50	0.05	2.69	0.05
-23.52	0.22	0.01	2.93	0.01	2.50	0.04	2.71	0.04
-20.72	0.22	0.01	2.99	0.01	2.54	0.03	2.77	0.03
-17.92	0.22	0.01	3.02	0.01	2.59	0.03	2.80	0.03
-15.12	0.23	0.01	3.10	0.01	2.69	0.03	2.89	0.03
-12.32	0.23	0.01	3.12	0.01	2.68	0.03	2.90	0.03
-9.52	0.23	0.01	3.16	0.01	2.66	0.02	2.91	0.02
-6.72	0.24	0.01	3.20	0.01	2.75	0.02	2.98	0.02
-3.92	0.24	0.01	3.18	0.01	2.60	0.02	2.89	0.02
-1.12	0.24	0.01	3.15	0.01	2.56	0.03	2.86	0.03
1.68	0.24	0.01	3.13	0.01	2.49	0.03	2.81	0.03
4.48	0.24	0.01	3.06	0.01	2.37	0.03	2.71	0.03
7.28	0.23	0.01	3.03	0.01	2.28	0.04	2.66	0.04
10.08	0.23	0.01	3.02	0.02	2.25	0.04	2.63	0.04
12.88	0.23	0.01	3.02	0.02	2.23	0.05	2.62	0.05
15.68	0.22	0.02	3.00	0.02	2.10	0.05	2.55	0.05
18.48	0.21	0.02	2.97	0.02	2.02	0.06	2.49	0.06

IC 3370: MAJOR AXIS (CONTINUED)

r	Mg2	err	Fe5270	err	Fe5335	err	<Fe>	err
21.28	0.21	0.02	2.98	0.02	1.99	0.06	2.48	0.06
24.08	0.19	0.02	2.98	0.03	1.97	0.07	2.48	0.07
26.88	0.18	0.02	2.96	0.03	1.96	0.07	2.46	0.07
29.68	0.16	0.02	2.92	0.03	1.97	0.08	2.45	0.08
32.48	0.16	0.02	2.89	0.03	1.97	0.08	2.43	0.08
35.28	0.15	0.03	2.85	0.03	1.96	0.09	2.41	0.09
38.08	0.14	0.03	2.84	0.03	1.95	0.09	2.40	0.09
40.88	0.13	0.03	2.85	0.04	1.94	0.10	2.39	0.10
43.68	0.13	0.03	2.86	0.04	1.94	0.10	2.40	0.10
46.48	0.12	0.03	2.88	0.04	1.98	0.11	2.43	0.11
49.28	0.11	0.03	2.86	0.04	2.00	0.11	2.43	0.11
52.08	0.10	0.03	2.77	0.04	2.04	0.12	2.40	0.12
54.88	0.09	0.03	2.71	0.04	2.04	0.12	2.37	0.12
57.68	0.08	0.04	2.58	0.05	2.01	0.13	2.30	0.13
60.48	0.08	0.04	2.50	0.05	1.98	0.13	2.24	0.13
63.28	0.08	0.04	2.44	0.05	1.87	0.14	2.15	0.14
66.08	0.08	0.04	2.43	0.05	1.76	0.14	2.09	0.14
68.88	0.07	0.04	2.44	0.05	1.62	0.15	2.03	0.15
71.68	0.07	0.04	2.42	0.05	1.57	0.15	1.99	0.15
74.48	0.07	0.04	2.36	0.06	1.55	0.16	1.95	0.16

TABLE A6-18

IC 3370: MINOR AXIS

r	Mg2	err	Fe5270	err	Fe5335	err	<Fe>	err
-81.20	0.20	0.05	2.15	0.07	1.84	0.19	2.00	0.19
-78.40	0.20	0.05	2.28	0.07	1.88	0.19	2.08	0.19
-75.60	0.20	0.05	2.39	0.07	1.82	0.18	2.11	0.18
-72.80	0.20	0.05	2.39	0.06	1.73	0.18	2.06	0.18
-70.00	0.20	0.05	2.31	0.06	1.56	0.17	1.93	0.17
-67.20	0.19	0.05	2.25	0.06	1.48	0.17	1.87	0.17
-64.40	0.17	0.04	2.21	0.06	1.52	0.16	1.87	0.16
-61.60	0.16	0.04	2.23	0.06	1.64	0.16	1.94	0.16
-58.80	0.14	0.04	2.27	0.05	1.84	0.15	2.05	0.15
-56.00	0.14	0.04	2.31	0.05	1.92	0.14	2.11	0.14
-53.20	0.13	0.04	2.30	0.05	1.94	0.13	2.12	0.13
-50.40	0.13	0.04	2.24	0.05	1.88	0.13	2.06	0.13
-47.60	0.13	0.03	2.18	0.04	1.77	0.12	1.98	0.12
-44.80	0.13	0.03	2.14	0.04	1.70	0.11	1.92	0.11
-42.00	0.14	0.03	2.12	0.04	1.60	0.10	1.86	0.10
-39.20	0.14	0.03	2.14	0.03	1.59	0.10	1.87	0.10
-36.40	0.14	0.03	2.25	0.03	1.66	0.09	1.95	0.09
-33.60	0.15	0.02	2.35	0.03	1.75	0.09	2.05	0.09
-30.80	0.15	0.02	2.52	0.03	1.94	0.08	2.23	0.08
-28.00	0.16	0.02	2.62	0.03	2.03	0.08	2.32	0.08
-25.20	0.17	0.02	2.70	0.03	2.11	0.07	2.41	0.07
-22.40	0.17	0.02	2.78	0.02	2.15	0.06	2.47	0.06
-19.60	0.18	0.02	2.82	0.02	2.26	0.06	2.54	0.06
-16.80	0.19	0.01	2.82	0.02	2.22	0.05	2.52	0.05
-14.00	0.19	0.01	2.85	0.02	2.23	0.04	2.54	0.04
-11.20	0.20	0.01	2.90	0.01	2.26	0.04	2.58	0.04
-8.40	0.21	0.01	3.04	0.01	2.36	0.03	2.70	0.03
-5.60	0.22	0.01	3.11	0.01	2.40	0.03	2.75	0.03
-2.80	0.23	0.01	3.23	0.01	2.46	0.03	2.84	0.03
0.00	0.24	0.01	3.30	0.01	2.59	0.03	2.95	0.03
2.80	0.24	0.01	3.31	0.01	2.54	0.03	2.92	0.03
5.60	0.25	0.01	3.29	0.01	2.55	0.03	2.92	0.03
8.40	0.25	0.01	3.27	0.01	2.55	0.03	2.91	0.03
11.20	0.25	0.01	3.19	0.01	2.46	0.03	2.82	0.03
14.00	0.25	0.01	3.15	0.01	2.41	0.04	2.78	0.04
16.80	0.25	0.01	3.12	0.02	2.40	0.05	2.76	0.05
19.60	0.24	0.02	3.04	0.02	2.44	0.05	2.74	0.05
22.40	0.24	0.02	2.93	0.02	2.37	0.06	2.65	0.06
25.20	0.23	0.02	2.75	0.02	2.43	0.07	2.59	0.07

IC 3370: MINOR AXIS (CONTINUED)

r	Mg2	err	Fe5270	err	Fe5335	err	<Fe>	err
28.00	0.23	0.02	2.69	0.03	2.49	0.07	2.59	0.07
30.80	0.22	0.02	2.64	0.03	2.59	0.08	2.62	0.08
33.60	0.21	0.02	2.64	0.03	2.62	0.08	2.63	0.08
36.40	0.20	0.03	2.64	0.03	2.65	0.09	2.65	0.09
39.20	0.19	0.03	2.63	0.03	2.62	0.09	2.62	0.09
42.00	0.18	0.03	2.57	0.04	2.47	0.10	2.52	0.10
44.80	0.17	0.03	2.51	0.04	2.34	0.11	2.42	0.11
47.60	0.16	0.03	2.42	0.04	2.13	0.12	2.28	0.12
50.40	0.15	0.03	2.41	0.04	2.02	0.12	2.21	0.12
53.20	0.14	0.04	2.49	0.05	1.95	0.13	2.22	0.13
56.00	0.13	0.04	2.56	0.05	1.94	0.14	2.25	0.14
58.80	0.13	0.04	2.65	0.05	1.97	0.14	2.31	0.14
61.60	0.13	0.04	2.68	0.05	1.98	0.15	2.33	0.15
64.40	0.12	0.04	2.60	0.06	2.00	0.16	2.30	0.16
67.20	0.11	0.05	2.46	0.06	1.98	0.16	2.22	0.16
70.00	0.10	0.05	2.17	0.06	1.88	0.17	2.02	0.17
72.80	0.09	0.05	1.93	0.06	1.77	0.18	1.85	0.18
75.60	0.08	0.05	1.58	0.07	1.66	0.19	1.62	0.19
78.40	0.07	0.05	1.39	0.07	1.65	0.19	1.52	0.19
81.20	0.06	0.06	1.28	0.07	1.76	0.20	1.52	0.20

TABLE A6-19

IC 3370: INTERMEDIATE AXIS

r	Mg2	err	Fe5270	err	Fe5335	err	<Fe>	err
-81.20	0.21	0.05	2.47	0.06	1.28	0.18	1.87	0.18
-78.40	0.21	0.05	2.48	0.06	1.28	0.17	1.88	0.17
-75.60	0.21	0.04	2.36	0.06	1.22	0.16	1.79	0.16
-72.80	0.20	0.04	2.23	0.06	1.17	0.16	1.70	0.16
-70.00	0.18	0.04	2.08	0.05	1.13	0.15	1.61	0.15
-67.20	0.16	0.04	2.04	0.05	1.18	0.14	1.61	0.14
-64.40	0.15	0.04	2.10	0.05	1.40	0.14	1.75	0.14
-61.60	0.14	0.04	2.22	0.05	1.62	0.13	1.92	0.13
-58.80	0.14	0.03	2.38	0.05	1.98	0.13	2.18	0.13
-56.00	0.14	0.03	2.50	0.04	2.16	0.12	2.33	0.12
-53.20	0.14	0.03	2.58	0.04	2.31	0.11	2.45	0.11
-50.40	0.14	0.03	2.59	0.04	2.32	0.11	2.45	0.11
-47.60	0.15	0.03	2.62	0.04	2.29	0.10	2.45	0.10
-44.80	0.15	0.03	2.65	0.03	2.27	0.10	2.46	0.10
-42.00	0.16	0.03	2.69	0.03	2.27	0.09	2.48	0.09
-39.20	0.16	0.02	2.72	0.03	2.30	0.08	2.51	0.08
-36.40	0.16	0.02	2.73	0.03	2.35	0.08	2.54	0.08
-33.60	0.16	0.02	2.72	0.03	2.37	0.07	2.55	0.07
-30.80	0.16	0.02	2.70	0.02	2.41	0.07	2.55	0.07
-28.00	0.17	0.02	2.68	0.02	2.40	0.06	2.54	0.06
-25.20	0.17	0.02	2.67	0.02	2.39	0.06	2.53	0.06
-22.40	0.18	0.01	2.73	0.02	2.40	0.05	2.56	0.05
-19.60	0.18	0.01	2.78	0.02	2.51	0.04	2.64	0.04
-16.80	0.19	0.01	2.81	0.01	2.48	0.04	2.64	0.04
-14.00	0.20	0.01	2.88	0.01	2.52	0.03	2.70	0.03
-11.20	0.21	0.01	2.94	0.01	2.57	0.03	2.75	0.03
-8.40	0.22	0.01	3.09	0.01	2.70	0.03	2.90	0.03
-5.60	0.22	0.01	3.15	0.01	2.72	0.03	2.94	0.03
-2.80	0.23	0.01	3.24	0.01	2.74	0.02	2.99	0.02
0.00	0.24	0.01	3.29	0.01	2.85	0.02	3.07	0.02
2.80	0.24	0.01	3.26	0.01	2.72	0.02	2.99	0.02
5.60	0.25	0.01	3.22	0.01	2.69	0.03	2.96	0.03
8.40	0.25	0.01	3.19	0.01	2.64	0.03	2.91	0.03
11.20	0.25	0.01	3.10	0.01	2.51	0.03	2.80	0.03
14.00	0.25	0.01	3.03	0.01	2.42	0.04	2.73	0.04
16.80	0.25	0.01	2.98	0.02	2.38	0.04	2.68	0.04
19.60	0.24	0.01	2.90	0.02	2.37	0.05	2.64	0.05
22.40	0.23	0.02	2.83	0.02	2.26	0.05	2.54	0.05
25.20	0.23	0.02	2.72	0.02	2.22	0.06	2.47	0.06

IC 3370: INTERMEDIATE AXIS (CONTINUED)

r	Mg2	err	Fe5270	err	Fe5335	err	<Fe>	err
28.00	0.22	0.02	2.71	0.02	2.21	0.06	2.46	0.06
30.80	0.21	0.02	2.73	0.03	2.18	0.07	2.45	0.07
33.60	0.21	0.02	2.75	0.03	2.13	0.08	2.44	0.08
36.40	0.20	0.02	2.78	0.03	2.06	0.08	2.42	0.08
39.20	0.19	0.02	2.80	0.03	2.01	0.09	2.40	0.09
42.00	0.18	0.03	2.82	0.03	1.95	0.09	2.38	0.09
44.80	0.18	0.03	2.84	0.04	1.91	0.10	2.38	0.10
47.60	0.16	0.03	2.85	0.04	1.89	0.11	2.37	0.11
50.40	0.16	0.03	2.83	0.04	1.90	0.11	2.36	0.11
53.20	0.15	0.03	2.79	0.04	1.95	0.12	2.37	0.12
56.00	0.14	0.03	2.73	0.04	1.99	0.12	2.36	0.12
58.80	0.14	0.04	2.63	0.05	2.03	0.13	2.33	0.13
61.60	0.13	0.04	2.63	0.05	2.02	0.13	2.33	0.13
64.40	0.13	0.04	2.69	0.05	1.96	0.14	2.33	0.14
67.20	0.12	0.04	2.78	0.05	1.91	0.15	2.34	0.15
70.00	0.11	0.04	2.93	0.05	1.85	0.15	2.39	0.15
72.80	0.10	0.04	2.96	0.06	1.82	0.16	2.39	0.16
75.60	0.09	0.05	2.86	0.06	1.81	0.16	2.34	0.16
78.40	0.09	0.05	2.70	0.06	1.81	0.17	2.26	0.17
81.20	0.09	0.05	2.44	0.06	1.84	0.17	2.14	0.17

TABLE A6-20

NGC 3379: MAJOR AXIS

r	Mg2	err	Fe5270	err	Fe5335	err	<Fe>	err
-19.470	0.253	0.012	2.836	0.015	1.765	0.042	2.300	0.042
-18.290	0.255	0.011	2.848	0.014	1.827	0.038	2.338	0.038
-17.110	0.257	0.010	2.959	0.013	2.002	0.035	2.480	0.035
-15.930	0.259	0.009	2.971	0.012	2.057	0.032	2.514	0.032
-14.750	0.261	0.009	2.982	0.011	2.105	0.030	2.544	0.030
-13.570	0.262	0.008	2.992	0.010	2.147	0.027	2.570	0.027
-12.390	0.264	0.007	3.002	0.009	2.183	0.025	2.593	0.025
-11.210	0.265	0.007	3.011	0.009	2.214	0.024	2.613	0.024
-10.030	0.267	0.006	3.020	0.008	2.240	0.022	2.630	0.022
-8.850	0.268	0.006	3.028	0.008	2.262	0.021	2.645	0.021
-7.670	0.270	0.006	3.036	0.007	2.280	0.020	2.658	0.020
-6.490	0.271	0.006	3.157	0.007	2.469	0.019	2.813	0.019
-5.310	0.272	0.005	3.164	0.007	2.483	0.018	2.823	0.018
-4.130	0.273	0.005	3.170	0.006	2.496	0.018	2.833	0.018
-2.950	0.275	0.005	3.176	0.006	2.507	0.017	2.841	0.017
-1.770	0.276	0.005	3.181	0.006	2.516	0.017	2.849	0.017
-0.590	0.277	0.005	3.186	0.006	2.525	0.017	2.855	0.017
0.590	0.278	0.005	3.190	0.006	2.533	0.017	2.861	0.017
1.770	0.279	0.005	3.193	0.006	2.540	0.017	2.866	0.017
2.950	0.280	0.005	3.196	0.006	2.546	0.017	2.871	0.017
4.130	0.281	0.005	3.198	0.007	2.552	0.018	2.875	0.018
5.310	0.281	0.005	3.200	0.007	2.558	0.019	2.879	0.019
6.490	0.282	0.006	3.085	0.007	2.384	0.019	2.735	0.019
7.670	0.283	0.006	3.085	0.007	2.390	0.020	2.738	0.020
8.850	0.283	0.006	3.085	0.008	2.396	0.021	2.740	0.021
10.030	0.284	0.007	3.083	0.008	2.402	0.023	2.743	0.023
11.210	0.285	0.007	3.081	0.009	2.409	0.024	2.745	0.024
12.390	0.285	0.008	3.079	0.010	2.418	0.026	2.748	0.026
13.570	0.286	0.008	3.076	0.010	2.429	0.029	2.753	0.029
14.750	0.287	0.009	3.073	0.011	2.444	0.031	2.758	0.031
15.930	0.288	0.010	3.070	0.012	2.463	0.034	2.767	0.034
17.110	0.290	0.011	3.070	0.014	2.489	0.037	2.779	0.037
18.290	0.293	0.012	2.969	0.015	2.377	0.041	2.673	0.041
19.470	0.298	0.013	2.977	0.017	2.424	0.046	2.700	0.046

TABLE A6-21

NGC 4105: MAJOR AXIS

r	Mg2	err	Fe5270	err	Fe5335	err	<Fe>	err
-21.50	0.19	0.03	2.41	0.04	1.90	0.11	2.16	0.11
-19.49	0.19	0.03	2.43	0.04	1.92	0.10	2.17	0.10
-17.47	0.19	0.03	2.53	0.03	1.94	0.09	2.24	0.09
-15.46	0.20	0.03	2.62	0.03	1.93	0.09	2.28	0.09
-13.44	0.20	0.02	2.70	0.03	1.93	0.08	2.32	0.08
-11.42	0.20	0.02	2.73	0.03	1.95	0.07	2.34	0.07
-9.41	0.21	0.02	2.79	0.02	1.98	0.06	2.39	0.06
-7.39	0.22	0.01	2.83	0.02	2.00	0.05	2.42	0.05
-5.38	0.23	0.01	2.92	0.01	2.06	0.04	2.49	0.04
-3.36	0.24	0.01	3.00	0.01	2.15	0.03	2.58	0.03
-1.34	0.25	0.01	3.11	0.01	2.22	0.02	2.66	0.02
0.67	0.26	0.01	3.15	0.01	2.23	0.02	2.69	0.02
2.69	0.26	0.01	3.15	0.01	2.16	0.02	2.66	0.02
4.70	0.26	0.01	3.10	0.01	2.14	0.03	2.62	0.03
6.72	0.25	0.01	3.04	0.02	2.08	0.05	2.56	0.05
8.74	0.25	0.02	3.01	0.02	2.05	0.06	2.53	0.06
10.75	0.24	0.02	2.98	0.02	1.98	0.07	2.48	0.07
12.77	0.23	0.02	2.98	0.03	1.96	0.08	2.47	0.08
14.78	0.22	0.02	2.97	0.03	1.95	0.08	2.46	0.08
16.80	0.21	0.03	2.92	0.03	1.94	0.09	2.43	0.09
18.82	0.21	0.03	2.86	0.04	1.90	0.10	2.38	0.10
20.83	0.20	0.03	2.83	0.04	1.87	0.11	2.35	0.11

TABLE A6-22

NGC 4105: MINOR AXIS

r	Mg2	err	Fe5270	err	Fe5335	err	<Fe>	err
-21.50	0.14	0.04	2.11	0.06	1.45	0.15	0.00	1.78
-19.49	0.14	0.04	2.05	0.05	1.86	0.14	0.00	1.95
-17.47	0.15	0.04	1.94	0.05	2.08	0.13	0.00	2.01
-15.46	0.16	0.03	1.91	0.04	1.92	0.12	0.00	1.91
-13.44	0.16	0.03	1.86	0.04	1.52	0.10	0.00	1.69
-11.42	0.17	0.02	1.91	0.03	1.50	0.08	0.00	1.71
-9.41	0.19	0.02	2.21	0.03	1.90	0.07	2.05	0.07
-7.39	0.21	0.02	2.43	0.02	2.12	0.06	2.27	0.06
-5.38	0.24	0.01	2.82	0.02	2.28	0.04	2.55	0.04
-3.36	0.25	0.01	2.97	0.01	2.32	0.03	2.65	0.03
-1.34	0.27	0.01	3.13	0.01	2.29	0.02	2.71	0.02
0.67	0.27	0.01	3.17	0.01	2.30	0.02	2.73	0.02
2.69	0.27	0.01	3.19	0.01	2.27	0.03	2.73	0.03
4.70	0.26	0.01	3.15	0.02	2.28	0.04	2.72	0.04
6.72	0.25	0.02	3.08	0.02	2.29	0.06	2.69	0.06
8.74	0.24	0.02	3.01	0.03	2.28	0.07	2.65	0.07
10.75	0.23	0.02	2.80	0.03	2.21	0.08	2.50	0.08
12.77	0.22	0.03	2.68	0.04	2.16	0.10	2.42	0.10
14.78	0.22	0.03	2.44	0.04	1.97	0.11	2.21	0.11
16.80	0.21	0.04	2.29	0.05	1.82	0.13	2.06	0.13
18.82	0.20	0.04	2.02	0.05	1.56	0.17	1.79	0.17
20.83	0.19	0.05	1.91	0.06	1.57	0.36	1.74	0.36

References

Ashman, K.M.: 1992, *Publ. Astron. Soc. Pacific*, **104**, 1109.

Bacon, R., Copin, Y., Monnet, G., Miller, B.W., Allington-Smith, J.R., Bureau, M., Carollo, C.M., Davies, R.L., Emsellem, E., Kuntschner, H., Peletier, R.F., Verolme, E.K. and Tim de Zeeuw, P.T.: 2001, *Mon. Not. R. Astron. Soc.*, **326**, 23.

Bahcall, J., Piran, T. and Weinberg, S. (eds.): 2004, Dark Matter in the Universe, second edition, World Scientific Publishing.

Bahcall, N.A., Lubin, L.M. and Dorman, V.: 1995, *Astrophys. J.*, **447**, L81.

Barnes, J.E.: 2006, home page `http://www.ifa.hawaii.edu/~barnes/`

Bendo, G.J. and Barnes, J.E.: 2000, *Mon. Not. R. Astron. Soc.*, **316**, 315.

Bertin, G.: 2000, Dynamics of Galaxies, Cambridge University Press.

Bertin, G., Saglia, R.P. and Stiavelli, M.: 1992, *Astrophys. J.*, **384**, 423.

Bertin, G., Ciotti, L. and Del Principe, M.: 2002, *Astron. Astrophys.*, **386**, 149.

Bertola, F., Pizzella, A., Persic, M. and Salucci, P.: 1993, *Astrophys. J.*, **416**, L45.

Binney, J.J.: 2004, in the proceedings of IAU Symposium 220, "Dark Matter in Galaxies", S. Ryder, D.J. Pisano, M. Walker and K. Freeman (eds.), Astronomical Society of the Pacific, 3.

Binney, J.J. and Mamon, G.: 1982, *Mon. Not. R. Astron. Soc.*, **200**, 361.

Binney, J.J., Davies, R.D., and Illingworth, G.D.: 1990, *Astrophys. J.*, **361**, 78.

Binney, J.J. and Tremaine, S.: 1987, Galactic Dynamics, Princeton University Press.

Binney, J.J. and Merrifield, M.R.: 1998, Galactic Astronomy, Princeton University Press.

Borriello, A., Salucci, P. and Danese, L.: 2003, *Mon. Not. R. Astron. Soc.*, **341**, 1109.

Bosma, A: 2004, in the proceedings of IAU Symposium 220 "Dark matter in galaxies", S. Ryder, D.J. Pisano, M. Walker, and K. Freeman (eds.), 39.

Bridges, T., Beasley, M., Faifer, F., Forbes, D., Forte, J., Gebhardt, K., Hanes, D., Sharples, R. and Zepf, S.: 2003, `preprint astro-ph/0310324`

Bridges, T., Gebhardt, K., Sharples, R., Faifer, F., Forte, J., Beasley, M., Zepf, S., Forbes, D.A., Hanes, D. and Pierce, M.: 2006, *Mon. Not. R. Astron. Soc.* accepted, astro-ph/0608661

Brighenti, F., Mathews, W.G.: 1997, *Astrophys. J.*, **486**, L83.

Brown, B.A. and Bregman, J.N: 1998, *Astrophys. J.*, **495**, L75.

Brown, B.A. and Bregman, J.N: 2000, *Astrophys. J.*, **539**, 592.

Brown, B.A. and Bregman, J.N: 2001, *Astrophys. J.*, **547**, 154.

Buson, L.M., Sadler, E.M., Zeilinger, W.W., Bertin, G., Bertola, F., Danziger, I.J., Dejonghe, H., Saglia, R.P. and de Zeeuw, P. T.: 1993, *Astron. Astrophys.*, **280**, 409.

Calura, F.: 2004, PhD thesis, Univ. of Trieste.

Caon, N., Capaccioli, M. and D'Onofrio, M.: 1994, *Astron. Astrophys. Suppl. Series*, **106**, 199.

Capaccioli, M., Held, E.V., Lorenz, H. and Vietri, M.: 1990, *Astron. J.*, **99**, 1813.

Cappellari, M., Bacon, R, Bureau, M. et al.: 2006, *Mon. Not. R. Astron. Soc.*, **360**, 1126.

Cappellari, M., Verolme, E.K., van der Marel, R.P., Verdoes Kleijn, G.A., Illingworth, G.D., Franx, M., Carollo, C.M. and de Zeeuw, P.T.: 2002, *Astrophys. J.*, **578**, 787.

Carollo, C.M., Danziger, I.J. and Buson, L.: 1993, *Mon. Not. R. Astron. Soc.*, **265**, 553.

Carollo, C.M., and Danziger, I.J.: 1994a, *Mon. Not. R. Astron. Soc.*, **270**, 523.

Carollo, C.M., and Danziger, I.J.: 1994b, *Mon. Not. R. Astron. Soc.*, **270**, 743.

Carollo, C.M., de Zeeuw, P.T., van der Marel, R.P., Danziger, I.J. and Qian, E.E.: 1995, *Astrophys. J.*, **441**, L25.

Ciardullo, R., Jakoby, G.H. and Dejonghe, H.G.: 1993, *Astrophys. J.*, **414**, 454.

Cinzano, P., and van der Marel, R.P.: 1994, *Mon. Not. R. Astron. Soc.*, **270**, 325.

Ciotti, L.: 1991, *Astron. Astrophys.*, **249**, 99.

Ciotti, L.: 2001, Lecture Notes on Stellar Dynamics, Scuola Normale di Pisa editore.

Ciotti, L. and Pellegrini, S.: 2004, *Mon. Not. R. Astron. Soc.*, **350**, 609.

Clowe, D., Bradač, M., Gonzalez, A.H., Markevitch, M, Randall, S.W., Jones, C. and Zaritsky, D.: 2006, *Astrophys. J.L.* in press, `preprint astro-ph/0608407`

Côté, P., McLaughlin, D.E., Cohen, J.G. and Blakeslee, J.P.: 2003, *Astrophys. J.*, **591**, 850.

Craig, I.J.D and Brown, J.C.: 1986, Inverse Problems in Astronomy, Adam Hilger, Bristol.

Cretton, N. and van der Bosch, F.C: 1999, *Astrophys. J.*, **514**, 704.

Cretton, N., Rix, H-W. and de Zeeuw, P.T.: 2000, *Astrophys. J.*, **536**, 319.

Danziger, I.J.: 1997, Dark and Visible Matter in Galaxies, ASP Conference Series, Vol. 117, M. Persic and P. Salucci (eds.), 28.

David, L.P., Jones, C., Forman, W., Daines, S.: 1994, *Astrophys. J.*, **428**, 544.

Davies, R.L., Burstein, D., Dressler, A., Faber, S.M., Lynden-Bell, D., Terlevich, R.J. and Wegner, G.: 1987, *Astrophys. J. Suppl. Series*, **64**, 581.

Davis, D.S. and White, R.E.: 1996, *Astrophys. J.*, **470**, L35.

Davis, P.J. and Rabinowitz, P.: 1984, Methods of Numerical Integration, second edition, Academic Press, Inc., Harcourt Brace Jovanovich, Publishers.

De Bruyne, V., Dejonghe, H., Pizzella, A., Bernardi, M. and Zeilinger, W.W.: 2001, *Astrophys. J.*, **546**, 903.

Dekel, A., Stoehr, F., Mamon, G.A., Cox, T.J. and Primack, J.R.: 2005, *Nature*, **437**, 707.

De Rijcke, S., Dejonghe, H., Zeilinger, W.W. and Hau, G.K.T.: 2003, *Astron. Astrophys.*, **400**, 119.

de Vaucouleurs, G., de Vaucouleurs, A. Corwin, H.G. Jr. et al.: 1991, Third Reference Catalogue of Bright Galaxies, Springer-Verlag, New York.

de Zeeuw, P.T., Bureau, M., Emsellem, E., Bacon, R., Carollo, C.M., Copin, Y., Davies, R.L., Kuntschner, H., Miller, B.W., Monnet, G., Peletier, R.F. and Verolme, E.K.: 2002, *Mon. Not. R. Astron. Soc.*, **329**, 513.

Diehl, S. and Statler, T.S.: 2006, *Astrophys. J.*, submitted, preprint astro-ph/0606215

Dirsch, B., Richtler, T., Geisler, D., Forte, J.C., Bassino, L.P. and Gieren, W.P.: 2003, *Astron. J.*, **125**, 1908.

Dirsch, B., Richtler, T., Geisler, D. et al.: 2004, *Astron. J.*, **127**, 2114.

Djorgovski, G. and Davis, M.: 1987, *Astrophys. J.*, **313**, 59.

Dressler, A.: 1987, *Astrophys. J.*, **317**, 1.

Evans, N.W., Wilkinson, M.I., Perrett, K.M. and Bridges, T.J.: 2003, *Astrophys. J.*, **583**, 752.

Fabbiano, G., Kim, D.-W. and Trinchieri, G.: 1992, *Astrophys. J. Suppl. Series*, **80**, 531.

Fabbiano, G., Elvis, M., Markoff, S., Siemiginowska, A., Pellegrini, S., Zezas, A., Nicastro, F., Trinchieri, G. and McDowell. J.: 2003, *Astrophys. J.*, **588**, 175.

Faber, S.M., Friel, E.D., Burstein, D. and Gaskell, C.M.: 1985, *Astrophys. J. Suppl. Series*, **57**, 711.

Fabricant, D., Lecar, M. and Gorenstein, P.: 1980, **241**, 552.

Fasano, G. and Bonoli, C. : 1989, *Astron. Astrophys. Suppl. Series*, **79**, 291.

Ferguson, H.C.: 1989, *Astron. J.*, **98**, 367.

Fisher, D.: 1997, *Astron. J.*, **113**, 950.

Forbes, D.A., Reizel, D.B. and Williger, G.M.: 1995, *Astron. J.*, **109**, 1576.

Forman, W., Jones, C. and Tucker, W.: 1985, *Astrophys. J.*, **293**, 102.

Forte, J.C., Faifer, F. and Geisler, D.: 2005, *Mon. Not. R. Astron. Soc.*, **357**, 56.

Franx, M. and Illingworth, G.D.: 1988, *Astrophys. J.*, **324**, L55.

Fukazawa, Y., Botoya-Nonesa, J.G., Pu, J., Ohto, A. and Kawano, N.: 2006, *Astrophys. J.*, **636**, 698.

Gebhardt, K., Richstone, D., Kormendy, J., Lauer, T.R., Ajhar, E.A., Bender, R., Dressler, A., Faber, S.M., Grillmair, C., Magorrian, J. and Tremaine, S.: 2000, *Astron. J.*, **119**, 1157.

Gebhardt, K.: 2004, Coevolution of Black Holes and Galaxies, from the Carnegie Observatories Centennial Symposia, Cambridge University Press, L. C. Ho (Ed.), 248.

Gebhardt, K., Richstone, D., Tremaine, S. Lauer, T.R., Bender, R., Bower, G., Dressler, A. aber, S.M., Filippenko, A.V., Green, R., Grillmair, C., Ho, L.C., Kormendy, J., Magorrian, J. and Pinkney, J.: 2003, *Astrophys. J.*, **583**, 92.
Gerhard, O.: 1993, *Mon. Not. R. Astron. Soc.*, **265**, 213.
Gonzales, J.J.: 1993, Ph.D. Thesis, Univ. of California, Santa Cruz.
Graham, A.W, Colless, M.M, Busarello, G., Zaggia, Z. and Longo, G.: 1998, *Astron. Astrophys. Suppl. Series*, **133**, 325.
Gregg, M.D, Ferguson, H.C., Minniti, D., Tanvir, N. and Catchpole, R.: 2004, *Astron. J.*, **127**, 1441.
Grillmair, C. J., Freeman, K. C., Bicknell, G. V., Carter, D., Couch, W. J., Sommer–Larsen, J. and Taylor, K.: 1994, *Astrophys. J.*, **422**, L9.
Halliday, C.: 1998, Ph.D. Thesis, Univ. of Durham.
Hansen, P.C.: 2001, Regularization Tools. A Matlab Package for Analysis and Solution of Discrete Ill-Posed Problems. Software described in this report is published in Numerical Algorithms, 1994, 6, 1.
Henon, M. and Heiles, C.: 1964, *Astron. J.*, **69**, 73.
Hernquist, L.: 1990, *Astrophys. J.*, **356**, 359.
Hui, X., Ford, H.C., Ciardullo, R. and Jacoby, G.H.: 1993, *Astrophys. J.*, **414**, 463.
Hui, X., Ford, H.C., Freeman, K.C., Dopita, M.A.: 1995, *Astrophys. J.*, **449**, 592.
Humphrey, P.J., Buote, D.A., Gastaldello, F., Zappacosta, L., Bullock, J.S., Brighenti, F. and Mathews, W.G.: 2006, *Astrophys. J.*, **646**, 899.
Irwin, J.A. and Sarazin, C.L.: 1996, *Astrophys. J.*, **471**, 683.
Israel, F.P.: 1998, *Astron. Astrophys. Rev.*, **8**, 237.
Jaffe, W.: 1983, *Mon. Not. R. Astron. Soc.*, **202**, 995.
Jarvis, B.: 1987, *Astron. J.*, **94**, 30.
Jones, C., Stern, C., Forman, W., Breen, J., David, L., Tucker, W. and Franx, M.: 1997, *Astrophys. J.*, **482**, 143.
Jozsa, G., Oosterloo, T. and Morganti, R.: 2003, in the proceedings of IAU Symposium 220 "Dark matter in galaxies", S. Ryder, D.J. Pisano, M. Walker, and K. Freeman (eds.), Astronomical Society of the Pacific, 177.
Kim, D.-W. and Fabbiano, G.: 1995, *Astrophys. J.*, **441**, 182.
Kleinheinrich, M., Schneider, P., Erben, T., Schirmer, M., Rix, H-W., Meisenheimer, K. and Wolf, C.: 2003, `preprint astro-ph/0304208`
Kohonen, T.: 1997, Self-Organizing Maps, Springer-Verlag.
Koopmans, L.V.E. and Treu, T.: 2003, *Astrophys. J.*, **583**, 606.
Kraft, R.P., Vázquez, S.E., Forman, W.R., Jones, C., Murray, S.S., Hardcastle, M.J., Worrall, D.M. and Churazov, E.: 2003, *Astrophys. J.*, **592**, 129.
Kronawitter, A, Saglia, R.P., Gerhard, O. and Bender, R: 2000, *Astron. Astrophys. Suppl. Series*, **144**, 53.
Kuntschner, H.: 2000, *Mon. Not. R. Astron. Soc.*, **315**, 184.
Kuntschner, H., Lucey, J.R., Smith, R.J., Hudson, M.J., Davies, R.L. 2001, *Mon. Not. R. Astron. Soc.*, **323**, 615.
Lawson, C.L. and Hanson, R.J.:1974, Solving Least Squares Problems, Englewood Cliffs, New Jersey: Prentice–Hall.
Loewenstein, M. and White, R.E.: 1999, *Astrophys. J.*, **518**, 50.
Loewenstein, M., Mushotzky, R.F., Angelini, L., Arnaud K.A., Quataert E.: 2001, *Astrophys. J.*, **555**, L21.
Mamon, G.A. and Łokas, E.L.: 2005, *Mon. Not. R. Astron. Soc.*, **362**, 95.
Mateo, M.L.: 1998, *Annu. Rev. Astron. Astrophys.*, **36**, 435.
Mathews, W.G. and Brighenti, F.: 2003a, *Annu. Rev. Astron. Astrophys.*, **41**, 191.
Mathews, W.G. and Brighenti, F.: 2003b, *Astrophys. J.*, **599**, 992.
Matteucci, F.: 2001, Chemical Evolution of the Galaxy, Kluwer Academic Publishers, Dordrecht.
Merritt D.: 1997, *Astron. J.*, *114*, 228.

Milgrom, M.: 1983, *Astrophys. J.*, *270*, 365.
Morganti, R., Pizzella, A., Sadler, E.M. and Bertola, F.: 1995, PASA, **12**, 143.
Morrison H., Flynn C. and Freeman K.C.: 1990, *Astron. J.*, **100**, 1191.
Mould, J.R., Oke, J.B., de Zeeuw, P.T. and Nemec, J.M.: 1990, *Astron. J.*, **99**, 1823.
Murtagh, F.: 1995, *Pattern Recognition Letters*, **16**, 399.
Murtagh, F. and Hernandez-Pajeres, M.: 1995, *Journal of Classification*, **12**, 165.
Napolitano, N.R., Capaccioli, M., Romanowsky, A.J., Douglas, N.G., Merrifield, M.R., Kuijken, K., Arnaboldi, M., Gerhard, O. and Freeman, K.C.: 2005, *Mon. Not. R. Astron. Soc.*, **357**, 691.
Navarro, J.F., Frenk, C. S., White, S.D.M.: 1996, *Astrophys. J.*, **462**, 563.
Oosterloo, T.A., Morganti, R. Sadler, E.M., Vergani, D. and Caldwell, N.: 2002, *Astron. J.*, **123**, 729.
Paolillo, M., Fabbiano, G., Peres, G. and Kim, D.-W.: 2002, *Astrophys. J.*, *565*, 883.
Pellegrini, S. and Ciotti, L.: 2006, *Mon. Not. R. Astron. Soc.*, **370**, 1797.
Peng, E.W., Ford, H.C. and Freeman, K.C.: 2003, *Astrophys. J.*, **602**, 685.
Peng, E.W., Ford, H.C. and Freeman, K.C.: 2004a, *Astrophys. J. Suppl. Series*, **150**, 367.
Peng, E.W., Ford, H.C. and Freeman, K.C.: 2004b, *Astrophys. J.*, **602**, 685.
Peng E.W., Ford, H.C. and Freeman, K.C.: 2004c, *Astrophys. J.*, **602**, 705.
Persic, M., Salucci, P. and Stel, F.: 1996, *Mon. Not. R. Astron. Soc.*, **281**, 27.
Pierce, M., Beasley, M.A., Forbes, D.A., Bridges, T., Gebhardt, K., Faifer, F.R., Forte, J.C., Zepf, S.E., Sharples, R., Hanes, D.A. and Proctor, R.: 2006, *Mon. Not. R. Astron. Soc.*, **366**, 1253.
Pipino, A. and Matteucci, F.: 2003, *Mon. Not. R. Astron. Soc.*, **347**, 968.
Pizzella, A. Amico, P., Bertola, F., Buson, L.M., Danziger, I.J., Dejonghe, H., Sadler, E.M., Saglia, R.P., de Zeeuw, P.T. and Zeilinger, W.W.: 1997, *Astron. Astrophys.*, **323**, 349.
Prada, F., Vitvitska, M., Klypin, A., Holtzman, J.A., Schlegel, D.J., Grebel, E.K., Rix, H-W., Brinkmann, J., McKay, T.A. and Csabai, I.: 2003, *Astrophys. J.*, **598**, 260.
Press, W.H., Teukolsky, S.A., Vetterling, W.T. and Flannery, B.P.: 1994, Numerical Recipes in Fortran, Cambridge University Pres.
Pryor, C. and Meylan, G.: 1993, in Djorgovski, S.G., Meylan, G., eds., ASP Conf. Ser. Vol. 50, Structure and Dynamics of Globular Clusters, p. 357.
Rejkuba, M.: 2004, *Astron. Astrophys.*, **413**, 903.
Richstone, D.O.: 1982, *Astrophys. J.*, **252**, 496.
Richtler T., Dirsch B., Gebhardt K. et al.: 2004, *Astron. J.*, **127**, 2094.
Rix, H.-W., de Zeeuw, P.T., Cretton, N., van der Marel, R.P. and Carollo, C.M.: 1997, *Astrophys. J.*, **488**, 702.
Romanowsky, A.J. and Kochanek, C.S.: 2001, *Astrophys. J.*, **553**, 722.
Romanowsky,A.J., Douglas, N.G., Arnaboldi, M., Kuijken, K., Merrifield, M.R., Napolitano, N.R., Capaccioli, M. and Freeman, K.C.: 2003, *Science*, **5640**, 1696.
Saglia, R.P., Bertin, G. and Stiavelli, M.: 1992, *Astrophys. J.*, **384**, 433.
Saglia, R.P., Bertin, G., Bertola, F., Danziger, I.J., Dejonghe, H., Sadler, E.M., Stiavelli, M., de Zeeuw, P.T. and Zeilinger, W.W.: 1993, *Astrophys. J.*, **403**, 567.
Saglia, R.P., Kronawitter, A., Gerhard, O. and Bender, R.: 2000, *Astron. J.*, **119**, 153.
Samurović, S.: 2003, in the Proceedings of the IV Serbian Conference on Spectral Line Shapes, Arandjelovac, Serbia, 10-15 October 2003, *Publ. Astron. Obs. Belgrade*, **76**, 117.
Samurović, S.: 2005, in the Proceedings of the V Serbian Conference on Spectral Line Shapes, Vršac, Serbia, 6-10 June 2005, *Memorie della Società Astronomica Italiana Supplement*, **7**, 68.
Samurović, S.: 2006, *Serb. Astron. J.*, **173**, 35.
Samurović, S., Ćirković, M.M. and Milošević-Zdjelar, V.: 1999, *Mon. Not. R. Astron. Soc.*, **309**, 63.
Samurović, S. and Danziger, I.J.: 2005, *Mon. Not. R. Astron. Soc.*, **363**, 769.
Samurović, S. and Danziger, I.J.: 2006, *Astron. Astrophys.*, **458**, 79.

Sansom, A.E., O'Sullivan, E., Forbes, D.A., Proctor, R.N. and Davis, D.S.: 2006, *Mon. Not. R. Astron. Soc.*, **370**, 1541.
Sargent, W.L.W., Schechter, P.L., Boksenberg, A. and Shortridge, K. : 1977, *Astron. J.*, **212**, 326.
Schwarzschild, M.: 1979, *Astrophys. J.*, **232**, 236.
Simkin, S.M.: 1974, *Astron. Astrophys.*, **31**, 129.
Sivakoff, G.R., Sarazin, C.L. and Carlin J.L.: 2004, *Astrophys. J.*, **617**, 262.
Slee, O. B., Sadler, E. M., Reynolds, J. E. and Ekers, R. D.: 1994, *Mon. Not. R. Astron. Soc.*, **269**, 928.
Sluis, A.P.N. and Williams, T.B.: 2006, *Astron. J.*, **131**, 2089.
Sofue, Y. and Rubin, V.: 2001, *Annu. Rev. Astron. Astrophys.*, **39**, 137.
Sparks, W.B., Hough, J.H., Axon, D.J., and Bailey, J.: 1986, *Mon. Not. R. Astron. Soc.*, **218**, 429.
Statler, T., Dejonghe, H., and Smecker-Hane, T.: 1999, *Astron. J.*, **117**, 126.
Statler, T. and McNamara, B.R.: 2002, *Astrophys. J.*, **581**, 1032.
Statler, T.: 1987, *Astrophys. J.*, **321**, 113.
Statler, T.: 1995, *Astron. J.*, **109**, 1371.
Statler, T., and Smecker-Hane, T.: 1999, *Astrophys. J.*, **117**, 839.
Statler, T., Smecker-Hane, T. and Cecil, G.N: 1996, *Astron. J.*, **111**, 1512.
Tantalo, R., Bressan, A. and Chiosi, C.: 1998, *Astron. Astrophys.*, **333**, 419.
Teodorescu, A.M., Méndez, R.H., Saglia, R.P. et al.: 2005, *Astrophys. J.*, **635**, 290.
Tonry, J. and Davis, M.: 1979 : *Astron. J.*, **84**, 1511.
Tonry, J.L.: 1983, *Astrophys. J.*, **266**, 58.
Treu, T. and Koopmans, L.V.E.: 2002, *Astrophys. J.*, **575**, 87.
Treu, T., Koopmans, L.V.E., Sand, D.J., Smith, G.P. and Ellis, R.S: 2004, in the proceedings of IAU Symposium 220 "Dark matter in galaxies", S. Ryder, D.J. Pisano, M. Walker, and K. Freeman (eds.), Astronomical Society of the Pacific, 159.
Trinchieri, G., Fabbiano, G., Canizares, C.R.: 1986, *Astrophys. J.*, **310**, 637.
Trinchieri, G, Kim, D.-W., Fabbiano, G. and Canizares, C.R.C.: 1994, *Astrophys. J.*, **428**, 555.
van der Marel, R.P.: 1991, *Mon. Not. R. Astron. Soc.*, **253**, 710.
van der Marel, R.P.: 2006, homepage at : `http://www-int.stsci.edu/~marel/`
van der Marel, R.P., Binney, J. and Davies, R.L.: 1990, *Mon. Not. R. Astron. Soc.*, **245**, 582.
van der Marel, R.P., Cretton, N., de Zeeuw, P.T. and Rix, H-W.: 1998, *Astrophys. J.*, **493**, 613.
van der Marel, R.P., and Franx, M.: 1993, *Astrophys. J.*, **407**, 525.
van Gorkom, J.H., van der Hulst, J.M., Haschick, A.D. and Tubbs, A.D.: 1990, *Astron. J.*, **99**, 1781.
Verdoes Kleijn, G.A., van der Marel, R.P., Carollo, C.M., and de Zeeuw, P.T.: 2000, *Astron. J.*, **120**, 1221.
Williams, T.B. and Schwarzschild, M.: 1979, *Astrophys. J.*, **227**, 56.
Woodley, K.A.: 2006, *Astron. J.* accepted, preprint astro-ph/0608497
Woodley, K.A., Harris, W.E. and Harris, G.L.H.: 2005, *Astron. J.*, **129**, 2654.
Worthey, G.: 1994, *Astrophys. J. Suppl. Series*, **95**, 107.
Zeilinger, W.W., Pizzella, A., Amico, P., Bertin, G., Bertola, F., Buson, L. M., Danziger, I.J., Dejonghe, H., Sadler, E.M., Saglia, R.P. and de Zeeuw, P.T.: 1996, *Astron. Astrophys. Suppl. Series*, **120**, 257.